

MOTION CONTRAST USING OPTICAL COHERENCE TOMOGRAPHY

Thesis by

Jeffrey Paul Fingler

In Partial Fulfillment of the Requirements for the

degree of

Doctor of Philosophy



CALIFORNIA INSTITUTE OF TECHNOLOGY

Pasadena, California

2007

(Defended May 3, 2007)

© 2007

Jeffrey Paul Fingler

All Rights Reserved

ACKNOWLEDGEMENTS

I would like to my advisor, Professor Scott Fraser, for being the ideal mentor for me during my Ph.D. research. Through all the continual “threats” of a terminal Master’s degree, Scott has provided me with the freedom to explore in my research while still giving solid direction when I needed it. The most amazing thing is that Scott predicted where my research would be at the end of my thesis in one of the first meetings we ever had.

I would like to thank my committee members Professors Rob Phillips, Kerry Vahala, and Changhuei Yang for their continued patience and support since the time of my candidacy exam. Additional thanks go to Changhuei Yang for providing me with advice and lab space for more than two years in which I was missing lab space of my own.

The work in this thesis would not have been completed without the help of many people. I would like to thank Dr. Dan Schwartz, an ophthalmologist at UCSF, for acquiring funding for this project as well as providing guidance for the research progression. For the zebrafish experiments, Le Trinh was instrumental in teaching me to breed, handle, and mount these animals for imaging. Julien Vermot was very helpful in providing me with extra zebrafish for imaging when I did not have the time to breed some of my own. For the mice imaging, Carol Readhead was responsible for all of the details associated with the acquisition and handling of the animals, which allowed me to focus on only the imaging considerations and saving me a lot of time and effort. Special thanks also go out to Rusty Lansford, David Huss, and Greg Poynter for setting up some sample systems for me. Thanks also go out to my officemate, labmate, and fellow optical experimenter Jon Williams for all the experimental discussions over the years.

I would like to thank the entire Fraser lab group for providing a very social atmosphere which included a weekly beer hour to allow the required unwinding after a long week. For all of the help these people have contributed to make my thesis research possible, I would like to thank all of them. Finally I would like to acknowledge myself, without whom none of this thesis would be possible.

ABSTRACT

Diagnosis of ophthalmic diseases like age-related macular degeneration is very important for treatment of the disease as well as the development of future treatments. Optical coherence tomography (OCT) is an optical interference technique which can measure the three-dimensional structural information of the reflecting layers within a sample. In retinal imaging, OCT is used as the primary diagnostic tool for structural abnormalities such as retinal holes and detachments. The contrast within the images of this technique is based upon reflectivity changes from different regions of the retina.

This thesis demonstrates the developments of methods used to produce additional contrast to the structural OCT images based on the tiny fluctuations of motion experienced by the mobile scatterers within a sample. Motion contrast was observed for motions smaller than 50 nm in images of a variety of samples. Initial contrast method demonstrations used Brownian motion differences to separate regions of a mobile Intralipid solution from a static agarose gel, chosen in concentration to minimize reflectivity contrast.

Zebrafish embryos in the range of 3-4 days post fertilization were imaged using several motion contrast methods to determine the capabilities of identifying regions of vascular flow. Vasculature identification was demonstrated in zebrafish for blood vessels of all orientations as small as 10 μm in diameter. Mouse retinal imaging utilized the same motion contrast methods to determine the contrast capabilities for motions associated with vasculature within the retina. Improved contrast imaging techniques demonstrated comparable images to fluorescein angiography, the gold standard of retinal vascular imaging. Future studies can improve the demonstrated contrast analysis techniques and apply them towards human retinal motion contrast imaging for ophthalmic diagnostic purposes.

TABLE OF CONTENTS

Acknowledgements	iii
Abstract	iv
Table of Contents.....	v
List of Figures	vii
Chapter 1: Introduction.....	1
1.1 Introducing Age-related Macular Degeneration.....	1
1.2 Current Approaches to Disease Treatment.....	11
1.3 Current Diagnostic Technologies and Limitations.....	13
1.4 References	23
Chapter 2: Optical Coherence Tomography	25
2.1 Basics of Optical Coherence Tomography (OCT).....	25
2.2 Axial Resolution.....	29
2.3 Acquiring Fringe Data to Create OCT Images.....	33
2.4 SNR of Time Domain OCT	36
2.5 Spectral Domain OCT (SDOCT).....	38
2.6 SNR of SDOCT.....	41
2.7 SDOCT Limitations	47
2.8 Phase Changes as Basis of Contrast	49
2.9 Choosing Between TDOCT and SDOCT.....	51
2.10 References	53
Chapter 3: Tradeoffs and Experimental Methods.....	55
3.1 OCT System Tradeoffs	55
3.2 Imaging Tradeoffs	65
3.3 Phase Contrast Tradeoffs	69
3.4 Phase Contrast Method: MB-scan	82
3.5 Phase Contrast Method: BM-scan	90
3.6 References	100
Chapter 4: Motion Contrast Imaging using Zebrafish.....	101
4.1 Choosing Zebrafish as the Animal Model.....	101
4.2 Creating SDOCT Images	103
4.3 Sample Preparation.....	106
4.4 Bulk Motion Removal.....	108
4.5 Zebrafish Tail Contrast Imaging: MB-scan versus BM-scan	110
4.6 Zebrafish Tail Motion Contrast over Time.....	117
4.7 Segmental Vessel Imaging.....	123
4.8 En face Images over Zebrafish Heart	126
4.9 References	130

Chapter 5: Mouse Retinal Imaging	131
5.1 Human Retinal OCT Imaging Explained	131
5.2 Differences between Human and Mouse Eye Imaging.....	133
5.3 Aligning Retinal SDOCT Images	136
5.4 Phase Contrast Imaging.....	138
5.5 En face Motion Contrast Images.....	156
5.6 Improving BM-scan Capabilities.....	164
5.7 Discussions of Human Contrast Imaging	171
5.8 References	174
Chapter 6: Summary and Conclusions.....	175

LIST OF FIGURES

<i>Figure</i>	<i>Page</i>
1.1. Side View Image of the Eye	2
1.2. Schematic Image of Retina	2
1.3. Daily Photoreceptor Renewal Process	4
1.4. Lipid Content of Bruch's Membrane versus Age	5
1.5. Electron Micrograph Images of Bruch's Membrane.....	6
1.6. Histology of Normal and Lipid-filled Retinas	6
1.7. Bruch's Membrane Hydraulic Conductivity versus Age	7
1.8. Bruch's Membrane Permeability versus Age.....	7
1.9. Fundus Photography Image of Healthy Eye.....	8
1.10. Simulated Images of AMD Vision Loss	9
1.11. Wet AMD Schematic	10
1.12. AMD Prevalence Statistics for the United States.....	11
1.13. Retinal Histology Comparison with Schematic Image	14
1.14. Snellen Chart for Visual Acuity Diagnostic	15
1.15. Amsler Grid for Wet AMD Diagnostic	16
1.16. Fundus Photography Images for AMD Eyes	17
1.17. Fluorescein Angiography Images	18
1.18. Absorption Spectra of Water.....	20
1.19. Labeled Schematic Image of Retina	21
1.20. Stratus OCT Image of Retina.....	22
2.1. Michelson Interferometer Schematic.....	26
2.2. Interference for Narrow and Broadband Light Sources	28
2.3. Reflectivity Profile versus Interference Signal.....	28
2.4. Gaussian and Top-Hat Spectral Functions	31
2.5. Coherence Function Calculations	32
2.6. Illustration of Single Point Measurement.....	34
2.7. Illustration of Fringe Sampling	35
2.8. SDOCT Image Mirroring Example	47
3.1. Absorption Spectra of Retinal Rods and Cones	58
3.2. Spectral Shape of Superluminescent Diode.....	59
3.3. Coherence Function of Superluminescent Diode.....	60
3.4. Fiber Optic Michelson Interferometer Schematic	61
3.5. Optimizing Coupler Parameters to Maximize Light Collection	62
3.6. OCT Signal Drop with Axial Motion	67
3.7. Minimum Transverse Scan to Reduce OCT Signal	68
3.8. OCT Signal Drop for Fixed Transverse Scan.....	69
3.9. Schematic of Flow Measurement	71
3.10. Phase Errors Created by Transverse Scanning.....	75

<i>Figure</i>	<i>Page</i>
3.11. Minimum Flow Velocity to Demonstrate Variance Contrast	77
3.12. Non-averaged MB-scan Intensity Images of Agarose/Intralipid	83
3.13. Averaged MB-scan Intensity Images of Agarose/Intralipid	84
3.14. Varying Time Separation of MB-scan Phase Variance Image	85
3.15. Altering Statistics of MB-scan Phase Variance Image	86
3.16. Varying Imaging Time of MB-scan Phase Contrast Image	87
3.17. Applying Thresholds to MB-scan Phase Contrast Images	88
3.18. Schematic of Transverse Scan Patterns	91
3.19. Measured SNR-limited Phase Noise	93
3.20. BM-scan Intensity Images of Agarose Wells	94
3.21. Altering Statistics of BM-scan Phase Variance Image	96
3.22. Altering Statistics of BM-scan Phase Contrast Image	96
3.23. Median Filtering of BM-scan Contrast Image	97
3.24. Varying Bulk Phase Removal Method	98
4.1. Bright Field Illumination Image of Zebrafish	102
4.2. Vascular Image of Zebrafish	102
4.3. Schematic of SDOCT Microscopy System	103
4.4. Improving Background Spectrum Removal	106
4.5. Data Processing Schematic for Phase Information	108
4.6. Simulated Phase Change Data for Large Bulk Motion	110
4.7. Zebrafish Tail Contextual Images	111
4.8. MB-scan Images over Zebrafish Tail	112
4.9. BM-scan Images over Zebrafish Tail	113
4.10. Contrast Visualization Compared to Histology Venus	115
4.11. MB-scan Zebrafish Tail Images	116
4.12. Comparison of Zebrafish Contrast Visualization	117
4.13. BM-scan Zebrafish Tail Contrast Images over Time	118
4.14. Schematic of Summation Images	119
4.15. Segmental Vessel Contrast over Time	120
4.16. Dorsal Aorta and Axial Vein Contrast over Time	120
4.17. High-Resolution Confocal Images of Tail Vasculature	122
4.18. Schematic Description of En face Image Locations	124
4.19. En face Intensity and Phase Contrast Segmental Vessel Images	125
4.20. BM-scan Images over Zebrafish Heart	127
4.21. Zebrafish Heart Contrast Image over Time	128
4.22. Zebrafish Heart Contrast over Time	129
4.23. En face Images over Zebrafish Heart	130

<i>Figure</i>	<i>Page</i>
5.1. Schematic of Human Retinal SDOCT System.....	132
5.2. Retinal Images from Commercial OCT system	132
5.3. Photograph of Mouse	133
5.4. Schematic of Mouse Retinal SDOCT System.....	134
5.5. Photograph of Sample Arm of Mouse SDOCT System	136
5.6. Dilation of Mouse Pupil.....	137
5.7. Fundus Camera Image of Mouse Retina	137
5.8. Mouse Retinal B-scan Comparison	139
5.9. MB-scan Doppler Images of Retina	140
5.10. MB-scan Variance Images of Retina.....	142
5.11. MB-scan Contrast Images of Retina.....	143
5.12. Single Scan Contrast Method Images.....	145
5.13. High Density Single Scan Contrast Images.....	147
5.14. BM-scan Images of Retina.....	149
5.15. En face Intensity Images Demonstrating Transverse Motion.....	150
5.16. En face Single Scan Contrast Images during Transverse Motion ..	151
5.17. BM-scan Contrast Image for Large Transverse Motion	152
5.18. Additional Motion Removal Images	153
5.19. Comparison of Low Noise and Noise Removal Cases	154
5.20. Noise Removal Comparison for Contrast Image over Time	154
5.21. En face BM-scan Images during Transverse Motion.....	155
5.22. En face Single Scan Contrast Images	157
5.23. En face BM-scan Contrast Images.....	158
5.24. Schematic Limitation of Curved Retina	159
5.25. Demonstration of Retinal Flattening.....	159
5.26. Overlay of BM-scan Intensity and Contrast Images	160
5.27. En face BM-scan Images: Top of Retina.....	161
5.28. En face BM-scan Images: Bottom of Retina.....	161
5.29. En face BM-scan Contrast Image Comparison	162
5.30. Fluorescein Angiography of Mouse Retina.....	163
5.31. En face BM-scan Retinal Comparison Images.....	165
5.32. Repeating BM-scan En face Contrast Images: Top of Retina	165
5.33. Comparing Mean En face Contrast Images.....	166
5.34. Comparing Images with Different Scan Directions	167
5.35. Mean Contrast Image of Multiple Data Sets	168
5.36. Comparison of Phase Contrast with Angiography.....	169
5.37. Sliding Summation Window Phase Contrast Images.....	170
5.38. Ultra-high Resolution SDOCT Image of Human Retina.....	172
5.39. High Resolution Fluorescein Angiography Images	173

INTRODUCTION

1.1 Introducing Age-related Macular Degeneration

Age-related macular degeneration (AMD) is the most common form of vision loss in the western world for people over the age of 50. Approximately 9 million people in the United States suffer diminished vision due to AMD, with a prevalence that increases with the age of patients. While 7% of the population between the ages of 60-69 have this disease, the percentages increase to approximately 14% for the ages of 70-79 and over 35% for the population over the age of 80 [1,2]. With the aging population in this country (the first baby boomers turn 65 in 2011), the number of people in the high-prevalence age ranges increases over time [3]. The occurrence of AMD is estimated to double within approximately the next 15 years [4].

To understand the source of age-related macular degeneration, changes occurring within the retina of the eye over time must be understood. The retina is a thin layer of tissue in the inner eye responsible for vision. With the front of the eye defined as the location of the pupil and lens, the retina is located in the inner globe at the back of the eye. There are many layers in the retina, but the region of interest is the outermost layers extending from the photoreceptors to the choroid, the ocular blood supply.

Light entering the eye is focused by the lens onto the retina at the back of the eye, including the central vision region called the macula. The light passes through the top layers of the retina which contain blood vessels to supply the retina as well as the nerve fibers which combine to form the optic nerve to the brain. The light then arrives on the photoreceptors, the light sensitive cells which translate photons into electrical signals interpreted by the brain as vision. The highly pigmented membrane called the retinal pigment epithelium (RPE) reduces any incoming light penetrating deeper into the retina.

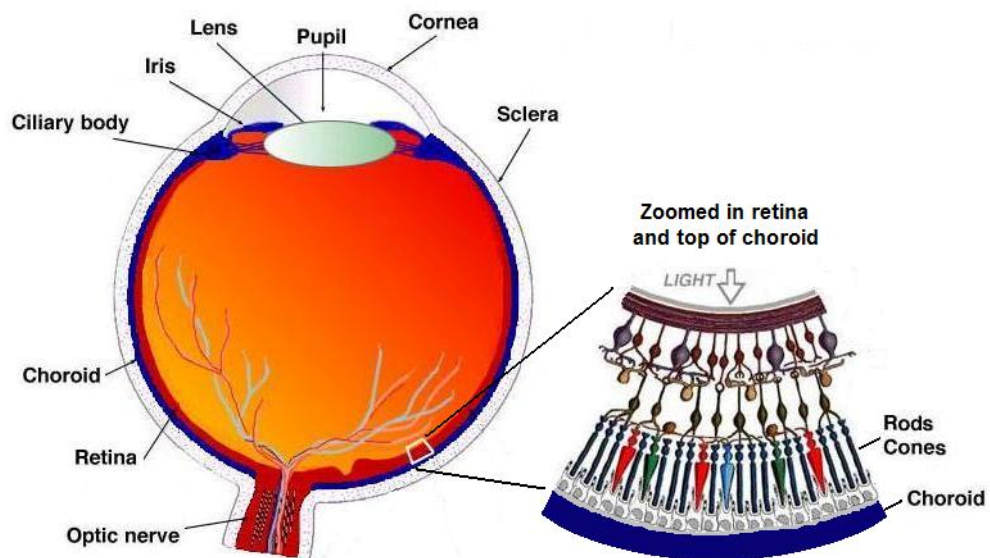


Figure 1.1: Schematic of a human eye with a zoomed-in region of the retina. Image reproduced from [5].

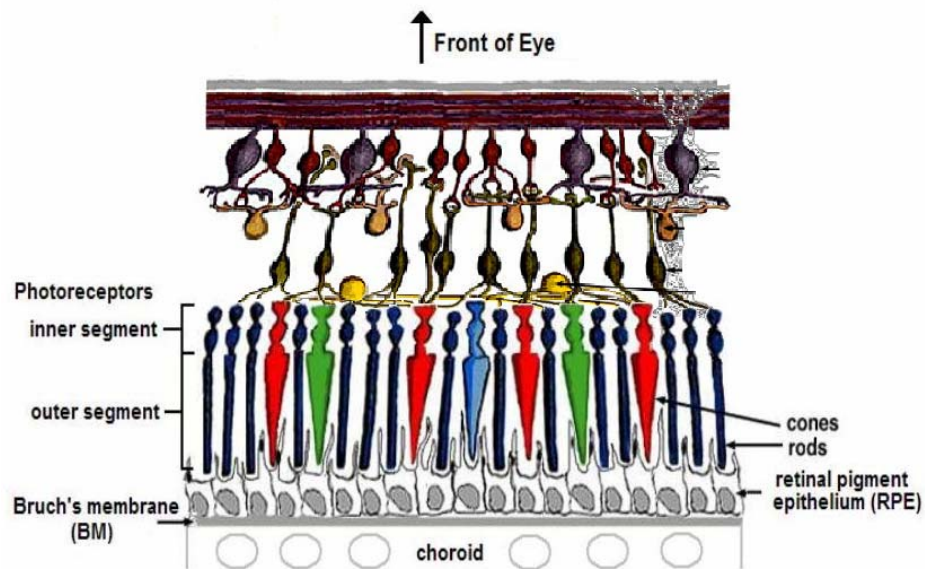


Figure 1.2: Schematic image of the major structures of the lower retina. Image reproduced from [5].

There are two types of photoreceptors, defined as rods and cones. Rods are extremely light-sensitive cells responsible for vision in low-light scenarios requiring night vision. Cones are the main cells responsible for daylight vision, less sensitive than rods and with three types differentiated by the three different spectral sensitivities of the cells. The variety of spectral sensitivities of the cones and the lack of color differentiation of the rods are the reasons normal vision is experienced in color but night vision is only in black and white.

High-resolution imaging occurs in the central part of the macular region of the retina, called the fovea. For this region, the cells located above the photoreceptors are thinned and contain no blood vessels. This allows minimal image signal degradation before arriving at the photoreceptors. While for most of the retina, the photoreceptors contain a mixture of rods and cones, the central fovea region contains only a tightly packed region of cones.

The process of converting incoming light into nerve signals in the photoreceptors is accomplished through photosensing pigments called rhodopsin. Disc-shaped lipid membranes containing rhodopsin are packed into the outer segments of the photoreceptors. As the chemical in the discs becomes bleached over the course of a day, the spent photoreceptor outer segment discs must be removed to maintain vision quality [6,7]. Approximately 10% of all outer segment discs are shed each day while the same amount of new discs is produced by the inner segment of the photoreceptors.

Phagocytosis is a process by which a cell engulfs and digests microorganisms and cellular debris. The RPE cells undergo the process of phagocytosis, in which the cells extend out and pinch off the outermost discs of the photoreceptors [8,9]. This circadian process is synchronized with the end of the daily cycle of the rods and cones separately [10,11]. (Early morning for rods and beginning of nightfall for cones) Metabolic waste produced by the cells passes from the RPE through Bruch's membrane (BM) to the choroidal blood supply for disposal.

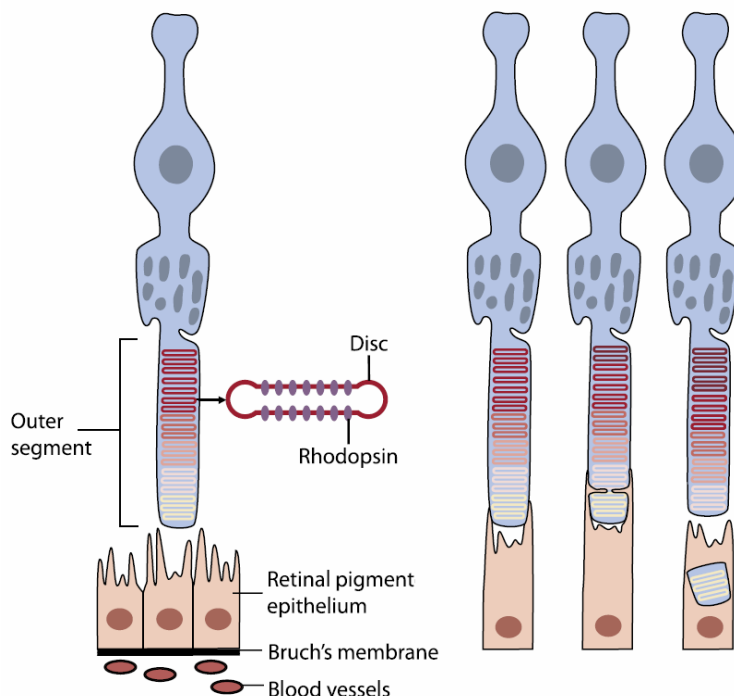


Figure 1.3: Schematic of daily phagocytosis process: RPE cells pinching off the used outer segments of photoreceptors while new segments grow in their place.

Bruch's membrane is a five-layer matrix separating the RPE from the choroid [12]. The collagenous fibers that compose these layers create a basket-weave-type structure. A decline in the RPE phagolysosomal processing associated with the accumulation of lipid-based molecules called lipofuscin within the RPE cells occurs over time within the eye [13,14,15]. Also occurring over time, a portion of the sticky lipid waste product passing through Bruch's membrane attaches itself to the structure. As the ability of the RPE to break down and metabolize the lipids of the photoreceptor discs decreases over time, the amount of "sticky" lipids that are likely to attach themselves to Bruch's membrane increases as well. With an increased amount of lipids attached to BM, there is an increased chance that future metabolic waste will also become blocked from passing through the membrane.

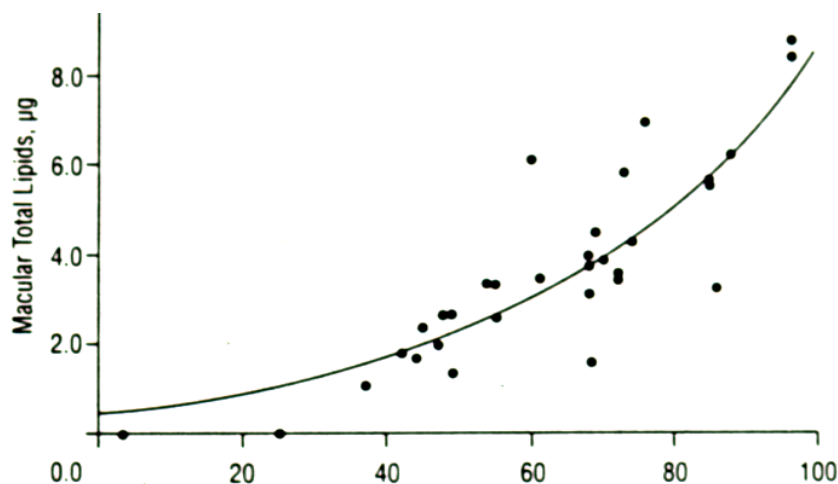


Figure 1.4: The total lipid content present in the macular region of Bruch's membrane as a function of the patient age. Data reproduced from [16].

With the decreased metabolism of the RPE cells and the increased blocking of waste passage by Bruch's membrane, the expected rate of lipids getting stuck to Bruch's membrane should increase in time. If this rate increases linearly with time, the resulting amount of lipids attached to BM should be an exponential increase over time. Using histological sections of human retinas and analyzing the total lipid content of Bruch's membrane of the macular region, this trend has been experimentally verified [16]. The rate of lipid deposition on Bruch's membrane depends on the amount of metabolic waste passing through the membrane. With the highest density of photoreceptors located within the macular region of the retina (high resolution central vision region), this region accumulates the largest amount of lipids over time.

The accumulation of lipids on and within Bruch's membrane does not change the fundamental structure of the membrane itself. Excised Bruch's membrane tissue of an aged eye has been demonstrated to contain an increased amount of lipids. Electron microscopy images of the tissue from an aged eye visualized a lipid-filled Bruch's membrane. Removal of the lipids using ethanol reveals the collagenous layered structure of Bruch's membrane as shown in Figure 1.5. The lipid accumulations which occur on and within Bruch's membrane are referred to as basal linear deposits and basal lamellar deposits. The build up

of these deposits thickens the membrane over the lifetime of patients. Histological measurements of excised retinal tissues have determined a typical thickness change of Bruch's membrane to more than double over ten decades of patient age [17].

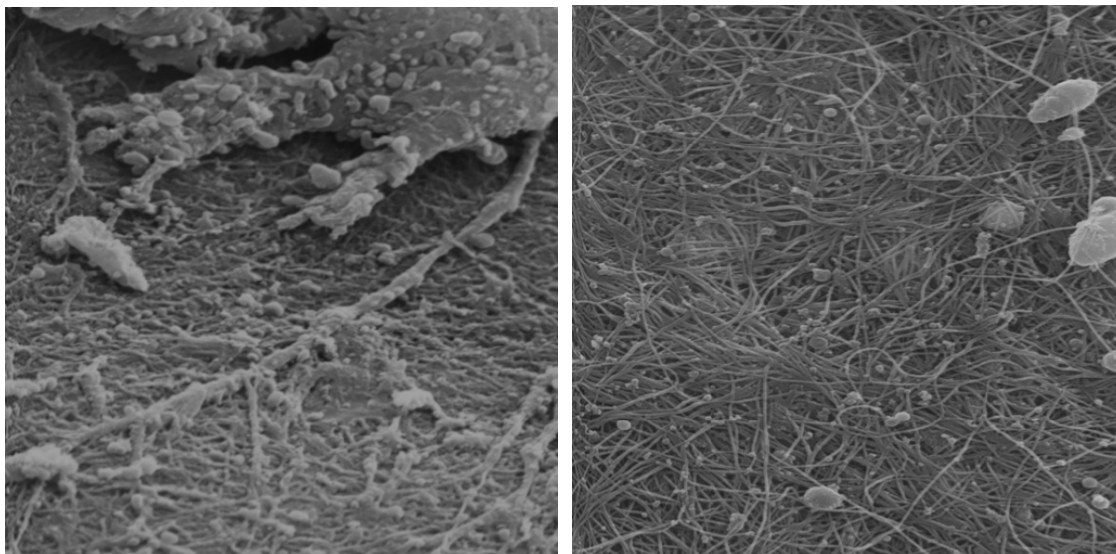


Figure 1.5: Electron micrograph images of Bruch's membrane with lipids before (left) and after (right) the application of ethanol. Images reproduced from [8].

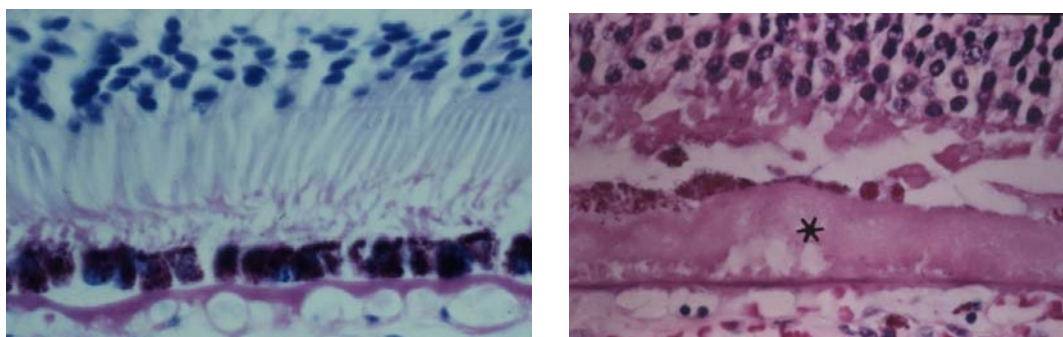


Figure 1.6: Histology images of normal retina (left) and retina containing thickened Bruch's membrane (right). Images reproduced from [18].

The result of this thickening does not only affect the amount of future metabolic waste that can pass through the membrane. The flow of nutrients and oxygen passing from the choroidal blood vessels through Bruch's membrane to supply the retina is also adversely

affected. [19,20] Experiments have demonstrated a measurable drop in the permeability of macromolecules and hydraulic conductivity through Bruch's membrane as a function of patient age. Limited sampling and variability between human subjects and experimental setups could be a cause for discrepancies to the functional form of the decrease over time (i.e., linear versus exponential decrease with respect to patient age).

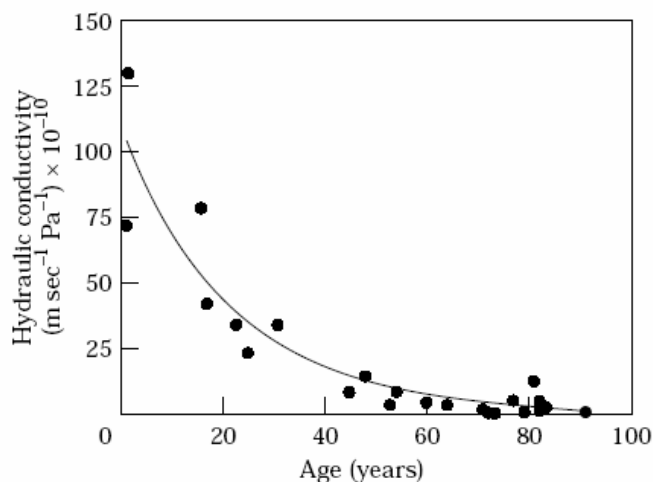


Figure 1.7: Decrease of the hydraulic conductivity of Bruch's membrane over patient age. Data reproduced from [19].

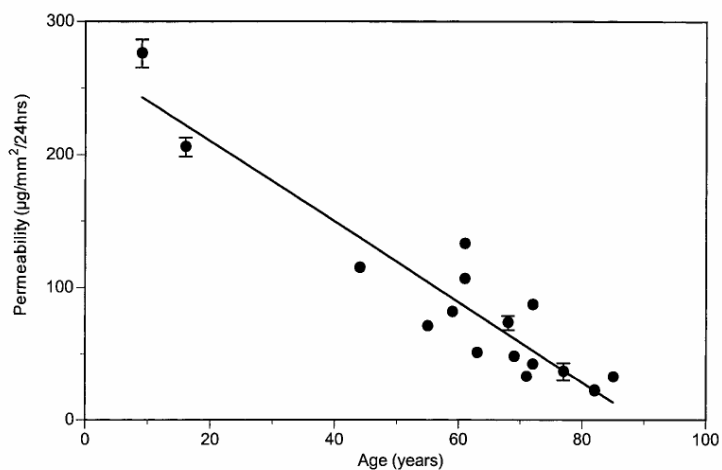


Figure 1.8: Decrease of the macromolecular permeability of Bruch's membrane over patient age. Data reproduced from [20].

With a decreased supply of oxygen from the choroidal blood vessels as Bruch's membrane becomes filled with lipids, there is an increased reliance on the retinal blood vessels which lie on top of the retina. These vessels are supplied directly from the optic nerve head, the ocular connection of blood and nerve signals to the rest of the body. Fundus photography takes a picture of the globe of the retina taken through the pupil of the eye. The shadowing of the reflected light due to the major retinal blood vessel absorption can be seen in this type of picture. The foveal region of the retina which produces the highest visual resolution does not have any major blood vessels on the top of the retina.

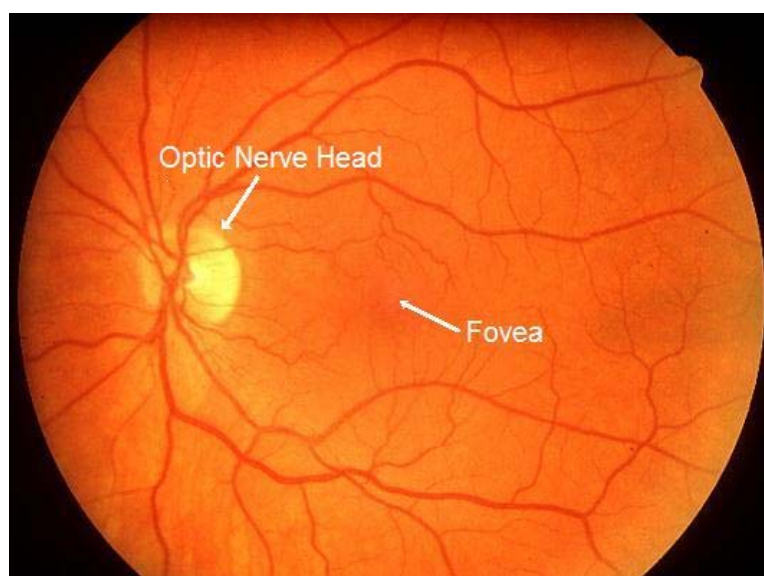


Figure 1.9: Fundus Photography image of normal healthy eye. The darker image regions demonstrate retinal blood vessel absorption. The fovea is the high-visual-resolution central vision region of the eye and the optic nerve head connects the eye to the rest of the body.

The oxygen deprivation of the photoreceptors in the fovea causes a decrease of photoreceptor operation in the central vision of the patient. The form of the disease causing vision loss due to the accumulation of lipids is called dry AMD. Over time, the lack of oxygen in dry AMD can result in death of retinal cells such as the RPE in the foveal region. For this form of the disease the majority of peripheral vision is maintained, allowing for a fraction of the original vision to be maintained.



Figure 1.10: Simulated images of normal vision (left) and AMD vision (right). Images reproduced from the National Eye Institute.

In many cases, once the photoreceptors have experienced enough of a decrease of oxygen, the retina will produce signaling to induce creation of new blood vessels to supply more oxygen to this region of the retina. These new blood vessels would extend from the choroid, breaking through Bruch's membrane in order to feed the retina. This form of the disease is called choroidal neovascularization (CNV), also referred to as wet AMD. VEGF (vascular endothelial growth factor) is a substance made by cells to stimulate the formation of blood vessels, a process called angiogenesis. VEGF was first discovered as occurring in cancerous situations in which blood vessels were created to improve tumor growth [21]. This factor was found to be expressed in human retinas during choroidal neovascularization [22,23,24].

Wet AMD is the major source of severe vision loss for AMD patients. The problem with this form of the disease is that the new blood vessels being created are very fragile and susceptible to leaks or bursting. As fluid leaks into the retina, distortions to vision can occur as the retinal layers are locally lifted up. This can lead to detaching retinal layers, killing photoreceptors and destroying regions of vision completely. Scar tissue can also form to affect regions of vision as well. While the vision loss associated with dry AMD can progress over the course of years, once the transition to wet AMD has been diagnosed the progression to severe vision loss can occur over the course of weeks [25].

Age-related macular degeneration is classified in three regimes: early, intermediate, and advanced. Early-stage AMD is difficult to identify without professional diagnosis because it occurs without any symptoms or vision loss. Intermediate AMD is the stage where the permeability of Bruch's membrane has decreased enough that there is a noticeable change in vision of the eye. Since most cases of AMD do not have identical disease progressions in both eyes, patient vision may not notice a change in one eye right away. Advanced AMD is the progression of the disease which can cause severe vision loss. This includes the advanced form of dry AMD as well as wet AMD. There are no early or intermediate stages of wet AMD.

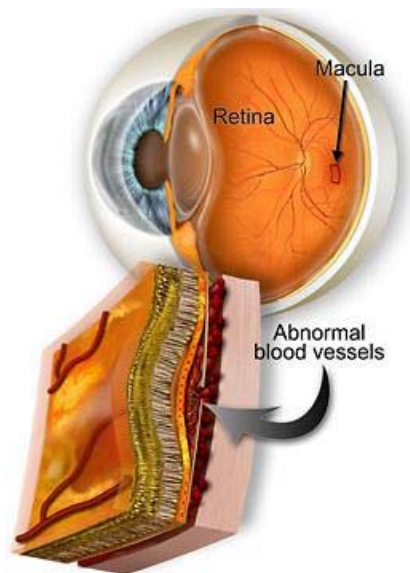


Figure 1.11: Wet AMD produces abnormal blood vessel growth which tries to break through the retinal layers, damaging the retina.

Looking at the prevalence of the disease is the best way to determine the age groups most at risk. Ophthalmologists generally diagnose patients who are suffering from a form of vision impairment so the prevalence of early stage AMD is not well accounted for. Statistics used by the National Eye Institute for the eye disease prevalence for the population over 60 (as well as the estimated population in the US currently in this category) are shown in Figure 1.12 [1].

Age Group	Advanced AMD prevalence estimated for age group	Intermediate AMD prevalence estimated in age group
60-69	0.7% (147,000 people in US)	6.4% (1,290,000 people in US)
70-79	2.4% (388,000)	12.0% (1,950,000)
≥80	11.8% (1,080,000)	23.6% (2,160,000)

Figure 1.12: AMD prevalence statistics for the United States [1].

In considering current US statistics of AMD prevalence, about 90% of all classified AMD cases are dry AMD versus wet AMD. But, if only advanced forms of AMD are considered, about 2/3 of cases are wet AMD.

1.2 Current Approaches to Disease Treatment

There are two main approaches in current treatment options for age-related macular degeneration: preventative and stop-gap measures. Preventative treatments attempt to delay the progression of early stage AMD with no vision loss to intermediate and advanced AMD stages where vision loss occurs.

The latest developments on the study of preventative management come from the National Eye Institute supported Age-Related Eye Disease Study (AREDS). AREDS is a 10-year study on the effects of a regimented daily supplement of vitamins and minerals on the progression of AMD for an at-risk patient group already presenting with intermediate stage AMD.

The results, according to NEI director Paul A. Sieving, M.D., Ph.D [26]: “This study found that high-dose antioxidant vitamins and minerals (vitamins C and E, beta-carotene, zinc, and copper), taken by mouth by people at risk of developing advanced AMD, reduced the risk of progression to advanced AMD by 25 percent and the risk of moderate vision loss by 19 percent. People at risk for AMD are advised to not smoke and to maintain a healthy lifestyle, with a diet including leafy green vegetables and fish”.

The dietary recommendations come from multiple studies which suggest that while many foods do not seem to have any impact on the progression of AMD, a couple of specific foods have shown very promising results. Consumption of dark leafy green vegetables like spinach, which contain lutein, have demonstrated a decrease in incidences of late stage AMD. Certain types of fish containing omega-3 fatty acids have also shown similar beneficial effects [27].

The NEI has just launched a nationwide study to see if a modified combination of vitamins, minerals, and fish oil can further slow the progression of vision loss from AMD. This new study, called the Age-Related Eye Disease Study 2 (AREDS2), will build upon results from the earlier AREDS study [28].

Stop-gap measures are the only way to describe the treatments for people who are currently suffering from wet AMD. Early treatments of this disease used photodynamic therapy (PDT) to photocoagulate leaking vessels in the eye to prevent future leakage damage from those vessels. To avoid laser damage to the central vision during treatment, only a fraction of wet AMD patients with particular locations of vessels qualified for treatment. Even for the treated patients, within 18 months nearly all had a reoccurrence of wet AMD.

The current popular approach for treatment is to produce drugs which can target the VEGF signaling of the retina. The assumption is that if VEGF was blocked, the retina would not grow any new vessels and wet AMD would not occur. Recent drugs including Avastin (Bevacizumab), Macugen (Pegaptanib), and Lucentis (Ranibizumab) have been designed towards this purpose with varying degrees of success. For all of these type of anti-VEGF drug treatments, there is one consistent trend: Once treatment is stopped, wet AMD progression will continue.

A primary concern with these drug treatments is the cost associated with them. Some of these drugs, which may need to be injected as often as once a month, can cost as much as \$2000 per injection. If money were not a concern, the next major issue is related to the drug delivery system, which is accomplished through an injection directly into the patient's eye.

Approximately 1% of patients following a 2-year regiment of eye injections will suffer an infection in the eye as a result. This type of infection generally leads to a complete loss of vision in the eye.

Developments of future treatments will be helped by the diagnostic capabilities of visualizing the disease progression. AREDS was a 10-year study which had effectiveness determined by visual acuity measurements. With the ability to measure the more subtle changes associated with the transitions in AMD, the effectiveness of treatments can be determined in shorter times and adjustments can be made to ineffective treatment regimes for patients.

1.3 Current Diagnostic Technologies and Limitations

AMD treatments are partly limited by the availability of diagnostic technologies able to screen the general population for disease management. An ideal screening tool for AMD needs to be able to:

- a) Identify the earliest stages of AMD before patient has visual symptoms so that preventative treatments can be applied
- b) Identify the earliest transitions from dry AMD to wet AMD to improve the efficiency of treatments directed towards wet AMD
- c) Monitor quantitative changes of disease progression and treatment efficacy to improve future disease treatments

The earliest symptoms of AMD do not usually cause noticeable changes in a patient's vision. It is important to be able to have an instrument which is quick, easy to operate, cheap, comfortable, carries no risk to the patient, and provides quantitative information about the disease. This would allow a diagnostic to be incorporated into a regular eye examination for determining at-risk patients to be referred for further study or treatment.

There are many technologies currently in use for diagnostic purposes for ocular exams. Each has its own benefits and limitations that need to be discussed in order to determine which one has the greatest potential of being the primary screening diagnostic for AMD.

1.3.1 Histology

Histology has always been a valuable tool for understanding tissue morphology over the course of a disease progression. Most of the structural models of the retina have been developed through study of the excised retinal tissues using optical microscopy. Histological staining combined with microscopy adds an additional level of contrast for improved visualization at a very high resolution. Unfortunately, biopsy of the retina to get the excised tissue would have a severe negative impact on the vision of any living eye so this technique is limited to post-mortem subjects only. Monitoring progress of a disease within one individual is not possible with this method.

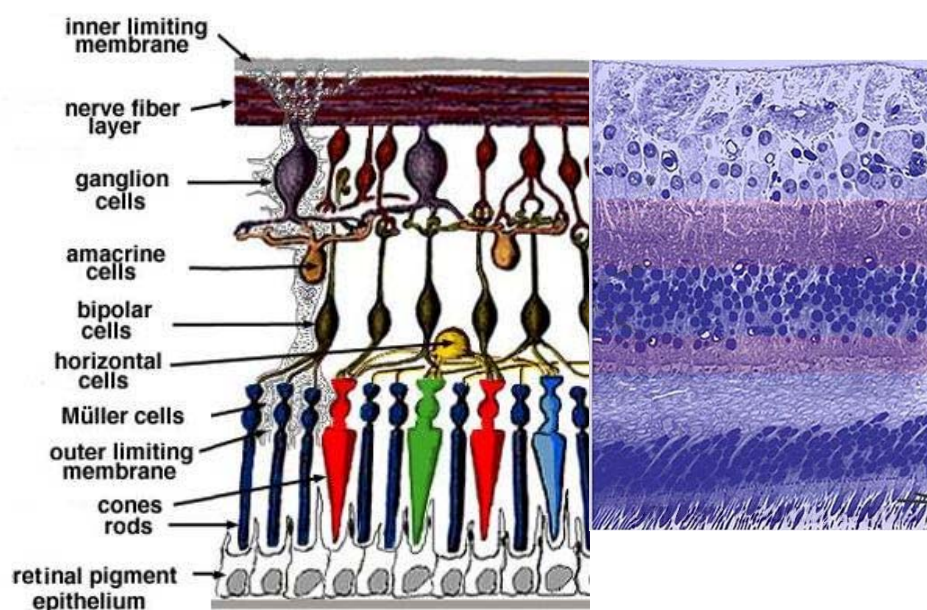


Figure 1.13: Histology image of retina compared to labeled schematic image.

1.3.2 Visual Acuity

Visual acuity is a coarse measurement of the sharpness of the retinal focus within the eye. It is the standard measurement used by optometrists to determine prescriptions for glasses. Used in AMD diagnostics, visual acuity has been used to determine wet AMD drug effectiveness. As sub-retinal fluid accumulates in wet AMD, the lifting of the retina causes a change in the patient's visual acuity.

There are two main issues with using visual acuity as the main diagnostic measurement [29]. First, as a coarse measurement of the mean visual acuity over the fovea, visual acuity is not designed to quantify very small localized changes due to disease progression [30]. Large visual acuity drops measured with this method correspond very well with the progression of the disease. Improvements of visual acuity measured over time for a patient could correspond to an improvement of the disease progression. They could just as easily be explained by a patient adapting to their current vision or adapting to the test itself. Without additional diagnostics, it would be difficult to discern the true scenario.

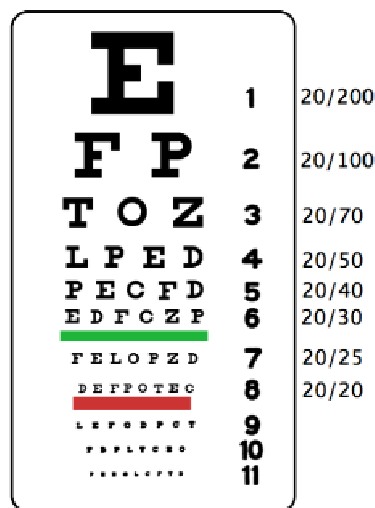


Figure 1.14: Scaled picture of traditional Snellen chart used for visual acuity tests.

1.3.3 Amsler Grid

The Amsler grid is a simple grid composed of horizontal and vertical lines with a dot in the center. When a patient focuses on the dot and observes any of the lines as distorted or missing, this might identify the existence of locations of sub-retinal fluid associated with a leak from choroidal neovascularization.

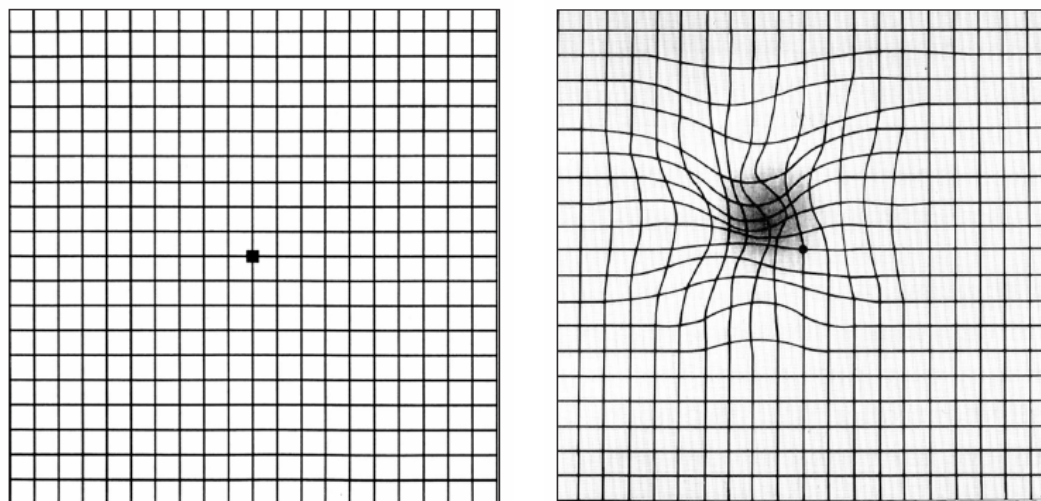


Figure 1.15: Amsler grid viewed under normal vision versus simulated wet AMD leak.

This test is user-based and very qualitative, making it a poor diagnostic tool by itself. The Amsler grid is ideal for directing to an eye care professional potential wet AMD patients who otherwise may not have gotten an examination until much later in the progression of the disease.

1.3.4 Fundus Photography

The most common diagnostic technique is based on the ophthalmoscope, an instrument which allows a doctor the ability to look through the pupil of a patient's eye to view the back globe of their eye, called the fundus. Fundus photography uses the exact same principle while transferring the image of the fundus to a camera for acquisition. The earliest stages of AMD are characterized using the images of this technique.

Early stages of dry AMD are roughly linked to the appearance of localized fatty deposits called drusen. By identifying the color, size, and number of drusen which appear on the fundus image, the early stage of AMD can be classified. Fundus photography is capable of visualizing many aspects of AMD progression including pigment abnormalities, regional cell death in the retina (called geographic atrophy), and choroidal neovascularization (CNV). With blood contrast occurring due to the regional light absorption for the image, the earliest stages of CNV may experience limited contrast in this technique.

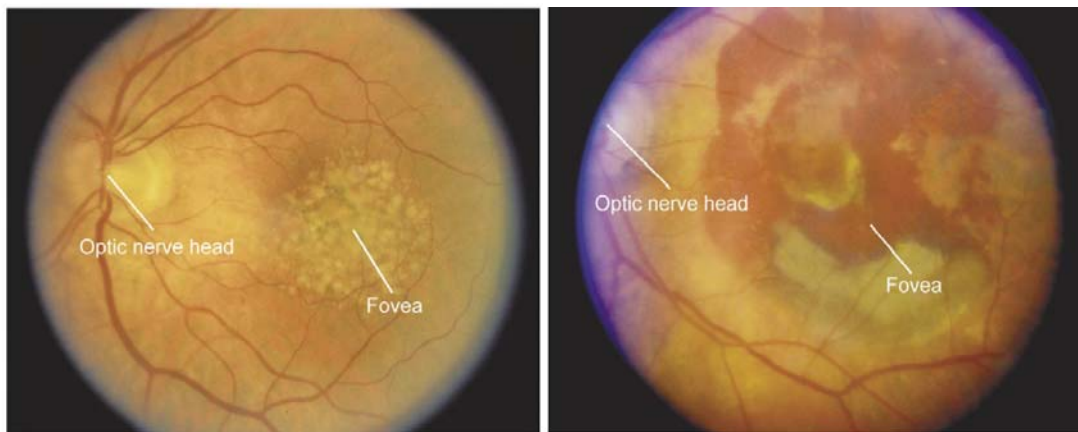


Figure 1.16: Fundus photography images for AMD eyes. Drusen deposits in the fovea region are associated with dry AMD (left) and observed blood vessel leaks are caused by wet AMD (right). Images reproduced from [8].

Fundus photography has a lot of characteristics that make it ideal as a screening tool: It is quick, easy, risk-free, and relatively comfortable for patients. Until the relationship between the drusen observed in AMD patients and the progression of the disease can be understood, this technique will remain a qualitative measure for early AMD diagnostics. With absorption as the main blood contrast observed, the earliest stages of wet AMD will remain very difficult to discern.

1.3.5 Fluorescein Angiography

Fluorescein angiography (FA) is one of the gold standards for visualizing vasculature in the retina, as well as leaks caused by wet AMD. A fluorescein solution is injected into the patient's blood stream and the retina is viewed using an altered fundus photography

system. Fluorescein is a molecule which will fluoresce green at a wavelength around 521 nm while undergoing absorption of blue light at a wavelength around 494 nm. Fundus photography with blue light illumination and a green filter on the camera will allow visualization of the fluorescein as it circulates through the retinal vasculature.

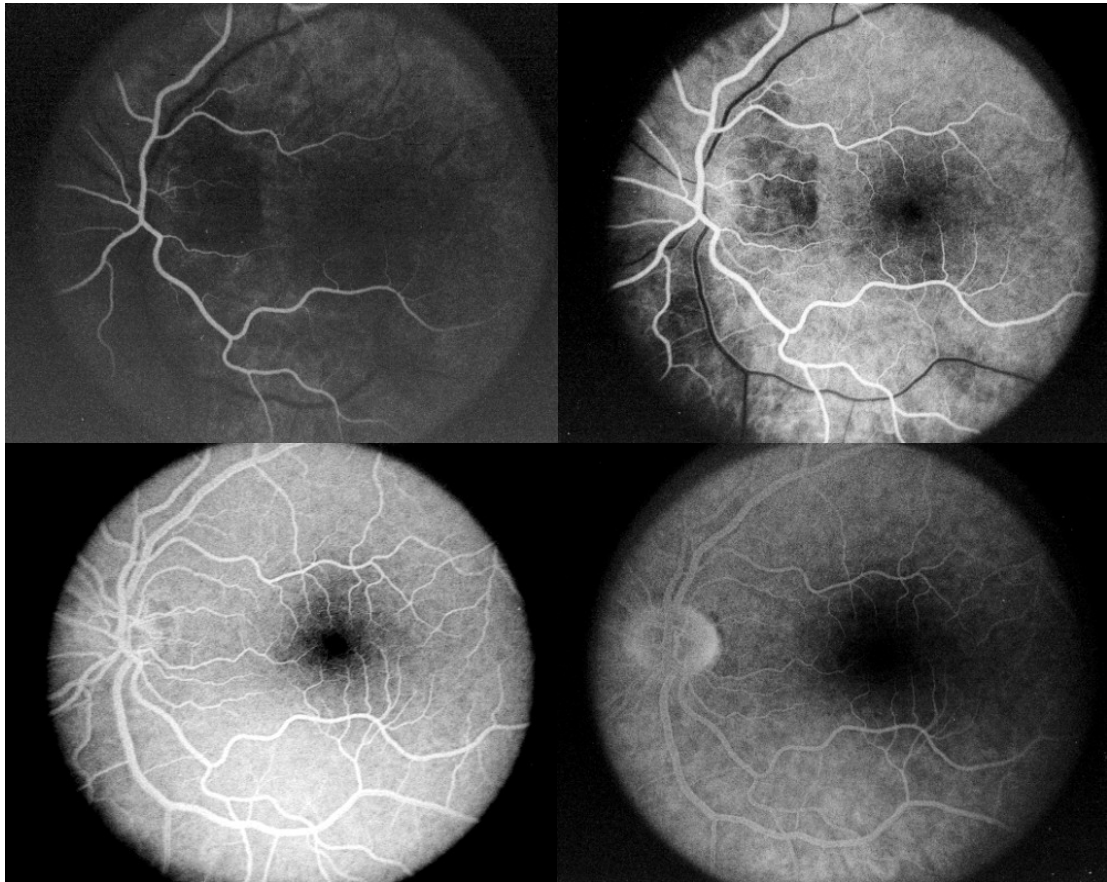


Figure 1.17: Fluorescein angiography images taken at different time points after dye injection. The time sequence of stages are the arterial stage (upper left), the venous stage (upper right), the mid phase (lower left), and the late phase (lower right).

By taking angiography images at different time points, the arteries and veins in the retina can be identified as well as any leaks caused by CNV [31]. The lack of retinal blood vessels in the fovea region can also be visualized using this method. Another form of angiography utilizing indocyanine green uses higher-wavelength light to illuminate the molecules, allowing for deeper penetration of the light into the retina. Indocyanine green angiography

(ICGA) allows improved visualization of the deeper choroidal blood vessels as well as the retinal vessels.

The injections required for this technique limit the general screening capabilities of this technique. Possible adverse reactions to injections or to the fluorescein sodium solution used are the main concerns with this method [32,33]. If the diagnostic capabilities of the angiography techniques were possible without the injections, it would be an ideal screening tool for identifying the earliest stages of wet AMD.

1.3.6 Ultrasound

Ultrasound uses sound waves to identify interfaces within the sample. Each depth reflection is separated from each other by the differing travel times of the sound waves reflecting back to the detector. Typical high-resolution ultrasound is capable of separating distinct layers 20 microns from each other. To allow the sound waves to propagate to the retina, the sound wave transducer must be placed in physical contact on the eye which may not be comfortable for all patients. Ultrasound is commonly used to assess the retina for cases with dense cataracts which limit the optical accessibility of the retina. Optical imaging is generally preferable to ultrasound as a screening instrument.

1.3.7 Scanning Laser Ophthalmoscope

The major limitation to optically image the retina depends on the optical properties of the eye. With the sclera considered optically opaque, the retina is accessible by imaging through the cornea and lens of the eye. The aqueous humor is the fluid which fills the globe of the eye between the lens and the retina, which optically can be considered as water. The absorption profile of water limits the available wavelengths to use for retinal imaging.

With a total path length that illumination and collected light travels in the eye being approximately 5 cm (twice the length of the eye), absorption coefficients of greater than 0.2 cm^{-1} will allow $< 70\%$ of the light to propagate through the medium. The additional

absorption of the light in these cases limit the usefulness of certain wavelength ranges of illumination light sources.

The scanning laser ophthalmoscope (SLO) performs confocal microscopy imaging of the retina, using the lens of the eye as the focusing element. By scanning a laser transversely across the retina and measuring the reflected light, an image comparable to fundus photography is created. In this system, the image is created from monochromatic laser light. Through the appropriate selection of laser wavelength and illumination power levels, image contrast can be adjusted with a higher level of flexibility than standard fundus photography [34].

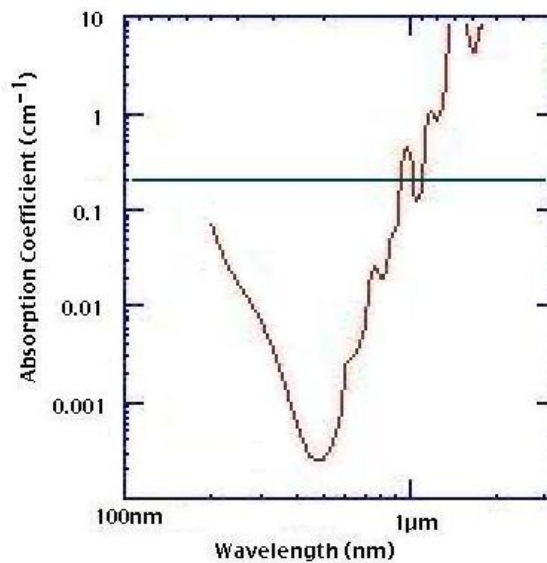


Figure 1.18: Wavelength absorption spectra of water. Horizontal line corresponds to absorption of 0.2 cm⁻¹.

1.3.8 Optical Coherence Tomography

Optical coherence tomography (OCT) is a relatively new technology. Incorporation into regular clinical use for ophthalmologists has been increasing steadily over the past 10 years as the instrumentation capabilities have been improving. OCT can be considered as the optical analogue of ultrasound: light reflecting off of each retinal layer in the eye will be delayed based on the distance the light has traveled. With the speed of light so much faster

than the speed of sound in tissue, it is technologically challenging to temporally separate out the reflections. Instead of pushing technology to attempt to distinguish femtosecond temporal resolution, an interferometric technique was developed which allows the separation of retinal layers through spatial discrimination.

OCT is sometimes considered in vivo optical histology because it is capable of producing 3D structural information of a sample. The most popular OCT retinal imaging system (Stratus OCT, created by Carl Zeiss Meditec) demonstrates a depth resolution in retinal images of 10 μm in tissue [35]. While it has not reached the resolution level of current histology imaging capabilities, this technique creates images which correlate to expected histological measurements.

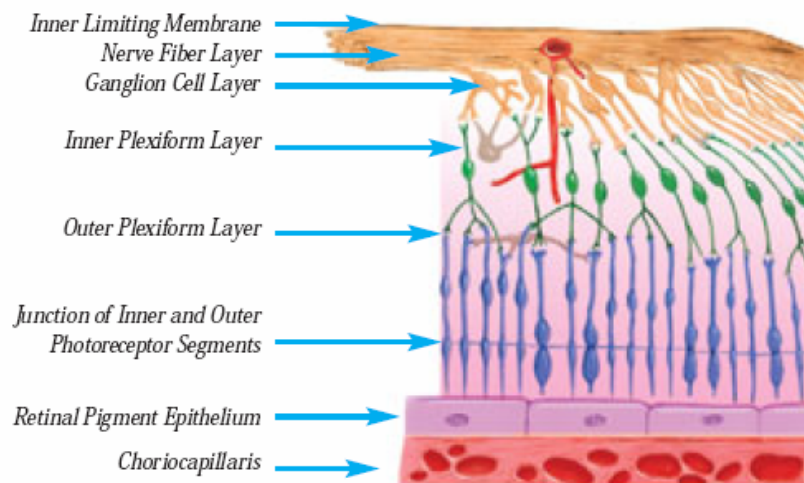


Figure 1.19: Schematic image of retina with the retinal layers identified. Image reproduced from reference [34].

Current usages of retinal OCT are primarily limited to structural abnormalities such as macular holes and retinal detachments. With imaging improvements and clinical studies with current systems, additional functionality for this technique will be applied to clinical eye examinations.

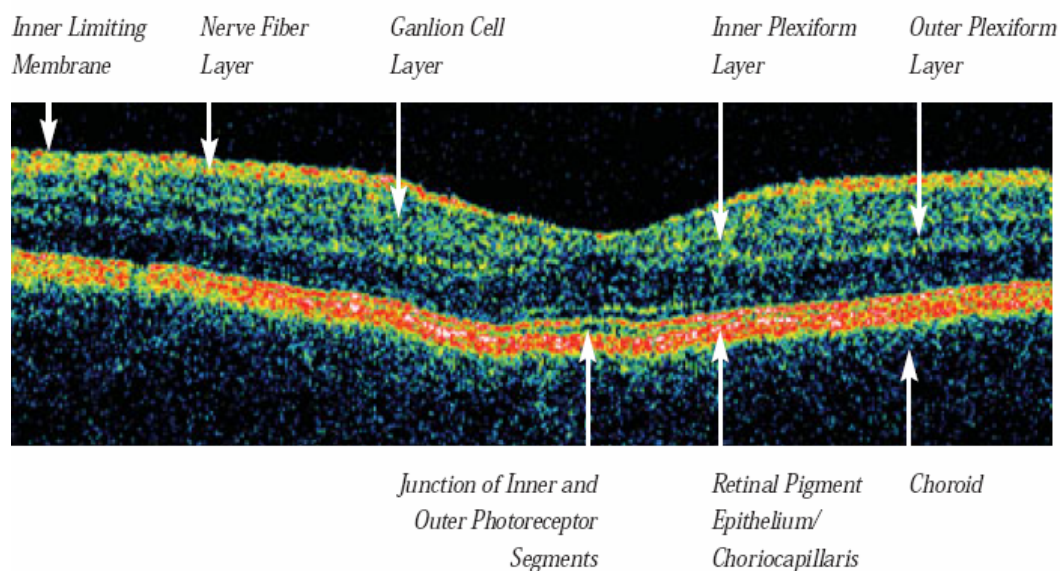


Figure 1.20: OCT Image acquired with Carl Zeiss Meditec Stratus OCT system, with labeling of identified retinal layers. The structure is consistent with the expected layering of the schematic of the retina in Figure 1.19. Image reproduced from [34].

1.3.9 Summary of Diagnostic Technologies

Optical imaging techniques are very capable as a quick and risk-free screening tool for patients. For AMD diagnostics, fundus photography and fluorescein angiography are currently the most valuable diagnostic tools available. The diagnostic capabilities would be enhanced further with additional quantitative information of the fundus images as well as the possibility of achieving fluorescein angiography images without requiring the dye injection.

Optical coherence tomography is a non-invasive method capable of three dimensional structural imaging. Commercially available systems are capable of nearly real time two-dimensional images which can separate out retinal layers of interest. With resolution and speed improvements, this technique can add accessibility as a screening tool. Functional improvements also have the possibility of improving the capabilities to diagnose AMD disease progression.

1.4 References

1. "Prevalence of Blindness data tables—Based on Archives of Ophthalmology, Volume 122, April 2004 Data," National Eye Institute, http://www.nei.nih.gov/eyedata/pbd_tables.asp.
2. N. Congdon et al., "Causes and prevalence of visual impairment among adults in the United States," *Arch. Ophthalmol.* 122, 477 (2004).
3. "65+ in the United States: 2005—Current Population Reports," <http://www.census.gov/prod/2006pubs/p23-209.pdf>.
4. "Defining the Prevalence of AMD and Investigating Racial Differences," *Retina Today*, January/February 2007, http://www.retinatoday.com/Html%20Pages/0107/RT0107_cover_bressler.html.
5. "Simple anatomy of the retina," Webvision, <http://webvision.med.utah.edu/sretina.html>.
6. R.W. Young, "The renewal of photoreceptor cell outer segments," *J. Cell Biol.* 33, 61 (1967).
7. R.W. Young et al., "The renewal of rod and cone outer segments in the rhesus monkey," *J. Cell Biol.* 49, 303 (1971).
8. S.E. Fraser, "New Sight for Old Eyes," *California Institute of Technology Engineering and Science Magazine* 64, 3 (2006).
9. R.W. Young et al., "Participation of the retinal pigment epithelium in the rod outer segment renewal process," *J. Cell Biol.* 42, 392 (1969).
10. M.M. LaVail et al., "Rod outer segment disk shedding in rat retina: relationship to cyclic lighting," *Science* 194, 1071 (1976).
11. R.W. Young et al., "The daily rhythm of shedding and degradation of cone outer segment membranes in the lizard retina," *J. Ultrastruct. Res.* 61, 172 (1977).
12. M.J. Hollenberg et al., "The fine structure of Bruch's membrane in the human eye," *Can J. Ophthalmol.* 4, 296 (1969).
13. F. Emeline et al., "Loss of Synchronized Retinal Phagocytosis and Age-related Blindness in Mice Lacking $\alpha\beta 5$ Integrin," *J. Exp. Medicine* 200, 1539 (2004).
14. L. Feeney, "Lipofuscin and melanin of human retinal pigment epithelium. Fluorescence, enzyme cytochemical, and ultrastructural studies," *Invest. Ophthalmol. Vis. Sci.* 17, 583 (1978).
15. L. Feeney-Burns et al., "The fate of the phagosome: conversion to 'age pigment' and impact in human retinal pigment epithelium," *Trans. Ophthalmol. Soc. U.K.* 103, 416 (1983).
16. F. G. Holz et al., "Analysis of lipid deposits extracted from human macular and peripheral Bruch's membrane," *Arch. Ophthalmol.* 112, 402 (1994).
17. R.S. Ramrattan et al., "Morphometric analysis of Bruch's membrane, the choriocapillaris, and the choroid in aging," *Invest. Ophthalmol. Vis. Sci.* 35, 2857 (1994).
18. W.R. Green and C. Enger, "Age-related Macular Degeneration Histopathologic Studies: The 1992 Zimmerman Lorenz Lecture," *Ophthalmology* 100, 1519 (1993).
19. C. Starita et al., "Hydrodynamics of Ageing Bruch's Membrane: Implications for Macular Disease," *Exp. Eye Res.* 62, 565 (1996).

20. D.J. Moore et al., "The Effect of Age on The Macromolecular Permeability of Human's Bruch's Membrane," *Invest. Ophthalmol. Vis. Sci.* 42, 2970 (2001).
21. D.R. Senger et al., "Tumor cells secrete a vascular permeability factor that promotes accumulation of ascites fluid," *Science* 219, 983 (1983).
22. M.D. Sternfeld et al., "Cultured human retinal pigment epithelial cells express basic fibroblast growth factor and its receptor," *Curr. Eye Res.* 8, 1029 (1989).
23. A.P. Adamis et al., "Synthesis and secretion of vascular permeability factor/vascular endothelial growth factor by human retinal pigment epithelial cells," *Biochem. Biophys. Res. Commun.* 193, 631 (1993).
24. A. Kvanta, "Expression and regulation of vascular endothelial growth factor in choroidal fibroblasts," *Curr. Eye Res.* 14, 1015 (1995).
25. Macular Degeneration International: The Foundation Fighting Blindness, <http://www.maculardegeneration.org/agedex.html>.
26. "Laser Treatment Does Not Prevent Vision Loss For People With Early Age-Related Macular Degeneration," US Environmental Protection Agency, http://www.epa.gov/aging/press/othernews/2006/2006_1101_ons_1.htm.
27. "Age-related Macular Degeneration: What you should know," NEI Publication, <http://www.nei.nih.gov/health/maculardegen/webAMD.pdf>.
28. "Age-Related Eye Disease Study 2 (AREDS2)," <https://web.emmes.com/study/areds2/>.
29. "The importance of Vision-Related Quality of Life in Patients Treated with Neovascular AMD," *Retina Today*, January/February 2007, http://www.retinatoday.com/Html%20Pages/0107/RT0107_medical_chang.html.
30. "Visual Acuity," Wikipedia, http://en.wikipedia.org/wiki/Visual_acuity.
31. S.O. Sykes et al., "Detecting recurrent choroidal neovascularization. Comparison of clinical examination with and without fluorescein angiography," *Arch. Ophthalmology* 112, 1561 (1994).
32. L. Yannuzzi et al., "Fluorescein angiography complication survey," *Ophthalmology* 93, 611 (1986).
33. M. Hope-Ross et al., "Adverse reactions to indocyanine green," *Ophthalmology* 101, 529 (1994).
34. P.F. Sharp et al., "The scanning laser ophthalmoscope," *Phys. Med. Biol.* 42, 951 (1997).
35. "Stratus OCT™: Real Answers in Real Time," Brochure from Carl Zeiss Meditec, [http://www.meditec.zeiss.com/88256DE3007B916B/0/C26634D0CFF04511882571B1005DECFD/\\$file/stratusoct_en.pdf](http://www.meditec.zeiss.com/88256DE3007B916B/0/C26634D0CFF04511882571B1005DECFD/$file/stratusoct_en.pdf).

OPTICAL COHERENCE TOMOGRAPHY

Through the understanding of optical coherence tomography (OCT), the fundamental limits of imaging performance can be identified. Within these limits functionality improvements can be identified to move beyond the capabilities of currently available OCT systems. It is important to determine the ability of OCT to adapt towards quantitative diagnostics for AMD progression.

2.1 Basics of Optical Coherence Tomography (OCT)

2.1.1 Michelson Interferometer with Single Wavelength Light Source

Optical coherence tomography is based upon a Michelson interferometer configuration. Consider a single wavelength narrow bandwidth laser source incident on a Michelson interferometer. The incoming light is split using a beamsplitter into two interferometer arms, designated as the reference and sample arms. The light is reflected back through the beamsplitter to be collected by the photodetector, which converts the measured power into an electrical current.

Looking at the complex form of the electric field of the laser light, the light traveling through the reference arm of the interferometer arrives at the detector has the form of $\tilde{E}_R = E_R \exp(i(kz_{total,R} + \varphi_0))$, where $z_{total,R} = z_1 + 2z_R + z_4$ is the total optical path the light has traveled through the interferometer, φ_0 is phase of electric field of light source before it enters the interferometer, and $k=2\pi/\lambda$ for the light source of wavelength λ . Similarly, the electric field traveling through the sample arm of the interferometer is of the form $\tilde{E}_S = E_S \exp(i(kz_{total,S} + \varphi_0))$, where $z_{total,S} = z_1 + 2z_S + z_4$ is the total optical path traveled in this case.

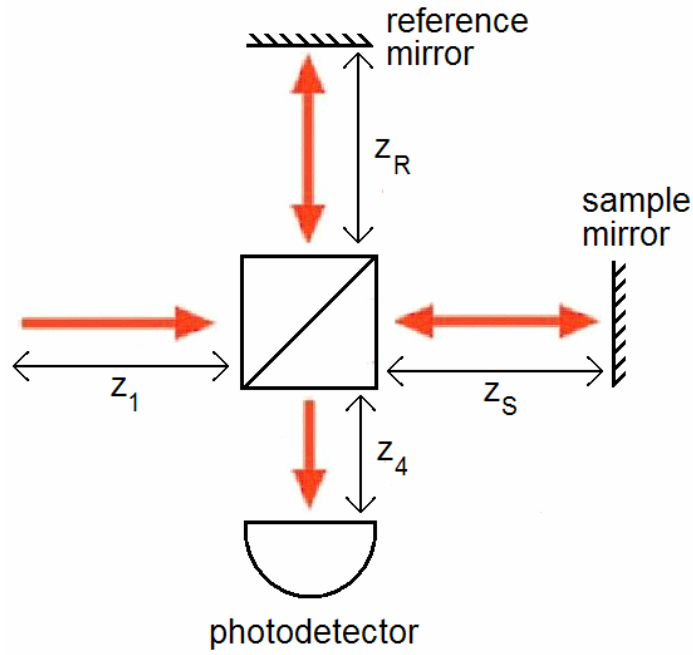


Figure 2.1: Free space Michelson interferometer with single reflector in each arm, designated as reference and sample.

The photodetector measures intensity of light, calculated by the magnitude of the total electric field arriving at the detector.

$$\begin{aligned}
 I_{Detector} &= \left| \tilde{E}_S + \tilde{E}_R \right|^2 = \left| E_S \exp(i(kz_{total,S} + \varphi_0)) + E_R \exp(i(kz_{total,R} + \varphi_0)) \right|^2 \\
 &= E_S^2 + E_R^2 + 2E_S E_R \cos(kz_{total,S} + \varphi_0 - kz_{total,R} - \varphi_0) \\
 &= E_S^2 + E_R^2 + 2E_S E_R \cos(2k(z_S - z_R)) \\
 &= I_S + I_R + 2\sqrt{I_S I_R} \cos(2k(z_S - z_R)) = I_{Detector}(k, z_S - z_R)
 \end{aligned} \tag{2.1}$$

where $I_S = \left| \tilde{E}_S \right|^2 = E_S^2$ and $I_R = \left| \tilde{E}_R \right|^2 = E_R^2$.

The interferometric signal measured only depends on relative optical path differences of the two interferometer arms.

2.1.2 Michelson with Broad Bandwidth Light Source

For a broad bandwidth light source, treat each wavelength component as an individual light source which does not interfere with any other wavelength than itself. Define $I_R = R_R I_0 S(k)$ and $I_S = R_S I_0 S(k)$, where $S(k)$ is normalized spectral function of the light source, and R_a is percentage of original light intensity I_0 reaching the detector for light traveling through arm a . Assuming uniform efficiency of the detector over the light source spectra, the detector measures the sum of all light source contributions for all wavelengths. Calculating in terms of k -space:

$$\begin{aligned}
 I(z_S - z_R) &= \int_k I_{Detector}(k, z_S - z_R) dk \\
 &= \int_k ((R_S I_0 + R_R I_0) S(k) + 2\sqrt{R_S R_R} I_0 S(k) \cos(2k(z_S - z_R))) dk \\
 &= (R_S + R_R) I_0 + 2\sqrt{R_S R_R} I_0 \int_k S(k) \cos(2k(z_S - z_R)) dk . \tag{2.2}
 \end{aligned}$$

The function $\int_k S(k) \cos(2k(z_S - z_R)) dk$ is an autocorrelation of the light source spectra that is defined as the Weiner-Khinchin theorem (Fourier transform of the magnitude of the electric field). The coherence function, which will be defined as $f_C(z)$ and is centered around $z = z_S - z_R$, is a function which determines the effect on the interference signal when reflections from the two arms of the interferometer are not of equal path length.

The coherence length l_C is the quantitative metric of the spatial extent each interference reflection is measured over. This is defined as the full width half-maximum (FWHM) of the envelope of the spatial measurement of the coherence function. The coherence length describes the ability of the system to separate different interference reflections from each other.

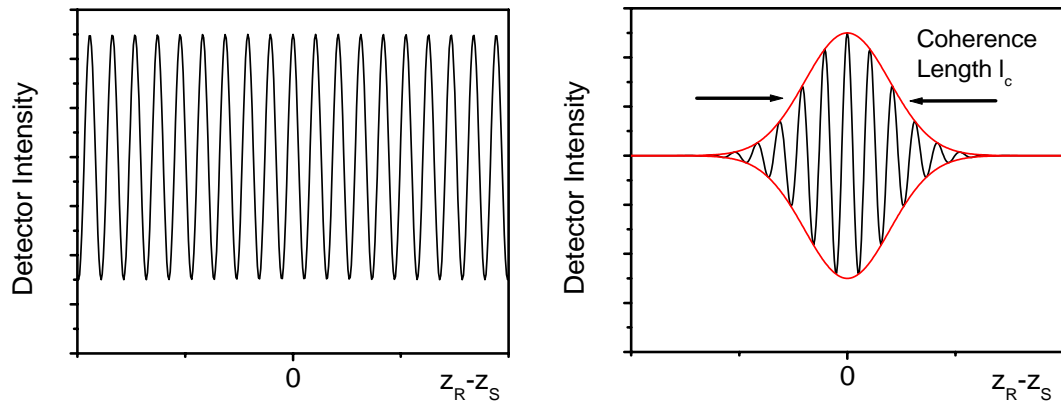


Figure 2.2: Measured light intensity at output of the Michelson interferometer as a function of the difference of the optical path lengths from the interferometer arms for the cases of single wavelength light (left) and broad bandwidth light (right). The full width half maximum (FWHM) of the interference fringe maximum is labeled as the coherence length.

2.1.3 Comparing Reflectivity to Interferometer Detector Signal

Consider the Michelson interferometer setup with a layered structure in the sample arm instead of a single reflector. The interference signal measured is the coherence function convoluted with the reflectivity profile of the sample.

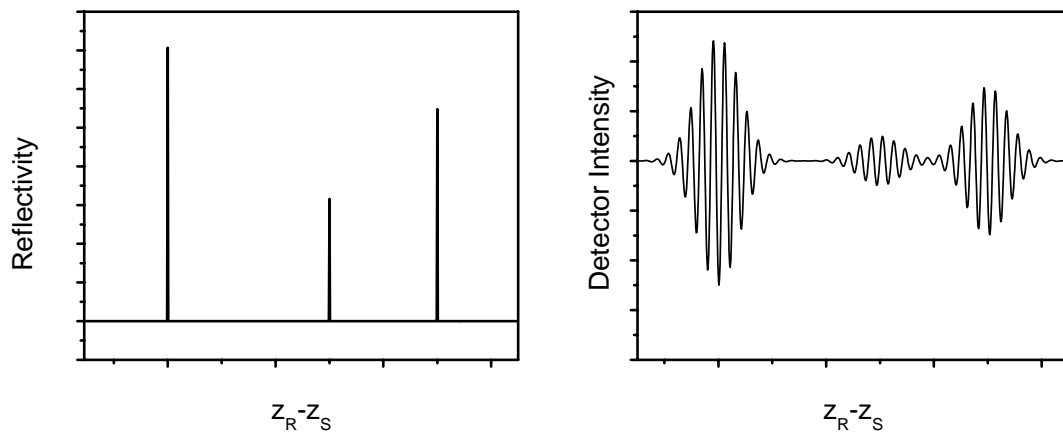


Figure 2.3: Ideal reflectivity profile over depth versus theoretical intensity signal over depth. The interference fringe signal is the convolution of the reflection profile with the coherence function.

2.2 Axial Resolution

The ability to separate fringes from reflections of different depths depends on the shape of the coherence function, which relies on the light source properties. This depth separation is referred to as the axial resolution. Consider the extreme cases:

a) For an infinitely narrow light source spectrum such that $S(k) = S_0 \delta(k - k_0)$,

$$f_C(z) = \int_k S(k) \cos(2k(z_S - z_R)) dk \propto \cos(2k_0(z_S - z_R)). \quad (2.3)$$

In this case, interference fringes are observed for all $z_S - z_R$ values. All reflections from every depth within the same are observed all at the same time, resulting in the measurements being dominated by the strongest reflection.

b) For an infinitely broadband light source such that $S(k) = 1$ for all k ,

$$f_C(z) = \int_k S(k) \cos(2k(z_S - z_R)) dk \propto \delta(z_S - z_R). \quad (2.4)$$

For this case, no interference would be observed unless the interferometer arms were of identical optical path lengths.

Spectral Shape and Coherence Function Tradeoffs

A finite-width broad bandwidth light source will measure interference over a spatial extent determined by the light source properties. The coherence function $f_C(z)$ contains the oscillatory interference fringe function based on the center wavelength of the light source combined with an envelope function which defines the spatial extent of the interference measurement. The coherence length l_C can be considered as the axial resolution, which determines the minimum depth difference at which two identical distinct reflections can be differentiated from each other.

For a Gaussian source spectra where the interferometer arm length difference is defined $z = z_S - z_R$, the coherence function $f_C(z) = \int_k S(k) \cos(2kz) dk$ can be calculated using the light source spectral form $S(k) = S_0 \exp(-4 \ln 2 (k-k_0)^2 / \Delta k_{FWHM}^2)$, where the spectrum is centered around $k_0 = 2\pi/\lambda_0$ and λ_0 is the center wavelength of the light source:

$$\begin{aligned} f_C(z) &= \int_k S(k) \cos(2kz) dk = \operatorname{Re} \left(\int_k S(k) \exp(i2kz) dk \right) \\ &= \operatorname{Re} \left(\exp(i2k_0 z) \int_{k'} S(k') \exp(i2k' z) dk' \right). \end{aligned} \quad (2.5)$$

Using $S(k') = S_0 \exp(-C(k')^2)$, where $k' = k - k_0$ and $C = 4 \ln 2 / \Delta k_{FWHM}^2$:

$$\begin{aligned} f_C(z) &= \operatorname{Re} \left(S_0 \exp(i2k_0 z) \int_{k'} \exp(-Ck'^2) \exp(i2k' z) dk' \right) \\ &= \operatorname{Re} \left(f_0 \exp(i2k_0 z) \exp(-z^2 / C) \right) \\ &= f_0 \cos(2k_0 z) \exp(-\Delta k_{FWHM}^2 z^2 / 4 \ln 2). \end{aligned} \quad (2.6)$$

In this case, the envelope function is a Gaussian function with a full width half maximum (FWHM) of $\Delta z_{FWHM} = 4 \ln 2 / \Delta k_{FWHM} = l_C$. Defining the coherence length l_C in terms of

wavelength uses $\Delta k_{FWHM} = \left(2\pi / \lambda_0^2 \right) \Delta \lambda_{FWHM}$ to calculate:

$$l_C = \frac{2 \ln 2}{\pi} \frac{\lambda_0^2}{\Delta \lambda_{FWHM}} = 0.44 \frac{\lambda_0^2}{\Delta \lambda_{FWHM}}. \quad (2.7)$$

For the given light source bandwidth from the above equation, maximizing FWHM of the light source should produce the best axial resolution. Consider a top-hat spectra centered around k_0 with spectral width Δk_{FWHM} :

$$\begin{aligned}
f_C(z) &= \int_k S(k) \cos(2kz) dk = S_0 \int_{k_0 - \Delta k_{FWHM}/2}^{k_0 + \Delta k_{FWHM}/2} \cos(2kz) dk \\
&= f_0 \cos(2k_0 z) \frac{\sin(\Delta k_{FWHM} z)}{\Delta k_{FWHM} z},
\end{aligned} \tag{2.8}$$

which leads to a coherence length of:

$$l_C = \frac{3.79}{\Delta k_{FWHM}} = 0.60 \frac{\lambda_0^2}{\Delta \lambda_{FWHM}}. \tag{2.9}$$

To compare these coherence length calculations directly, consider the case of the top-hat spectrum and the Gaussian spectrum with similar spectral extent such that $\Delta \lambda_{FWHM, Tophat} = 2\Delta \lambda_{FWHM, Gaussian} = 2\Delta \lambda_{FWHM}$, as shown in Figure 2.4.

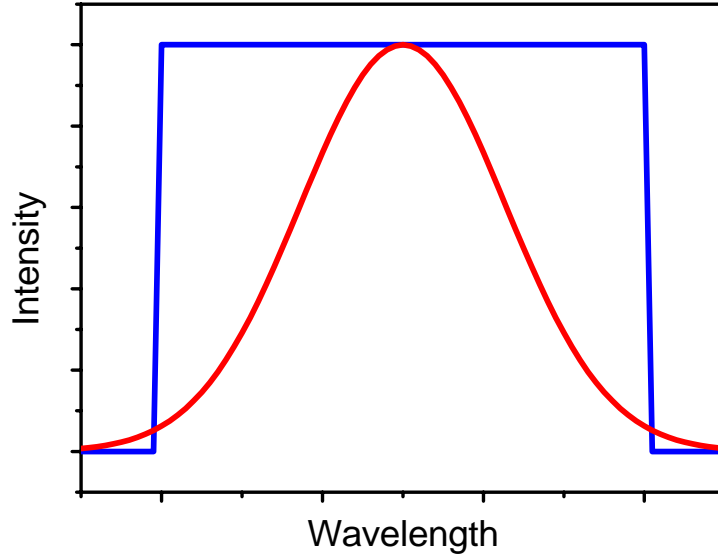


Figure 2.4: Plots of Gaussian (red) and top-hat (blue) spectral functions for the case of $\Delta \lambda_{FWHM, Tophat} = 2\Delta \lambda_{FWHM, Gaussian} = 2\Delta \lambda_{FWHM}$.

In this case, the top-hat source coherence function is $l_{C, Tophat} = 0.30 \frac{\lambda_0^2}{\Delta \lambda_{FWHM}}$, and the

Gaussian source coherence function is $l_{C, Gaussian} = 0.44 \frac{\lambda_0^2}{\Delta \lambda_{FWHM}} = 1.47(l_{C, Tophat})$.

The coherence length l_c cannot be considered as the only important factor to consider. With the typical sample containing reflections that vary over several orders of magnitude, the spatial form of the coherence function determines how the weaker reflections are identified when located close to a strong reflection. If all of the reflections were identical within a sample, this would not be a consideration.

The interference signal in OCT is defined by the magnitude of the envelope of the coherence function convoluted with the reflectivity profile of the sample over depth. So for a normalized OCT signal of a given reflector, the coherence length is defined by the width, defined by the -6dB points (as opposed to the -3dB points used for the FWHM of the coherence envelope). On a linear scale, the side lobe variations of the coherence function due to the top-hat spectra do not seem to have much of an effect. On a logarithmic scale, the side lobes of this function are significant and extend out spatially far beyond the coherence length. On this scale, the coherence function of the Gaussian source spectra can be seen to have a larger coherence length but without any side lobes.

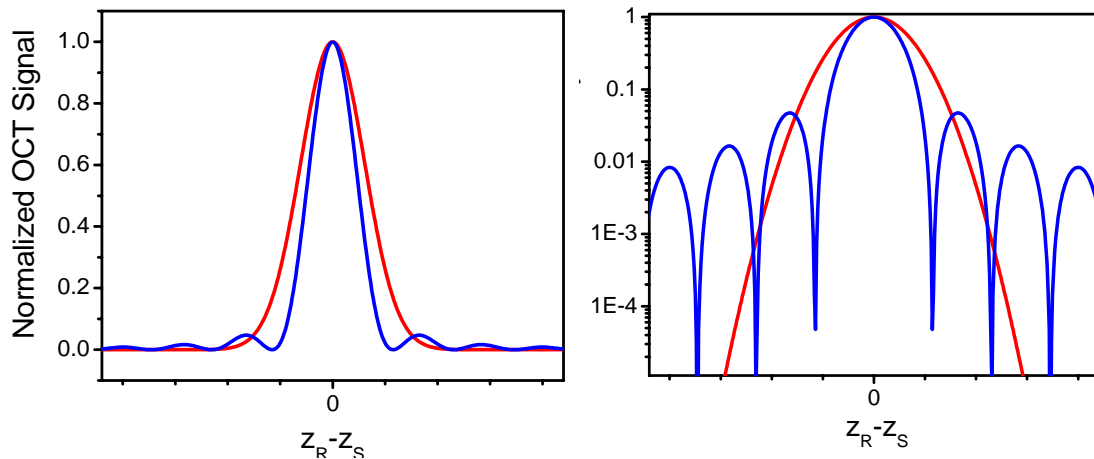


Figure 2.5: Calculated coherence functions of the spectra in Figure 2.4, plotted against the relative path length of the interferometer arm. The linear (left) and logarithmic (right) plots of the coherence functions are presented. The top-hat coherence function (blue) has a smaller coherence length, but has substantially more side lobes on the function. The Gaussian coherence function (red) shows no side lobes in either plot.

These two cases demonstrate the tradeoffs between coherence function shape and coherence length for a given source spectrum. The top-hat spectrum was the largest spectral FWHM for a given spectral width. The coherence length minimum for this given spectral width was at the tradeoff for the side lobes of the function. The coherence function created from the Gaussian spectra contains no side lobes, but has a relatively larger coherence length. Spectral shaping of the light spectrum allows adjustments between the coherence length and side lobes of the coherence function.

As illumination spectral widths become wider, dispersion compensation becomes more important. Dispersion mismatch between the interferometer arms causes a reflection to appear at different optical depths for different wavelength components of the light source, effectively broadening the coherence function and increasing the coherence length.

2.3 Acquiring Fringe Data to Create OCT Images

Optical coherence tomography (OCT) is the method of imaging which plots the spatial distribution of the envelope of interference fringes from a broad bandwidth light source in a Michelson interferometer configuration. The main question is: How is the envelope of the interference fringes determined?

For a single photodetector power measurement of an interference fringe, the measurement is of the form:

$$\begin{aligned} P(z_S - z_R) &= P_{DC} + P_{INT} f_C(z_S - z_R) \\ &= P_{DC} + P_{INT} f_E(z_S - z_R) \cos(2k_0(z_S - z_R)) . \end{aligned} \quad (2.10)$$

P_{DC} is the sum of all the powers measured by the photodetector, P_{INT} is the maximum power of the interference fringe, and $f_E(z)$ is the envelope function portion of the coherence function, normalized to a maximum of 1. The quantity of interest is $P_{INT} f_E(z_S - z_R)$, which is the non-normalized envelope function. The difficulty in

determining this factor from one detector measurement is due to two additional unknown variables beyond the quantity of interest: P_{DC} and $z_S - z_R$.

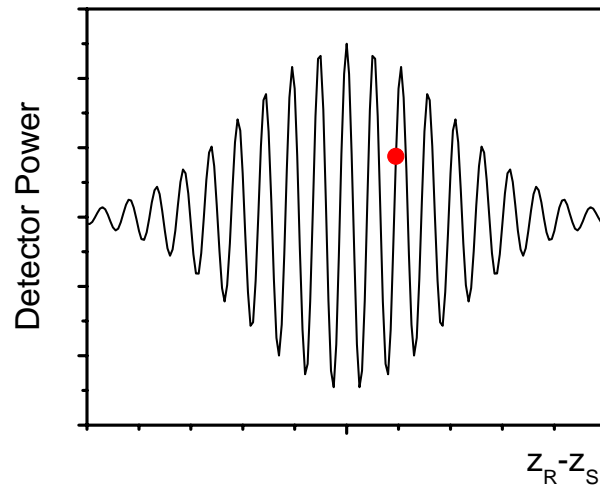


Figure 2.6: Schematic illustrating the lack of information for using a single point measurement to measure the interference fringe intensity.

The interferometric portion of the signal $\cos(2k_0(z_S - z_R))$ is very sensitive to the relative position $z_S - z_R$ of the two reflections. It is easier to consider this signal in terms of the relative phase $\phi_S - \phi_R$ of the interference fringe because, while the envelope function $f_E(z_S - z_R)$ is sensitive to distance changes on the order of microns, the fringe oscillation $\cos(2k_0(z_S - z_R))$ is sensitive to changes on the order of nanometers (1000 times more sensitive).

The relative phase of the interferometer $\phi_S - \phi_R$ is defined as $4\pi(z_S - z_R)/\lambda_0$, so any relative motion in the system with a magnitude of at least $\lambda_0/2$ will see a full oscillation in the interference fringe. By controlling the relative motion between the two arms of the interferometer, the fringe amplitude can be sampled and identified. The method of sampling the fringes through the change of interferometer optical path length is referred to as time domain optical coherence tomography (TDOCT) [1,2].

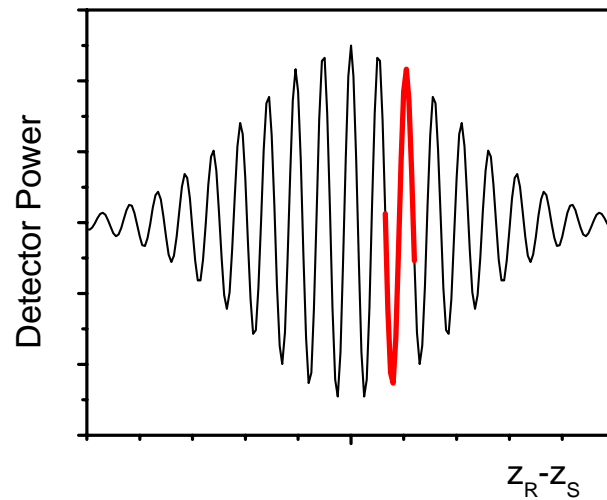


Figure 2.7: Schematic image of an interference fringe sampled using a small interferometer path length change.

There are several methods to sample the interference fringes to produce an OCT image. The most commonly used method utilizes a linear scan of the reference arm path length to sample all of the interference fringes over the entire depth of the sample. Keeping consistent with ultrasound scan terminology, a single scan along the depth of the sample is called an A-scan. Creating a two dimensional reflectance image through multiple A-scans over a range of transverse locations is called a B-scan.

As a screening tool for the retina, there is an additional interest in flexibility of the scan directions. Transverse images, also called en face images or C-scans, allow imaging at one depth of the interference fringes over the entire plane of the retina. If the primary acquisition of OCT data is through A-scans, the only way an en face image could be created would be through a 3D data set composed of A-scans measured over all transverse locations of interest. With mechanical scanning technologies limiting the maximum A-scan rate in TDOCT, it is not practical to produce transverse images this way.

To improve the flexibility of the imaging of the TDOCT system, the primary scan direction should be transverse to the direction of the incoming light (defined as axial). In this case, transverse scans followed by depth or axial scans would produce B-scan images.

Transverse scans followed by transverse scans in the perpendicular direction would produce C-scans. En face images are ideal in retinal imaging to screen an entire retina for signs of a disease, but allowing for it to occur at a single tissue depth of interest.

To acquire fringe information to allow for transverse scanning as the primary scan direction, the interference fringes must be sampled. The easiest way to sample requires changes in the relative optical path length much smaller than the axial resolution, which has numerous options available for creating small phase changes in the system at high speeds to measure the fringes [3-7].

2.4 SNR of Time Domain OCT

In TDOCT, the interferometric signal is measured as a current by the photodetector. Looking at the maximum fringe signal, the interferometer current $i(z_S - z_R)$ is given by:

$$i(z_S - z_R) = \frac{2\eta' \sqrt{P_R P_S}}{h\nu_0} \cos(2k(z_S - z_R)) \quad (2.11)$$

where η' is the quantum efficiency of the photodetector to convert photons to electrons. P_R, P_S are the powers arriving at the detector from the reference and sample arms of the interferometer, respectively and $h\nu_0$ is the average energy of the photon from the light source.

The signal in OCT $I(z)^2$ is the spatial average of the square of the interferometer current over several fringes:

$$I(z)^2 = \langle i(z)^2 \rangle_z = \frac{2\eta'^2 P_R P_S}{(h\nu_0)^2}. \quad (2.12)$$

The signal-to-noise ratio (SNR) in OCT is defined by the ratio of the OCT signal by the variance of the total noise of the system:

$$\text{SNR} = I(z)^2 / \sigma_{\text{noise}}^2. \quad (2.13)$$

There are three types of noise sources occurring over time τ' acquisition of a given pixel in the TDOCT acquisition: detector noise, shot noise, and relative intensity noise (which is also referred to as excess noise). The total noise in OCT is determined by the summation of the variance of all three types of noise sources:

$$\sigma_{\text{noise}}^2 = \sigma_{\text{detector}}^2 + \sigma_{\text{shot}}^2 + \sigma_{\text{excess}}^2. \quad (2.14)$$

The detector noise can be considered a constant source of noise, independent of the amount of power incident on the detector.

$$\sigma_{\text{detector}}^2 = \text{constant} \quad (2.15)$$

Shot noise is defined by the statistical fluctuations which occur for the measure of a finite number of particles in a detector over a given amount of time. For electrical currents, the expected probability distribution for the number of electrons during the acquisition of the detector is given by a Poissonian distribution around the expected mean number of electrons. For this distribution, the variance of the measured electrons is equal to the mean number electrons measured within the time τ' of the detector, which is determined from the total power incident on the detector. For the case of $P_R \gg P_S$, which is applicable for most OCT imaging scenarios, the shot noise variance is given by:

$$\sigma_{\text{shot}}^2 = \frac{\eta'(P_R + P_S)}{(h\nu_0)\tau'} \approx \frac{\eta'P_R}{(h\nu_0)\tau'}. \quad (2.16)$$

Relative intensity noise (RIN) describes the optical intensity fluctuation noise of the light source [8]. With the same assumption of $P_R \gg P_S$:

$$\sigma_{\text{excess}}^2 = \left(\frac{\eta'(P_R + P_S)}{h\nu_0} \right)^2 \frac{\tau_{\text{coh}}}{\tau'} \approx \left(\frac{\eta'P_R}{h\nu_0} \right)^2 \frac{\tau_{\text{coh}}}{\tau'}. \quad (2.17)$$

In this equation τ_{coh} is the coherence time, defined by $\tau_{coh} = \left(\frac{2 \ln 2}{\pi}\right)^{1/2} \frac{\lambda_0^2}{c \Delta \lambda_{FWHM}}$, where c is the speed of light, λ_0 is the center wavelength, and $\Delta \lambda_{FWHM}$ is the bandwidth of the light source.

Each of the different noise sources dominate in different regimes, which are determined by the total incident power on the detector, which is approximately described by P_R . From the properties of the individual noise sources and the OCT signal dependence on P_R , the ideal SNR performance would occur in the regime where the shot noise dominated the noise sources.

For the ideal SNR shot-noise limited case, given a TDOCT pixel acquisition time τ' :

$$\text{SNR}_{\text{TDOCT}} = \frac{2\eta'^2 P_R P_S / (h\nu_0)^2}{\eta' P_R / (h\nu_0) \tau'} = \frac{2\eta' P_S \tau'}{(h\nu_0)}. \quad (2.18)$$

2.5 Spectral Domain Optical Coherence Tomography (SDOCT)

Time domain optical coherence tomography (TDOCT) measures the interference in the case where a sample reflection has the same optical path length as the reference reflection. By measuring all of the interference fringes from all wavelength components at the same time within a photodetector, all of the non-equal path length fringes are rejected through destructive interference with each other.

The interference fringes have the form of $\cos(2k(z_S - z_R))$ for a given optical path difference of the interferometer arms of $z_S - z_R$. Measuring the interference fringes in k -space allows for the measurement of all of the interferometer fringes, not just the ones at equal path length. Each depth reflection will produce fringes of different spectral frequencies. The Fourier transform of the measurement of the interference fringes in k -space separates the reflections from different depths. This technique is referred to as Fourier domain optical coherence tomography (FDOCT) [9].

There are two different methods which fall under the category of FDOCT. The first method measures the interference fringes in k-space using a spectrometer to separate the wavelength components for measurement. This technique is called spectral domain optical coherence tomography (SDOCT) [10,11]. The other method utilizes a swept source laser with a narrow-band instantaneous spectral line width in the interferometer to vary the wavelength over time to be measured by a photodetector. This technique is referred to as swept source optical coherence tomography (SSOCT) or optical frequency domain imaging (OFDI) [12,13]. Regardless of the FDOCT method chosen, the calculation of the OCT signal from the spectral information remains the same.

Power measured in k-space for sample reflections (labeled by j, sample path locations $z_j = 2(z_{Sj} - z_R)$) with reflected power labeled as P_{Sj} :

$$P(k) = P_R(k) + \sum_j P_{Sj}(k) + \sum_j 2\sqrt{P_R(k)P_{Sj}(k)} \cos(kz_j) + \frac{1}{2} \sum_{\substack{i,j \\ i \neq j}} 2\sqrt{P_{Si}(k)P_{Sj}(k)} \cos(k(z_i - z_j)). \quad (2.19)$$

For most scenarios $P_{Sj} \ll P_R$ which allows the last term to be ignored. By removing the DC component of the measured power signal $\sim P_R(k)$, we are left with the approximate summation of all the sample reflections interfering with the reference reflection.

$$P(k) - P_R(k) \approx \sum_j 2\sqrt{P_R(k)P_{Sj}(k)} \cos(kz_j) \approx \sum_j 2\sqrt{P_R P_{Sj}} S(k) \cos(kz_j) \quad (2.20)$$

The function $S(k)$ is the normalized spectral function of the light source defined earlier. Taking the Fourier transform of this interferometric signal in k-space allows the separation of the reflections from different depths:

$$FT(P(k) - P_R(k)) \approx \sum_j 2\sqrt{P_R P_{Sj}} \int_{-\infty}^{\infty} S(k) \cos(kz_j) \exp(ikz) dk. \quad (2.21)$$

With the assumption that $S(k)$ changes slowly relative to $\cos(kz_j)$, and making the assumption that $z_j = 2(z_{Sj} - z_R) \geq 0$ simplifies the equation to:

$$\begin{aligned} \tilde{I}(z) = FT(P(k) - P_R(k)) &\approx \sum_j \sqrt{P_R P_{Sj}} \int_{-\infty}^{\infty} S(k) \exp(ik(z - z_j)) dk \\ &= \sum_j \sqrt{P_R P_{Sj}} \tilde{f}_C(z - z_j). \end{aligned} \quad (2.22)$$

$\tilde{f}_C(z - z_j)$ is the complex form of the coherence function derived earlier in this chapter such that $\text{Real}[\tilde{f}_C(z - z_j)] = f_C(z - z_j)$ and the amplitude of this function is the definition of the envelope of the coherence function. The signal in OCT is the magnitude of the Fourier transform of the interference signal in k-space:

$$|\tilde{I}(z)|^2 = |FT(P(k) - P_R(k))|^2 \approx \sum_j P_R P_{Sj} |\tilde{f}_C(z - z_j)|^2. \quad (2.23)$$

The result is a summation of the magnitude of the envelope of the coherence functions centered around each of the sample reflection locations $z_j = 2(z_{Sj} - z_R)$, weighted by the power collected from each of the reflections P_{Sj} . This is identical to the form of the OCT signal measured in TDOCT.

One option available to SDOCT is the ability to adjust the coherence function through numerical spectral shaping. With the direct measurement of the spectral interference fringes, numerical shaping of the fringes before the Fourier transform is performed can alter the shape of the coherence function $f_C(z)$ and improve the coherence length while suppressing the side lobes.

For retinal imaging, the ideal method of FDOCT is not easy to determine. Only recently has there been developments of fast swept source lasers centered at wavelengths capable of retinal imaging (1300 nm light is absorbed too much while propagating through the 5cm of aqueous humor of the eye) [14,15,16]. High-speed line scan CCD cameras are readily available for incorporation into a spectrometer design [17,18,19]. For the extent of this project, SDOCT is chosen as the FDOCT method used for retinal imaging.

2.6 SNR of SDOCT

Define spectral domain optical coherence tomography (SDOCT) system, where the power from the reference arm arriving at the spectrometer is P_R and power from the sample arm arriving at the spectrometer is P_S . Assume that $P_S \ll P_R$. Integration time of the spectrometer is τ . The spectrometer has M pixels used in k -space measurements. Assume shot-noise-limited performance of the SDOCT system.

Number of electrons on CCD pixel in k -space:

$$F(k) = \sum_j 2S_j(k) \cos(kz_j + \phi_{Sj}) + F_{DC}(k) + N(k). \quad (2.24)$$

$S_j(k)$ is the interferometric signal is defined as $S_j(k) = \eta \sqrt{P_R(k)P_S(k)R_j} \tau / h\nu_0$ for a sample reflection R_j at optical path difference $z_j = 2(z_{Sj} - z_R)$ of interferometer. The summation of this signal is taken over all of the sample reflections. Define $P_R = \sum_k P_R(k)$, $P_S = \sum_k P_S(k)$.

$F_{DC}(k) + N(k)$ is the shot noise distribution of electrons. The mean number of electrons $F_{DC}(k)$ is given by $\eta P_R(k) \tau / h\nu_0$, where η is the combined light collection and electron conversion efficiency of the spectrometer for photons of energy $h\nu_0$. $N(k)$ is the random portion of the Gaussian distribution with variance $\sigma^2_{N(k)} = \eta P_R(k) \tau / h\nu_0$ and zero mean.

Using the property of the Fourier transform: $FT(A + B) = FT(A) + FT(B)$, the Fourier transform (FT) of $F(k)$ produces the OCT intensity amplitude $\tilde{I}(z)$:

$$\tilde{I}(z) = FT(F(k)) = \sum_j FT(2S_j(k) \cos(kz_j + \phi_{Sj})) + FT(F_{DC}(k)) + FT(N(k)) . \quad (2.25)$$

Breaking it into the real and imaginary components of the complex Fourier transform of M data points in k-space:

$$\begin{aligned} \tilde{I}(z) &= I(z) \exp(i\phi(z)) = FT(F(k)) = \sum_k^M F(k) \exp(-ikz) \\ &= I_{\text{Re}}(z) + iI_{\text{Im}}(z) = \sum_k^M F(k) \cos(kz) - i \sum_k^M F(k) \sin(kz) . \end{aligned} \quad (2.26)$$

Assume the number of data points in FT, defined as M, is large enough such that a delta function accounts for the Fourier transform of an oscillatory function. Let the arbitrary choice of $z_j \geq 0$ for all reflection locations be taken into account as well.

These assumptions lead to:

$$\sum_k^M \cos(kz) \cos(kz_j) = \sum_k^M \sin(kz) \sin(kz_j) = \frac{M}{2} \delta(z - z_j), \quad \sum_k^M \cos(kz) \sin(kz_j) = 0 . \quad (2.27)$$

DC Term

$$\begin{aligned} FT(F_{DC}(k)) &= \sum_k^M F_{DC}(k) \exp(-ikz) \approx \delta(z) \sum_k^M F_{DC}(k) = \delta(z) \frac{\eta\tau}{h\nu_0} \sum_k^M P_R(k) \\ &= \delta(z) \frac{\eta P_R \tau}{h\nu_0} \end{aligned} \quad (2.28)$$

Interferometric Signal

Define the signal $\tilde{S}(z) = S(z) \exp(i\phi_S(z)) = \sum_k^M \sum_j 2S_j(k) \cos(kz_j + \phi_{Sj}) \exp(-ikz)$. Using the identity $\cos(kz_j + \phi_{Si}) = \cos(kz_j) \cos(\phi_{Sj}) - \sin(kz_j) \sin(\phi_{Sj})$:

$$\tilde{S}(z) = \sum_k \sum_j^M 2S_j(k)(\cos(kz_j)\cos(\phi_{Sj}) - \sin(kz_j)\sin(\phi_{Sj}))\exp(-ikz). \quad (2.29)$$

Assume $S_j(k)$ changes slowly compared to $\cos(kz_j)$ and $\sin(kz_j)$. With this assumption make the approximation within the summation: $\cos(kz)\cos(kz_j) = \sin(kz)\sin(kz_j) = \frac{1}{2}\delta(z - z_j)$

$$\begin{aligned} \tilde{S}(z) &= \sum_k \sum_j^M 2S_j(k)(\cos(kz_j)\cos(kz)\cos(\phi_{Sj}) + i\sin(kz_j)\sin(kz)\sin(\phi_{Sj})) \\ &= \sum_k \sum_{j=1}^M S_j(k)(\cos(\phi_{Sj}) + i\sin(\phi_{Sj}))\delta(z - z_j) = \sum_j \exp(i\phi_{Sj}) \sum_k^M S_j(k)\delta(z - z_j) \\ &= \frac{\eta\tau}{h\nu_0} \sum_j \exp(i\phi_{Sj}) \sum_k^M \sqrt{P_R(k)P_S(k)R_j} \delta(z - z_j) \\ &= \frac{\eta\sqrt{P_R P_S} \tau}{h\nu_0} \sum_j \exp(i\phi_{Sj}) \sqrt{R_j} \delta(z - z_j) = S(z) \exp(i\phi_S(z)). \end{aligned} \quad (2.30)$$

Noise Analysis

The noise calculated in OCT comes from the Fourier transform component of the noise distribution in k-space:

$$FT(N(k)) = \tilde{N}(z) = N(z) \exp(i\phi_N(z)). \quad (2.31)$$

To understand how the noise transforms, Parseval's theorem for finite length Fourier transforms is required.

Using $\tilde{f}(z) = \sum_k^M f(k) \exp(-ikz)$, where $f(k)$ is a real function such that $(f(k))^* = f(k)$:

$$\sum_z^M \tilde{f}(z)(\tilde{f}(z))^* = \sum_z^M \tilde{f}(z) \sum_k^M f(k) \exp(ikz)$$

$$\begin{aligned}
\sum_z^M |\tilde{f}(z)|^2 &= \sum_k^M f(k) \sum_z^M \tilde{f}(z) \exp(ikz) = \sum_z^M \sum_k^M f(k) \exp(ikz) \sum_{k'}^M f(k') \exp(-ik'z) \\
&= \sum_k^M f(k) \sum_{k'}^M f(k') \sum_z^M \exp(i(k-k')z) \\
\sum_z^M |\tilde{f}(z)|^2 &= M \sum_k^M f(k) \sum_{k'}^M f(k') \delta(k-k') = M \sum_k^M |f(k)|^2. \tag{2.32}
\end{aligned}$$

This theorem is important for relating the Fourier transforms of the shot noise distribution in k-space $N(k)$, measured on the CCD. With $\tilde{N}(z) = N(z) \exp(i\phi_N(z)) = \sum_k^M N(k) \exp(ikz)$:

$$\sum_z^M |\tilde{N}(z)|^2 = M \sum_k^M |N(k)|^2. \tag{2.33}$$

With the definition for the mean variation over all k-space measured as $\langle N(k) \rangle = 0$:

$$\sum_z^M |\tilde{N}(z)|^2 = M \left\langle |\tilde{N}(z)|^2 \right\rangle_z = M \sum_k^M |N(k)|^2 = M^2 \left\langle |N(k)|^2 \right\rangle_k = M^2 \left\langle \sigma^2_{N(k)} \right\rangle_k \tag{2.34}$$

$$\left\langle |\tilde{N}(z)|^2 \right\rangle_z = M \left\langle \sigma^2_{N(k)} \right\rangle_k = \frac{\eta\tau}{h\nu_0} M \left\langle P_R(k) \right\rangle_k = \frac{\eta P_R \tau}{h\nu_0} \tag{2.35}$$

$$\tilde{N}(z) = N(z) \exp(i\phi_N(z)) = N_{\text{Re}}(z) + iN_{\text{Im}}(z). \tag{2.36}$$

Each component of Fourier Transform of random Gaussian noise distribution results in a Gaussian distribution as well. The real and imaginary components $N_{\text{Re}}(z)$, $N_{\text{Im}}(z)$ of the Fourier transform of the noise distribution $N(k)$ are random Gaussian distributions, all centered around zero mean such that $\langle N(k) \rangle = \langle N_{\text{Re}}(z) \rangle = \langle N_{\text{Im}}(z) \rangle = 0$. With each component being independent of each other, the phase of the noise $\phi_N(z)$ is completely random. Determining the properties of the noise components:

$$|\tilde{N}(z)|^2 = N_{\text{Re}}(z)^2 + N_{\text{Im}}(z)^2 \tag{2.37}$$

$$\left\langle |\tilde{N}(z)|^2 \right\rangle = \left\langle N_{\text{Re}}(z)^2 \right\rangle + \left\langle N_{\text{Im}}(z)^2 \right\rangle = \sigma_{N_{\text{Re}}}^2 + \sigma_{N_{\text{Im}}}^2. \tag{2.38}$$

The transform components $N_{\text{Re}}(z)$, $N_{\text{Im}}(z)$ have identical distributions, which means that $\sigma_{N_{\text{Re}}}^2 = \sigma_{N_{\text{Im}}}^2$. Therefore:

$$\sigma_{N_{\text{Re}}}^2 = \sigma_{N_{\text{Im}}}^2 = \frac{1}{2} \left\langle \left| \tilde{N}(z) \right|^2 \right\rangle = \frac{\eta P_R \tau}{2h\nu_0}. \quad (2.39)$$

The probability distribution of the real noise component, which is identical to the imaginary component distribution is calculated to be of the form:

$$P(N_{\text{Re}}) = P_o \exp(-N_{\text{Re}}^2 / 2\sigma_{N_{\text{Re}}}^2). \quad (2.40)$$

The probability distribution of the noise amplitude $N(z)$ is determined from the individual component distributions:

$$\begin{aligned} P(N) &= \int_0^N P(N_{\text{Re}}) P(N_{\text{Im}} = \sqrt{N^2 - N_{\text{Re}}^2}) dN_{\text{Re}} \\ &= \int_0^N P_o^2 \exp(-N_{\text{Re}}^2 / 2\sigma_{N_{\text{Re}}}^2) \exp(-(N^2 - N_{\text{Re}}^2) / 2\sigma_{N_{\text{Re}}}^2) dN_{\text{Re}} \\ &= \int_0^N P_o^2 \exp(-N^2) / 2\sigma_{N_{\text{Re}}}^2 dN_{\text{Re}}. \end{aligned} \quad (2.41)$$

Normalizing the distribution for the noise amplitude:

$$P(N) = \frac{2}{\langle \left| \tilde{N}(z) \right|^2 \rangle} N \exp(-N^2) / \langle \left| \tilde{N}(z) \right|^2 \rangle. \quad (2.42)$$

Using the probability distribution, the standard deviation of the magnitude of the noise N^2 is calculated:

$$\sigma_{N^2} = \left\langle \left| \tilde{N}(z) \right|^2 \right\rangle = \frac{\eta P_R \tau}{h\nu_0}. \quad (2.43)$$

OCT Calculations

Combining all of this analysis, the OCT intensity amplitude, given by the Fourier transform of $F(k)$ is of the form, at $z \neq 0$:

$$\begin{aligned}\tilde{I}(z) &= I(z) \exp(i\phi(z)) = FT(F(k)) = \tilde{S}(z) + \tilde{N}(z) \\ &= S(z) \exp(i\phi_S(z)) + N(z) \exp(i\phi_N(z)).\end{aligned}\quad (2.44)$$

The properties of the signal and noise terms have been derived previously. The magnitude of the OCT intensity can be calculated:

$$|\tilde{I}(z)|^2 = I(z)^2 = S(z)^2 + N(z)^2 - 2S(z)N(z) \cos(\phi_S(z) - \phi_N(z)). \quad (2.45)$$

Averaging the OCT intensity, since ϕ_N is completely random:

$$\langle |\tilde{I}(z)|^2 \rangle = S(z)^2 + \langle N(z)^2 \rangle. \quad (2.46)$$

SNR Definition

System SNR sensitivity definition in OCT is described by the ratio of magnitude of the signal S^2 where the reflection $R=1$ to the standard deviation of the noise magnitude:

$$\text{SNR}_{\text{SDOCT}} = \frac{S(z, R=1)^2}{\sigma_{N^2}} = \frac{S^2}{\langle N(z)^2 \rangle} = \frac{\left((\eta\tau/h\nu_0) \sqrt{P_R P_S} \right)^2}{(\eta\tau/h\nu_0) P_R} = \frac{\eta P_S \tau}{h\nu_0}. \quad (2.47)$$

Compare this to TDOCT SNR of equation (2.18): $\text{SNR}_{\text{TDOCT}} = \frac{2\eta' P_S \tau'}{(h\nu_0)}$.

If SDOCT can acquire an entire depth scan (A-scan) in the same time TDOCT acquires one depth location data τ , both techniques will produce comparable SNR. The efficiency of data collection using SDOCT is much greater than that of TDOCT [20,21,22].

2.7 SDOCT Limitations

2.7.1 SDOCT Limitation #1: Mirror Terms in SDOCT

In SDOCT, the OCT intensity is determined by the Fourier transform of the interference fringes measured in k-space:

$$\tilde{I}(z) \approx \sum_j 2\sqrt{P_R P_{Sj}} \int_{-\infty}^{\infty} S(k) \cos(kz_j) \exp(ikz) dk \quad (2.48)$$

The assumption is made that all of the sample reflections are located at longer path lengths than the reference path length, such that $z_j = 2(z_{Sj} - z_R) \geq 0$. Because $\cos(kz_j)$ cannot distinguish between reflections located at $|z_j|$ and $-|z_j|$, all images will experience a mirroring effect over the sample interferometer arm position equal to path length position of the reference arm.

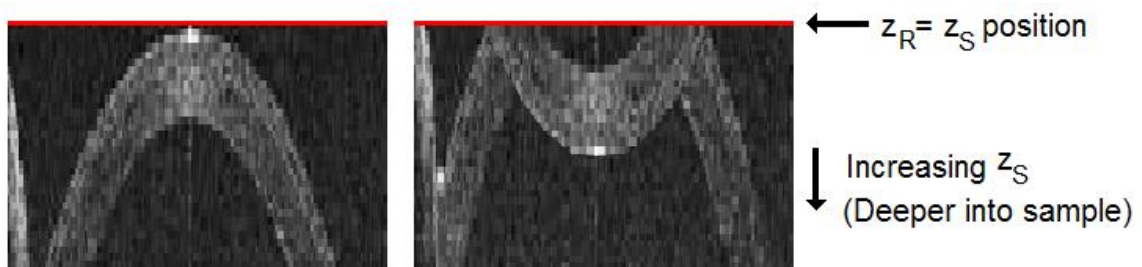


Figure 2.8: Mirroring example of the SDOCT image for two different reference arm positions. The change in the reference arm position of an intensity image (left) creates a mirrored image (right) in this case.

2.7.2 SDOCT Limitation #2: Maximum Imaging Depth in SDOCT

Nyquist theorem defines for a sampling rate of f_0 , the maximum resolvable frequency is $f_0/2$. Frequencies of $f_0 - f$ are aliased due to limited sampling to a measured frequency of f . The fastest oscillation that can be measured completes a full oscillation in exactly two sampled points.

In terms of k-space measurements of the interference fringes, with an average sampling spacing of δk , the maximum resolvable signal completes a full oscillation within $2\delta k$.

With the interference signal $\propto \cos(2k(z_S - z_R))$, the maximum resolvable path length

difference of $(z_S - z_R)_{MAX} = \frac{\pi}{2\delta k} = \frac{\lambda_0^2}{4\delta\lambda}$ in air, where $\delta k = \frac{2\pi}{\lambda_0^2} \delta\lambda$.

2.7.3 SDOCT Limitation #3: SNR Drop with Depth in SDOCT

The spectrometer used in SDOCT creates k-space measurements by integrating over a finite region of k-space. Oscillations in k-space are affected by this finite sampling method.

Looking at the interference fringe power measured on the spectrometer at wavenumber k for interference signal $\cos(2k(z_R - z_S))$:

$$P(k) \propto \frac{1}{\delta k} \int_{k-\delta k/2}^{k+\delta k/2} \cos(2k'(z_R - z_S)) dk' . \quad (2.49)$$

Using the assumption that $\delta k \ll k$, the interference measurement can be approximated as:

$$P(k) \propto \cos(2k(z_R - z_S)) \left(1 - \frac{\delta k^2 (z_R - z_S)^2}{6} \right). \quad (2.50)$$

Comparing the fringe power amplitude measurement to an ideal case where $\delta k \rightarrow 0$:

$$\frac{P(k)}{P(k, \delta k = 0)} = \left(1 - \frac{\delta k^2 (z_R - z_S)^2}{6} \right). \quad (2.51)$$

This ratio translates to drop in the measured OCT signal over the image depth in SDOCT:

$$\frac{SNR(z = z_R - z_S)}{SNR(z = 0)} = \left(1 - \frac{\delta k^2 (z_R - z_S)^2}{6} \right)^2 . \quad (2.52)$$

In the ideal case, δk in this definition would be the minimum k-space separation of the CCD pixels, designated by δk_{CCD} . In reality, δk is also determined by the ability of the imaging elements to focus an individual wavelength onto each CCD pixel. If the focused spot size of a given wavelength is larger than the CCD pixel, the OCT signal drop will depend on the focused spot size in k-space, designated by δk_{FOCUS} . Assuming that the focused spot size makes the SNR drop over depth dependant on δk_{FOCUS} , the maximum imaging depth is dependant on δk_{CCD} .

Looking at the SNR drop at the maximum imaging depth $(z_S - z_R)_{MAX} = \frac{\pi}{2\delta k_{CCD}} = \frac{\lambda_0^2}{4\delta\lambda_{CCD}}$:

$$\frac{SNR(z = (z_R - z_S)_{MAX})}{SNR(z = 0)} = \left(1 - \frac{\pi^2}{24} \frac{\delta k_{FOCUS}^2}{\delta k_{CCD}^2}\right)^2. \quad (2.53)$$

In terms of wavelength:

$$\frac{SNR(z = (z_R - z_S)_{MAX})}{SNR(z = 0)} = \left(1 - 0.41 \frac{\delta\lambda_{FOCUS}^2}{\delta\lambda_{CCD}^2}\right)^2. \quad (2.54)$$

In the ideal case where the spectrometer measurement is limited by the CCD pixel width, the SNR drop at the maximum depth is calculated:

$$\frac{SNR(z = (z_R - z_S)_{MAX})}{SNR(z = 0)} = (1 - 0.41)^2 = 0.348 = -4.6 \text{ dB}. \quad (2.55)$$

2.8 Phase Changes as Basis of Contrast

As described in Chapter 2.3, the oscillatory portion of the interferometric signal $\cos(2k_0(z_S - z_R))$ can be described by a relative phase $\phi_S - \phi_R$ such that:

$$\cos(2k_0(z_S - z_R)) = \cos(\phi_S - \phi_R). \quad (2.56)$$

The limitation of the phase is the inability to determine the relative position of the reflections from each interferometer arm beyond an accuracy of $\lambda_0/2$. This results in a phase accuracy limitation of 2π :

$$\phi_S - \phi_R = 4\pi(z_S - z_R) / \lambda_0 + 2\pi m \quad (2.57)$$

where m is an integer to limit the phase measurement to $-\pi \leq \phi_S - \phi_R \leq \pi$. The cyclic nature of the phase measurements limits the usefulness of the absolute phase measurement of a sample reflection. Changes in the phase measurement can be useful due to the sensitivity to small relative motions occurring between the sample and reference reflections:

$$\Delta\phi = \Delta(\phi_S - \phi_R) = 2k_0\Delta(z_S - z_R) = \frac{4\pi}{\lambda_0} \Delta z. \quad (2.58)$$

Due to the cyclic nature of the phase, only phase changes between the limits $-\pi \leq \Delta\phi \leq \pi$ can be identified properly. Phase changes can identify motions up to a maximum of $\lambda_0/4$, much smaller than the resolution capabilities of the OCT system. The motion calculated by the phase change is only along the axial direction, parallel to the imaging light direction. Using the phase change information of the scatterers within a sample, the tiny motions measured can provide additional contrast to the structural information provided by OCT imaging.

2.8.1 Definition of Phase Noise

With the OCT signal $\tilde{I}(z)$, the calculated phase $\phi(z)$ can deviate from the expected sample phase $\phi_S(z)$ depending on the relative noise properties:

$$\tilde{I}(z) = I(z) \exp(i\phi(z)) = \tilde{S}(z) + \tilde{N}(z) = S(z) \exp(i\phi_S(z)) + N(z) \exp(i\phi_N(z)). \quad (2.59)$$

To determine the noise effects on the error on phase measurements, a probability analysis of the phase is required. Since the phase accuracy does not depend on the sample phase, set

$\phi_s(z) = 0$ for convenience. For this case, the phase can be determined through trigonometric means:

$$\tan(\phi(z)) = \frac{N_{\text{Im}}(z)}{S(z) + N_{\text{Re}}(z)}. \quad (2.60)$$

The noise components $N_{\text{Re}}(z)$ and $N_{\text{Im}}(z)$ have the same Gaussian distribution described earlier. For the case where $S \gg N$, the phase determination can be simplified.

$$\phi(z) \approx \frac{N_{\text{Im}}(z)}{S(z)}. \quad (2.61)$$

The probability distribution of the phase $\phi(z)$ is proportional to the distribution of the noise component, calculated earlier:

$$P(\phi) = P(N_{\text{Im}} = \phi S) = P_o \exp(-\phi^2 S^2 / \langle N(z)^2 \rangle^2) \quad (2.62)$$

which has a calculated variance of:

$$\sigma_{\phi}^2(z) = \frac{|\tilde{N}(z)|^2}{2S(z)^2}. \quad (2.63)$$

Phase error is dependant on the local signal to noise ratio for a given reflector. Phase changes measured for a reflector of OCT signal $S^2(z)$ require two phase measurements, each with phase error associated with it. The phase variance determined for phase changes is twice the value of the error for a single phase measurement:

$$\sigma_{\Delta\phi}^2(z) = 2\sigma_{\phi}^2(z) = \frac{|\tilde{N}(z)|^2}{S(z)^2} = \frac{1}{\text{SNR}(z)}. \quad (2.64)$$

2.9 Choosing Between TDOCT and SDOCT

There are several factors that need to be compared in deciding between TDOCT and SDOCT as the ideal system to produce phase contrast imaging for retinal imaging.

2.9.1 SNR Comparison

Comparing the SNR of 1 pixel in TDOCT to the SNR of an A-scan of SDOCT:

$$\text{SNR}_{\text{TDOCT}} = \frac{2\eta_{TD}P_s\tau_{TD}}{h\nu_0}, \text{SNR}_{\text{SDOCT}} = \frac{\eta P_s\tau}{h\nu_0}. \quad (2.65)$$

It can be approximated that $\text{SNR}_{\text{TDOCT}} \approx \text{SNR}_{\text{SDOCT}}$ when the acquisition time of 1 depth location in TDOCT matches the acquisition time of an entire depth scan in SDOCT. With such a large improvement of image acquisition efficiency, SDOCT is the optimum choice in general.

2.9.2 Phase measurements with TDOCT versus SDOCT

SDOCT intrinsically measures the phase from all of the depth reflections at the same time. Any unwanted bulk axial motion of the sample can be analyzed and removed from contrast measurements. TDOCT has only one measurement of phase for each pixel acquired. If bulk sample motion removal is required, additional hardware and analysis would be required in the TDOCT system to measure a reference phase for removal. With the ease of simultaneously acquiring the phases from all of the sample depths, SDOCT is the optimum choice under this regard.

2.9.3 Spectral shaping and Dispersion compensation

As described in Chapter 2.2, optimal imaging in OCT depends on the shape of the coherence function. The width of the function determines the axial resolution, while the shape and side lobes of the function determine the image artifacts created by strong reflections within the sample. Another factor which determines the shape of the coherence function is the relative dispersion between the optical paths of the interferometer arms in the system. Mismatches between sample and reference interferometer arms can broaden and distort the coherence function, reducing image quality.

Variations in the dispersion properties of different samples can ultimately limit the axial resolution without any further adjustment to the system dispersion. SDOCT can numerically compensate for dispersion mismatches between the interferometer arms as well as adjust the spectral shape to improve the coherence function shape. TDOCT can only alter these factors through optical adjustment to the system.

2.9.4 Minimum time required per transverse location

The minimum time per transverse location in SDOCT is determined by the acquisition rate of the spectrometer camera, which is limited by currently available commercial technologies. TDOCT can theoretically achieve a much faster acquisition rate of each pixel for currently available hardware. If faster acquisition speeds are required than can be achieved with SDOCT, TDOCT is the only available option to meet those requirements.

2.9.5 Limitations of SDOCT

Considering all of the limitations of SDOCT described in Chapter 2.7, proper optical alignment of the thin retinal sample can reduce most of the negative effects of these limitations.

Unless the OCT imaging situation requires a transverse pixel dwell time shorter than SDOCT is capable of, SDOCT has comparable or superior performance to TDOCT and is clearly the optimal choice for proceeding with phase contrast imaging.

2.10 References

1. D. Huang et al., "Optical coherence tomography," *Science* 254, 1178 (1991).
2. W. Drexler et al., "In vivo ultrahigh resolution optical coherence tomography," *Opt. Letters* 24, 1221 (1999).
3. Z. Yaqoob et al., "Homodyne en face optical coherence tomography," *Opt. Letters* 31, 1815 (2006), <http://www.opticsinfobase.org/abstract.cfm?URI=ol-31-12-1815>.
4. B. Hoeling et al., "Phase modulation at 125kHz in a Michelson interferometer using an inexpensive piezoelectric stack driven at resonance," *Rev. Sci. Instr.* 72, 1630 (2001).

5. M. Pircher et al., "Retinal cone mosaic imaged with transverse scanning optical coherence tomography," *Opt. Letters* 31, 1821-1823 (2006).
6. K. Grieve et al., "Ocular tissue imaging using ultrahigh-resolution, full-field optical coherence tomography," *Invest. Ophthalmol. Vis. Sci.* 45, 4126 (2004).
7. R.G. Cucu et al., "Combined confocal/en face T-scan based ultrahigh-resolution optical coherence tomography in vivo retinal imaging," *Opt. Letters* 31, 1684 (2006)
8. B. Bouma, E. Tearney, *Handbook of Optical Coherence Tomography*, (Marcel Dekker, Inc., 2002).
9. A.F. Fercher et al., "Measurement of intraocular distances by backscattering spectral interferometry," *Opt. Commun.* 117, 43 (1995).
10. M. Wojtkowski et al., "In vivo human retinal imaging by fourier domain optical coherence tomography," *J. Biomed. Opt.* 7, 457-463 (2002).
11. R. Leitgeb et al., "Ultrahigh resolution Fourier domain optical coherence tomography," *Opt. Express* 12, 2156 (2004). <http://www.opticsexpress.org/abstract.cfm?id=79930>.
12. S. R. Chinn et al., "Optical coherence tomography using a frequency-tunable optical source," *Opt. Letters* 22, 340-342 (1997).
13. B. Golubovic et al., "Optical frequency-domain reflectometry using rapid wavelength tuning of a Cr⁴⁺:forsterite laser," *Opt. Letters* 22, 1704-1706 (1997).
14. E. C. Lee et al., "In vivo optical frequency domain imaging of human retina and choroid," *Opt. Express* 14, 4403-4411 (2006),
<http://www.opticsexpress.org/abstract.cfm?id=89920>.
15. H. Lim et al., "Optical frequency domain imaging with a rapidly swept laser in the 815-870 nm range," *Opt. Express* 14, 5937-5944 (2006),
<http://www.opticsexpress.org/abstract.cfm?id=90546>.
16. R. Huber et al., "Amplified, frequency swept lasers for frequency domain reflectometry and OCT imaging: design and scaling principles," *Opt. Express* 13, 3513-3528 (2005),
<http://www.opticsexpress.org/abstract.cfm?id=83745>.
17. "Line Scan Cameras," Basler Vision Technologies,
http://www.baslerweb.com/beitraege/beitrag_en_17842.html.
18. "CCD Monochrome Linescan Cameras," Atmel Corporation,
http://www.atmel.com/dyn/products/devices.asp?family_id=612.
19. "Line Scan Cameras," DALSA, <http://vfm.dalsa.com/products/linescan.asp>.
20. M. Choma et al., "Sensitivity advantage of swept source and Fourier domain optical coherence tomography," *Opt. Express* 11, 2183-2189 (2003),
<http://www.opticsinfobase.org/abstract.cfm?URI=oe-11-18-2183>.
21. R. Leitgeb et al., "Performance of fourier domain vs. time domain optical coherence tomography," *Opt. Express* 11, 889-894 (2003),
<http://www.opticsinfobase.org/abstract.cfm?URI=oe-11-8-889>.
22. J. F. de Boer et al., "Improved signal-to-noise ratio in spectral-domain compared with time-domain optical coherence tomography," *Opt. Letters* 28, 2067-2069 (2003).

TRADEOFFS AND EXPERIMENTAL METHODS

3.1 OCT System Tradeoffs**3.1.1 Resolution****a) Transverse resolution**

In optical coherence tomography, the transverse resolution of the image is dominated by the same Gaussian optics which limits the resolution for confocal imaging. For light of wavelength λ_0 focused on a medium of index n , the minimum focused spot size diameter d (measured at the $1/e^2$ intensity locations) is calculated as [1]:

$$d \cong \frac{2\lambda_0}{n\pi\theta}. \quad (3.1)$$

By definition, θ is the half-angle of the focused cone of light on the sample. The numerical aperture (NA) is a common parameter for defining the focusing ability of a lens, given by $NA = n \sin \theta \cong n\theta$ for small angle approximation [2].

For retinal imaging, the final focusing lens was the human eye itself. For pupil diameters smaller than 1 mm, the human eye is nearly diffraction limited. For larger pupils, aberrations distort the focused light and limit the optical performance of the lens, with varying levels of aberrations between patients. Using a pupil diameter of 1 mm, a typical human eye with a length of ~ 25 mm will have an illumination half-angle θ of:

$$\theta \cong \frac{0.5mm}{25mm} = 0.02 \text{ radians} = 1.1^\circ. \quad (3.2)$$

With an approximate refractive index of water inside the eye, this leads to a numerical aperture $NA \sim 0.027$. For a light source of wavelength $\lambda_0=800$ nm, using a 1 mm illumination pupil leads to a focus spot size diameter on the retina of $d=20$ μm .

SDOCT measures reflections over a range of depths within a sample. Like confocal imaging, the transverse resolution of these measurements changes over the entire depth of the OCT image. The depth of focus is the confocal parameter which determines the depth range where the beam waist was smaller than $\sqrt{2}d$ (which is approximated as the depth region of constant transverse resolution) [3,4]. This parameter b is calculated in Gaussian optics as:

$$b = \frac{\pi d^2}{2\lambda_0}. \quad (3.3)$$

For retinal imaging in the case of $d=20$ μm the confocal parameter b is determined to be approximately 750 μm , which is approximately the entire depth of the retina. In this case, it is expected that a SDOCT image of a human retina can be achieved with approximately uniform transverse resolution over the depth of the sample.

b) Axial/ Depth resolution

In confocal imaging, the axial resolution (also called the depth resolution) is determined by the confocal parameter. A pinhole used in conjunction with the focusing lens can improve the depth resolution further with the sacrifice of the light collection efficiency from the sample. In optical coherence tomography, the axial resolution is determined by the minimum of the coherence length l_c of the broadband light source and the confocal parameter. In most low NA scenarios such as retinal imaging, the coherence length dominates the axial resolution. In a tissue of refractive index n , the coherence length l_c describes the optical path discrimination ability, which results in an axial resolution in tissue of l_c/n .

With the ability of spectral shaping in SDOCT, the important parameter of the light source is the full spectral width, designated by $\Delta\lambda_{SOURCE}$. For a top-hat spectrum, where $\Delta\lambda_{SOURCE} = \Delta\lambda_{FWHM}$, the coherence length has been calculated as:

$$l_{C,Tophat} = 0.60 \frac{\lambda_0^2}{\Delta\lambda_{FWHM}} = 0.60 \frac{\lambda_0^2}{\Delta\lambda_{SOURCE}}. \quad (3.4)$$

For a Gaussian spectrum where $\Delta\lambda_{SOURCE} \approx 2.3\Delta\lambda_{FWHM}$ (defined by the spectral points of 3% of the maximum source power), the coherence length is:

$$l_{C,Gaussian} = 0.44 \frac{\lambda_0^2}{\Delta\lambda_{FWHM}} \approx \frac{\lambda_0^2}{\Delta\lambda_{SOURCE}}. \quad (3.5)$$

In general, the coherence length can be considered of the general form:

$$l_C = \gamma \frac{\lambda_0^2}{\Delta\lambda_{SOURCE}} \quad (3.6)$$

where $0.60 \leq \gamma \leq 1$ depends on the spectral shape of the light source.

3.1.2 System Component Tradeoffs

a) Light Source

Optical imaging of the retina of the eye is not only limited by the optical absorption of 5cm of aqueous humor in the eye, but also by the sensitivity of the photoreceptors. When two different wavelengths of light illuminate the retina with identical intensities, the wavelength at which the photoreceptors are more sensitive appears brighter to the patient and imaging with this light is more uncomfortable. The ideal wavelengths to image the retina with are in the near infrared spectral regime, where there is almost no visual response to the incoming light. Combined with the expected water absorption spectra, this leads to the ideal

wavelength choices of around 800 nm and near 1.05 μm (small absorption window in water spectrum).

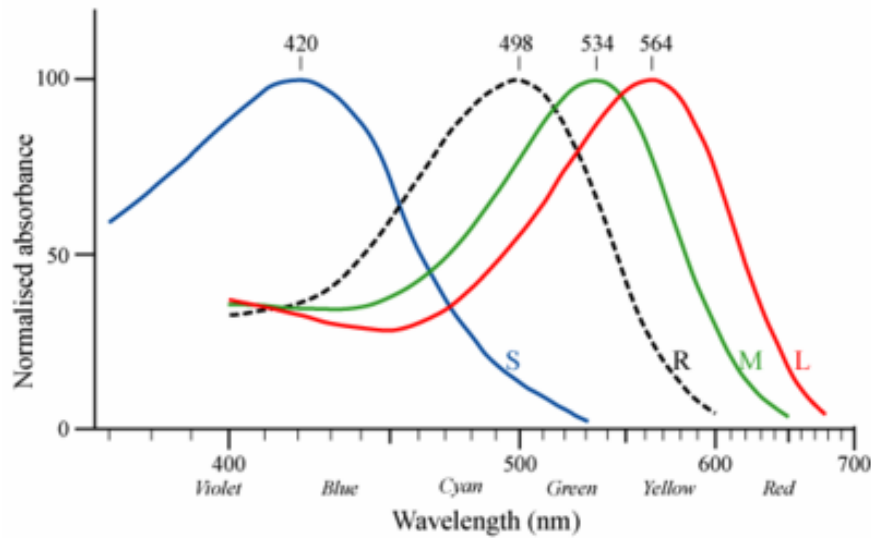


Figure 3.1: Absorption spectra of the rods (labeled R) and the three different types of cones sensitive to short (S), medium (M), and long (L) wavelengths in the retina.

With the coherence length of the form $l_c = \gamma \lambda_0^2 / \Delta \lambda_{SOURCE}$ determining the imaging axial resolution, a light source centered around 1.05 μm with a given spectral width would result in a coherence length approximately 70% larger than for the exact same spectral width around 800 nm. Two of the most important parameters of the light source for a given central wavelength are the bandwidth and the power. With an increased bandwidth, there is an increased possible axial resolution for the system. Increased light source power results in more flexibility in OCT imaging options including the system sensitivity. A source power of > 3 mW is ideal for retinal OCT imaging systems. In many cases, there is a tradeoff in light sources between bandwidth and power.

The availability of low-cost broadband light sources is the major limiting factor of achieving high-resolution OCT imaging. The highest resolution demonstrated in retinal OCT imaging utilizes a femtosecond titanium-sapphire laser [5,6]. The cost of such a laser

is typically greater than \$100,000 (more than twice the cost of the current commercial OCT imaging system) which limits the feasibility for widespread patient screening.

The most popular option for a low-cost broadband light source is a superluminescent diode (SLD), a very high power form of a light emitting diode (LED) which has been designed so that lasing does not occur. Technological developments of numerous companies have increased the selection of commercially available superluminescent diodes, with a variety of bandwidth and powers available [7].

To improve the bandwidth of the light source, multiple SLDs are commonly coupled together to produce a spectrum which is the sum of the individual SLD spectra. The limitation is that each SLD requires its own current supply and temperature controller, which multiplies the cost of the light source by the number of SLDs used. The experimental system uses a single broadband superluminescent diode to reduce the total cost of the light source. The broadest spectrum in a commercially available SLD around 800 nm has $\lambda_0=840$ nm and $\Delta\lambda_{FWHM}=50$ nm with a total source power of 16 mW (SLD-37-HP, Superlum Diodes Ltd.). The typical spectrum of this light source is plotted in Figure 3.2.

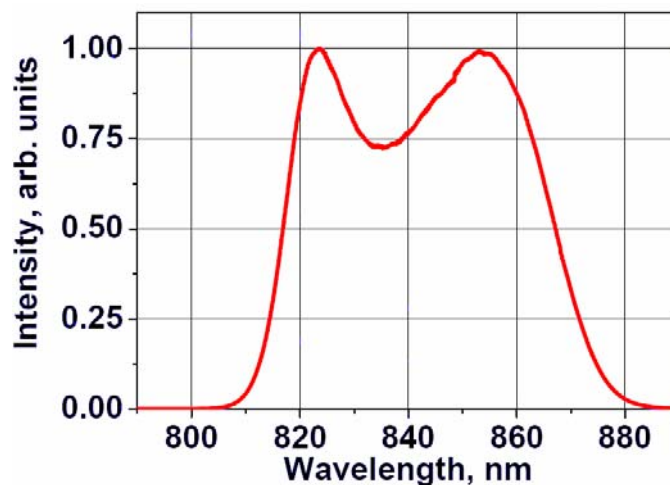


Figure 3.2: Expected spectral shape of the superluminescent diode SLD-37-HP. Image reproduced from [7].

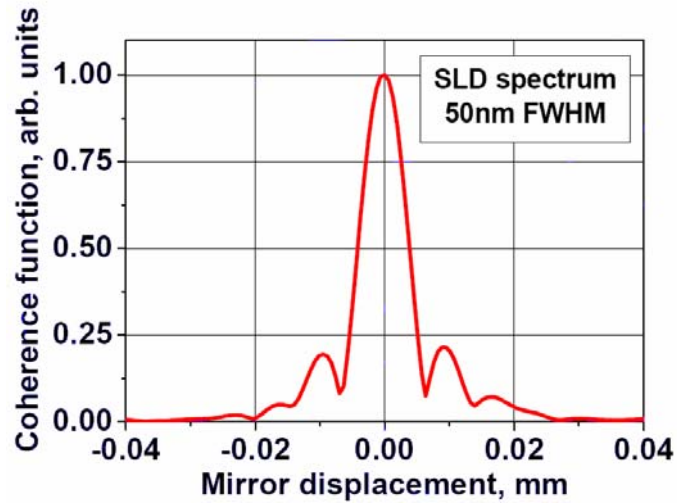


Figure 3.3: Expected coherence function for the light source of Figure 3.2. Image reproduced from [7].

With spectral shaping, the experimental light source with FWHM of 50 nm can achieve a range of coherence lengths, with a range of coherence functions as well. With a coherence length definition of $l_C = \gamma \lambda_0^2 / \Delta \lambda_{SOURCE}$, where $0.60 \leq \gamma \leq 1$ and $\Delta \lambda_{SOURCE} \approx 70$ nm for this light source, the expected coherence length range is $6.1 \mu\text{m} \leq l_C \leq 10.1 \mu\text{m}$ in air. In tissue of refractive index $n=1.38$, the coherence length in tissue is $4.4 \mu\text{m} \leq l_C / n \leq 7.3 \mu\text{m}$.

b) Fiber Optic Coupler

In the previous descriptions of the Michelson interferometer, a free space beamsplitter was used to split the incoming light into the reference and sample interferometer arms. A fiber optic coupler can accomplish the same task without requiring the same static optical alignment of the previous setup. The properties of the fiber optic coupler can be tailored to adjust the splitting ratio between the two sides of the coupler, allowing for the optimum splitting ratio to be determined.

For light of power P_0 entering the fiber optic coupler, the exiting power is split between the reference arm $((1-\eta)P_0)$ and the sample arm (ηP_0) of the interferometer. While the power

returning through the reference arm to the detector is important to determine shot noise limited operation, the power collected from the sample arm determines the system SNR performance. The power returning through the sample arm of the fiber coupler from an ideal reflector is $\rho\eta P_0$, where ρ is the geometrical coupling efficiency of the sample arm optics. The power collected from the sample arm which arrives at the detector is of the form $\rho\eta(1-\eta)P_0$, which is referred to as P_s in the SNR calculations of equation (2.47).

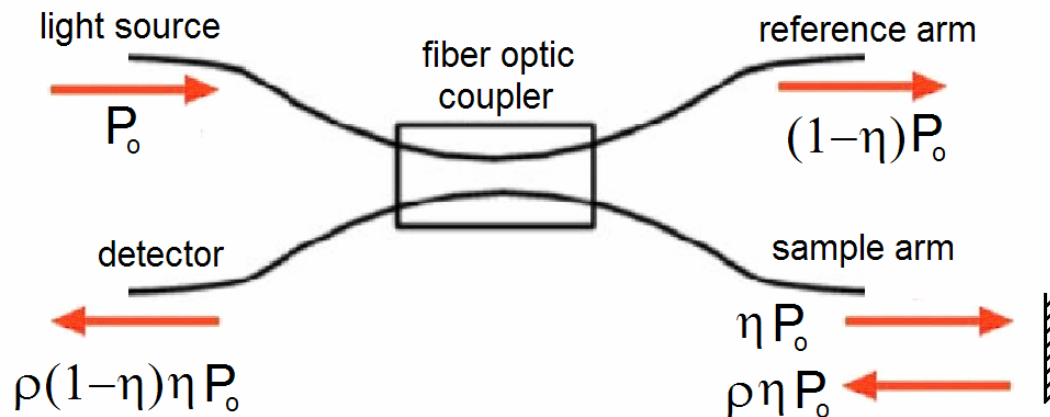


Figure 3.4: Schematic of fiber optic Michelson interferometer system with η of source power coupling into the sample arm.

As described earlier, shot noise limited SDOCT operation has a calculated SNR of:

$$\text{SNR}_{\text{SDOCT}} = \frac{\eta P_s \tau}{h \nu_0}. \quad (3.7)$$

By maximizing $P_s = \rho\eta(1-\eta)P_0$, the system performance will be improved. In general for a fixed coupling efficiency ρ , the sample power collected would be at a maximum for $\eta=0.50$ ($0 \leq \eta \leq 1$) which is the standard 50/50 coupler. This optimization is appropriate when there are no constraints on the maximum sample illumination.

The American National Standards Institute (ANSI) [8] sets limits on the maximum power exposures allowed for biomedical imaging. These restrictions protect the sample from various forms of thermal damage created from excessive energy deposition from incoming

photons. ANSI standards for retinal imaging are even more restrictive due to the added complications of possible damage to the photosensitive cells within the eye. For a light source centered about 800 nm, approximately 700 μW is allowed for constant viewing.

Retinal imaging is limited by the sample illumination power ηP_0 , so maximizing the sample power collected, $P_s = \rho(1-\eta)(\eta P_0)$ requires minimizing η . For a fixed maximum light source power P_0 , the highest efficiency occurs for a splitting factor η where ηP_0 reaches the imposed power limit or $\eta=0.5$, whichever is smaller.

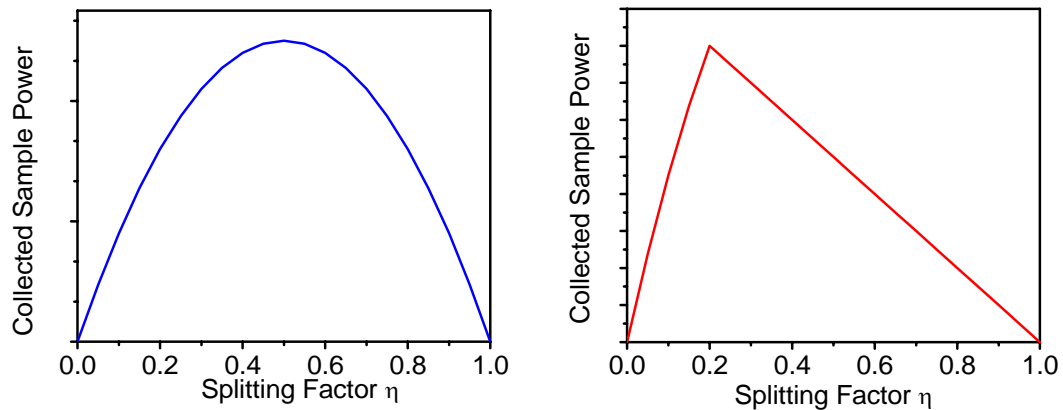


Figure 3.5: Normalized Sample Power collection versus splitting factor η for a fixed source power of P_0 with no restrictions (left) and for a case where the maximum sample power is limited to be $0.2 P_0$ (right).

3.1.3 SDOCT Specific Tradeoffs

a) Maximum A-scan rate

In SDOCT, the minimum time required to transfer the spectral data from the line scan CCD camera to the computer limits the A-scan rate of the imaging system. For the available high-speed line scan cameras, the technological limitation is the data transfer protocol Camera Link®, which transfers data from a single CCD pixel at a maximum rate of 60 MHz. For M CCD pixels acquired for each spectrometer measurement to be converted into

a single A-scan, the minimum time τ_{MIN} is given by the inverse of the maximum A-scan rate $f_{A-scan,MAX}$:

$$\tau_{MIN} = \frac{1}{f_{A-scan,MAX}} = \frac{M}{60MHz}. \quad (3.8)$$

The SDOCT system in this experiment uses $M = 2048$ in the line scan camera of the spectrometer. From this value, the minimum acquisition time and the maximum A-scan rate are calculated:

$$\tau_{MIN} = \frac{2048}{60MHz} = 34.1\mu s, \quad f_{A-scan,MAX} = 29.3 \text{ kHz}. \quad (3.9)$$

Using a 100 kHz clock rate to trigger the spectrometer acquisition, the SDOCT system uses a spectrometer read rate of 25 kHz, leading to a maximum acquisition time for the CCD pixels of 40 μs . To avoid possible crosstalk between successive spectrometer measurements, an integration time of $\tau=36.1 \mu s$ was used.

b) Tradeoffs between axial resolution and imaging depth

Previously, the coherence length was defined as $l_C = \gamma\lambda_0^2 / \Delta\lambda_{SOURCE}$ where $0.60 \leq \gamma \leq 1$ for most shapes of the light source spectrum. The maximum imaging depth of the SDOCT system was also defined as $\Delta z_{MAX} = (z_S - z_R)_{MAX} = \lambda_0^2 / 4\delta\lambda$. If we assume that the total light source spectrum is spread out over M' CCD pixels of the spectrometer (where $M' \leq M$ with M defined as the total number of CCD pixels), then

$$\Delta\lambda_{SOURCE} = M' \delta\lambda. \quad (3.10)$$

With these definitions, the relationship between the coherence length, the maximum imaging depth and the number of CCD pixels used is determined:

$$l_C = \gamma \frac{\lambda_0^2}{M' \delta\lambda} = \frac{4\gamma\Delta z_{MAX}}{M'}. \quad (3.11)$$

3.1.4 System Data Acquisition

The imaging capabilities are limited by the amount of raw data that can be handled in one acquisition. For the experimental system, each data set contains multiple spectrometer measurements, each of which contain 10-bit data acquired over 2048 CCD pixels. There are three common types of data acquisition methods for large numbers of sequential spectrometer measurements:

- i) Buffered raw data acquisition: The system memory stores all of the spectrometer data from one streamed acquisition with this option. After acquisition, the data is transferred to the computer storage for future processing and analysis. The maximum number of spectrometer measurements that can be acquired in one session is limited by the total memory (RAM) of the computer.
- ii) Data streaming to disk: This method takes the raw data from the spectrometer and transfers the information directly to the computer hard drive. If the streaming ability is faster than the data read rate of the spectrometer, the only limitation is the ultimate storage capacity of the data acquisition computer.
- iii) Real-time processing and analysis: By processing the incoming spectrometer data into OCT images, the total amount of data that needs to be stored is reduced. The ultimate limits to real-time processing depend on many factors, including the computer processor performance and the processing algorithms for the spectrometer data.

During development of analysis techniques, the ability to re-analyze previously acquired data is important. Real-time processing and analysis is useful after analysis algorithms have been finalized. To keep the cost and complexity at a minimum for this system, the buffered data acquisition method was used to acquire the spectrometer data.

The maximum number of spectrometer measurements which can be stored in system memory is approximately half of the total RAM capacity. The remaining system memory is required for the system to transfer the buffered data to disk. For 10-bit spectrometer data of

2048 individual CCD pixels, 1 GB of system RAM can buffer $256 \times 256 = 65536$ successive spectrometer scans and 2 GB of system RAM can buffer $256 \times 512 = 131072$ successive scans (which can be processed into the equivalent amount of A-scans).

3.2 Imaging Tradeoffs

Through the buffer limitations of the SDOCT system, there are a maximum number of A-scans which can be acquired in succession. Each spectrometer measurement was acquired and transferred in the time $\tau_0 = 40 \mu\text{s}$. Buffered acquisition of spectrometer data utilizes successive measurements for storage into the system memory. For 2 GB of system RAM, this translates into a total acquisition time of spectrometer data of 5.26 s, which is equivalent to 512×256 total A-scans.

Transfer of the spectrometer data from the system memory to the computer hard drive can be longer than a minute. This data transfer limits the time between sequential buffered acquisitions. To create a full 3D data set using several memory buffers of data to break up the large region of interest into parts, it is important to have a sample which is stationary enough during the data transfer time. For microscopy, many samples do not move enough within a minute to be a problem for this type of 3D image acquisition. Retinal imaging, on the other hand, suffers from numerous forms of sample motion which general increase in amplitude and frequency with acquisition time. While it is possible to perform retinal imaging using sequential buffered acquisitions to break up a 3D image into sections, it is better to optimize the data acquisition such that one memory buffer contains the entire region of interest.

To consider the transverse scan region of the 3D image, the primary transverse scan direction will be designated as x , with the secondary scan direction designated as y . The total distance scanned in each direction of the data set are given by x_{SCAN} and y_{SCAN} such that:

$$x_{SCAN} = X_{DUTY} N_x \Delta x \quad (3.12)$$

$$y_{SCAN} = N_Y \Delta y . \quad (3.13)$$

N_X and N_Y are the total number of spectrometer acquisitions used for each scan direction. The memory buffer puts the limitation $N_X N_Y \leq \sim 131072$.

X_{DUTY} describes the percentage of A-scans measured in the x-scan which are used in the 3D image. For a bi-directional scan pattern where only the scans in one direction are used for the 3D image, $X_{DUTY}=0.5$. For the same bi-directional scan where both directions are used, $X_{DUTY}=1$. Uni-directional scan patterns with fly back can tailor the duty cycle to maximize the duty cycle and optimize the buffer acquisition efficiency.

The parameters Δx and Δy describe the spatial displacement in the x and y directions between successive locations in the scan patterns. In general confocal imaging, the scan distance between different transverse locations in both the x and y directions can be chosen to be identical, such that $\Delta x = \Delta y$. In SDOCT the interferometric signal is integrated over the x-scan displacement Δx , affecting the interference fringes depending on the sample properties.

For a sample illumination beam of profile $g(x, y) \approx \exp(-4(x^2 + y^2)/d^2)$, the beam diameter d in this case is defined as the $1/e^2$ of the beam profile. Scanning across uncorrelated scatterers with this beam by a distance Δx during the spectrometer integration results in a decrease in the calculated SDOCT SNR. This decrease is of the approximate form [9]:

$$\text{SNR decrease (dB)} \approx -5 \log(1 + 0.5 \Delta x^2 / d^2) . \quad (3.14)$$

For the scan parameter choice of $\Delta x = d$ the SNR decrease is approximately -1 dB, a negligible effect on the OCT image. This decrease in SNR assumes uncorrelated scatterers, which is not always the case for samples like the human retina which contain layered structures. Constant reflecting layers are a series of correlated scatterers, and any tilt of the layer along the scan direction causes an effective axial motion to be measured. Axial

motion during spectrometer acquisition has the ability to blur interference fringes and drop the measured OCT signal considerably.

Axial motion during the integration time of the spectrometer τ can be considered as a constant velocity in the z-direction v_z . In this case, the interference fringe signal which is measured in k-space is of the form:

$$P(k) \propto \int_0^{\tau} \cos(2k(z_0' + v_z t)) dt = \frac{1}{v_z} \int_{z_0 - \Delta z/2}^{z_0 + \Delta z/2} \cos(2kz) dz. \quad (3.15)$$

In this case, the axial motion during the integration time was $\Delta z = v_z \tau$. For no motion, the interference signal $P(k) \propto \cos(2kz_0) = P_0$. In general, the normalized interference power measured is:

$$\frac{P(k)}{P_0} = \frac{\sin(k\Delta z)}{k\Delta z}. \quad (3.16)$$

This results in a normalized OCT intensity:

$$\left(\frac{I}{I_0} \right)^2 = \left(\frac{\sin(k_0 \Delta z)}{k_0 \Delta z} \right)^2. \quad (3.17)$$

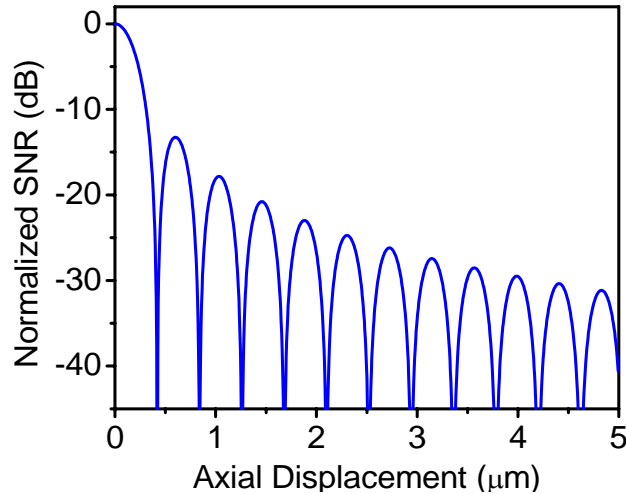


Figure 3.6: Normalized OCT intensity signal in logarithmic scale as a function of the axial motion which occurs during the spectrometer integration time. Center wavelength of 840 nm used for calculation.

The first minimum in this function $(I/I_0)^2 = 0$ occurs when $k_0\Delta z = \pi$, which results in $\Delta z = \lambda_0/2$. For a x-scan displacement of Δx , there is a maximum tilt angle of a correlated layer which can be measured before $(I/I_0)^2 = 0$. Defining a tilt angle θ such that $\theta = 0^\circ$ for a horizontal layer, the maximum transverse scan before the OCT signal is completely blurred out for a layer of a given tilt θ is calculated to be:

$$\Delta x = \frac{\lambda_0/2}{\tan \theta}. \quad (3.18)$$

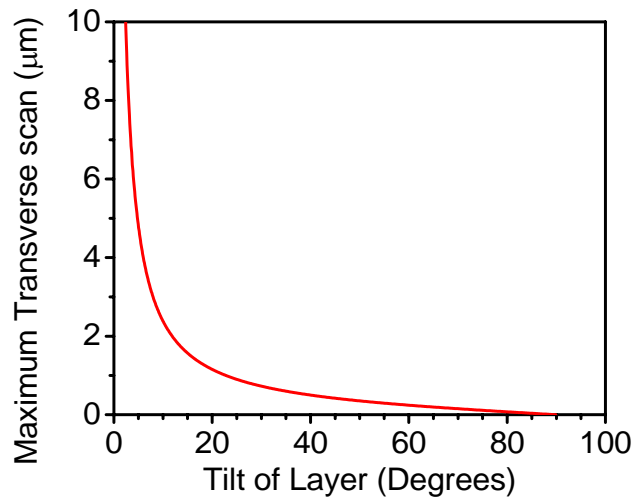


Figure 3.7: Minimum transverse scan Δx required to completely remove the OCT signal for a given tilt of a correlated scatterer layer.

The maximum transverse scan for a given tilt angle is independent of the diameter of the illumination beam. This is adequate for high transverse resolution scenarios such as microscopy, but seriously limits low transverse resolution situations such as retinal imaging. To reduce these issues, a high-density scan along the x-direction chosen such that $\Delta x \ll d$ is generally employed.

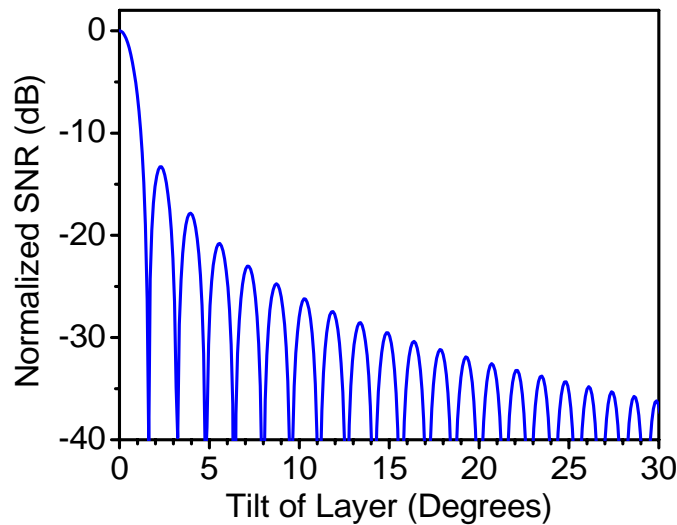


Figure 3.8: Normalized OCT intensity signal as a function of tilt angle for a transverse scan $\Delta x = 15 \mu\text{m}$.

For a transverse scan size of 15 mm, a comparable size to the transverse resolution experienced in retinal imaging, the OCT signal measured depends heavily on the tilt and correlation of the scatterer layers in the eye.

3.3 Phase Contrast Tradeoffs

The phase change measured for a given depth z with a time separation T , designated as $\Delta\phi(z,T)$, has a combination of several factors affecting the accuracy of the measurement:

$$\Delta\phi(z,T) = \Delta\phi_{\text{scatterer}}(z,T) + \Delta\phi_{\text{bulk}}(T) + \Delta\phi_{\text{SNR}}(z) + \Delta\phi_{\text{error,other}}(T). \quad (3.19)$$

The motion of interest is from the scatterers located at the depth z , referred to as the phase change term $\Delta\phi_{\text{scatterer}}(z,T)$. The total phase change $\Delta\phi(z,T)$ also contains the bulk motion of the entire sample along the imaging (axial) direction $\Delta\phi_{\text{bulk}}(T)$, caused by relative phase motion between the sample and the system and ideally is independent of depth z of the scatterers. $\Delta\phi_{\text{SNR}}(z)$ designates a phase error associated with the local SNR of the data calculated at the depth z and is independent of time for a constant SNR. Experimental and

theoretical results have determined that the standard deviation of SNR-limited phase error for phase changes has the form of equation 2.64 [10,11]:

$$\sigma_{\Delta\phi, \text{SNR}}(z) = \frac{1}{\sqrt{\text{SNR}(z)}}. \quad (3.20)$$

$\Delta\phi_{\text{error,other}}(z,T)$ encompasses the other phase errors which may occur for SDOCT phase measurements, including but not limited to phase changes caused by transverse motion across a scatterer at depth z , artifacts associated with limited depth sampling during axial motion of the sample or other computational based phase anomalies. By understanding the effects $\Delta\phi_{\text{bulk}}(T)$, $\Delta\phi_{\text{SNR}}(z)$, and $\Delta\phi_{\text{error,other}}(z,T)$ have on the accuracy of phase measurements in a SDOCT system, improvements can be made to reduce the adverse effects of these terms in the phase contrast images.

3.3.1 Doppler Flow Contrast

The phase change measured for a given reflection with a time separation T , defined as $\Delta\phi(T)$, corresponds to the net axial motion which has occurred during the time T . Observing flow of velocity v , oriented at an angle θ from the horizontal (in the case of the interferometer light arriving vertically upon the sample) results in the phase measurement proportional to the flow component along the imaging direction, designated as v_z [12,13]:

$$\Delta z(T) = \frac{\lambda_0}{4\pi} \Delta\phi(T) = v_z T = v T \sin \theta. \quad (3.21)$$

There are limits to the calculation of the axial flow component using the mean phase change of the scatterers. With the phase determined within a range of 2π , there is a limit to the maximum phase change that can be determined due to phase wrapping. Phase wrapping is created by the cyclic nature of the phase measurement. With phase determined from 0 to 2π , any phase change from $0 \rightarrow -\delta\phi$ appears as $0 \rightarrow 2\pi - \delta\phi$. This effect limits the maximum discernable phase change as $\Delta\phi_{\text{MAX}} = \pm\pi$. Using the minimum possible time

separation of phase changes $T=\tau_0=40\mu\text{s}$, the maximum possible axial velocity component that can be calculated in a medium of refractive index $n=1.35$ is:

$$v_{Z,MAX} = \frac{\Delta z_{MAX}}{\tau_0} = \frac{\lambda_0}{4\pi n} \frac{\Delta\phi_{MAX}}{\tau_0} = \pm \frac{\lambda_0}{4\tau_0} = \pm 3.9\text{mm/s.} \quad (3.22)$$

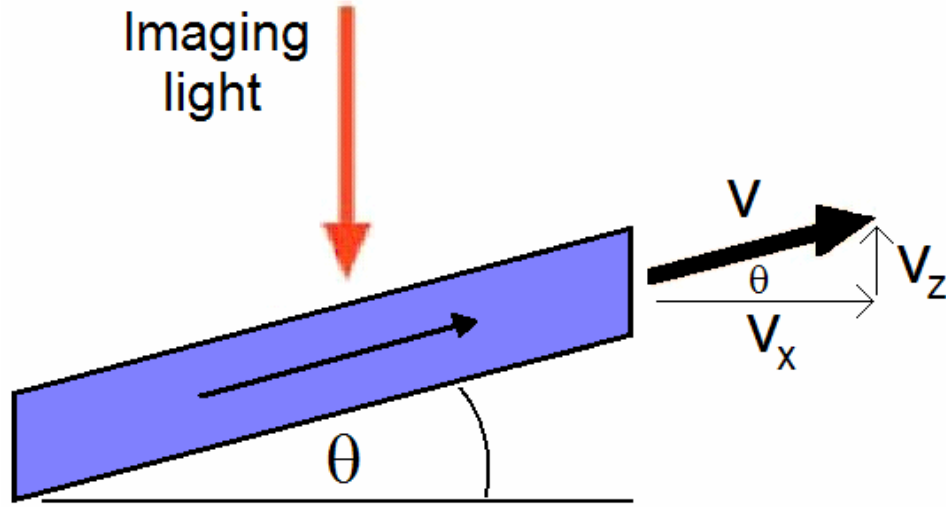


Figure 3.9: Schematic of flow measurement alignment for Doppler flow contrast.

The minimum possible velocity that can be identified is determined by the SNR-limited phase error of the OCT image. For a general Doppler image, assume that the maximum phase variance error in the image $\sigma_{\Delta\phi,MAX}$ determines the minimum observable axial flow. In that case set $\sigma_{\Delta\phi,MAX}=1$, which corresponds to $\text{SNR}(z)=1$ for the image. For N averages of the phase change measurements, the phase error measured reduces to $\sigma_{\Delta\phi,MAX}/\sqrt{N}=1/\sqrt{N}$ for the above assumption. For the minimum time separation $T=\tau_0$ of N phase changes, the minimum measurable axial velocity is:

$$v_{Z,MAX} = \frac{\lambda_0}{4\pi n \tau_0} \frac{\sigma_{\Delta\phi,MAX}}{\sqrt{N}} = \frac{1.23\text{mm/s}}{\sqrt{N}}. \quad (3.23)$$

With the axial flow component defined as $v_z = v \sin \theta$, visualization of flow is very difficult when the flow is slow or oriented horizontally such that $\theta \sim 0^\circ$. With an increased time separation T between phase measurements, the minimum and maximum axial velocities that can be quantitatively measured are reduced. This improves the minimum velocity visualization while hindering the faster flow imaging. Different analysis of the phase information has the potential of improving on the visualization abilities of the Doppler flow technique, allowing for visualizing slow and horizontal flows as well as the fastest flows in the system.

3.3.2 Phase Variance Contrast

Variance is another statistical analysis tool which looks at different properties of the data. While the average phase change describes the net axial motion occurring during the imaging time, the variance of the phase deals with the fluctuations in the measured motion. The variance of the phase changes $\Delta\phi(z,T)$ for scatterers at a depth z with a time separation T is calculated using the form of the statistical variance:

$$\sigma_{\Delta\phi}^2(z,T) = \langle \Delta\phi(z,T)^2 \rangle - \langle \Delta\phi(z,T) \rangle^2. \quad (3.24)$$

Assuming no correlation between the different phase factors which compose the phase change measured in equation 3.20, the variance of the phase changes can be calculated as the summation of the variances of the individual components:

$$\sigma_{\Delta\phi}^2(z,T) = \sigma_{\Delta\phi,scatterer}^2(z,T) + \sigma_{\Delta\phi,bulk}^2(T) + \sigma_{\Delta\phi,SNR}^2(z) + \sigma_{error,other}^2(z). \quad (3.25)$$

The primary source of motion contrast in this variance calculation is $\sigma_{\Delta\phi,scatterer}^2(z,T)$, which in general depends on the time separation T of the phase changes. $\sigma_{\Delta\phi,bulk}^2(T)$ describes the variance of the bulk axial motion of the sample for time separations T over the imaging time. For extremely stable imaging scenarios, this factor is not a major consideration. The phase error due to SNR limitations $\sigma_{\Delta\phi,SNR}^2(z)$ for a given depth z has been described previously in equation 3.21. One factor to note is the time independence of this factor,

assuming approximately constant OCT signal over the total imaging time. All of the other possible phase error sources are encompassed into one term $\sigma_{\text{error,other}}^2(z)$ for current analysis purposes.

There are four types of motion which contain components that are observable through the variance measurement of the phase motion:

- Variations in the axial component of flow
- Transverse flow effects of uncorrelated scatterers
- Axial component of Brownian-type random motion
- Ensemble statistical effects of uncorrelated scatterers

To understand the expected form of the motion variance, each of these scenarios must be individually analyzed. For adequate contrast to be observed, imaging parameters must be chosen such that the phase variance measured from the above-mentioned motion surpasses the variance limitations imposed by the SNR-limited phase error and the other phase noise factors.

3.3.3 Variations in Axial Flow

In situations containing flow, the macroscopic flow determination describes the mean flow from all the individual particles which compose the flowing media. It is typical to expect the flow from a given particle to experience flow variations from the measured mean flow. Collisions between flowing particles, variations in directionality of an individual particle's motion, or interference with static barriers at the edge of the flow region are all possible sources of flow variations within an ensemble of flowing particles.

For this analysis, assume that the distribution of velocities is independent in time. Define the distribution to have a mean axial velocity of v_z and a standard deviation of σ_{v_z} . Using

a time between phase measurements of T , the calculated standard deviation of the phase changes is determined as:

$$\sigma_{\Delta\phi}(T) = \frac{4\pi n \sigma_{vz} T}{\lambda_0}. \quad (3.26)$$

Using $T = \beta\tau_0$ and requiring $\sigma_{\Delta\phi}(T) > 1$ to create contrast beyond the SNR-limited phase error, the axial velocity variation able to produce contrast in a tissue of index $n=1.35$ is:

$$\sigma_{vz} > \frac{\lambda_0}{4\pi n T} = \frac{1.23 \text{ mm/s}}{\beta}. \quad (3.27)$$

While a large variation is required for phase measurements between sequential A-scans such that $\beta=1$, for the case of $\beta=250$ the required variation drops down to $\sigma_{vz} > 5 \mu\text{m/s}$.

3.3.4 Transverse Flow Effects

B. Park et al. [14] theoretically calculated and experimentally measured the error of phase change measurements of uncorrelated scatterers when the two phase measurements were taken at different transverse locations. The intention of this work was to determine the limitations of Doppler flow imaging while scanning transversely across a sample. Using a Gaussian beam with a $1/e^2$ beam width = d at the focus, the standard deviation of the phase changes was determined for a transverse scan of the beam Δx between A-scans. Defining the fraction of the beam width as $\Delta x/d$, the variance of the phase error due to the transverse motion was calculated to be:

$$\sigma^2_{\Delta\phi} = \frac{4\pi}{3} \left(1 - \exp\left(-2\left(\frac{\Delta x}{d}\right)^2\right) \right). \quad (3.28)$$

The functional form of this phase error calculation was verified through experimental measurements. For very small transverse motions, the phase error is dominated by the SNR-limited phase error (described by the horizontal dotted line on Figure 3.10) as

expected. For transverse motions of approximately the full beam width d , the experimental phase error was lower than theoretically predicted. This discrepancy is caused by the limitations imposed on the maximum phase change measured in the SDOCT system of $\pm\pi$. For a completely random distribution of phase changes, the expected phase error is $\sigma_{\Delta\phi} = 1.815$ radians, which gives a phase variance of $\sigma^2_{\Delta\phi} = 3.29$ radians². This maximum phase error is consistent with the experimental data of the paper.

The theory of the phase error during transverse scanning only assumes a relative transverse motion between the sample illumination light and the sample. If the scanning beam is held stationary, any transverse flow of uncorrelated scatterers would provide the same relative transverse motion. This allows motion contrast to be observed in transverse flow regions and no contrast to be observed in the other regions of the static sample.

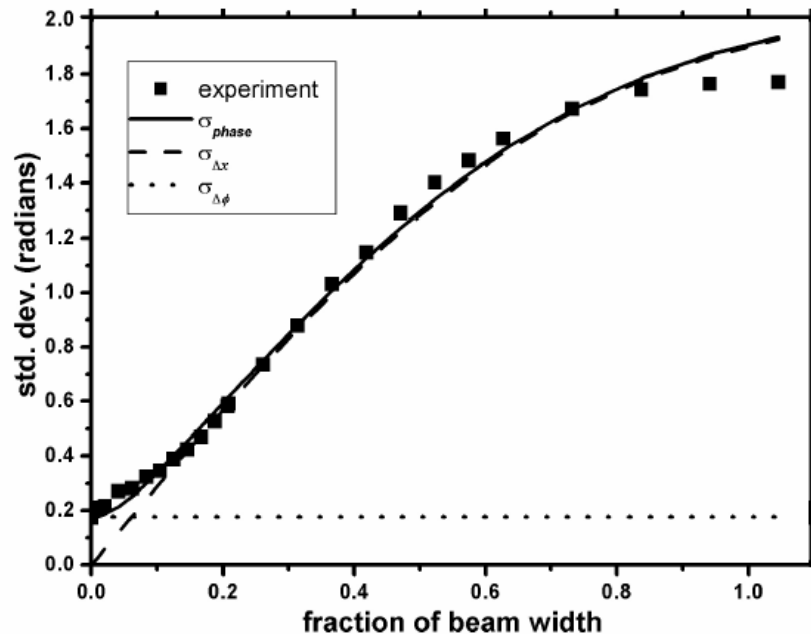


Figure 3.10: Experimentally measured phase change errors as a function of the transverse displacement between Λ -scans. Theoretical phase error estimates are also plotted. Data reproduced from [14].

Using the previously determined phase error form, the phase variance contrast $\sigma^2_{\Delta\phi} = 1$ occurs for the case of $\Delta x / d = 0.37$. Using the same flow terminology as described earlier,

the transverse displacement caused by the flow within a time T for a velocity v oriented at an angle θ to the horizontal is:

$$\Delta x(T) = v_x T = v T \cos \theta. \quad (3.29)$$

For the phase variance contrast $\sigma^2_{\Delta\phi} > 1$ case using $d = d_0 \times 10^{-6}$ m and $T = \beta\tau_0 = \beta \times 40\mu\text{s}$, the conditions for contrast are:

$$\frac{\Delta x(T)}{d} = \frac{v_x T}{d} > 0.37 \quad (3.30)$$

$$v_x > 9.25 \frac{d_0}{\beta} \text{ mm/s}. \quad (3.31)$$

This form of variance contrast is the only one which depends on the diameter of the focused light on the sample. For retinal imaging cases where $d=20 \mu\text{m}$, sequential A-scans such that $\beta=1$ requires a substantial transverse velocity $> 185 \text{ mm/s}$ to be visualized due to this form of contrast. For the case of $\beta=250$, the required velocity component reduces to $v_x > 0.74 \text{ mm/s}$.

Comparing the phase variance contrasts due to flow can determine the dominant process for various flow velocities and angles. Each of the lines plot the minimum velocity required for a given flow angle to achieve phase variance contrast from the motion. For the case of retinal imaging, let the focus spot diameter $d=20 \mu\text{m}$. The blue line is the minimum velocity to observe transverse flow phase variance effects. For graphical representation, it is assumed that the variance of the velocity distribution is a percentage of the mean velocity. The minimum velocity required to view phase variance contrast is plotted in the cases where the velocity variance is 1% (red line) and 10% (green line) of the total mean velocity. The velocity regimes were examined in Figure 3.11 for different time separations T of the phase change, in the cases where $\beta=1$ ($T=40 \mu\text{s}$), $\beta=25$ ($T=1 \text{ ms}$) and $\beta=250$ ($T=10 \text{ ms}$).

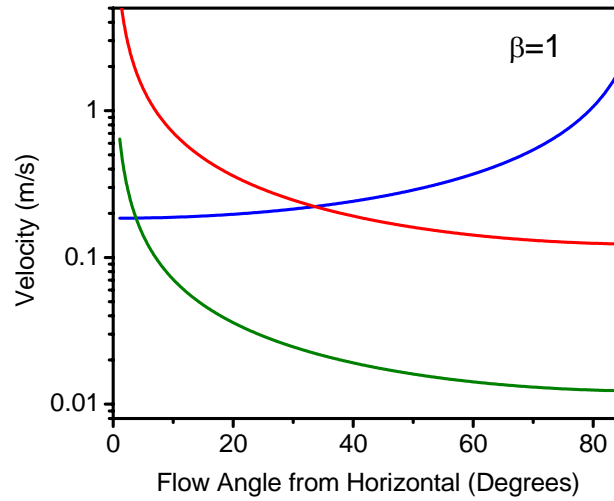


Figure 3.11 a): Minimum flow velocity required to demonstrate phase variance contrast in three different scenarios of transverse flow and axial flow variance. The time between phase measurements is $40 \mu\text{s}$ for this estimate.

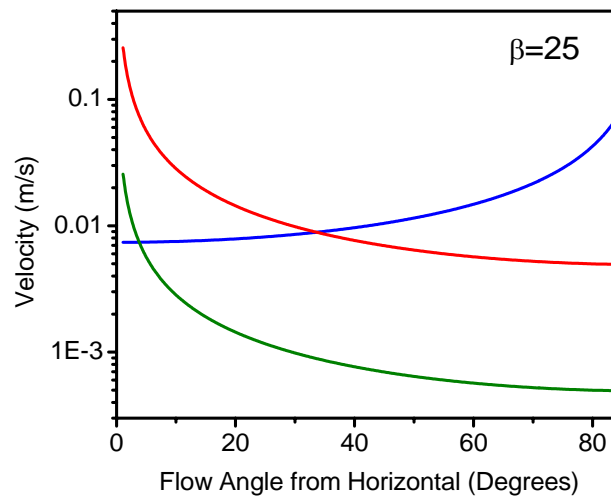


Figure 3.11 b): Minimum flow velocity required to demonstrate phase variance contrast in three different scenarios of transverse flow and axial flow variance. The time between phase measurements is 1 ms for this estimate.

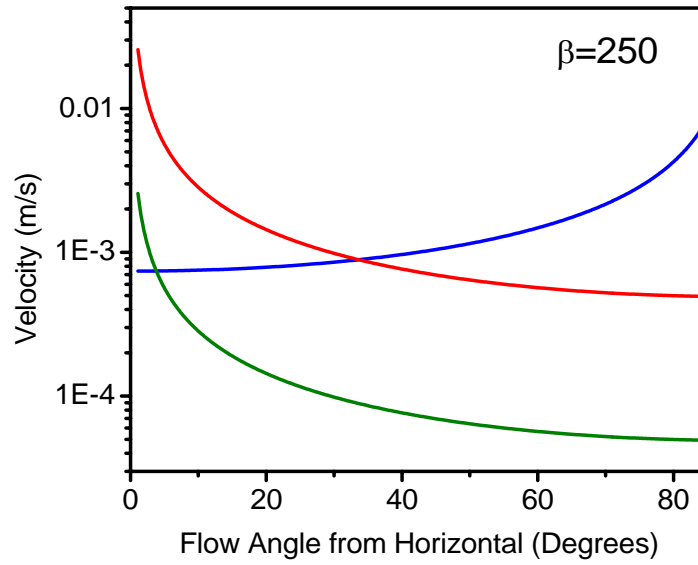


Figure 3.11 c): Minimum flow velocity required to demonstrate phase variance contrast in three different scenarios of transverse flow and axial flow variance. The time between phase measurements is 10 ms for this estimate.

With the fact that most of the retinal vessels lie nearly horizontal, perpendicular to the imaging direction, the phase effects due to transverse flow become the most dominant. For cases in which the velocity distributions have a variance $> 10\%$ of the mean velocity, the axial flow variations become just as important, assuming that $\theta \neq 0^\circ$.

3.3.5 Axial Component of Brownian Motion

The random motion of diffusion spheres, referred to as Brownian motion, is caused by the thermal fluctuations of the mobile scatterers. While the net motion along any direction is zero, the variance of the motion is a measurable quantity which increases with time between position measurements T . Assuming an isotropic scenario where the scatterers can move freely in all directions, the variance of motion along the axial direction $\sigma_{\Delta z}^2(T) = \langle (\Delta z)^2 \rangle$ is one third of the total diffusive motion variance $\langle (\Delta r)^2 \rangle$. The transverse motion creates an effective axial motion as described by equation (3.28), with a variance defined as

$\sigma_{\Delta z, \text{eff}}^2(T)$. The axial motion variance and the effective axial motion variance for a focused illumination beam diameter d are described by the diffusion constant D of the form [15]:

$$\sigma_{\Delta z}^2(T) = \langle (\Delta z)^2 \rangle = \frac{1}{3} \langle (\Delta r)^2 \rangle = \frac{DT}{3} = \frac{E_B}{3\pi\eta r} T$$

$$\sigma_{\Delta z, \text{eff}}^2(T) \cong \frac{1}{3\pi} \left(\frac{\lambda}{d} \right)^2 \sigma_{\Delta z}^2(T) \quad (3.32)$$

For most OCT imaging systems, the beam diameter is large enough that the effective axial motion caused by the transverse Brownian motion is negligible. In the definition of the diffusion constant, E_B is the thermal energy term which is calculated using the Boltzmann constant times the temperature $E_B = k_B T_{TEMP}$. The term η describes the viscosity of the media in which the scatterers are moving. The last term r is the radius of the spheres undergoing the thermal motion. For the case of room temperature water, $E_B = k_B T_{TEMP} = 4.04 \times 10^{-21}$ J and $\eta = 1.00 \times 10^{-3}$ Pa-sec. Defining the radius $r = r_0 \times 10^{-6}$ m and the time $T = \beta \tau_0 = \beta \times 40$ μ s, The expected motion is:

$$\sigma_{\Delta z}(T) = \sqrt{\frac{E_B}{3\pi\eta r} T} = 4.1 \sqrt{\frac{\beta}{r_0}} \text{ nm.} \quad (3.33)$$

For the same phase contrast requirement used earlier $\sigma_{\Delta\phi}(T) = (4\pi m / \lambda_0) \sigma_{\Delta z}(T) > 1$ radian, the parameters required to visualize Brownian motion are determined:

$$\frac{\beta}{r_0} > 146. \quad (3.34)$$

In this case, spheres of radius 1 μ m require phase changes with time separations of > 5.8 ms to see substantial motion contrast. This approximate parameter determination assumes free scatterers in room-temperature water. Different media and non-isotropic diffusion will require different imaging times to adequately visualize contrast.

3.3.6 Ensemble Phase Effects

All of the OCT analysis so far has assumed interference from a single reflector for a given depth within the sample. In reality, due to the finite size of the imaging voxel (the three dimensional spatial extent which defines the volumetric OCT resolution) there can exist multiple reflectors inside of one of them. The volume of a voxel can be approximated as $V = l_c d^2$, where l_c is the coherence length of the imaging system and d is the $1/e^2$ diameter of the focused light at the given depth. With the large d associated with retinal imaging, there is an increased possibility of multiple scatterers residing within one voxel.

Multiple scatterers within a voxel each have their own interference signal $\tilde{R}_j = R_j \exp(i\phi_j)$. The measured OCT interference signal is the summation of all of the individual scatterers within the voxel of interest:

$$\tilde{S} = S \exp(i\phi_s) = \sum_j \tilde{R}_j = \sum_j R_j \exp(i\phi_j). \quad (3.35)$$

Correlated scatterers are static reflections with fixed distances between all of the scatterers. For the case of correlated scatterers within the voxel, the resulting measured interferometric signal appears the same as if there was a single reflector. Uncorrelated scatterers are independent of each other in terms of relative distance and motion and reflection intensity. The phase measured for a voxel containing uncorrelated scatterers varies dynamically with the properties of the individual particles.

Consider the case of two identical scatterers located within a given voxel with a fixed distance between them. Let the maximum reflection for each of the scatterers be defined equally as $R_{1,MAX} = R_{2,MAX} = R_0$.

Let the reflections for each of the scatterers be defined as a time-varying function $R_j(t) = R_0 g_j(t)$, where $g_j(t)$ is a random distribution from zero to one which is independent of j . This function describes the percentage of reflected light directed towards the interferometer arm for collection. If we define the special case of the scatterer

separation distance such that the phase difference is given by π , the measured interferometric signal is of the form:

$$\begin{aligned}\tilde{S} &= S \exp(i\phi_s) = \sum_j \tilde{R}_j = R_1(t) \exp(i\phi_1) + R_2(t) \exp(i\phi_2) \\ &= R_0(g_1(t) - g_2(t)) \exp(i\phi_1).\end{aligned}\quad (3.36)$$

With the requirement of $S > 0$, the calculated phase of the interferometric signal ϕ_s is ϕ_1 for the case of $g_1(t) - g_2(t) > 0$ and $-\pi + \phi_1$ for the case of $g_1(t) - g_2(t) < 0$.

With $g_1(t)$ and $g_2(t)$ describing independent random distributions of equal magnitude, there exists an equal probability of measuring a phase of ϕ_1 as $-\pi + \phi_1$. Therefore half of the measured phase changes = 0 and the other half would be split evenly between $-\pi$ and π . The resulting calculation for the variance of the phase change is given by:

$$\begin{aligned}\sigma_{\Delta\phi}^2(z, T) &= \langle \Delta\phi(z, T)^2 \rangle - \langle \Delta\phi(z, T) \rangle^2 \\ \langle \Delta\phi \rangle &= \frac{1}{2}(0) + \frac{1}{4}(\pi) + \frac{1}{4}(-\pi) = 0 \\ \langle \Delta\phi^2 \rangle &= \frac{1}{2}(0) + \frac{1}{4}(\pi^2) + \frac{1}{4}(\pi^2) = \frac{\pi^2}{2} \\ \sigma_{\Delta\phi}^2 &= \frac{\pi^2}{2} \neq 0.\end{aligned}\quad (3.37)$$

It is important to note that the mean phase change measured, which is associated with the Doppler flow measurement, is zero. On the other hand, the phase change variance calculated for this case is not zero.

In reality, the function $g_j(t)$ would not be completely random for short time changes but could be completely random for larger time separations. Also the probability is that these scatterers would be undergoing motion as well which would need to be considered. Regardless, for more scatterers, phase differences not equal to π , and non-stationary

scatterers the variance calculation becomes much more complicated (but will not be zero in general).

3.4 Phase Contrast Method: MB-Scan

In each of the forms of phase variance presented, the magnitude of the variance increases with the time separation between phase measurements. To maximize the phase contrast capabilities for measuring the motion variance, phase changes should be measured for time separations much larger than the readout time τ_0 of the spectrometer. The simplest way to acquire this phase information is to wait at a given transverse location, taking A-scans until enough phase information has been acquired before moving to the next location. By repeating this process over multiple transverse positions, a two-dimensional phase contrast image can be created.

The scan terminology used in optical coherence tomography was developed for ultrasound applications. Each depth scan of the interference fringe information, which corresponds to one measurement of the spectrometer data, is called an A-scan. The process of waiting at one transverse location, collecting multiple A-scans over time is referred to as an M-scan. Acquiring multiple A-scans over different transverse locations creates a B-scan, a two dimensional cross-sectional reflectivity image of the sample. For the work presented, the process of using multiple M-scans over different transverse locations to create a two-dimensional phase contrast image will be referred to as an MB-scan.

3.4.1 Varying MB-Scan Imaging Parameters

To determine the limitations of producing a contrast image, a test case was created capable of producing phase variance motion. An Intralipid solution was used to fill the molded wells created from agarose, a gelatin-like material. The Intralipid solution was diluted to approximately match the OCT intensity signal from the agarose, reducing the contrast between the regions observed within the intensity image. For 2% agarose wells, an Intralipid solution of approximately 0.1% was used to match the intensity image. Zooming

in on a single B-scan of the Intralipid-filled agarose wells, it is very difficult to identify the material occupying each region of the image.

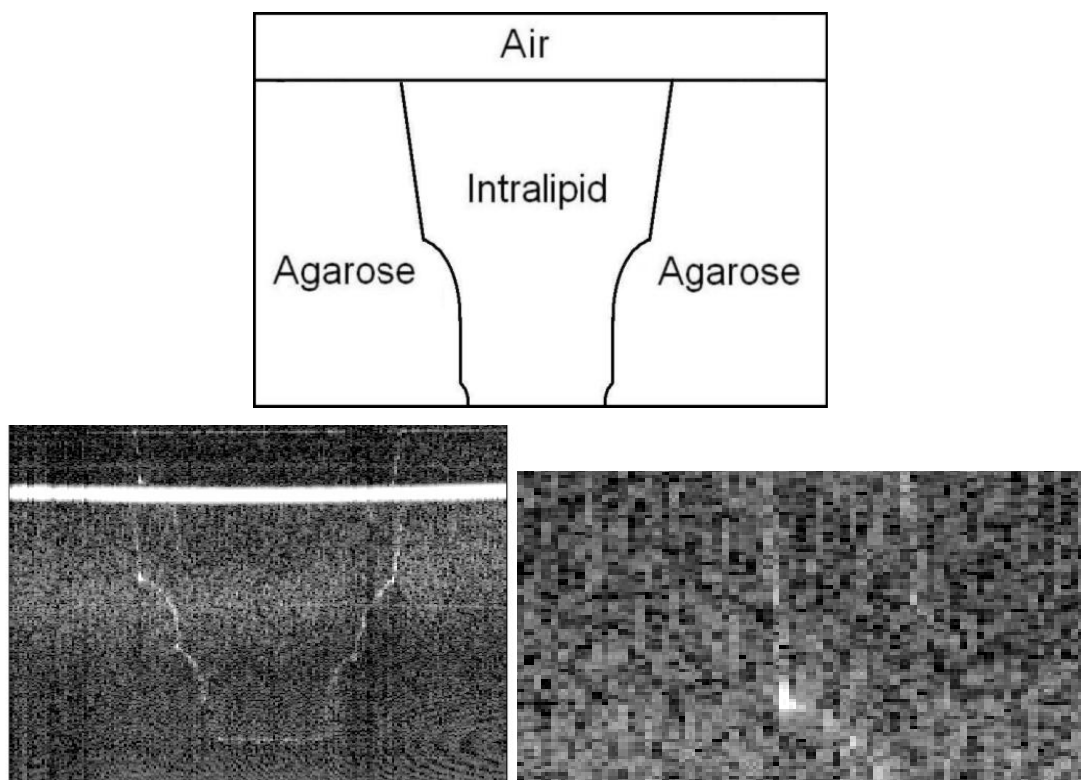


Figure 3.12: 2% Agarose well filled with intensity-matched 0.1% Intralipid solution. The schematic of the sample (top) corresponds with the non-averaged OCT intensity image (left). The zoomed-in portion of the intensity image (right) demonstrates the lack of intensity contrast within this image.

The static agarose is expected to produce no motion contrast while the Intralipid solution is expected to demonstrate Brownian motion. Some of the effects of the motion can be observed through the averaged OCT intensity image, created from 200 A-scans at each transverse location. During the imaging time, the Intralipid scatterers have moved enough to homogenize a region of the image which looked granular before averaging occurred. Textural differentiation of regions is not a new concept in OCT [16], but it usually requires large regions of the image to be effective. Phase variance does not have these spatial requirements to create contrast in images.

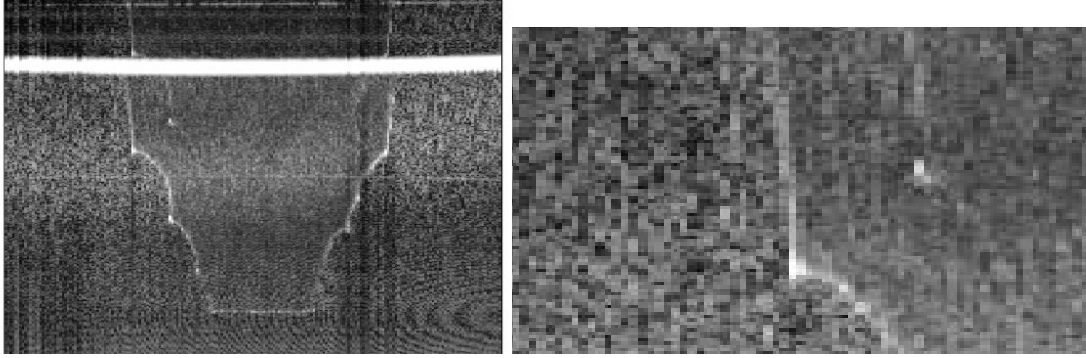


Figure 3.13: 2% Agarose well filled with intensity-matched 0.1% Intralipid solution. The averaged OCT intensity image (left) and the zoomed-in portion of the image (right) can observe textural changes between the two mobility regions.

The phase variance for phase changes separated by time $T = \beta\tau_0$ for a depth z for the agarose/Intralipid sample is of the form:

$$\sigma_{\Delta\phi}^2(z, T) = \sigma_{\Delta\phi, \text{scatterer}}^2(z, T) + \sigma_{\Delta\phi, \text{bulk}}^2(T) + \sigma_{\Delta\phi, \text{SNR}}^2(z). \quad (3.38)$$

From the previous derivations, the motion variance of the scatterers $\sigma_{\Delta\phi, \text{scatterer}}^2(z, T)$ is expected to increase with larger time separations while the SNR-limited phase noise $\sigma_{\Delta\phi, \text{SNR}}^2(z)$ is expected to remain constant over time. One assumption of these measurements is that for most short-time separations, the bulk motion will be small enough to have $\sigma_{\Delta\phi, \text{bulk}}^2(T)$ be considered negligible. This assumption can be tested through the phase variance measurement of the air/water interface of the OCT image, which is expected to have very low values of motion and SNR-limited phase error. Any significant uncorrected bulk motion during the analyzed A-scans will appear in the phase variance measured for that interface.

Using the SDOCT system with the sample arm of the interferometer set up for microscopy with an approximate transverse resolution of $d = 5 \mu\text{m}$, an MB-scan was acquired for 200 transverse locations extending over 1.6 mm, with each location containing 200 sequential A-scans. The entire data set was acquired in 1.6 s total time. For all of the phase data over time acquired for the image, the phase variance was calculated for each image pixel by using all of the phase changes for A-scans separated in time by $T = \beta\tau_0$. By increasing the time between phase measurements, the total number of phase changes that can be acquired

from 200 A-scans for one pixel is reduced as well. For 200 A-scans composing each M-scan, the phase variance image was calculated for time separations ranging from $T = \tau_0 = 40 \mu\text{s}$ to $T = 40\tau_0 = 1.6 \text{ ms}$. All of the presented images are dimensionally scaled and cropped to highlight the region of interest. The image scale for the variance images is a phase variance range of 0 to 2 radians².

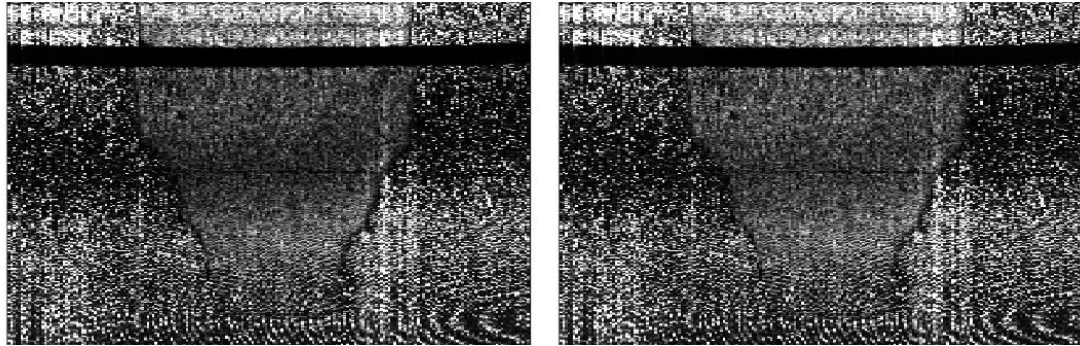


Figure 3.14 a): Phase variance images for phase change time separations $T = 40 \mu\text{s}$ (left) and $T = 80 \mu\text{s}$ (right).

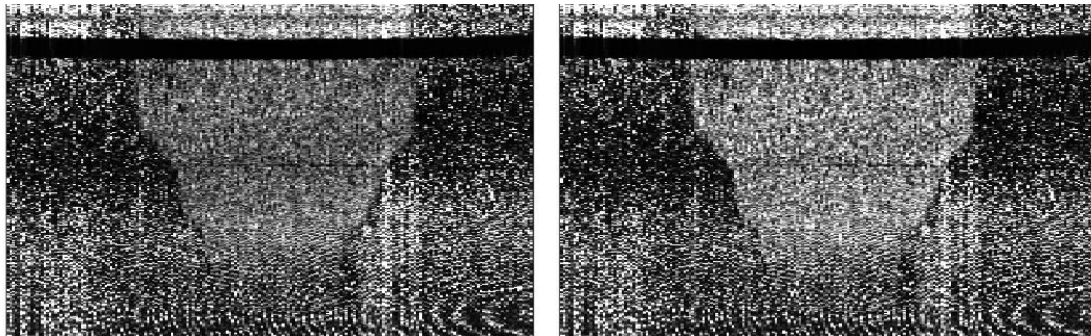


Figure 3.14 b): Phase variance images for phase change time separations $T = 200 \mu\text{s}$ (left) and $T = 400 \mu\text{s}$ (right).

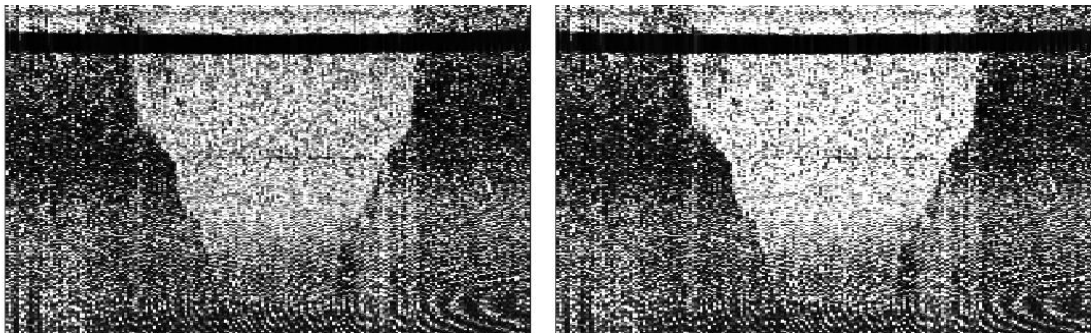


Figure 3.14 c): Phase variance images for phase change time separations $T = 800 \mu\text{s}$ (left) and $T = 1.6 \text{ ms}$ (right).

While the phase variance increased with time as expected, phase contrast can still be observed in all of the cases including the quickest $T = 40 \mu\text{s}$ case. This visualization is courtesy of the significant statistics used for creating the phase variance calculations. Even in the $T = 40 \mu\text{s}$ case, phase changes measured from successive A-scans used all 200 A-scans to create the phase variance (a total M-scan time of 8 ms). By reducing the total amount of statistics used to create the phase variance image, the contrast between the different regions is reduced.

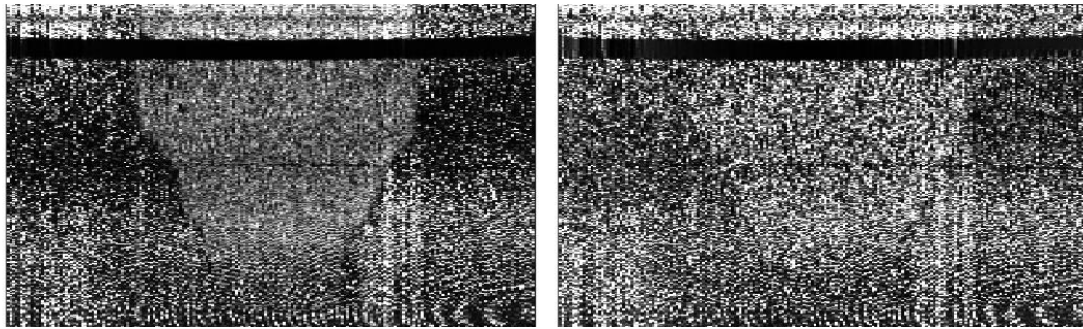


Figure 3.15: Comparing the effect of statistics on the phase variance image for time separations of $T=5\tau_0=200 \mu\text{s}$. The total number of A-scans used for statistics is 200 (left) and 30 (right). The total time to acquire the data required to create each of these images is 1.6 s (left) and 0.24 s (right).

Reducing statistics used for contrast imaging is important to optimize the buffered acquisition of the SDOCT system. The presented MB-scan contains 40,000 total A-scans, with 200 A-scans at each of 200 transverse locations. With a maximum buffer size of approximately 130,000 A-scans, the MB-scan in the current form is not a feasible option for 3D phase contrast imaging. To optimize the acquisition size of the data required to construct a 2D phase contrast image, the time between phase measurements must be reduced along with the total number of statistics. This will help determine the ideal time separations required to visualize the Brownian motion in this sample.

The major factor limiting contrast in the above images is the SNR phase error, which is independent of the time separation used for the phase variance calculations. With access to all of the phase information measured during the MB-scan, the phase variance for different time separations can be calculated for the same M-scan. Ignoring any effect of the bulk

motion on the phase variance calculation, the variances calculated for two different time separations T_1 and T_2 are given by:

$$\sigma_{\Delta\phi}^2(z, T_1) = \sigma_{\Delta\phi, \text{scatterer}}^2(z, T_1) + \sigma_{\Delta\phi, \text{SNR}}^2(z) \quad (3.39)$$

$$\sigma_{\Delta\phi}^2(z, T_2) = \sigma_{\Delta\phi, \text{scatterer}}^2(z, T_2) + \sigma_{\Delta\phi, \text{SNR}}^2(z). \quad (3.40)$$

By choosing the parameters $T_1 = \tau_0 = 40 \mu\text{s}$ and $T_2 = \beta\tau_0 = \beta(40 \mu\text{s})$ where $\beta \gg 1$, it is assumed that $\sigma_{\Delta\phi, \text{scatterer}}^2(z, T_2) \gg \sigma_{\Delta\phi, \text{scatterer}}^2(z, T_1)$. The basic phase contrast metric used for the MB-scan is chosen to be $\sigma_{\Delta\phi}^2(z, T_2) - \sigma_{\Delta\phi}^2(z, T_1)$ such that:

$$\sigma_{\Delta\phi}^2(z, T_2) - \sigma_{\Delta\phi}^2(z, T_1) \cong \sigma_{\Delta\phi, \text{scatterer}}^2(z, T_2). \quad (3.41)$$

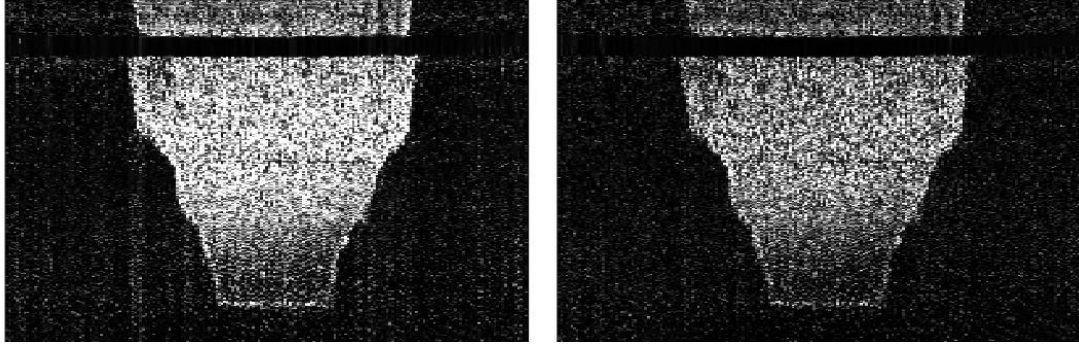


Figure 3.16 a): Phase variance contrast images for maximum phase change time separation of $T_2 = 40\tau_0 = 1.6 \text{ ms}$ (left) and $T_2 = 20\tau_0 = 800 \mu\text{s}$, (right). With M-scan acquisition times of $T_{\text{M-Scan}} = 8 \text{ ms}$ and $T_{\text{M-Scan}} = 4.8 \text{ ms}$ respectively, the total time required to acquire these contrast images is 1.6 s (left) and 0.96 s (right).

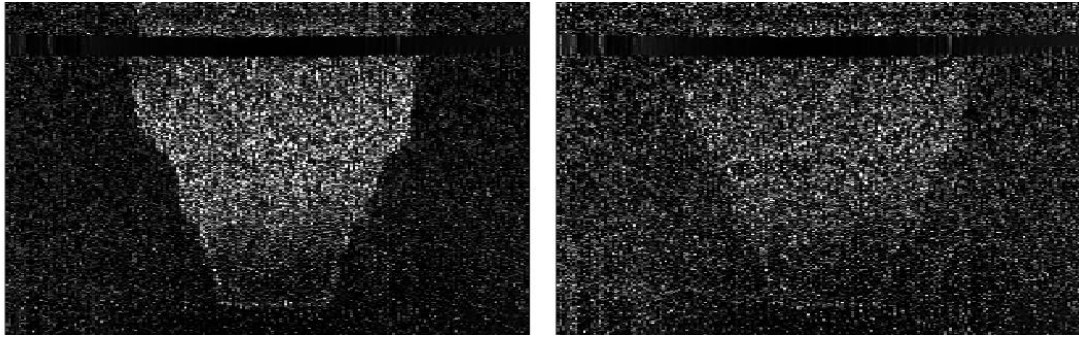


Figure 3.16 b): Phase variance contrast images for maximum phase time separation of $T_2 = 10\tau_0 = 400 \mu\text{s}$ (left) and $T_2 = 5\tau_0 = 200 \mu\text{s}$ (right). With M-scan acquisition times of $T_{\text{M-Scan}} = 2.4 \text{ ms}$ and $T_{\text{M-Scan}} = 1.2 \text{ ms}$ respectively, the total time required to acquire these images is 0.48 s (left) and 0.24 s (right).

To optimize the possible contrast for a given M-scan length and to allow for proper variance statistics, a maximum time separation for phase changes was chosen to be $T_2 = \beta\tau_0 = \beta(40 \mu\text{s})$ for an M-scan length of $T_{M\text{-Scan}} \approx 6T_2 = 6\beta(40 \mu\text{s})$. The result for a range of choices of β was plotted in Figure 3.16.

One of the major assumptions of the phase contrast image is that the SNR phase error remains constant over different time separations. The problem lies in the fact that even a small fluctuation of the phase variance calculations of the noise terms results in a non-negligible phase contrast being imaged. To further improve the phase contrast image, thresholds were applied to try and remove the effect of the noise pixels. Using phase variance contrast with $T_2 = 25\tau_0 = 1 \text{ ms}$ and statistics used from 200 A-scans, thresholds were applied based on $\sigma_{\Delta\phi}^2(z, T_1)$ or the averaged OCT intensity of the image. In the ideal case, $\sigma_{\Delta\phi}^2(z, T_1)$ contains only the SNR phase error and corresponds to the averaged OCT intensity of the image. To eliminate only the extremely noisy pixels, the upper bound threshold of $\sigma_{\Delta\phi}^2(z, T_1) = 3 \text{ radians}^2$ can be used, which is equivalent to setting a lower bound threshold on the averaged OCT intensity at the level of the mean OCT noise of the image, designated as $\langle N^2 \rangle$ previously.

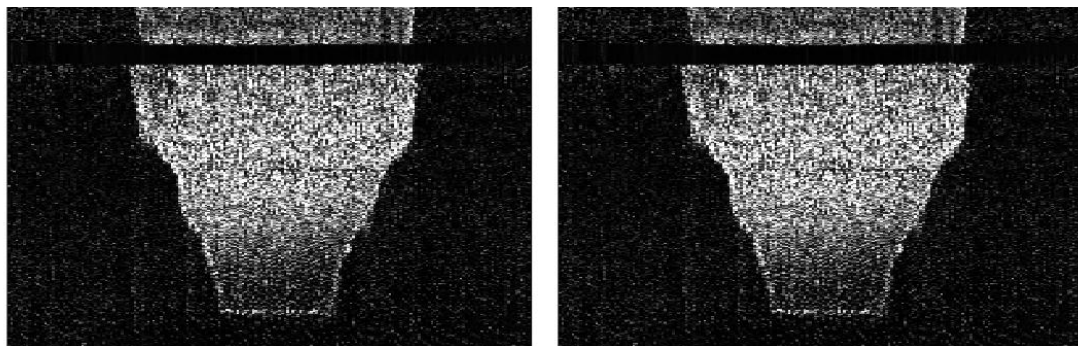


Figure 3.17 a): Phase variance contrast images for phase change time separation of $T_2 = 25\tau_0 = 1 \text{ ms}$, $T_{M\text{-Scan}} = 8 \text{ ms}$. The threshold applied to each image to reduce the noise terms are $\sigma_{\Delta\phi}^2(z, T_1) = 3 \text{ radians}^2$ (left) and OCT intensity = mean OCT noise level (right).

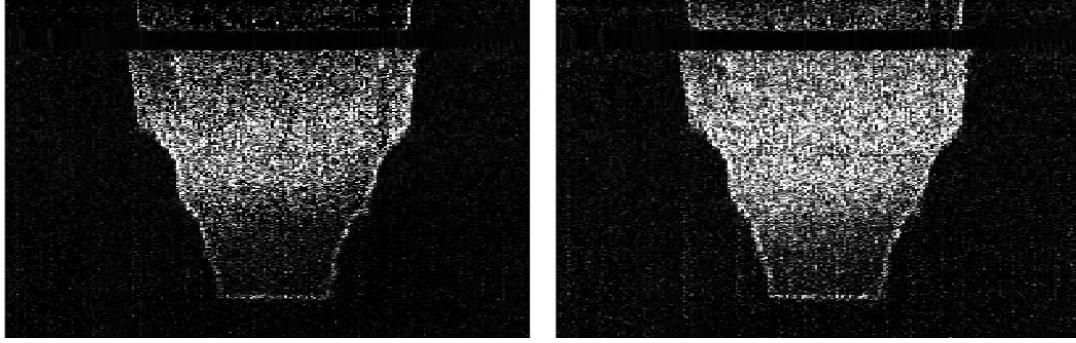


Figure 3.17 b): Phase variance contrast images for phase change time separation of $T_2 = 25\tau_0 = 1$ ms, $T_{M-Scan} = 8$ ms. The thresholds applied to each image to reduce noise terms are $\sigma_{\Delta\phi}^2(z, T_1) = 0.5$ radians² (left) and $\sigma_{\Delta\phi}^2(z, T_1) = 1$ radians² (right).

While thresholding more noise data does improve contrast in parts of the image, the sacrifice of the increased threshold is that interferometric signal near the noise level starts to become blocked by the threshold as well. This effect can be observed from the phase thresholds of $\sigma_{\Delta\phi}^2(z, T_1) = 0.5$ radians² and $\sigma_{\Delta\phi}^2(z, T_1) = 1$ radians², which corresponds to OCT signal 6 dB and 0 dB above the mean noise level respectively. The optimum threshold appears to be $\sigma_{\Delta\phi}^2(z, T_1) = 1$ radians², which corresponds to the point where SNR = 1.

The MB-scan has demonstrated the ability of using phase variance as a source of contrast not available from a single OCT intensity image. Although contrast has been demonstrated, there are serious limitations to the feasibility of using MB-scans to create 3D phase contrast imaging. The ideal phase contrast data set would be acquired within one memory buffer, limiting the effects of sample motion and alignment drift on the data acquisition. The MB-scan presented for the agarose/Intralipid sample contained a total of 40,000 A-scans, which allows for ~ 3 MB-scans of this size to be acquired within one buffer. By dropping the total acquisition time by reducing statistics so that contrast was still visible, the efficiency of the MB-scan can experience some improvement.

For the agarose/Intralipid case, phase variance contrast was still visible for the time separations of $T_2 = 10\tau_0 = 400$ μ s, requiring only 2.4 ms per M-scan of the MB-scan. With these statistics the MB-scan acquires a total of 12,000 A-scans, allowing for ~ 11 MB-scans

to be acquired within one buffer. While a 200×11 transverse pixel area of imaging may not be ideal for most cases, this can be adjusted to 45×45 transverse locations for the same phase contrast capabilities. Reducing the statistics of the MB-scan limits the observable motion with this technique. To acquire 3D phase contrast data, a different acquisition technique is required.

For 3D phase contrast imaging, the ideal acquisition would be able to (i) have large time separations between the phase measurements and (ii) acquire the entire data for a 2D phase contrast image in a minimum amount of time.

3.5 Phase Contrast Method: BM-Scan

To improve the efficiency of the data collection, a different approach is required to the transverse scan pattern during acquisition. The MB-scan presented earlier acquires data by moving to each transverse location and waiting until enough phase information has been acquired before moving onto the next position. A large portion of the acquisition with this method is wasted simply waiting for the motion of the scatterers to surpass the accuracy limitations of the measurement. Instead of waiting at one location acquiring information, acquisition efficiency can be improved by taking a single phase measurement at each of the transverse locations before returning to the original location to repeat the phase measurements.

Rather than acquiring successive A-scans while waiting at one transverse location, A-scans can be acquired while scanning across the sample. When the scan beam returns to the original location to acquire the next phase measurement, a large time separation has occurred which is ideal for phase variance contrast measurements. By repeating this measurement for enough statistics to calculate the phase variance, the 2D phase contrast image can be determined. The process of measuring multiple B-scans over time for the same transverse scan region will be referred to as a BM-scan.

The BM-scan is a very efficient method of acquiring 2D phase contrast image data. The minimum time between phase measurements is determined by the acquisition speed of the spectrometer τ_0 , the number of transverse pixels used in the B-scan and the speed capabilities of the transverse scanner in the system. To ensure a constant time separation of phase measurements across the entire image, only phases measured during one scan direction along the primary transverse scan axis will be used in phase variance calculations. With this constraint and the continuous acquisition of spectrometer data, all the data acquired during the fly-back of the transverse scan wastes space in the memory buffer.

Using the same terminology as used previously in Chapter 3.2, the total number of spectrometer acquisitions which are acquired in one cycle of the transverse scan is N_X . The percentage of spectrometer measurements which occur during the primary transverse scan which creates the B-scan was X_{DUTY} . The number of A-scans which compose each B-scan of the BM-scan is given by:

$$N_{XSCAN} = X_{DUTY} N_X . \quad (3.42)$$

This leads to a time separation between the phase measurements and successive B-scans within the BM-scan of $T = N_X \tau_0$.

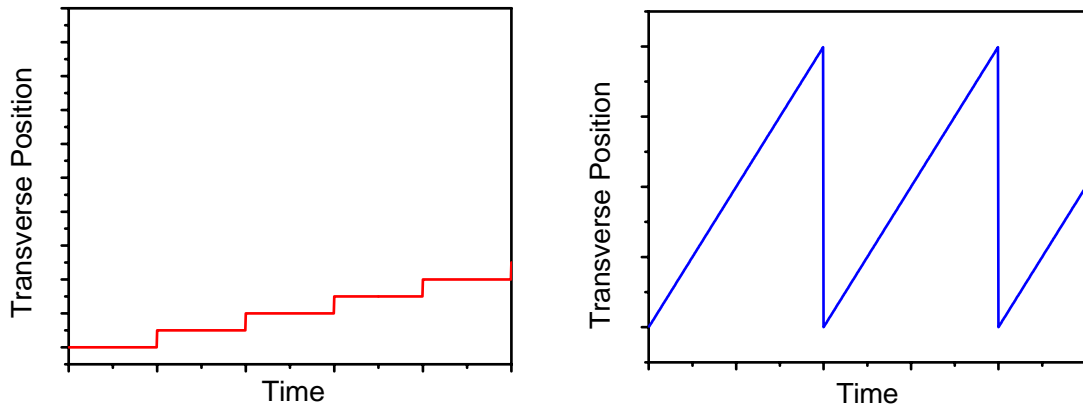


Figure 3.18: Schematic of transverse scan patterns for MB-scan (left) and BM-scan (right).

Phase contrast for an MB-scan is calculated using the difference between the phase variance calculated for successive A-scans and the variance for phase changes with much larger time separations. This method achieves motion contrast because the dominant source of phase noise in the successive A-scan phase change is the SNR-limited phase error. To achieve phase contrast for a BM-scan, the phase changes between successive A-scans can no longer be considered a good approximation of the SNR phase error. The transverse scan between successive A-scans in this method induces additional phase errors, as described in Chapter 3.3.4. Numerical estimates of the phase noise based on the averaged OCT intensity are an excellent alternative to allow creation of a phase variance contrast image.

Using an MB-scan, phase error is calculated from phase changes of all depths of the successive A-scan measurements of a stationary paper sample. The variance of the phase changes is compared against the averaged OCT intensity, to compare against the theoretical prediction of equation (3.21). By fitting the phase error data which occurs at intensities approximately 10–25 dB above the noise level of the system to the expected form of the SNR-limited phase noise, the mean OCT noise level $\langle N^2 \rangle$ was determined. The measured OCT intensity I^2 is a combination of the interferometric signal S^2 and the noise signal N^2 such that the averaged OCT intensity is of the form:

$$\langle | \tilde{I} |^2 \rangle = S^2 + \langle N^2 \rangle. \quad (3.43)$$

With the mean OCT noise level determined, the interferometric signal can be extracted from the measured OCT intensity. The measured SNR-limited phase noise is plotted against the interferometer signal, normalized to the mean OCT noise level. Phase error is calculated as a function of normalized OCT interferometer signal data. Noise estimation (red line) is performed by fitting data in the 10 dB to 25 dB range to the expected form of SNR-limited phase error.

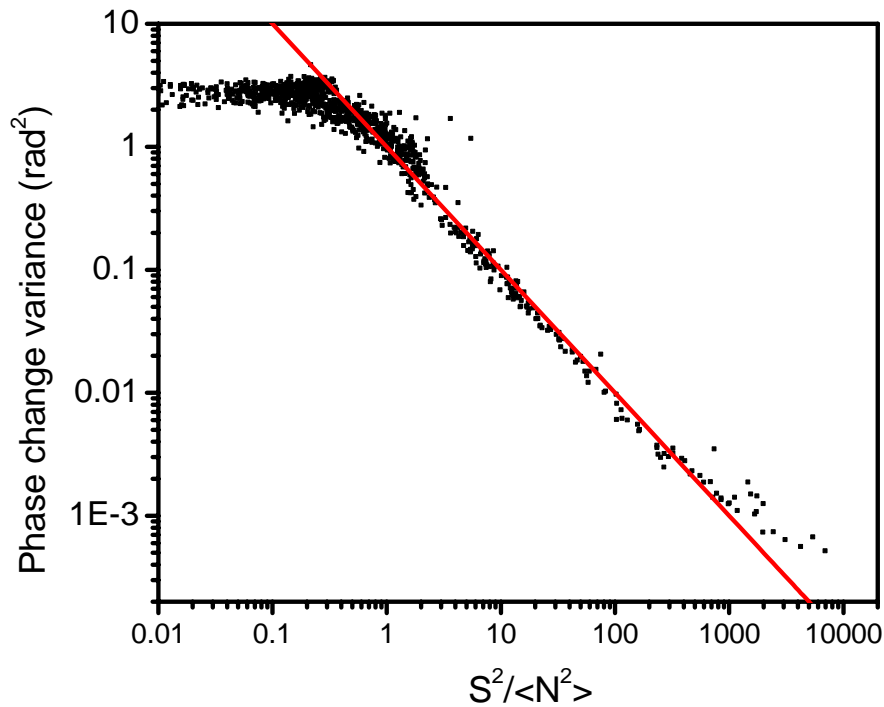


Figure 3.19: SNR-limited phase noise plotted versus averaged OCT intensity signal.

The expected form of the SNR-limited phase noise deviates from the measured values at very low and very high cases of $S^2/\langle N^2 \rangle$. For $S^2/\langle N^2 \rangle \sim 1$, this discrepancy is most likely caused by the statistical variations of the noise, limiting the calculation of the interferometric signal. The measured phase error reaches a maximum level at approximately 3 radians², which is caused by the imposed limitations of maximum phase changes between $-\pi$ and $+\pi$. For a completely random distribution of phase changes between $-\pi$ and $+\pi$, the standard deviation is approximately 1.8 radians. This limits the expected maximum phase variance measured for a purely noise situation to approximately 3.2 radians². For the very high $S^2/\langle N^2 \rangle$ case, the expected phase error is small enough that other sources of error can dominate. In this case, the limiting phase error is due to the bulk motion between the system and the sample during the acquisition of this phase data.

3.5.1 Varying BM-Scan Imaging Parameters

The BM-scan acquired data for the agarose/Intralipid sample used for the MB-scan, utilizing the same imaging parameters in this case. The BM-scan is composed of 200 transverse locations extending over 1.6 mm. All of the images presented are scaled to the appropriate dimensions. In the demonstrated BM-scan, the time between phase measurements, defined by the B-scan time and the fly-back time, is $T = 10$ ms. With 200 transverse pixels acquired at $40 \mu\text{s}$ each, this defines the x-scan duty cycle at $X_{\text{DUTY}}=0.8$.

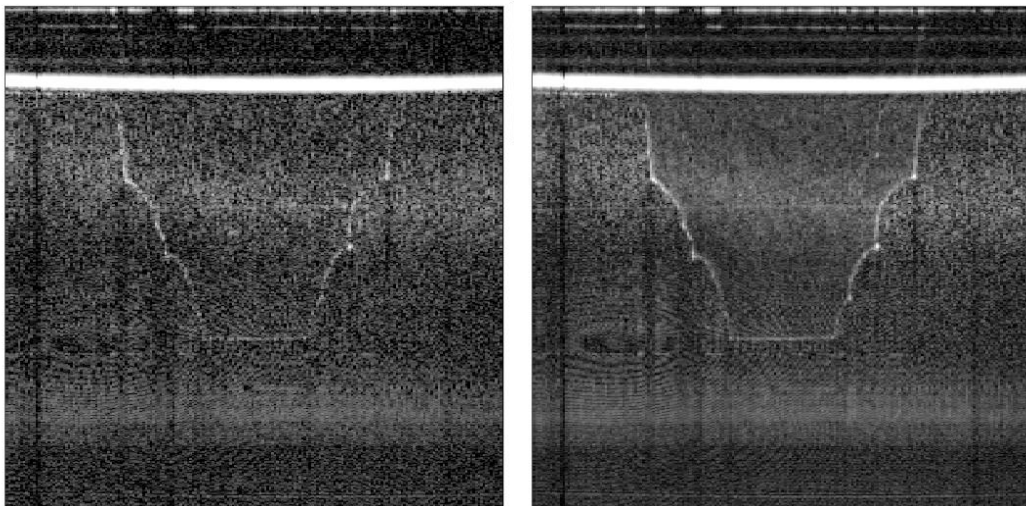


Figure 3.20: OCT intensity images of 2% agarose well filled with an 0.1% Intralipid solution for no averaging (left) and averaging over 5 sequential B-scans (right)

The intensity images created with the BM-scan are comparable to the case of the MB-scan. The B-scan containing no averaging still has limited contrast between the agarose and Intralipid regions, while contrast can be observed in the averaged image.

The phase variance imaging parameters for the BM-scan are slightly different than those of the MB-scan. The time between phase measurements for this BM-scan is $T = 10$ ms, with no flexibility available to alter this value after the data has been acquired. Choosing a different time separation in parameter space requires a different BM-scan acquisition pattern. The time separation for this BM-scan is more than six times larger than the longest

time separation used in the MB-scan presented earlier in Figure 3.17, which is expected to result in larger measured phase variances. The image scale for the phase variance images ranges from 0 to 3 radians². The main difference in the variance images is the implementation of a bulk motion removal algorithm, to reduce the effect relative motion between the sample and the system has on phase measurements.

A weighted mean technique was used to calculate the bulk motion, utilizing phase changes from all depths within a chosen region of the A-scan. Each phase change calculated was weighted by the intensity of the OCT signal for that depth to reduce the effect SNR-limited phase error $\sigma_{\Delta\phi, \text{SNR}}(z)$ has on the calculation of the bulk motion removal. For phase measurements separated by time T , the bulk axial motion is calculated as:

$$\Delta\phi_{\text{bulk}}(T) = \frac{\sum_z [I(z)\Delta\phi(z, T)]}{\sum_z [I(z)]}. \quad (3.44)$$

The signal amplitude $I(z)$ is the linear form of the OCT intensity $I^2(z)$, which is imaged in the form of $20 \log(I(z))$. The z summation for this equation is over a chosen depth region of the A-scan which contains the sample reflections. The phase changes $\Delta\phi(z, T)$ used were conditioned to limit phase changes between $-\pi$ and $+\pi$ to avoid phase wrapping issues. With this method of bulk phase removal from the entire depth sample reflections, the accuracy of this method becomes limited to approximately the SNR-limited phase error of the strongest sample reflection in the entire depth. This places an expected lower limit on identifiable phase changes after compensating for the other effects.

Before implementing the numerical phase noise removal, the phase variance image was plotted using 5 and 16 phase measurements to calculate the variance. With the parameters used in the BM-scan, the total imaging time for each of these images is 50ms and 0.16s respectively. These images demonstrate similar contrast to the largest time separations of the phase variance contrast images of the MB-scan in Figure 3.17.

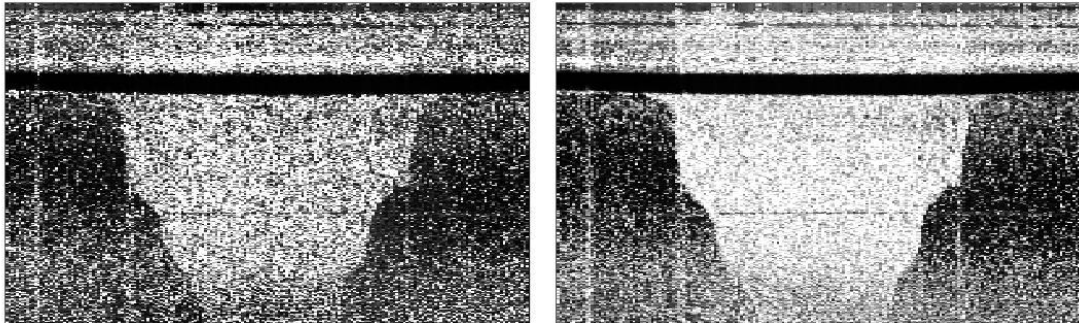


Figure 3.21: BM-scan phase variance images without thresholds or phase error removal. The total number of B-scans used to create the image is 5 (left) and 16 (right), requiring a total acquisition time for the image data of 50 ms (left) and 0.16 s (right).

The phase variance contrast images incorporate the removal of the numerically estimated phase error as well as a threshold on the phase data based on the averaged OCT intensity signal. The threshold used for the phase contrast images was the case where $SNR=1$ (where the measured OCT intensity equaled twice the mean OCT noise level). The two images presented demonstrate again the cases of 5 and 16 total B-scans to create the phase variance.

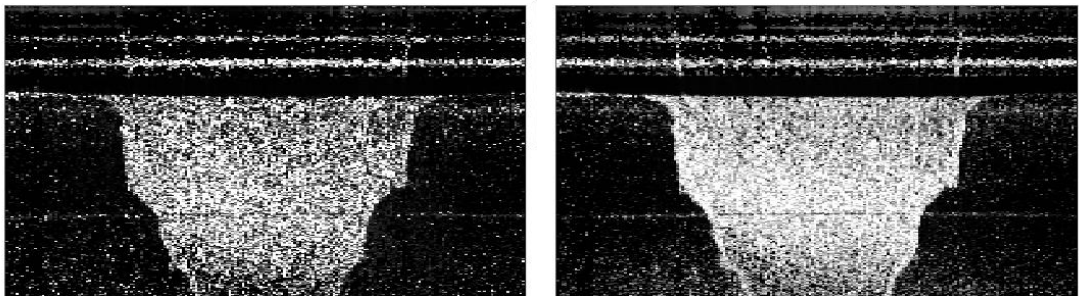


Figure 3.22: BM-scan phase variance contrast images with SNR-limited phase error removed and thresholds applied based on the intensity image. The total number of B-scans used to create the image is 5 (left) and 16 (right), requiring a total acquisition time for the image data of 50 ms (left) and 0.16 s (right).

To optimize the buffer acquisition with multiple BM-scans, the minimum number of statistics possible must be determined. For total of 5 B-scans used in a BM-scan results in a total of 4 phase changes calculated at a given location. Fewer than 5 B-scans would not produce enough statistics to properly calculate the variance of the phase changes.

There are several options available to improve the phase variance image contrast for a given BM-scan of fixed statistics. An overestimate of the phase error that is removed from the image would reduce the effects of noise terms that are not removed completely due to limited statistics in the calculation. A very useful tool for improving contrast is image filtering. Median filters were applied to the phase variance contrast image in the case of 5 B-scans, where the statistics are limited. A median filter of rank ζ for a given direction analyzes a given pixel and ζ pixels on each side of it, calculating the median of the group and replacing the value into the pixel location. This filter is very useful in reducing highly localized noise, like the cases found in the phase contrast images. Due to the oversampling in the axial direction of the image due to the spectrometer and the coherence length, a median filter of rank 2 was applied axially to the contrast image along with a median filter of rank 1 which was applied transversely.

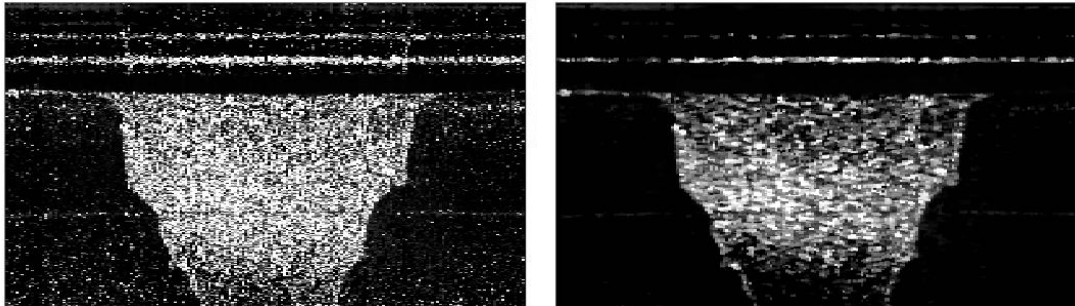


Figure 3.23: BM-scan phase variance contrast image for 5 total B-scans used. The right image applied a median filter of rank 2 axially (5 pixels) and rank 1 (3 pixels) transversely. Total time for both images is 50 ms.

After the filtering was applied to the image, there was a clear reduction of the noise in the image. The horizontal lines visible on the contrast image correspond to spectrometer noise that is very difficult to eliminate in general, of a form which differs between various CCD cameras. While the contrast of the Intralipid solution appears to have suffered slightly due to the filtering, this approach can be very useful to reduce OCT noise effects on phase contrast images.

To demonstrate the importance of bulk motion removal, the phase variance contrast image was re-analyzed with and without bulk motion removal. The images were not cropped like

the previous images to also demonstrate a limitation to bulk motion removal in scenarios where mirror terms appear in the image. In the first image containing no bulk motion removal, the large line corresponding to the air/water interface is expected to have no variance measured if no motion was occurring in the system, which is not the case here.

With the bulk motion removal, many portions of the phase contrast image which are expected to be static reduce in intensity. But there is a broad reflection at the bottom of the image which observes an increase in phase contrast after removal. From a static B-scan image, it is difficult to identify mirror term reflections which can limit the performance of a phase contrast image.

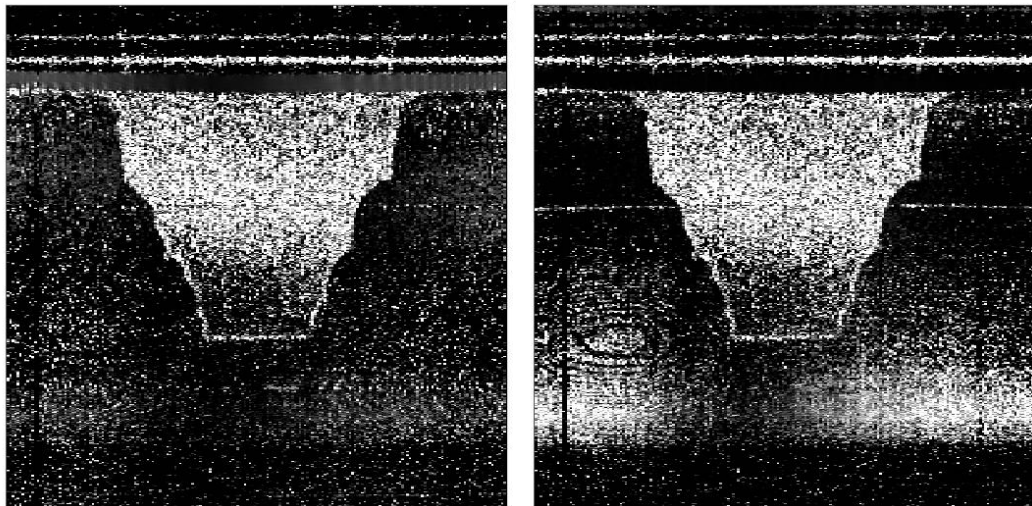


Figure 3.24 a): BM-scan phase variance contrast image for cases of no phase removal (left) and standard bulk phase removal method (right).

One option to deal with mirror terms present within a phase contrast image is to calculate the phase variance contrast for multiple cases and choose the minimum value as the image pixel value. By choosing the minimum value between the bulk removal contrast and the phase contrast without any removal, the result is the expected minimum of the previous two images. To properly remove the effect of the mirror terms, the contrast image should be the minimum between the bulk removal contrast image and the bulk addition contrast image, where the calculated bulk motion is added to the image to reduce only the contrast from the mirror terms. This method does remove the mirror term bulk motion effects while only

slightly affecting the contrast measured from the Intralipid solution by canceling out some scatterer motion in the cases where it was in the opposite direction to the bulk motion experienced.

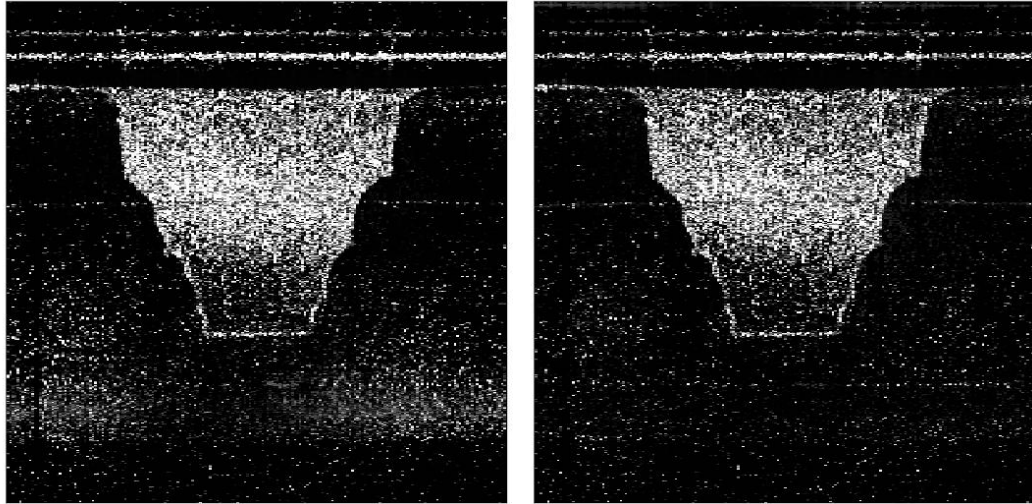


Figure 3.24 b): BM-scan phase variance contrast image calculated from the minimum of the cases of no phase removal versus bulk phase removal (left) and the minimum of the cases of bulk phase removal method and bulk phase addition method (right).

The BM-scan in its current configuration is ideal for 3D phase contrast imaging in one buffered acquisition. With the maximum possible computer memory buffer, a transverse scan area of 200 x 100 pixels is possible using the BM-scan with statistics limited to only 5 B-scans total. There is a lot of imaging potential for this method once all of the limits are understood.

The contrast methods developed in this chapter have demonstrated motion contrast in a sample without any induced flow. To fully understand the capabilities of these techniques to observe motion contrast, the next step is to use a living sample which will produce flow contrast to be evaluated.

3.6 References

1. "Gaussian beam," Wikipedia, http://en.wikipedia.org/wiki/Beam_waist.
2. "Numerical aperture," Wikipedia, http://en.wikipedia.org/wiki/Numerical_aperture.
3. J.W. Goodman, Introduction to Fourier Optics, 1st ed. (McGraw-Hill, 1968).
4. M. Born and E. Wolf, Principles of Optics; Electromagnetic Theory of Propagation, Interference and Diffraction of Light, (Pergamon Press, 1959).
5. W. Drexler, "Ultrahigh-resolution optical coherence tomography," J. Biomed. Opt. 9, 47 (2004).
6. W. Drexler et al., "Enhanced Visualization of Macular Pathology with the use of Ultrahigh-Resolution Optical Coherence Tomography," Arch. Ophthalmol. 121, 695 (2003).
7. SuperLum Diodes Ltd., www.superlumdiodes.com.
8. American National Standards Institute-ANSI, www.ansi.org.
9. S.H. Yun et al., "Motion Artifacts in OCT with Frequency Domain Ranging," Opt. Express 12, 2977 (2004), <http://www.opticsexpress.org/abstract.cfm?id=80320>.
10. S. Yazdanfar et al., "Frequency estimation precision in Doppler optical coherence tomography using the Cramer-Rao lower bound," Opt. Express 13, 410 (2005), <http://www.opticsexpress.org/abstract.cfm?id=82377>.
11. B. Vakoc et al., "Phase-resolved optical frequency domain imaging," Opt. Express 13, 5483 (2005), <http://www.opticsexpress.org/abstract.cfm?id=84914>.
12. B.R. White et al., "In vivo dynamic human retinal blood flow imaging using ultra-high-speed spectral domain optical coherence tomography," Opt. Express 11, 3490 (2003), <http://www.opticsexpress.org/abstract.cfm?id=78206>.
13. R.A. Leitgeb et al., "Real-time measurement of in vitro flow by Fourier-domain color Doppler optical coherence tomography," Opt. Letters 29, 171 (2004).
14. B. Park et al., "Real-time fiber-based multi-functional spectral-domain optical coherence tomography at 1.3 μm ," Opt. Express 13, 3931 (2005), <http://www.opticsexpress.org/abstract.cfm?id=84093>.
15. R.K. Pathria, Statistical Mechanics, 2nd ed. (Butterworth, 2001).
16. K.W. Gossage et al., "Texture analysis of optical coherence tomography images: feasibility for tissue classification," J. Biomed. Opt. 8, 570 (2003).

MOTION CONTRAST IMAGING USING ZEBRAFISH

To observe the earliest point of the transition between dry AMD and wet AMD, the choroidal neovascularization must be visualized before it tries to break through Bruch's membrane. Using the motion contrast methods of optical coherence tomography, the vascular visualization capabilities must be determined in order to apply it as a screening tool for eye care. For the first proof-of-concept experiments, an animal model of vasculature is used. By using a non-retinal vascular model in a microscopy setup, the expected bulk motion effects during imaging will be reduced compared to a retinal imaging system.

4.1 Choosing Zebrafish as the Animal Model

There are several requirements of an optimal animal model for SDOCT imaging, including but not limited to:

- Transparency allows for direct optical access to all of the layers within the animal
- Feature sizes approximately the same size as the resolution of the system
- Thickness of animal is less than the imaging depth of the SDOCT system
- A well established model of vasculature of the animal allows for direct comparison of measured motion contrast to expected

Zebrafish (*Danio rerio*) is an excellent animal model of vasculature. With the addition of the chemical phenylthiourea (PTU) applied to zebrafish embryos at time points earlier than 1 dpf (days post fertilization), the pigment production in the animal is inhibited. Without the production of the highly absorptive pigment, the zebrafish can grow for several days transparently, making it ideal for optical imaging. The ideal age to image the zebrafish is around 3-4 dpf, where the features have grown large enough to be visualized with an OCT

system but the entire animal thickness is small enough to be imaged using SDOCT. Around 5 dpf with the pigment blocker applied, the zebrafish begin to develop pigment, limiting the imaging regions of the sample.



Figure 4.1: Bright field illumination confocal image of 3 dpf zebrafish without the addition of the pigment blocker. Approximate scale bars were added to the image reproduced from [1].

Variant strains of zebrafish have been developed which contain green fluorescent protein (GFP) labeled vasculature. This has provided valuable insight into the vascular formation of the zebrafish during development for the ability to confocally image the vasculature for these zebrafish strains. These images can also be created by injecting a fluorescent dye and imaging the fluorescence confocally. With the availability of facilities allowing for the acquisition of zebrafish embryos and the short required development time for samples, the zebrafish is an ideal animal model for SDOCT motion contrast imaging.

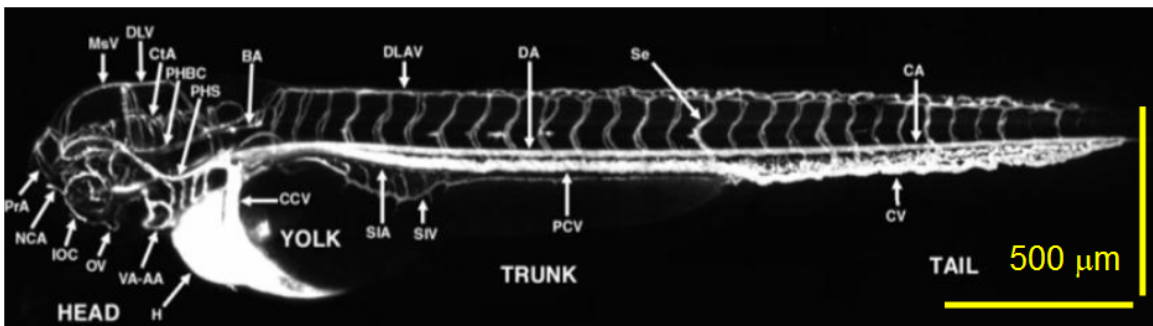


Figure 4.2: Confocal fluorescence image of 3 dpf zebrafish with fluorescent dye injected within its vasculature. Approximate scale was added to image reproduced from [2].

4.2 Creating SDOCT Images

To image the zebrafish in the SDOCT, the system must be set up for microscopy. With an expected axial resolution in tissue of approximately $6\ \mu\text{m}$ due to the light source properties, the transverse resolution was chosen to try and match this resolution. In SDOCT all of the depths are measured at the same time, each with its own transverse resolution. For a transverse resolution of approximately $5\ \mu\text{m}$ at the focus, the resolution decreases at depths away from the focus, increasing to $7\ \mu\text{m}$ over a depth range of $50\ \mu\text{m}$. The polarization controllers (PC) applied to each of the arms of the interferometer are used to adjust the polarization of the light traveling through the fiber coupler to maximize the interference fringe signals measured at the spectrometer.

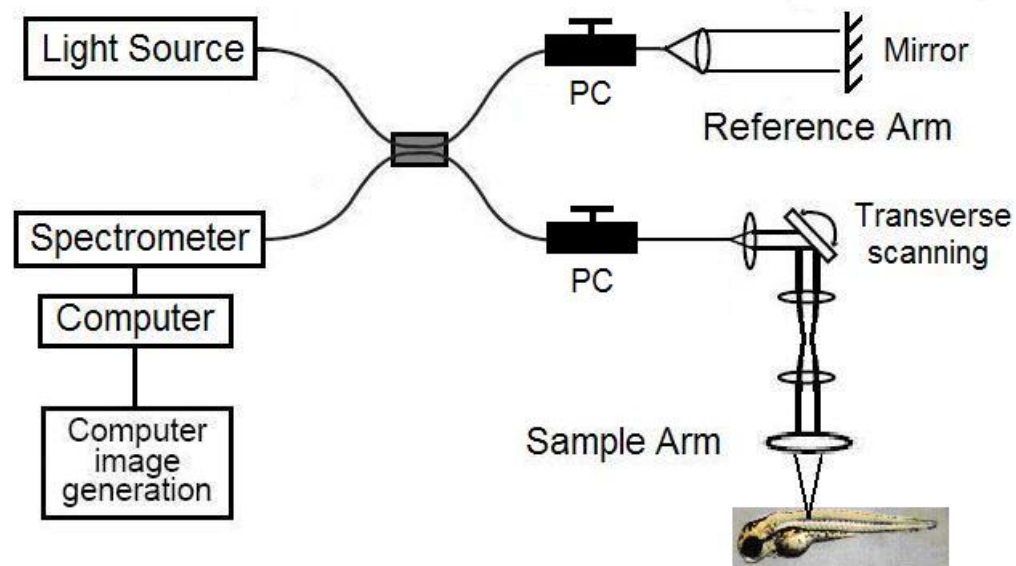


Figure 4.3: Schematic of the experimental fiber optic SDOCT microscopy system. PC: polarization controller.

Creating OCT images from the spectrometer data requires several processing steps before the Fourier transform is performed, with the most important being the linearization of the data to k -space. The spectrometer samples the interferometric signal in k -space, but in general the spacing between neighbouring CCD pixels is not uniform across the entire

measurement. The spectrometer data must be linearized in k-space to allow for a proper Fourier transform to be calculated.

To calculate an A-scan from the spectrometer measurements, it is also important to remove the source spectral component before computing the Fourier transform. Without removing the spectral component from the reference arm, the A-scan calculated as the magnitude of the Fourier transform appears in the form:

$$|FT(P(k))|^2 \propto P_R^2 |\tilde{f}_C(z)|^2 + \sum_j P_R P_{Sj} |\tilde{f}_C(z - z_j)|^2. \quad (4.1)$$

In this case the OCT coherence function $|\tilde{f}_C(z)|^2$, defined in Chapter 2.2 as determined by the shape of the light source spectra, sets a lot of the image properties. In general, for OCT imaging the power from the reference arm dominates over all of the sample reflections such that $P_R \gg P_{Sj}$. For this assumption the DC component of the image is substantial, causing the side lobes of the coherence function for this term to interfere with the rest of the image. As discussed in Chapter 2.8, the removal of the source spectra before the Fourier transform is expected to remove the DC component of the OCT image:

$$|\tilde{I}(z)|^2 = |FT(P(k) - P_R(k))|^2 \propto \sum_j P_R P_{Sj} |\tilde{f}_C(z - z_j)|^2. \quad (4.2)$$

There are several methods to determine the source spectra without the interference signal associated with a spectrometer measurement in SDOCT. By simply blocking the sample arm, the reference arm spectra can be measured directly. While this method is adequate for many methods, when the measured spectrum shape or intensity changes due to fluctuations or image re-alignment, artifacts appear in the B-scan based on the discrepancy between the measured and removed source spectra.

To reduce any of the fluctuation effects of the measured reference spectrum, the background spectra should be measured or calculated from data taken at the same time as

the SDOCT imaging. While mechanically diverting or blocking the sample arm during a buffered acquisition of the spectrometer data is possible, it is not ideal in many cases. There is a very simple method of calculating the background spectra using all of the data acquired during a single B-scan. The assumption is that all of the interference fringes within an image are of comparable intensity with a random distribution of depths such that averaging the fringes will all cancel each other out. For N_X A-scans used to create a B-scan, averaging all of the spectrometer measurements for this B-scan will create the background average spectra to use for A-scan calculation [3]:

$$\bar{P}(k) = \frac{1}{N_X} \sum_j P_j(k). \quad (4.3)$$

In certain imaging cases, the assumption used for determining the background spectra does not hold. One example is when the sample contains specular reflections, which are highly localized reflections which are much stronger than the rest of the sample reflections. Averaging the fringes in this case cannot completely cancel out these large reflections, causing the remaining portion of the fringe to appear across the entire B-scan when the averaged spectra is used in the calculation of each A-scan. A weighted average of the interference spectra makes it possible to minimize the effect of the scans which contain specular reflections.

For spectrometer measurement j which contains a maximum reflectance of $R_{j,Max}$ located at a depth position $z_{j,Max}$, the removal of the averaged spectra results in approximately the maximum interference reflection:

$$(P_j(k) - \bar{P}(k))^2 \propto R_{j,Max} \cos^2(kz_{j,Max}). \quad (4.4)$$

This fact results in the weighted background spectrum calculation of:

$$P_R(k) = \frac{\sum_j w_j P_j(k)}{\sum_j w_j}. \quad (4.5)$$

where the weighting factor w_j is defined as $w_j = 1/(P_j(k) - \bar{P}(k))^2$.

Demonstrating the effect of this weighted averaging, a B-scan taken through a zebrafish head was used. The pigmentation in the eyes of in this case causes specular reflections for a few A-scans within the B-scan. While the averaged background spectra method creates horizontal lines at the depth location of the major specular reflection, the weighted average reduces this effect and improves the image quality.

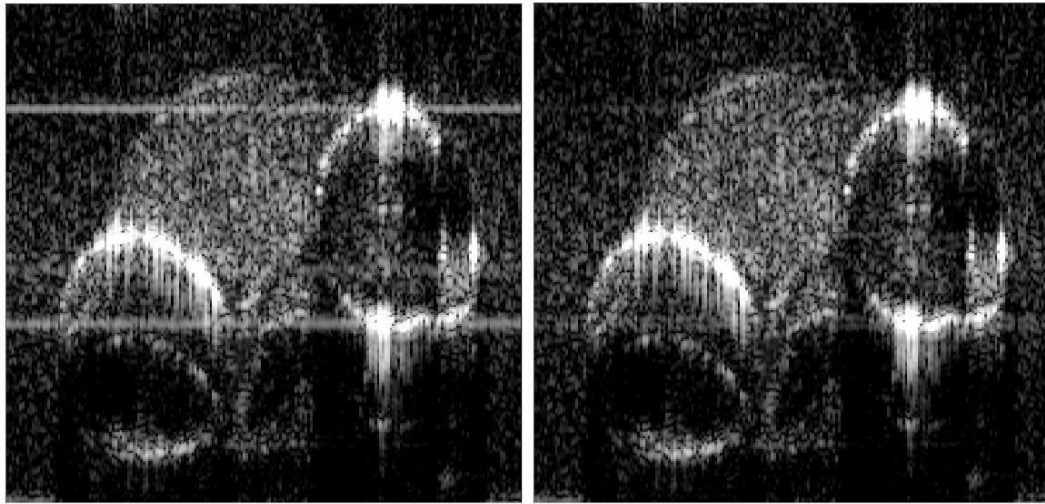


Figure 4.4: B-scans of 3dpf zebrafish head demonstrating specular reflection. The image created using an averaged B-scan as background (left) shows several artifacts. The weighted B-scan as background (right) demonstrates reduced artifacts in this case.

4.3 Sample Preparation

A key aspect in maintaining a stationary sample for in vivo zebrafish imaging is the mounting of the animal. While agarose is excellent for keeping objects stationary within its gelatinous structure, the heat of the liquid form can damage or kill the animal during the mounting process. Regular agarose has a melting point of 88.9 °C to transition from the solid into the liquid form and the gelling point begins at 36.7 °C. To mount the zebrafish, the agarose must remain liquid at a temperature lower than 37 °C to keep the embryo healthy. Low melt agarose is a variation of agarose which has a melting point of 65.1 °C and a gelling point of 26.4 °C, allowing for mounting for in vivo imaging [4]. The zebrafish

to be imaged were anesthetized using a Tricaine solution before being placed in the agarose. A 2% solution of low melt agarose in egg water was used to keep the zebrafish stationary while providing it with the required nutrients supplied by the egg water.

The orientation of the zebrafish while mounting determines the type of images possible with the system. The brightfield confocal image and the GFP labeled vascular image shown in Figures 4.1 and 4.2 both have the zebrafish aligned transversely, with the embryo resting on its side. Unless otherwise stated, the SDOCT images presented for zebrafish imaging were performed with the zebrafish resting on its side such that the major blood vessels along the tail are separated transversely from each other. This alignment also ensures that the majority of the blood flow runs transverse to the imaging direction, demonstrating phase variance motion contrast for the case of severely reduced axial flow components.

When aligning the SDOCT image of the zebrafish, there are several factors to consider for optimizing the image quality:

- Aligning focus of the sample arm is important to maximize the collection efficiency of the sample reflections and determine the transverse resolution. The maximum collection efficiency was aligned to halfway through the depth of the sample.
- Aligning the reference arm should position the interference image within the imaging depth of the SDOCT system. Keeping the sample image near the DC term of the OCT image reduces the SNR penalty that occurs over the imaging depth, but mirror terms and spectrometer noise terms limit the optimal alignment in the image.
- Optimizing the relative polarization between the two interferometer arms improves the SNR of the OCT image.
- Dispersion compensation, spectrometer calibration, and spectral reshaping all have an effect on the OCT image quality.

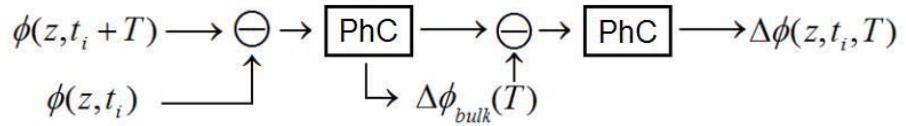
By maintaining a consistent practice of OCT imaging, any variability between phase contrast images can be attributed to sample properties.

4.4 Bulk motion removal

With the large time separations between phase measurements performed with the phase contrast calculations, the system becomes more sensitive to bulk motion between the system and sample. Axial motion of approximately 200 nm within this time will cause an apparent phase motion of the sample reflection of π , obscuring all other motion that can be observed. For $T = 10$ ms, this motion is caused by a bulk velocity of 20 $\mu\text{m/s}$. While minimizing this velocity is possible for the controlled situation observed in microscopy, it will not be the case in general for in vivo retinal imaging situations. It is important to develop methods to deal with the bulk motion experienced and remove it from the phase measurements in the system.

In the phase processing for a given pixel, each phase change calculated for a time separation T is subject to phase conditioning, a term referring in this system to the modulus limitation of phase changes to be within $-\pi$ to π (a phase change of $\pi + \delta$ is conditioned to be $-\pi + \delta$). After the bulk motion calculation of the system motion and the removal from the calculated phase change at a depth z , the resulting corrected phase change undergoes phase conditioning as well. After the second phase conditioning is the phase change used to calculate the variance for the phase contrast images.

For 2 phase measurements separated by time T :



Repeated for N phase changes :

$$\{\Delta\phi(z, t_i, T)\}_{i=1, \dots, N} \longrightarrow \sigma_{\Delta\phi}^2(z, T)$$

Figure 4.5: Data processing schematic for calculating phase variance. PhC: Phase conditioning method which uses a modulus function to limit the calculated phase changes between $-\pi$ and π .

There are several different methods used to determine the bulk axial motion of the sample during the time separation T . Using all of the measured phase changes from all of the

depths in the sample, the mode can calculate the most prevalent phase change within the sample. This method can be very accurate in determining bulk motion, but depends on the depth sampling of the image, as well as the binning parameters for the histogram used to calculate the mode [5].

The main limitation in the bulk phase motion is the SNR-limited phase error, obfuscating the motion calculated for the low signal pixels. While the mean phase change allows for the calculation of the bulk motion, the result can be skewed by the noise terms and the phase conditioning limitation of the range of phase changes. To reduce the effect of the noise terms on the bulk phase change calculation, a weighted mean calculation was used:

$$\Delta\phi_{\text{bulk}}(T) = \frac{\sum_z [I(z)\Delta\phi(z, T)]}{\sum_z [I(z)]}. \quad (4.6)$$

The weighting factor used in the calculations was the OCT signal amplitude $I(z)$, not the magnitude $|I(z)|^2$ as might be expected to remove the noise terms completely from the calculation. If the weighting was chosen based on the OCT signal magnitude, the bulk motion calculation is based too heavily on the assumption that the highest reflections within the sample were stationary, which is not the case for all samples. Using the amplitude $I(z)$ as the weighting factor does not completely remove all of the effect of the noise terms, so a selected depth region within the sample containing a minimal amount of noise terms must be chosen to calculate the bulk motion. An additional option which was not implemented in the experimental data is to add a Boolean function to the weighting factor, removing the effect of all phase changes with OCT intensity below a chosen value.

The limitations imposed on the maximum phase changes causes some miscalculations for the cases where $\Delta\phi_{\text{bulk}}(T) \approx \pi$. The spread of measured phases appears to be near both π and $-\pi$ for this scenario, as shown in Figure 4.6. The weighted mean in this case would appear to have little or no motion occurring during this time period, which causes false phase contrast to be calculated.

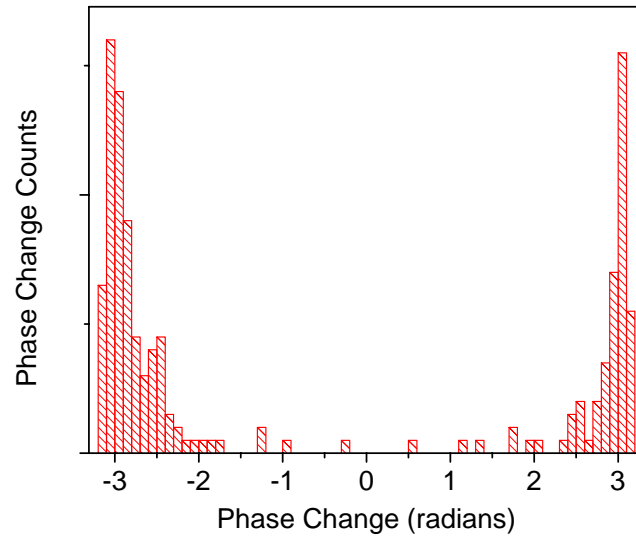


Figure 4.6: Simulated phase change data for bulk motion of $\sim \pi$ radians.

To identify the cases where the bulk motion is $\sim \pi$ radians and additional calculations are required for motion compensation, the phase change data was split up into the cases of $\Delta\phi(z,T) > 0$ and $\Delta\phi(z,T) < 0$. The mean values calculated for these two cases are designated μ_+ and μ_- , respectively. For the case of $\mu_+ > \pi/2$ and $\mu_- < \pi/2$, the phase change range is adjusted to be a 2π phase range centered around $\Delta\phi = (\mu_+ - \mu_-)/2$, and the bulk motion is recalculated properly.

4.5 Zebrafish Tail Contrast Imaging: MB-Scan versus BM-scan

To compare the phase contrast capabilities of the MB-scan and BM-scan methods, both techniques were applied to the same scan region over the tail and yolk sac of a 3 dpf zebrafish. The approximate scan location is depicted graphically on the confocal images of Figure 4.7. By scanning across the zebrafish from the dorsal to the ventral side, the OCT scan is expected to cross two main vessels along the tail, referred to in this case as the dorsal aorta and the axial vein. Through microscopy, estimates of the flow within these tail vessels for 3 dpf zebrafish are approximately 0.5 mm/s.

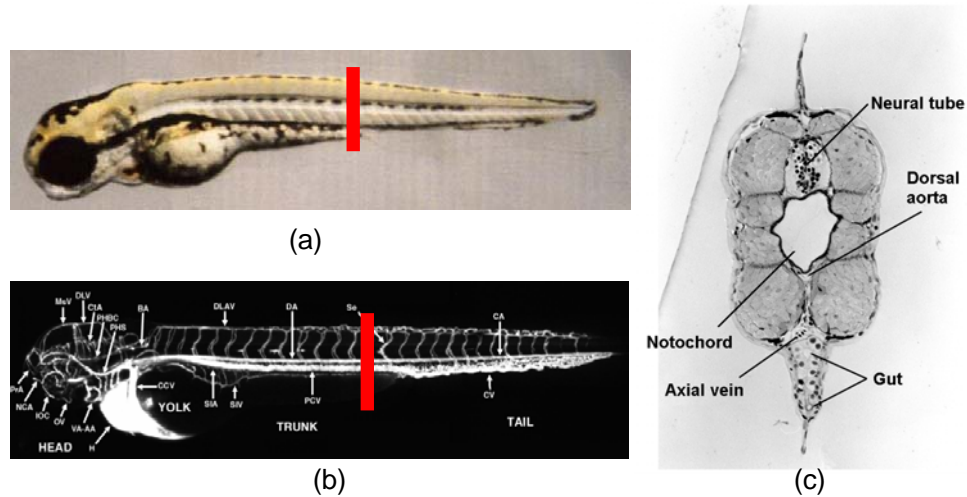


Figure 4.7 a): Confocal bright field image (a) and angiography vascular image (b) containing the approximate transverse scan location for the zebrafish tail phase variance contrast images. The expected histology for the approximate region (c) is also presented.

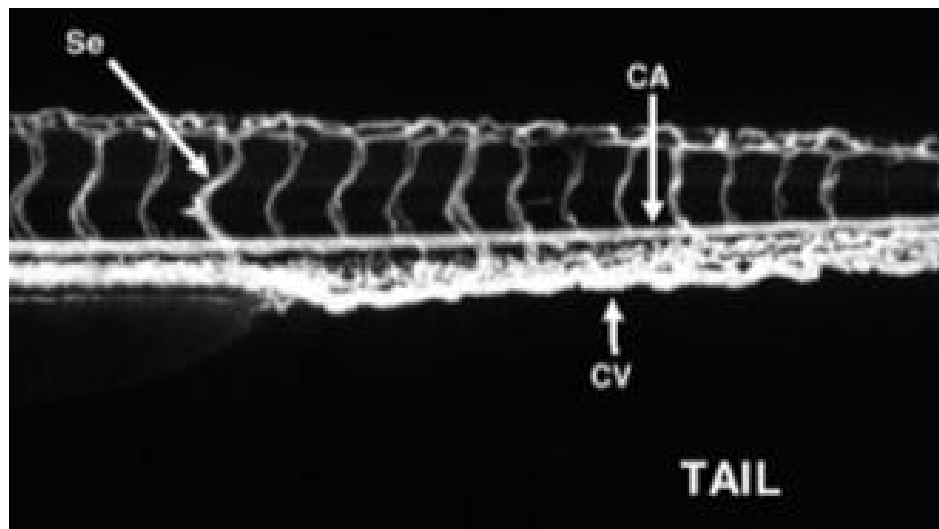


Figure 4.7 b): Zebrafish vascular image from Figure 4.2, zoomed in on tail to highlight the three major vasculature forms: the axial vein/caudal vein (CV), the dorsal aorta/carotid artery (CA) and the segmental vessels (Se).

The MB-scan and the BM-scan performed contrast imaging with 200 transverse pixels across a scan range of 480 μm . The averaged OCT intensity image and the phase variance contrast image are calculated as described in Chapter 3.3 for the case of time separation $T_2=1$ ms. The Doppler flow images plotted in Figure 4.8 are defined as the average phase change between successive A-scans. The total number of phase changes used in the

average calculation for the two images in Figure 4.8 is 5 and 100, respectively. While the maximum phase change scale for these images is $\pm \pi$ radians, both images use a phase scale of ± 0.12 radians which corresponds to an axial flow rate of $200 \mu\text{m/s}$. Using the same scale on both images demonstrates the reduction in phase noise which occurs with increased averaging.

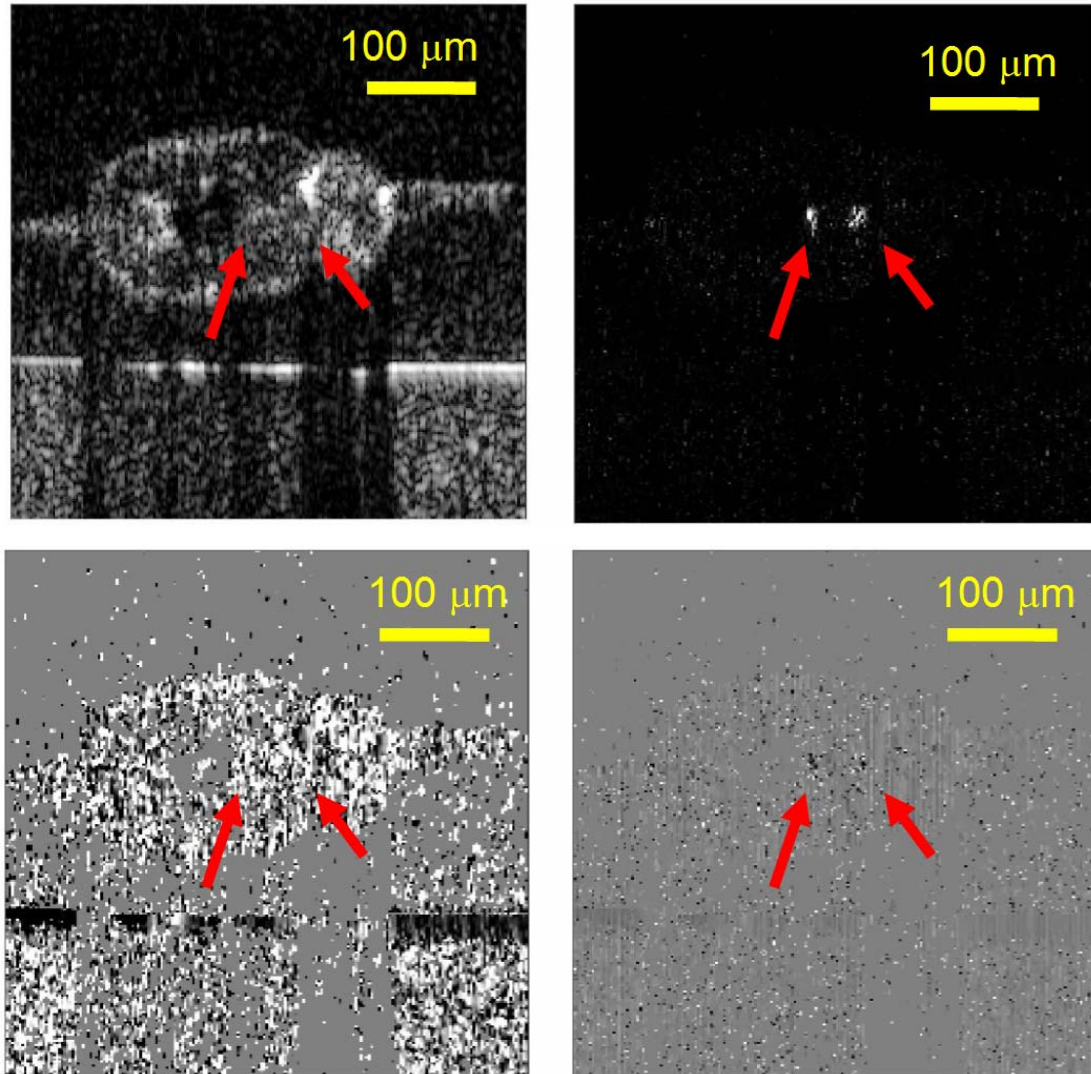


Figure 4.8: MB-scan zebrafish tail motion images with averaged intensity image (upper left). Phase contrast image (upper right) uses $T_2=1 \text{ ms}$ and $T_1= 40 \mu\text{s}$ with a variance scale of 0 to 2 radians². Doppler flow images use scale of ± 0.12 radians = $\pm 200 \mu\text{m/s}$ for the cases of 5 (lower left) and 100 (lower right) phase change averages. Arrows correspond to identified locations of dorsal aorta and axial vein.

The arrows on all four images correspond to the spatial locations of the dorsal aorta and the axial vein. While there is no discernable contrast of the OCT image for these locations, the phase contrast image identifies the motion associated with the flow within the vessels. The Doppler flow image for 5 averages similarly suffers from an inability to observe this flow, evident by the partial visualization which occurs when the averages increase to 100 for this case.

The BM-scan taken over the same region produces the averaged OCT images and phase variance contrast images with an acquisition time of 50 ms. The phase contrast image uses time separations for the phase changes of $T = 10$ ms and applies a rank 1 median filter in each direction of the image. There are no Doppler flow images with this case because the maximum axial flow that can be observed with this method before artifacts occur is 250 times smaller than the previously presented case.

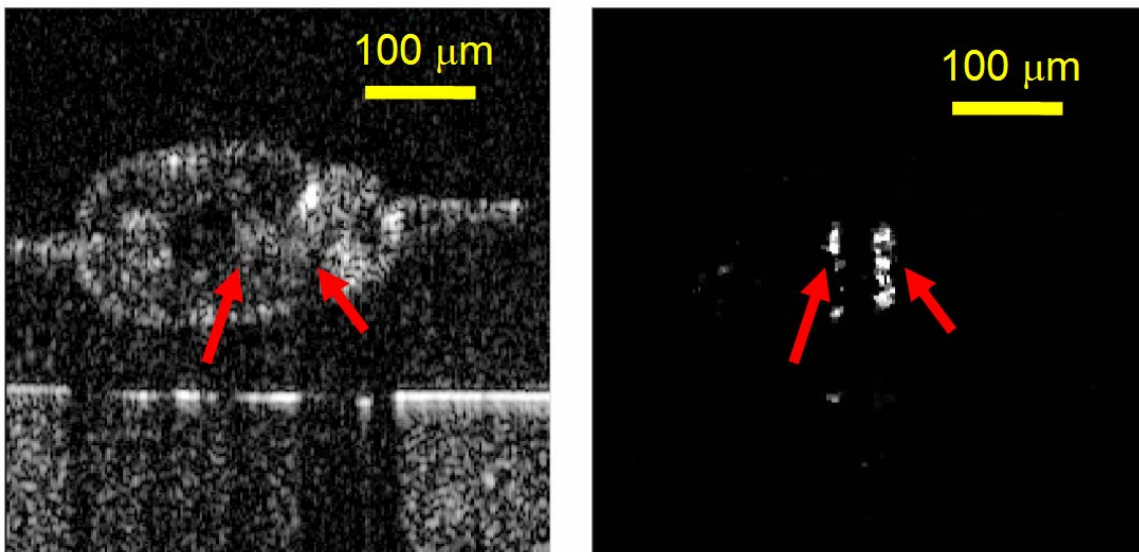


Figure 4.9: BM-scan zebrafish tail images. Averaged OCT intensity image (left) is compared against the phase variance contrast image, using 5 total B-scans, a rank 1 median filter in each direction, and a variance scale of 0 to 3 radians². Arrows correspond to identified locations of dorsal aorta and axial vein.

The major distinction between the phase variance contrast images of the MB-scan and the BM-scan is the visualization which occurs for motion in each method. While both methods observe motion contrast in the regions expected for the dorsal aorta and the axial vein

(designated by arrows), the BM-scan motion contrast also contains a shadowing artifact: motion contrast calculated below the regions of flow where no contrast is expected.

The phase measurement in OCT is not simply a change in the position of a given reflector; it is the change in the optical path length to that same reflector. Therefore, a phase change also measures all of the refractive index variations which have occurred during the time separation T over the entire depth until the measured reflection.

$$\Delta\phi(z, T) = \frac{4\pi}{\lambda_0} \left(\int_0^z \Delta n(z', T) dz' + n(z) \Delta z \right) \quad (4.7)$$

For a stationary reflector measured below a region of refractive index variations (i.e., flow) $\Delta n(z', T)$ which extends a depth of z_n , the calculated phase change is:

$$\Delta\phi(z, T) = \frac{4\pi}{\lambda_0} \Delta\bar{n}(T) z_n. \quad (4.8)$$

To create a completely random phase measurement measured below flow of a vessel of thickness $15 \mu\text{m}$, the required minimum average refractive index variation in this case is:

$$\frac{\Delta\bar{n}_{rms}(T)}{\bar{n}} \approx 0.006 = 0.6\%. \quad (4.9)$$

The observed contrast shadowing is not a complete line through the entire depth of the image due to the numerical SNR phase noise removal performed on the image. The purely noise pixels in the image have no way to differentiate these two types of phase variance, especially when the values are near to the random phase noise limit imposed through the phase conditioning of the data.

To compare the locations of motion contrast to the structural information, the phase variance contrast data over 1 radian^2 was overlapped on the averaged OCT intensity image. This overlap was produced for the MB-scan and the BM-scan to demonstrate consistency to the anatomical structure identified through histology for a similar location within the zebrafish.

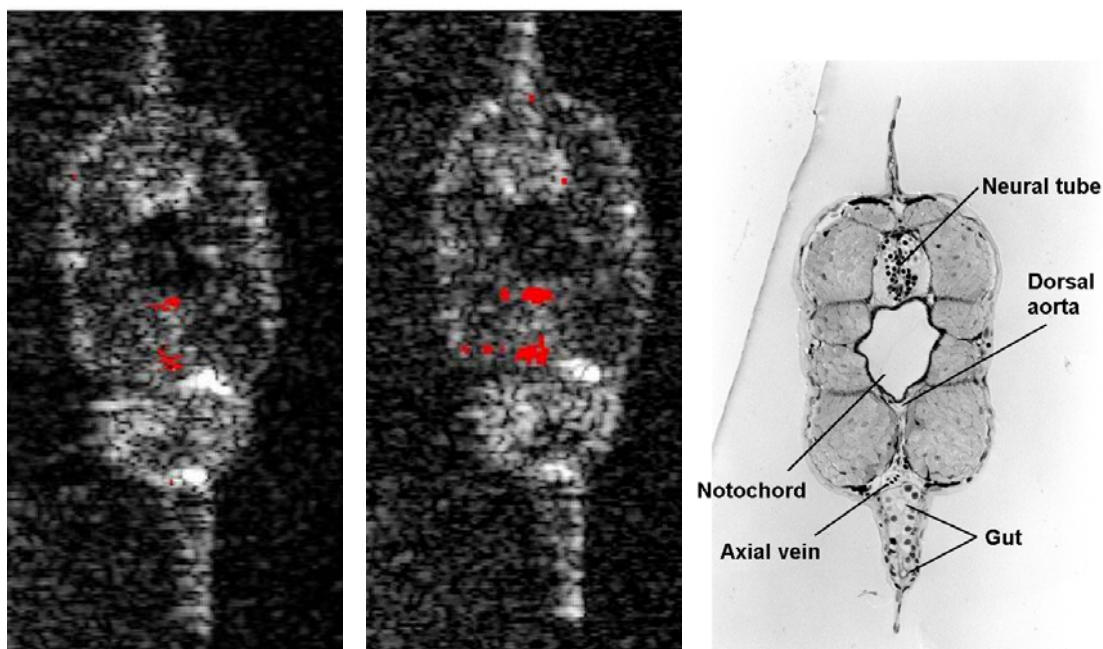


Figure 4.10: Overlay images created from intensity and phase contrast images for the cases of MB-scan (left) and BM-scan (center) compare with histology from similar transverse region of the zebrafish (right).

The MB-scan and BM-scan methods were repeated for a different region of zebrafish tail than used for the images of Figures 4.8 and 4.9, further along the tail past the end of the yolk sac. In this case, the MB-scan phase contrast image can just barely visualize three regions of motion (labeled by arrows) not easily observable in the Doppler flow image. These regions correspond to the dorsal aorta, the axial vein, and the vasculature which connects the segmental vessels on the dorsal side of the zebrafish, referred to as the dorsal longitudinal vessel (DLV). The phase noise image demonstrates, on the same scale as the phase contrast image, the minimum resolvable phase change for the given pixel of the image. The scales on the MB-scan images are identical to the parameters chosen for Figure 4.8.

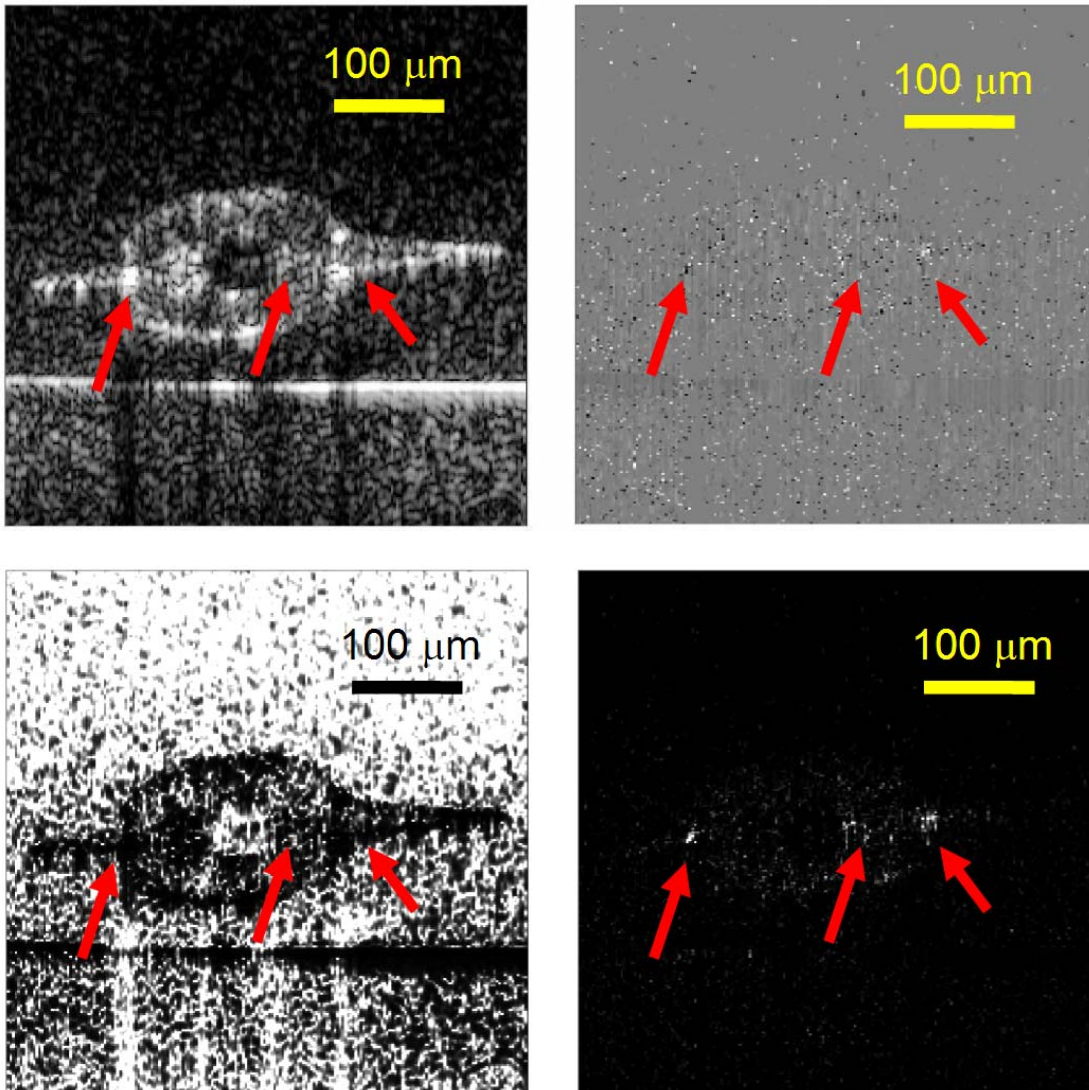


Figure 4.11: MB-scan averaged intensity image (upper left) and phase images for a different region of the zebrafish tail. The phase images include the Doppler flow image for 100 averages (upper right), the measured phase noise in image (lower left), and phase variance contrast (lower right) measured above phase noise. Arrows correspond to identified locations of the dorsal aorta, axial vein, and the dorsal longitudinal vessel.

Repeating the MB-scan over the same scan region, the calculated phase contrast image demonstrates different motion contrast than previously demonstrated. In this case, two of the three expected contrast regions are very hard to identify without prior knowledge of the vascular structure. The BM-scan over the same region does not appear to have any visualization problems observing the motion contrast from the transverse flow in the tail.

Therefore due to improved visualization of BM-scan over MB-scan for the visualization of the zebrafish vascular flow and the improved acquisition efficiency of the method, the BM-scan will be used for all further zebrafish contrast imaging.

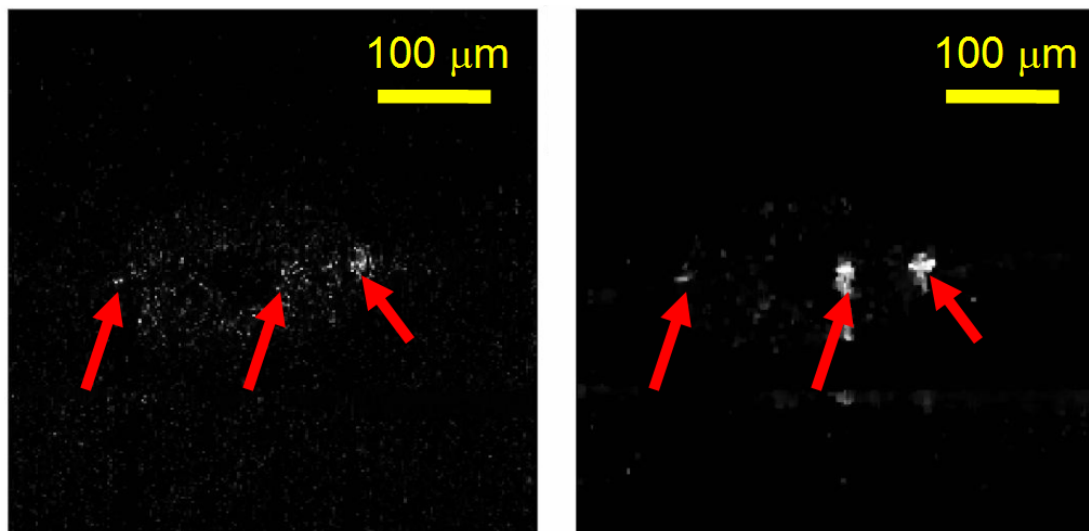


Figure 4.12: Comparing phase contrast images from the two different demonstrated methods for the zebrafish tail location used in Figure 4.11. The MB-scan contrast image (left) is presented with a variance scale of 0 to 2 radians² and the BM-scan (right) uses a scale of 0 to 3 radians². Arrows correspond to identified locations of the dorsal aorta, axial vein, and the dorsal longitudinal vessel.

4.6 Zebrafish Tail Motion Contrast over Time

The phase contrast observed in the zebrafish tail appeared to depend on the time of the image acquisition. Due to the pulsatility observation limitations of the MB-scan, this property could not be studied further using that method. The BM-scan has the ability of looking at the phase contrast image for a given 50 ms time window within a 2.6 s total time acquisition, which allows for the observation of phase variance contrast over time. Looking at multiple phase contrast images over time, five regions of contrast were observed (arrows). While the regions associated with the dorsal aorta and the axial vein maintained visualization over almost the entire acquisition time, the three regions associated with portions of the segmental vessels observed contrast that was almost random in time. Microscopy has confirmed that the blood cells are not flowing through the segmental

vessels for all time points, leading to the assumption that blood flow can be observed within the segmental vessels only when blood is located within the vessel at the acquisition time of the phase contrast image.

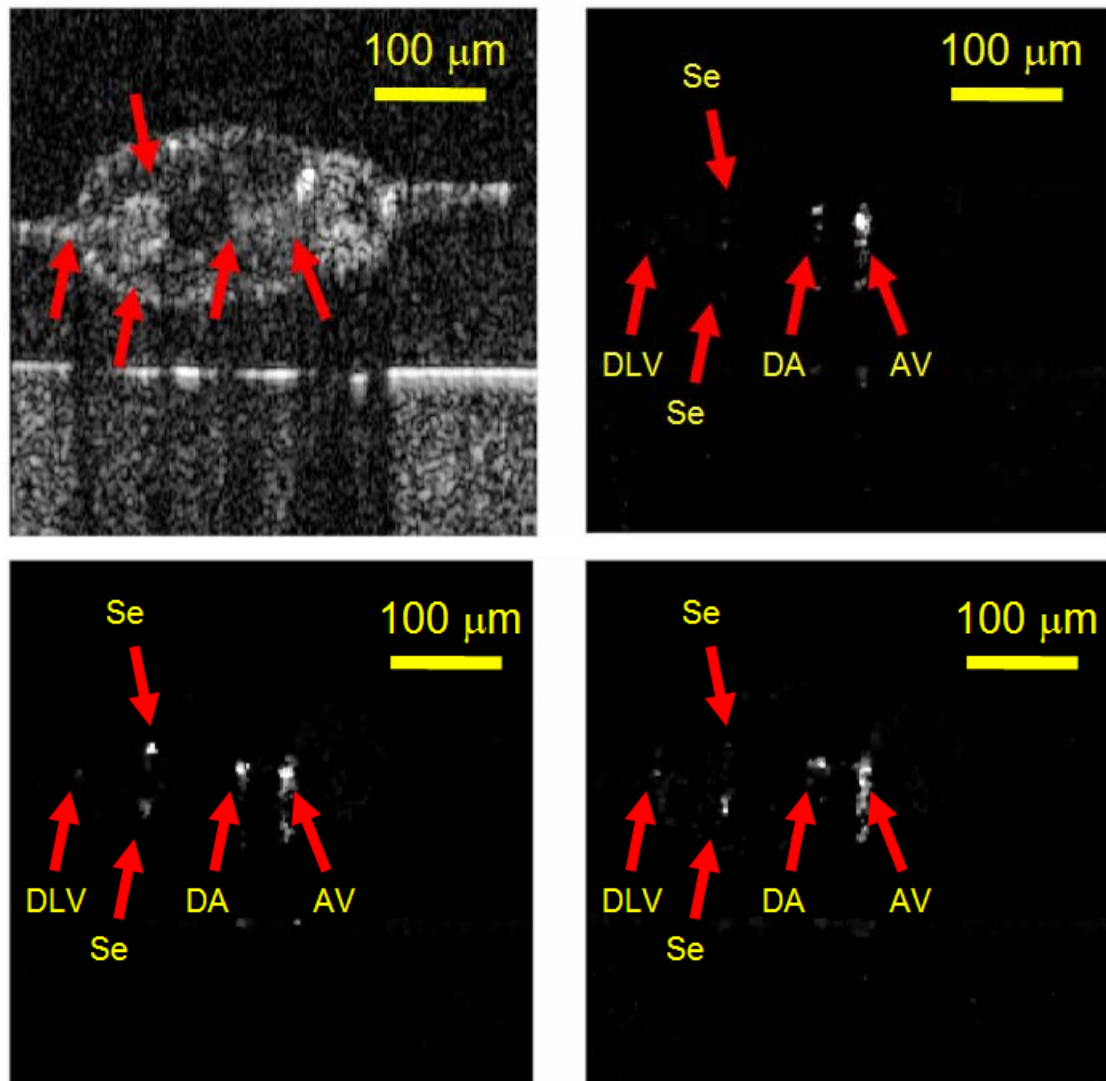


Figure 4.13: BM-scan averaged OCT intensity image (upper left) and three-phase variance contrast images acquired at different time points. Each image was acquired within a total time of 50 ms. The arrows correspond to locations of the dorsal longitudinal vessel, two different segmental vessels (Se), the dorsal aorta (DA), and the axial vein (AV).

To characterize the motion contrast over time for the five contrast regions, a summation image was used to simplify a two-dimensional phase contrast image into a one-dimensional contrast measurement over transverse location. To create a summation image, a depth region of an image is chosen over a portion of the entire depth. The image values for that depth region are summed for each transverse location to create a summation versus transverse pixel calculation. Repeating this method for multiple two-dimensional images of a three-dimensional data set creates an en face, or transverse image from the data set. Creating a summation calculation for multiple images over time allows for the phase contrast to be calculated over time for a given transverse location.

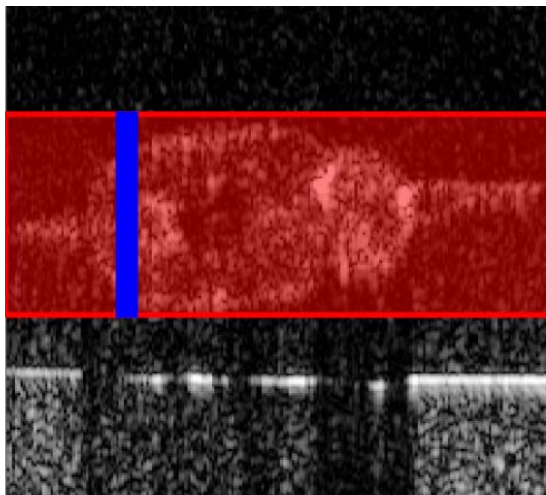


Figure 4.14: Summation images convert each 2D image into a 1D measurement through the depth summation of a chosen region at each transverse location. This method is used to convert a 3D data set into an en face image.

For the phase contrast images calculated for the same B-scan region of the zebrafish tail over time, the contrast was observed for the regions identified by the arrows in Figure 4.13. For each of the contrast summations used in the analysis of this data, the region used for each summation was 3 transverse pixels and 15 axial pixels, corresponding to a region of approximately $7 \mu\text{m} \times 29 \mu\text{m}$. The depth summation region was chosen to be larger than the expected motion contrast region to reduce the alignment errors of choosing the summation regions.

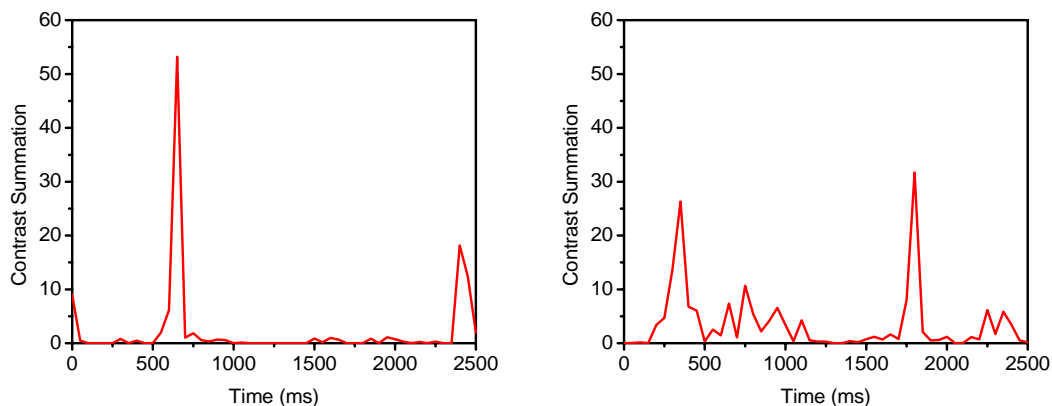


Figure 4.15: Segmental vessel phase variance contrast over time. The segmental vessel closer to top of image (left) was separated from the vessel deeper into sample (right) for contrast analysis. Contrast was summed over 3 transverse pixels and 15 pixels in depth corresponding to $7.2 \mu\text{m}$ in width and $29 \mu\text{m}$ in depth.

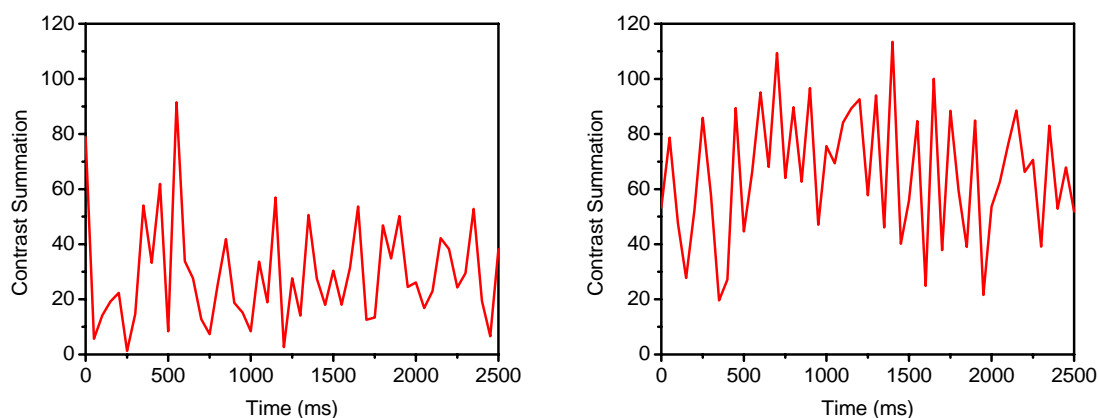


Figure 4.16: Contrast over time of the dorsal aorta (left) and the axial vein (right). Contrast was summed over 3 transverse pixels and 15 pixels in depth corresponding to $7.2 \mu\text{m}$ in width and $29 \mu\text{m}$ in depth.

Looking at the contrast of the segmental vessels over time, it does not match the expected form of contrast from a constant flow within the vessel. Through microscopy, it is observed that the blood cells are not constantly present at all locations within the segmental vessels for a given point in time. This is not an issue for the larger vessels like the dorsal aorta and the axial vein, which both appear to be full of blood cells flowing through them at any given time. This corresponds to the contrast summations taken for the dorsal aorta and the axial vein for the same summation region. While both vessels appear to have motion

contrast for almost all points during the 2.6 s of acquisition time of the phase contrast data, the contrast appears lower in general for the dorsal aorta. By comparing the mean contrast summation of the two cases, the axial vein contrast summation mean is 2.27 times larger than the calculated mean for the dorsal aorta. If we assume that there is identical flow in both of the vessels and the contrast summation captures all of motion of the vessel, this contrast difference would be caused by a vessel diameter of the axial vein approximately 50% larger than the diameter of the dorsal aorta.

Confocal microscopy was used to image the vasculature of a 3 dpf zebrafish, the same age as used in the previously demonstrated phase contrast images. A genetic strain of zebrafish called CT60 was used for imaging in this case. This particular strain of animal has the characteristic of expressing green fluorescent protein (GFP) within its vasculature, allowing for visualization using fluorescent imaging techniques. Using the Zeiss 5 Live laser scanning microscope, the zebrafish vasculature was imaged just posterior to the end of the yolk sac. The zebrafish was oriented on its side for the imaging procedure presented here. Using a high numerical aperture lens, the focal plane within the sample was only a few microns thick. Multiple images were created by focusing the light at different depths within the sample for a fluorescent image. The presented images from that data set are the locations of the dorsal longitudinal vessel and one side of the segmental vessels, the location of the dorsal aorta, and the location of the axial vein and the other segmental vessels.

From these confocal images, many parameters were determined for the 3 dpf zebrafish. The blood flow was approximately 0.5 mm/s for all of the vessels, when the blood cells were moving through them. The segmental vessels and the dorsal longitudinal vessel only contained blood cells within a given location for a fraction of the time. The dorsal aorta and the axial vein, on the other hand, appeared to hold blood cells at all points in time. The heartbeat of the zebrafish affects the pulsatility of the blood flow within the vessels at a rate of approximately 3 Hz.

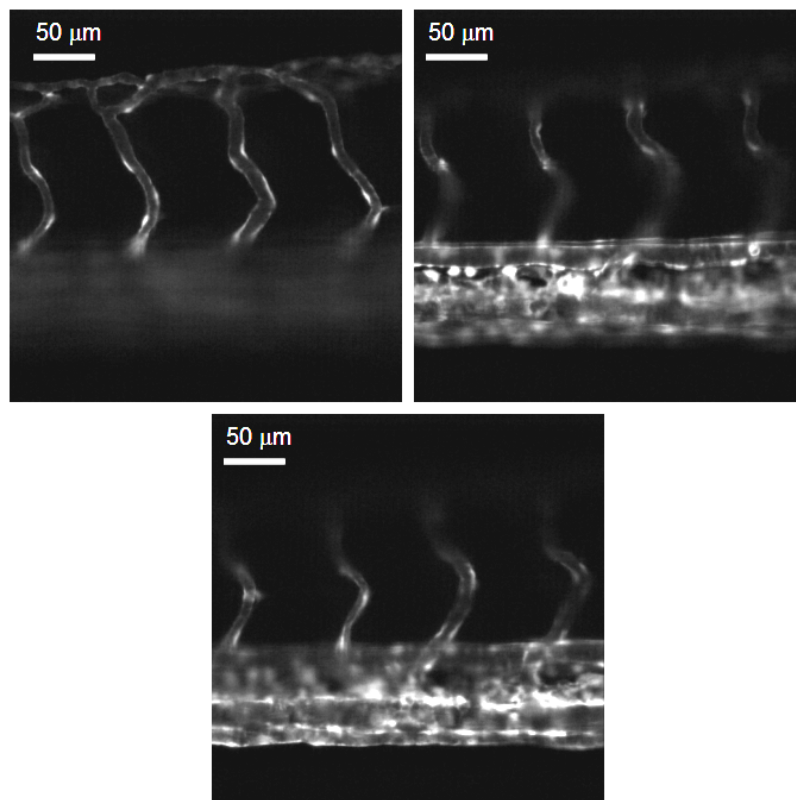


Figure 4.17: High resolution confocal images of GFP-labeled zebrafish vasculature from 3dpf zebrafish genetic strain CT60. Images were produced using Zeiss 5Live confocal microscope. The three images present different focuses within the sample, starting at the shallow segmental vessels and dorsal longitudinal vessel (upper left) and proceeding to focus on the dorsal aorta (upper right), and the deepest focus of the axial vein and the deeper segmental vessels (lower center).

The segmental vessels and the dorsal longitudinal vessel were measured to be 7–12 μm wide, depending on the vessel and the location of the measurement. The measured separation between neighbouring segmental vessels is 75–85 μm for this stage of zebrafish development. The dorsal aorta was measured to have a thickness of approximately 15 μm and the axial vein was the widest in the image with a range of thicknesses from 18–25 μm . The ratio of the range of diameters between the dorsal aorta and the axial vein is 1.2–1.7, consistent with the expected difference determined from the mean contrast summation.

4.7 Segmental Vessel Imaging

Comparing the zebrafish vascular structure to the case of AMD, the segmental vessels which extend from dorsal to ventral sides of the zebrafish might be analogous to choroidal neovascularization (CNV), the main component of wet AMD. In the case of the zebrafish, small vasculature measuring only 7–12 μm wide extends upwards from the blood supply on the ventral side of the zebrafish. This sounds very much like CNV, but in this case the segmental vessels are not leaking into the animal; they are connecting to the dorsal longitudinal vessel and from that to other segmental vessels. By demonstrating the capability of visualizing the segmental vessels using motion contrast, the likelihood of applying these techniques to wet AMD diagnosis is improved dramatically.

To mimic the alignment of CNV within a retinal imaging situation, a different orientation of the zebrafish from the previous images is required. In this case, the zebrafish is positioned with the dorsal side towards the imaging light, allowing the segmental vessels to extend along the depth of the OCT image being created.

The BM-scan parameters used to create the 3D phase contrast image in this case are different than the parameters used in previously presented data. With the small fraction of time in which the blood cells appear to be within a location inside the segmental vessels, the BM-scan acquisition time was increased to try and capture one of these events. The BM-scans used a time separation of $T = 40$ ms for the phase changes, extending over 512 transverse locations. 16 B-scans were used for each BM-scan phase variance contrast calculation and four of these calculations were performed for each transverse scan region by devoting one buffered acquisition of data to each 2D phase contrast image. The mean contrast calculated from the four BM-scans acquired over the same region was used in the 3D phase contrast data set.

By imaging the zebrafish along the dorsal axis for each BM-scan, a minimum number of BM-scans were required to capture all of the 3D data for the embryo. Each B-scan was acquired over a scan length of 650 μm . With an expected segmental vessel separation of

75–85 μm , the 3D zebrafish image over this length should encounter approximately 8 pairs of segmental vessels, increasing the likelihood of visualization. 35 different BM-scan locations were used with 5 μm separation between them, defining the other transverse dimension of the 3D data set as 175 μm .

En face images were created from the OCT averaged intensity 3D data as well as the 3D phase variance contrast data using the summation image method described previously. In this case, each en face image was created through the depth summation of 8 μm around the chosen depth in the data set. The intensity and phase contrast en face images are presented for three different depth locations, corresponding to the upper, middle, and lower bounds of the segmental vessels. The dorsal slice location intercepts the deepest location of the dorsal longitudinal vessel and images the dorsal portion of the segmental vessels. The central slice location is positioned through the notochord of the zebrafish, intercepting all of the segmental vessels along the entire length. The ventral slice location is the dorsal-most slice which encounters the dorsal aorta as well as the deepest portions of the segmental vessels.

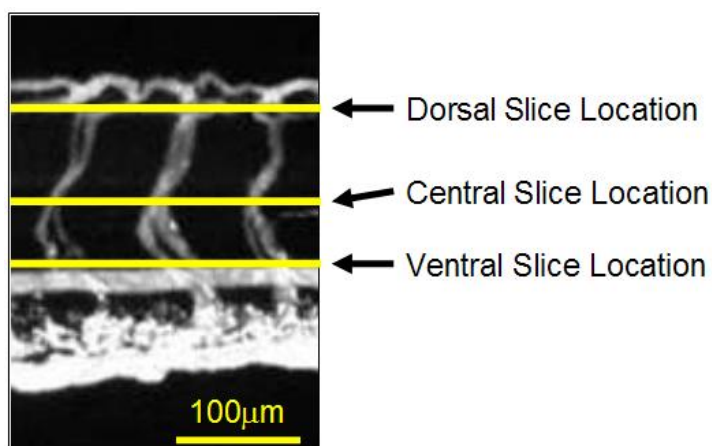


Figure 4.18: Approximate depth locations for the calculated en face slices, presented relative to zoomed in vascular image of Figure 4.2.

The en face intensity images created for the ventral and dorsal slice locations can visualize the main blood vessel due to the increased reflectance from the blood within the vasculature. The central slice, while being able to visualize the structure within the notochord is unable to identify the segmental vessel locations from reflection contrast.

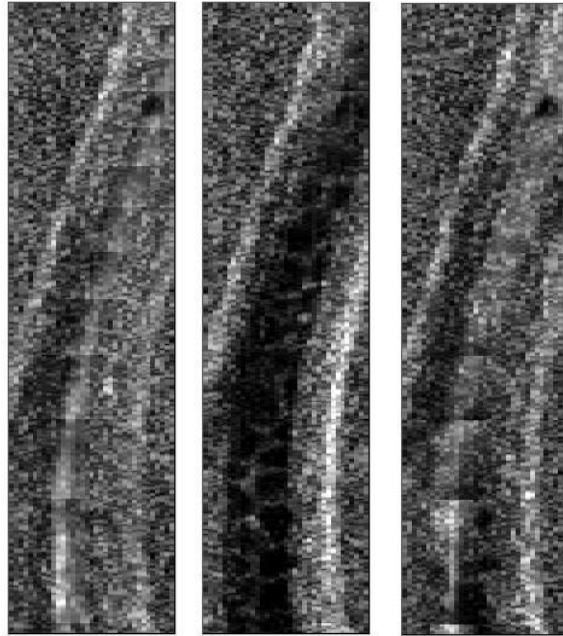


Figure 4.19 a): En face OCT intensity images for the ventral (left), central (middle), and dorsal (right) slice locations designated in Figure 4.18. Image size is $175\ \mu\text{m} \times 650\ \mu\text{m}$.

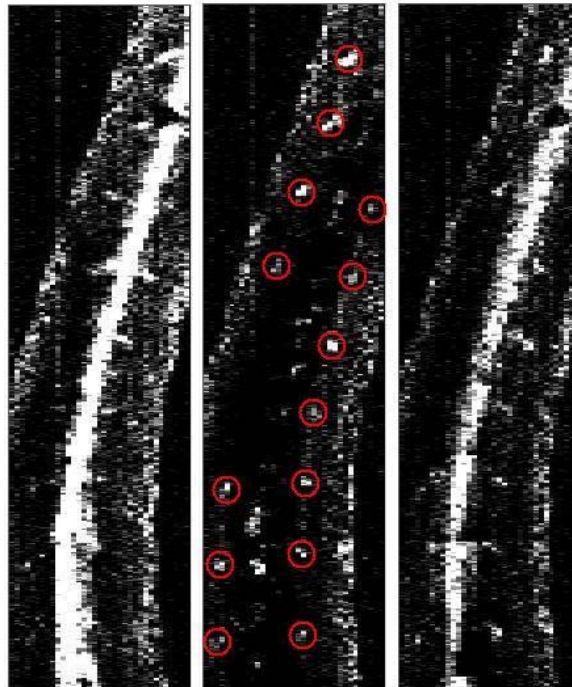


Figure 4.19 b): En face phase contrast images for the ventral (left), central (middle), and dorsal (right) slice locations designated in Figure 4.18. Image size is $175\ \mu\text{m} \times 650\ \mu\text{m}$.

The en face images created from the 3D phase contrast data demonstrate a lot of motion contrast within the zebrafish. The ventral and dorsal slices clearly visualize the transverse flow from the dorsal longitudinal vessel and the dorsal aorta as well as the branching segmental vessels. The central image slice contains many forms of motion contrast, which necessitated the circling of the identified segmental vessels to improve visualization within the image. The motion contrast along the center of the zebrafish in this image is the shadow artifact caused by the flow of the DLV vessel located above it. The contrast observed along the outer edges of the zebrafish is likely due to slight motions of the living embryo over the imaging time. The circled segmental vessels were identified not just from the single slice image, but through the locations of contrast which propagated through multiple depth slices to connect up to the larger vessels above and below. The spacing between the observed segmental vessels in this image is consistent with the expected separation of 75–85 μm along the length of the zebrafish. The two locations on the image which are expected to contain segmental vessel contrast may simply not have any vessels there. Zebrafish do not always create uniform pairs of segmental vessels across their entire length; sometimes there is only one segmental vessel at a position along the length of the embryo. If there are two vessels in the expected locations which do not demonstrate contrast in this data set, the visualization percentage of segmental vessels is 88%.

4.8 En face Images over Zebrafish Heart

Imaging over the zebrafish heart provides a new set of challenges in the data acquisition: the beating heart is moving at a rate faster than the total buffered acquisition of the spectrometer. A data acquisition of phase contrast was acquired while scanning over the beating zebrafish heart. The absorption observed by the light over depth within this region limited the maximum depth which could provide contrast data in this case. The B-scan presented here slices the zebrafish from the dorsal side to the ventral side, with the right portion of the image containing the location of the heart itself. Looking at two different phase contrast images taken through this heart separated spatially by 20 μm along the length of the fish and separated in time by 0.2 s, there is clearly a difference in the observed

size of the heart contrast. Whether this change is due to the spatial or temporal differences of the contrast images cannot be determined from this data set.

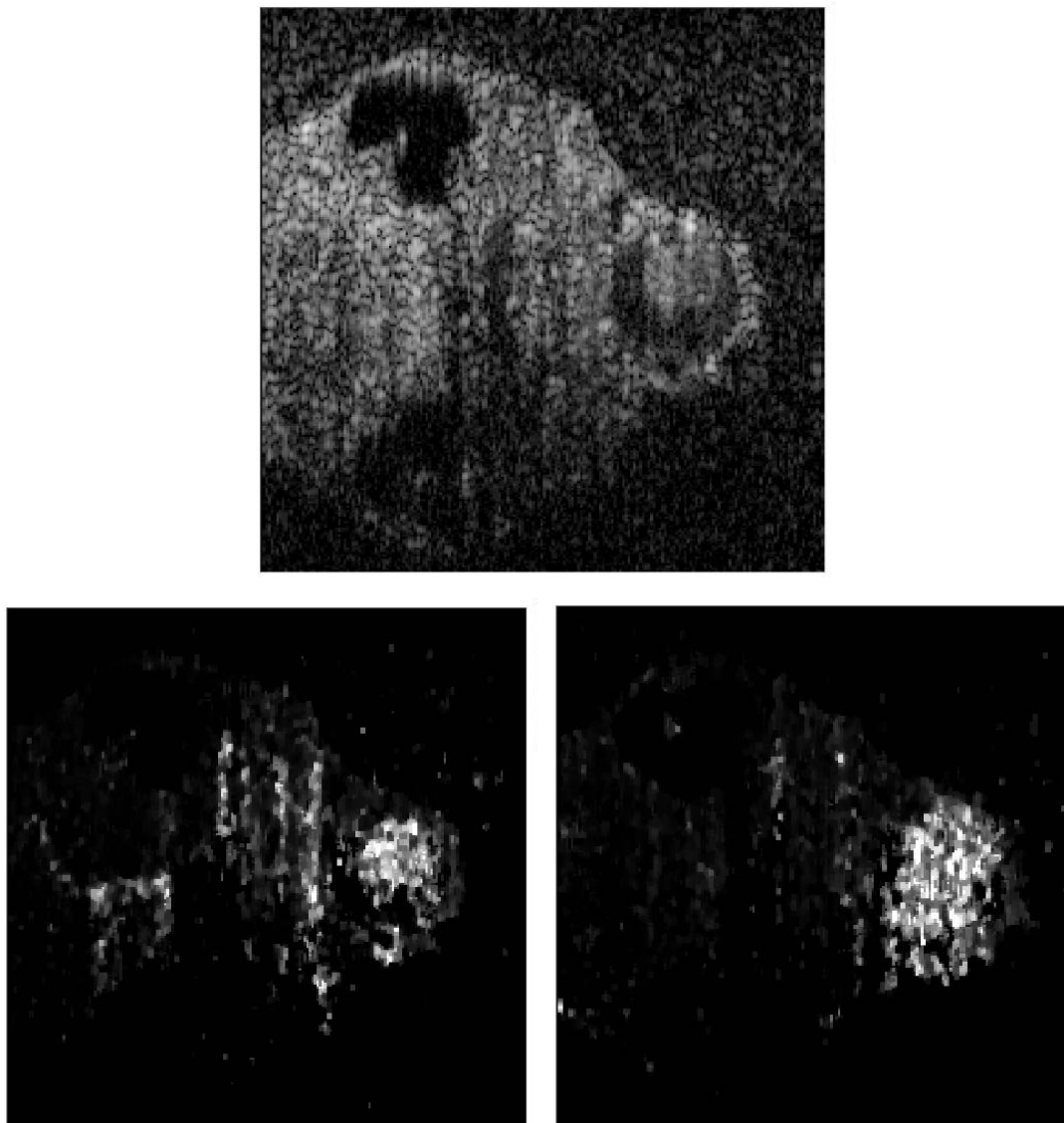


Figure 4.20: BM-scan images over zebrafish heart. The averaged intensity image (upper center) demonstrates the absorption limitation to deep penetration with this light source. The two phase contrast images (lower left and right) were acquired at different transverse slices along the zebrafish separated by $20\ \mu\text{m}$ and 0.2s .

To understand the time scale of the motions with the zebrafish heart, a data acquisition was taken for the same BM-scan location over the heart, acquired over time for 2.6 s. A contrast summation image was created over the entire depth of the image to view the contrast changes associated with the beating heart. While the vasculature near the heart appears to be affected by the beating heart, the contrast never fully disappears within the cycle of the heartbeat. The contrast variations of the heart slice itself can be attributed primarily to the heart physically moving through the chosen slice location during the heart cycle.

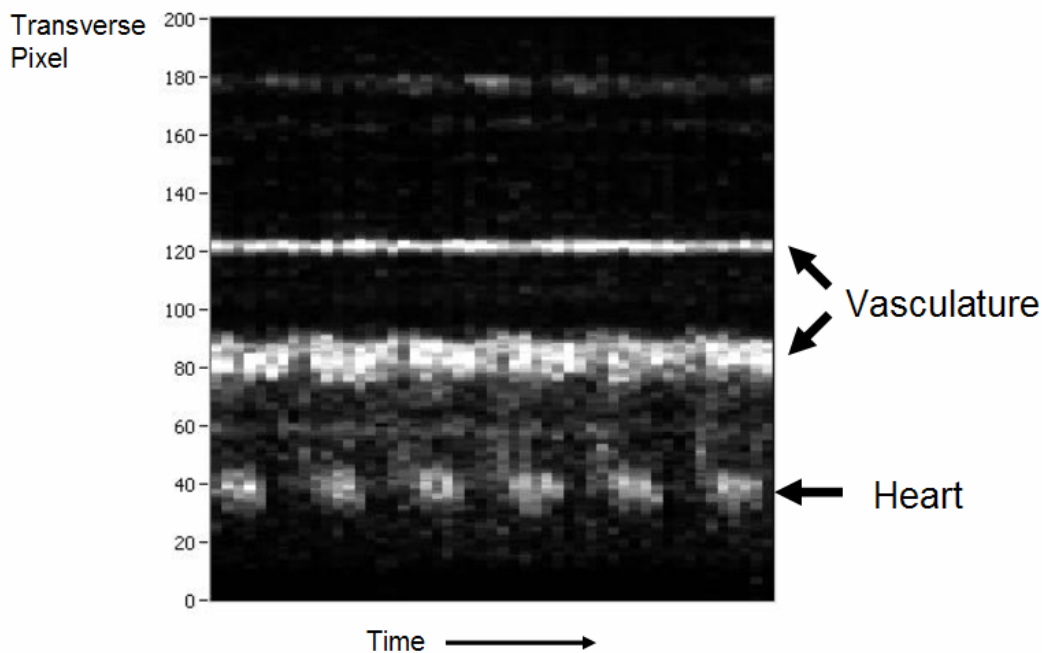


Figure 4.21: Phase contrast summation image over time for a transverse slice located over the zebrafish heart for a total time of 2.6 s. Each time point is acquired in 50 ms.

To analyze the heart contrast over time, the contrast summation was calculated for a region 7 μm wide taken on the heart over the entire depth of the image. The observed contrast in this data appears to have the cyclic nature attributed to the beating heart. From this data, the heartbeat of the imaged zebrafish is estimated to be approximately 2.2 Hz, slower than the expected 3 Hz heart rate determined from confocal microscopy for a similarly aged fish. It is very likely that during the OCT imaging, the zebrafish cooled closer to room temperature from the original temperature of 28 $^{\circ}\text{C}$ of the incubator, slowing the heartbeat.

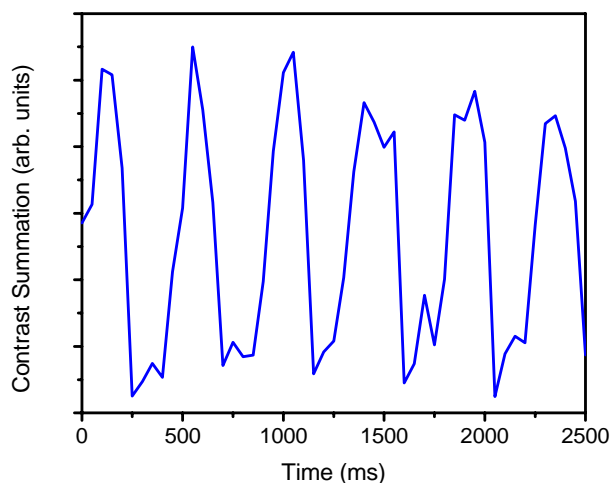


Figure 4.22: Contrast over time for the zebrafish heart at one transverse location. Contrast was summed over 3 transverse pixels ($7.2 \mu\text{m}$) and over the entire depth of the zebrafish.

En face summation images were created from summing over the entire depth of the 3D contrast data taken over the zebrafish heart. No additional data processing was introduced to deal with the beating heart of the zebrafish. Each of the calculated en face images are presented in logarithmic scale to reduce the effect of the contrast fluctuations over time as well as improving visualization of structures within the image itself. To compare against the expected vasculature in the zebrafish, a zoomed in version of the GFP labeled zebrafish confocal image of Figure 4.2 is presented as well. The calculated en face phase variance contrast image is consistent with the vasculature of the 3 dpf zebrafish.

The BM-scan demonstrated the ability to visualize contrast for the range of vasculature, including the segmental vessels, the major arteries of the tail and the heart of the zebrafish. While the zebrafish is a stationary sample in general, heartbeats, digestion, and general motion fluctuations can occur. With the bulk sample motion calculated from the scatterers within the zebrafish as well as the agarose, these motions can affect the bulk removal process. While further progress can be made to improve the analysis procedures, the contrast methods demonstrated show the potential for retinal vascular imaging.

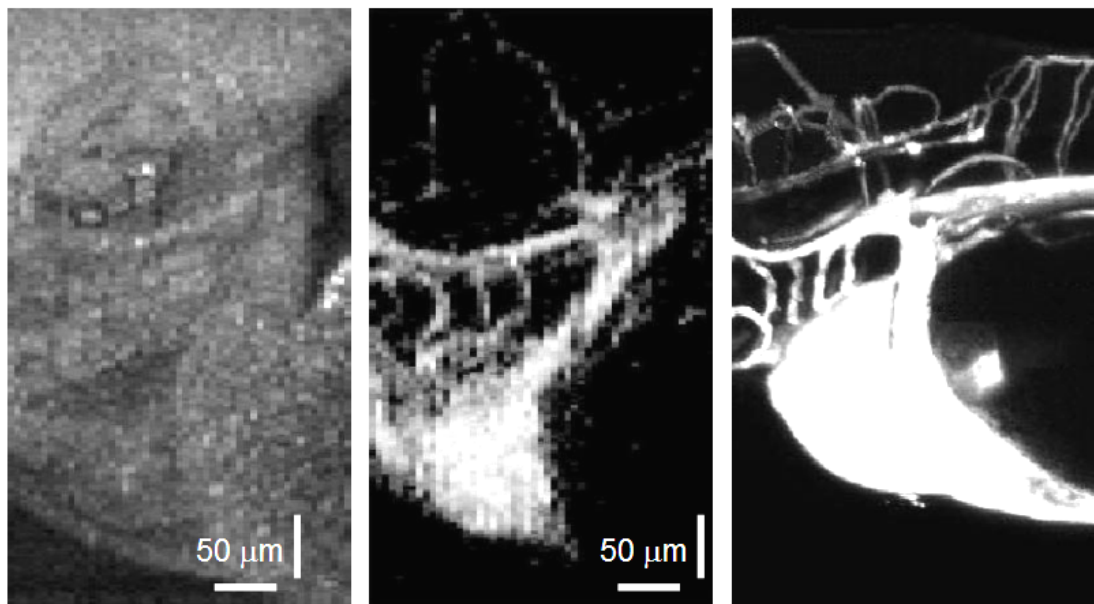


Figure 4.23: En face images over zebrafish heart. OCT intensity summation image was presented in logarithmic scale (left). The phase variance summation image was also presented in logarithmic scale (center) to improve visualization for comparison with a similar region of a confocal image of GFP-labelled 3 dpf zebrafish (right).

4.9 References

1. The Zebrafish Information Network, www.zfin.org .
2. S. Isogai et al., “The vascular anatomy of the developing zebrafish: an atlas of embryonic and early larval development,” *Developmental Biology* 230, 278 (2001).
3. N. Nassif et al., “In vivo human retinal imaging by ultrahigh-speed spectral domain optical coherence tomography,” *Optics Letters* 29, 480 (2004).
4. “Products Catalogue: Agaroses,” Laboratories EUROBIO, http://www.eurobio.fr/UK/secteurs_production/life_science/molecular_biology/Electrophoresis/Products/Agaroses.htm
5. S. Makita et al., “Optical Coherence Angiography,” *Opt. Express* 14, 7821 (2006), <http://www.opticsexpress.org/abstract.cfm?id=97672>.

MOUSE RETINAL IMAGING

Moving the demonstrated OCT phase contrast techniques into retinal imaging, the choice is whether to use human subjects or another animal model which will provide a similar retinal environment. All of the acquisition methods do not produce any more risk to the vision of a human patient than standard OCT imaging, which has been determined safe for given illumination levels determined by the American National Standards Institute (ANSI). The choice of retinal imaging subject becomes a matter of preference once there are no safety concerns.

While the contrast techniques are still in the developmental stages, mouse imaging has several advantages. With mouse animal models, a large population of subjects can be developed for imaging in a short amount of time, including numerous genetic strains to produce abnormalities in the structures of interest. With the short lifespan compared to humans, disease progression within a mouse will be much faster and easier to monitor experimentally. Unlike human subjects, histology of the imaged mouse subjects can be produced when necessary for comparisons to observed phenomena. Once all of the analysis techniques have been developed for retinal imaging in the mouse, they can be adapted for use in human retinal imaging systems.

5.1 Human Retinal OCT Imaging Explained

Retinal imaging with human subjects utilizes the patient's own eye as the final focusing lens of the imaging system, with all of its limitations. The transverse scanning of the imaging light pivots about the center of the eye lens, limiting aberrations introduced while scanning and minimizing clipping introduced by the pupil.

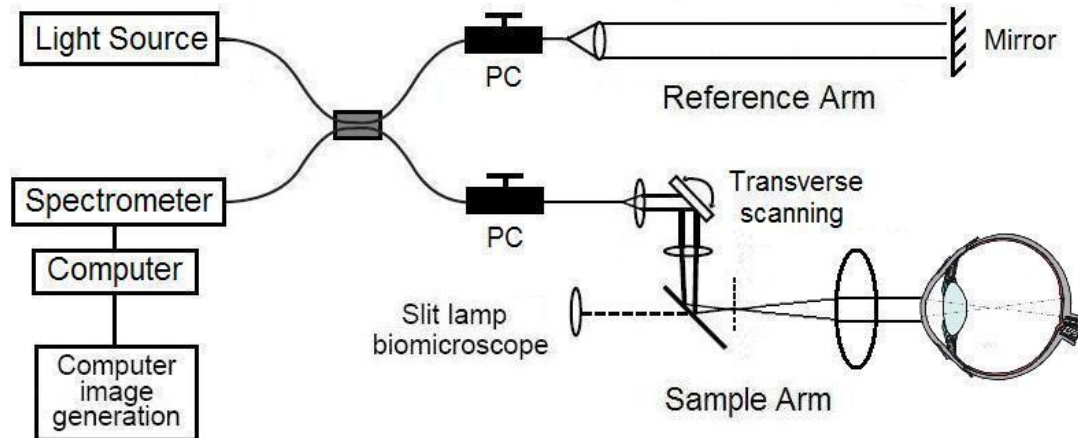


Figure 5.1: Schematic of fiber optic human retinal SDOCT system. PC: polarization controller. The slit lamp biomicroscope combines the OCT imaging with a fundus camera system.

One form of the retinal imaging sample arm of the interferometer is called a slit lamp biomicroscope, which is a combination of the confocal transverse scanning of the OCT interferometer as well as a slit lamp setup for creating a full field fundus image. The Stratus OCT retinal imaging system (Carl Zeiss Meditec) uses this type of sample arm to acquire simultaneous OCT and fundus images. The sensitivity of the fundus camera in this setup allows for visualization of the transverse scan location of the OCT image in addition to the fundus reflectivity.

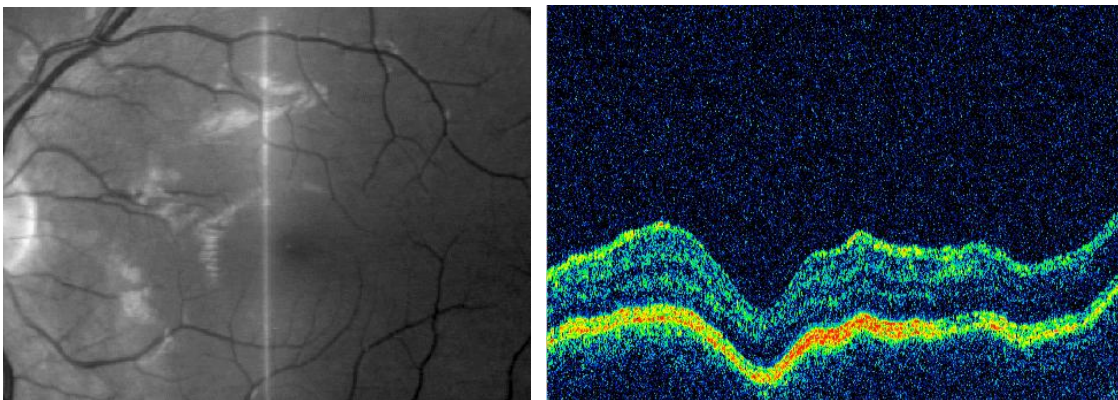


Figure 5.2: Fundus image and OCT intensity image acquired simultaneously with retinal Stratus OCT imaging system created by Carl Zeiss Meditec. The fundus image can visualize a fraction of the reflected OCT light source, demonstrating the transverse location of the corresponding OCT scan (vertical line on fundus image).

The experimental SDOCT system uses a slit lamp biomicroscope from a Stratus OCT system, adapted for use in mouse retinal imaging. To adapt the scanning system intended for human eyes to be able to image mouse eyes, the differences between imaging the two types must be understood.

5.2 Differences between Human and Mouse Eye Imaging

The major difference between human and mouse eyes are the size of the eyes. Human eyes have a typical length from the front of the cornea to the retina of 25 mm. Mouse eyes have a length of around 3 mm, depending on the age of the animal. This eye length determines the focal length of the lens, and with the maximum pupil diameter limits the minimum transverse resolution possible for the aberration-free retinal imaging case.



Figure 5.3: Photograph of mouse, demonstrating an eye length of approximately 3mm for this case.

As in the human imaging case, mouse eyes cannot be considered aberration-free in general. Mouse eyes contain multiple aberrations and are typically myopic (eye length is too long for the eye's focus length), limiting the resolution in the uncorrected case. While the lenses of the sample arm can be adjusted to compensate for some of the optical quality degradation, the result will still be aberration limited [1]. It is also important to maintain corneal hydration of the mouse eye to prevent optical focus and opacity changes which accompany dehydration [2].

To compensate for the majority of the aberrations and maintain hydration, the curvature of the mouse cornea must be altered while holding an aqueous solution at the surface of the cornea. A specially made contact lens can be created to compensate for the myopia of the mouse eyes, also reducing the aberrations introduced from the curvature of the cornea [3]. An easier approach is to remove the effect of cornea curvature by placing a flat cover glass in front of the eye while holding contact to the cornea with a saline solution [4]. With the majority of the focusing power removed from the eye itself, an external focusing lens can be added to replace the original focusing power. By relying on external focusing to image the mouse retina, the process of changing between different animal specimens becomes easier and less dependant on the individual optical quality of the eyes.

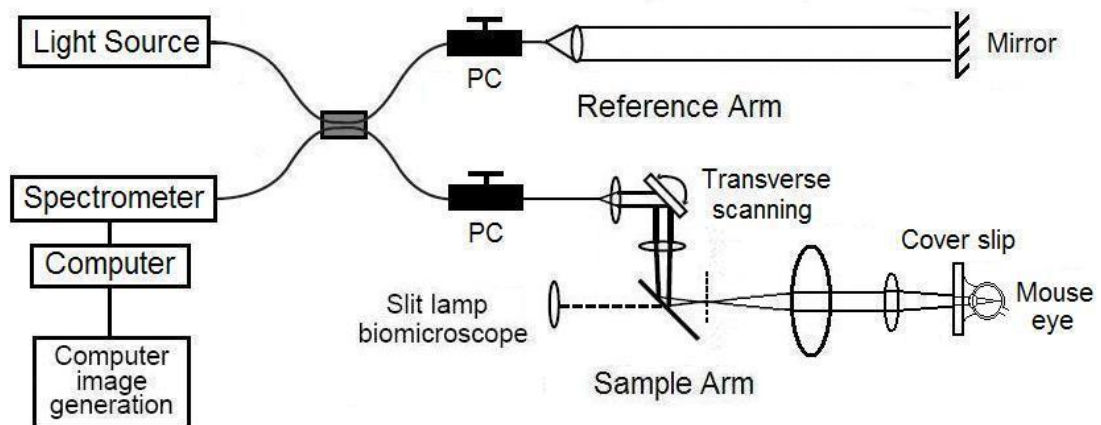


Figure 5.4: Schematic of fiber optic mouse retinal SDOCT system. PC: polarization controller. An additional focusing lens is added to the human retinal system to compensate for the focusing removed by the presence of the cover slip on the mouse eye.

Using the Stratus OCT scan optics, an additional focusing lens was used to allow imaging of the mouse retina. Using a cover slip to remove the focusing power of the mouse's eye, a focusing lens of focal length 18 mm would result in an estimated transverse resolution of approximately 14 μm . The depth of focus for this resolution would be approximately 370 μm , on the order of the retinal thickness in the mouse. For this retinal imaging system, the light source and the spectrometer can be utilized from the microscopy system described in Chapter 4. Due to different optical path lengths and dispersions of the sample interferometer arms for the two systems, different reference arms are required for each of the two imaging systems.

Aligning the human eye for retinal imaging is fairly simple with the help of an external fixation target which allows the patient to align their position to be able to visualize the target. The mouse, which cannot be aligned using a fixation target, requires additional positional alignment to align the retina for imaging. Five degrees of freedom are required to allow all range of alignments for imaging: three translational directions as well as rotation about the x-axis and the y-axis, where the z-axis is defined by the optical imaging direction. Due to the flexibility of the transverse scanning in the system, rotation about the z-axis is not required.

The average mouse will not remain stationary during this optical alignment and imaging, necessitating the use of anesthetic to put the animal to sleep. The lack of blinking experienced by the mouse during the anesthetic can be a main source of corneal dehydration discussed earlier. The anesthesia solution used for mice in the experiment was a combination ketamine/xylazine mixture, containing 0.1mL Xylaject (xylazine hydrochloride injection), 0.3 mL Ketaject (ketamine hydrochloride injection), and 4 mL sterile phosphate buffer solution (PBS).

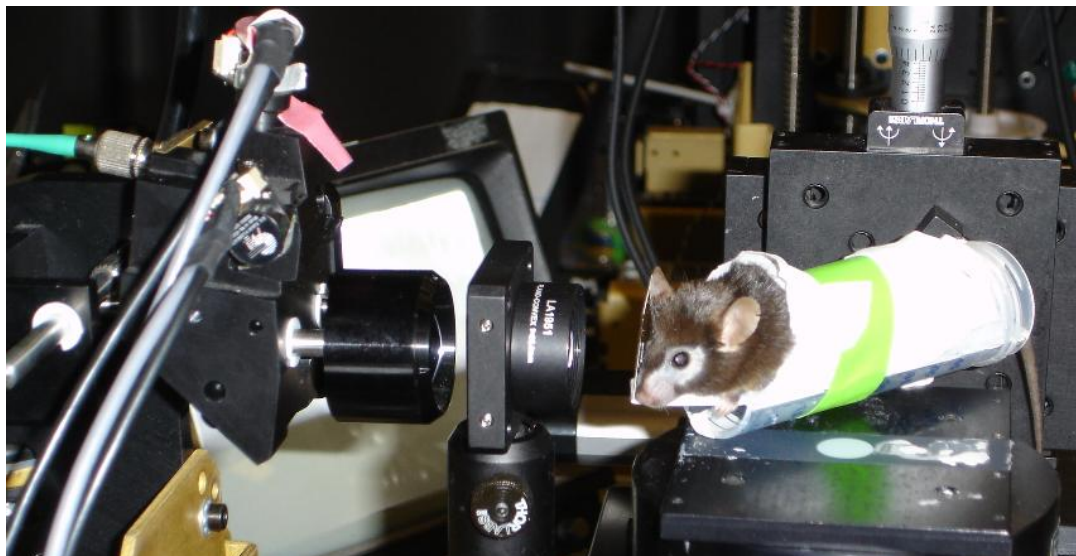


Figure 5.5: Photograph of sample arm of interferometer for mouse retinal system. Mouse is secured in holder after anesthetic with a cover slip attached to the cornea of the eye with a saline solution. The holder provides five degrees of freedom of alignment for the mouse relative to the imaging optics.

5.3 Aligning Retinal SDOCT Images

With the sample arm set up with external focusing, the maximum scan range of the retina is limited by the size of the pupil. Similar to ophthalmologic diagnosis for human eyes, a chemical was used to dilate the pupil and temporarily fix the accommodation of the lens, facilitating the imaging procedure. For the experiment, two drops of 1% tropicamide were used to dilate the pupils of each eye used for OCT imaging. Fundus camera images were taken before the chemical was applied and after full dilation, with both images acquired without a cover glass on top of the cornea.

With a cover glass placed on the eye with a saline buffer solution, the fundus image can be focused to visualize the retina. The optic nerve head and some of the vasculature can be seen with this image, but the image quality depends on the camera and the image parameters. With the ability of the fundus camera to visualize the scan line of the OCT light source, the camera can also act as a coarse alignment of the transverse position of the SDOCT images.

In the experimental system, the optimal focus for the retinal fundus image did not match the optimal alignment of the SDOCT images. To adjust the SDOCT image focus from the optimal fundus focus, there are three elements that can be adjusted in the system: the final two lenses of the sample arm and the depth position of the mouse. By aligning the optics for optimal OCT coupling of a static paper sample, the optical alignment of the lenses was determined. With these positions, only the depth position of the mouse eye was altered to maximize coupling from the retina.

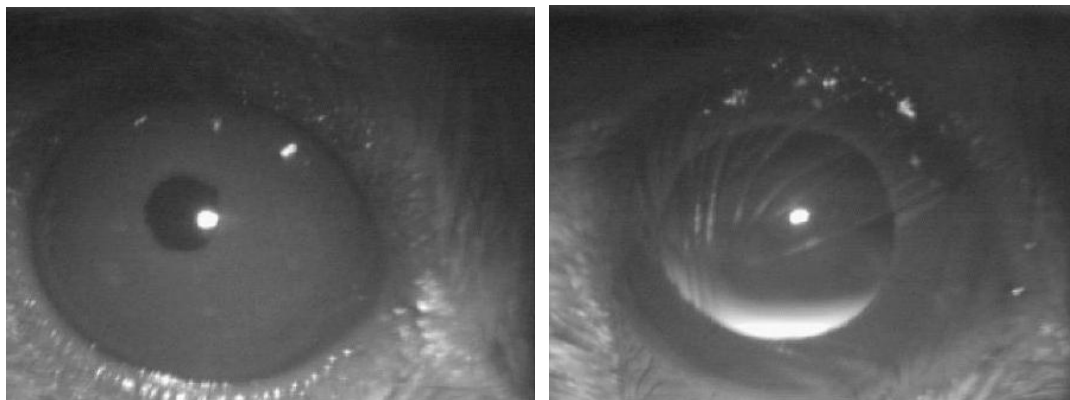


Figure 5.6: Fundus camera images demonstrating the dilation of pupils with application of tropicamide. The undilated pupil (left) is substantially smaller than the dilated case (right). Eye lashes of the mouse are present in front of the cornea on the dilated pupil image. No cover glass is used in these images.

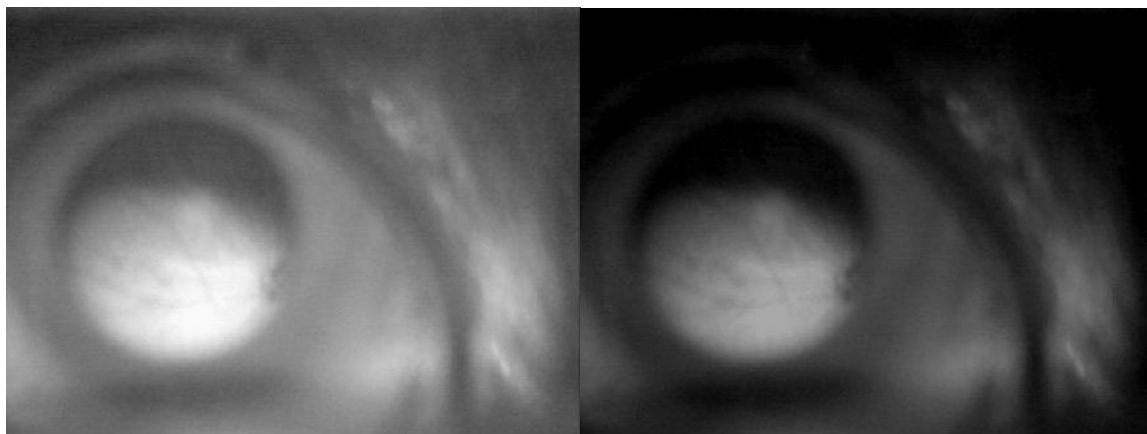


Figure 5.7: Fundus camera image after application of cover slip. Optic nerve head and some vasculature can be visualized in the retina. Two different image contrast parameters are presented to assist with visualization.

Retinal B-scan images were maximized through a series of alignments. Near the optimum sample focus, shadowing from the blood vessel absorption becomes more prominent. At the optimal focus, the reflection from the top of the surface retinal blood vessels is maximized. To maximize the interference signal, the polarization controllers were adjusted for each of the interferometer arms. The important factor to note during alignment is the reference arm coupling changes over extended changes in path length. As the sample position changes to deeper image locations (further away from the equal path length position of the reference arm), the signal will drop due to the SNR drop over depth. If the reference arm coupling decreases as the image is re-aligned back to the equal path length position, the image will appear lower in intensity than expected for a given coupling. Constant reference arm power during the alignment process is crucial for identifying the optimal sample coupling location.

The transverse scan length of the OCT imaging in the mouse retina can only be approximated due to the uncertainty of the contribution from the optics of the mouse eye on the imaging system. With the variability introduced by the alignment of the external optics to improve focusing, image feature sizes and previous images are used to help approximate the transverse scan length on the retina.

5.4 Phase Contrast Imaging

To determine if more system optimization is required before phase contrast analysis is performed, a sample B-scan created using the retinal imaging system is compared to one of the limited amount of high resolution SDOCT images published for the mouse retina [4]. The B-scan image from the previously published work identifies the different layered regions of the retina over the entire depth: the inner plexiform layer (IPL), inner nuclear layer (INL), outer plexiform layer (OPL), outer nuclear layer (ONL), photoreceptor inner segments (PR IS) and outer segments (PR OS), retinal pigment epithelium (RPE), and choroid (CH).

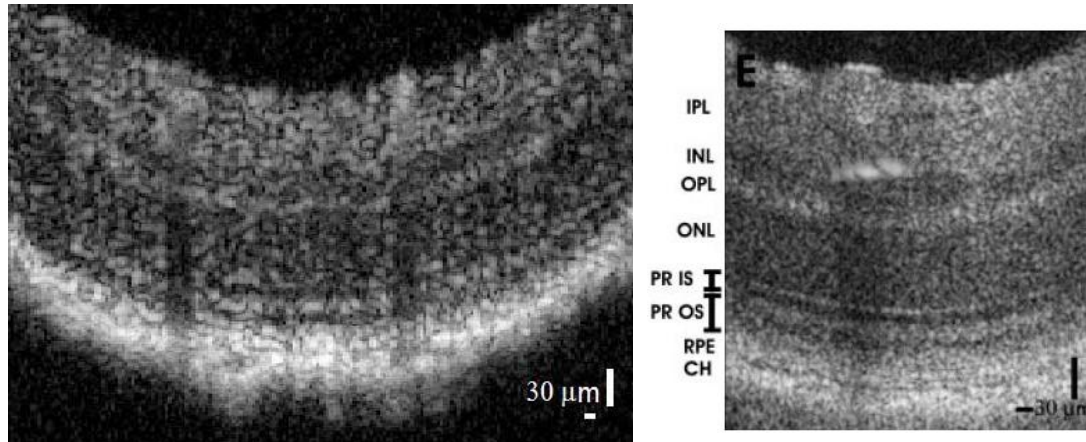


Figure 5.8: OCT intensity B-scan comparison between experimental retinal imaging system (left) and previously published results (right) [4]. The experimental B-scan is composed of 200 A-scans acquired over a scan length of approximately 2mm. Published results demonstrate a B-scan composed of 600 A-scans acquired over approximately 600 μm . Similar image scales are presented to improve comparison.

Comparing the images between the experimental system and previously published data, there are differences between the image parameters. The experimental system has an axial resolution of 6 μm in tissue, while the published system has an axial system of approximately 2 μm in tissue (2.8 μm in air). The published B-scan also has a higher density of A-scans within the image: it uses 600 A-scans over approximately 600 μm while the B-scan from the experimental system uses 200 A-scans over approximately 2 mm.

As expected, both images demonstrate a mouse retinal thickness of approximately 300 μm . The separation of the retinal layers can be observed in both images, but the published image appears to have improved visualization of the layers over regions of the image. This visualization improvement is likely due to the higher sampling density, which is 1 μm between A-scans, compared to the 10 μm spacing used in the experimental image. The increased density not only reduces the speckle observed in the image, but it reduces the SNR loss experienced while scanning over tilted correlated scatterers as explained in Chapter 3.2. The only portion of the retinal image which appears to depend on the axial resolution difference between images is the separation of the RPE and choroidal layers of the published image, which is not evident in the experimental image. With general

consistency between the two images, it is concluded that the performance of the experimental system is adequate for comparison to previously demonstrated systems.

Due to the thin structure of the retina, visualization is improved by using different scaling on the transverse and axial directions of the image. Unless otherwise stated, the presented images within this chapter uses a relative scaling of 3:1 to expand the axial direction of the image and make the retina appear thicker as demonstrated in Figure 5.8.

5.4.1 MB-scan

With the amount of statistics available to be analyzed, the first phase contrast acquisition method for the retina is the MB-scan. Using a buffered acquisition for a total of 1.6 s, 200 A-scans were acquired for each of 200 transverse locations along the retina. From the averaged OCT intensity image, it is obvious that the situation has changed from the zebrafish imaging of Chapter 4. The averaged intensity image shows the retinal layered structure, which becomes blurred in regions which can be assumed are associated with flow. The Doppler flow image is calculated for the case of 5 phase change averages with a scale of ± 2 radians, which is equivalent to an axial flow rate of ± 2.5 mm/s. On this image, large axial flow is observed in the same transverse locations as the blurred regions of the intensity image.

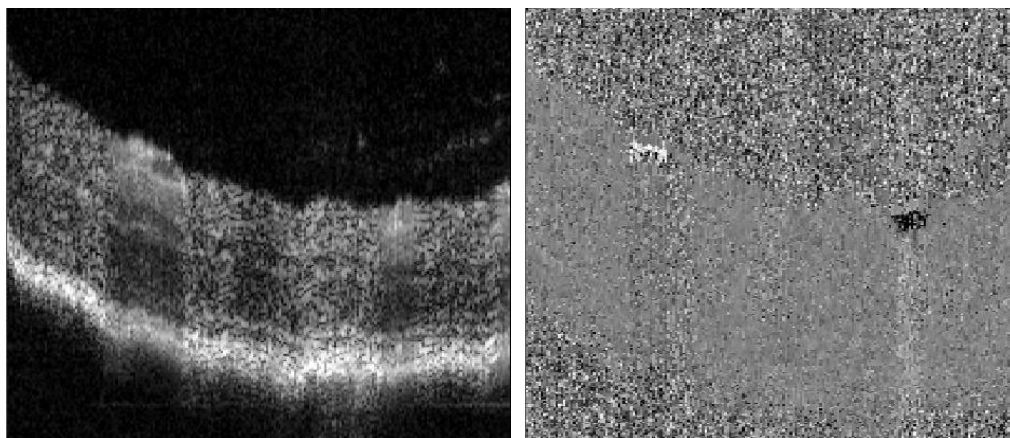


Figure 5.9 a): MB-scan averaged intensity image (left) and Doppler flow image from successive phase changes using 5 averages (right). The Doppler flow image does not use any thresholds and has a scale which corresponds to ± 2.5 mm/s.

While the fast flows are easily observable in the Doppler image, the identification of slower flow is important for the visualization of the smallest vessels. There are two main methods to improve the flow visualization with the Doppler flow technique: averaging more to reduce phase noise, and using larger time separations of phase changes to observe slower flow. The minimum axial velocity that can be visualized is determined by the phase noise divided by the time between phase measurements. One of the consequences of the increased time separation is the reduction of the maximum axial flow that can be measured before phase wrapping takes effect.

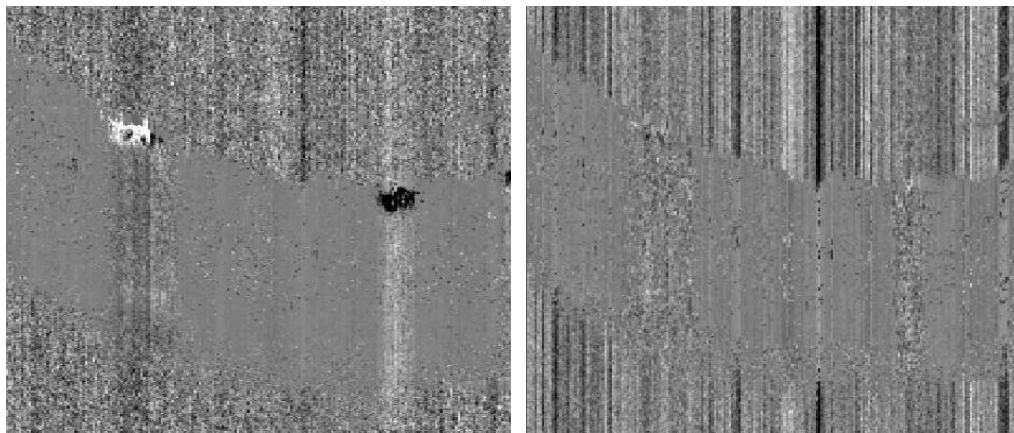


Figure 5.9 b): MB-scan Doppler flow images created using 50 averages for the phase change time separations of by 40 μs (left) and 200 μs (right). The axial flow scale on the images are ± 1.25 mm/s (left) and ± 2.5 mm/s (right), with no thresholds applied to either image.

By increasing the statistics of the averaging from 5 to 50, the phase noise of the Doppler image is expected to reduce by a factor of $10^{1/2}$. To take advantage of the reduced noise, the scale of the flow image is reduced to ± 1 radians = ± 1.25 mm/s. It is unclear whether additional flow locations can be observed even with this improved noise situation. Using the time separation of 200 μs , 5 times the acquisition time between successive A-scan acquisition, the Doppler flow image is calculated with 50 averages as well using a scale of ± 2 radians. As with the increased statistics case, there are no obvious new flow locations associated with this new analysis method. With this method, the phase wrapping on the fast flows caused a decreased visualization without any demonstrated benefits. It should be

noted that the lines of contrast on the Doppler images are artifacts located on the noise pixels caused by the bulk axial motion removed during the acquisition time at each transverse location.

To work on the phase variance contrast, the phase variance was calculated for time separation of $40 \mu\text{s}$, previously considered to be a good approximation of the SNR-limited phase noise of the image. With the calculation of bulk motion removal but without using any thresholds or numerical phase removal, the phase variance was plotted for the cases of 10 phase changes and 200 phase changes.

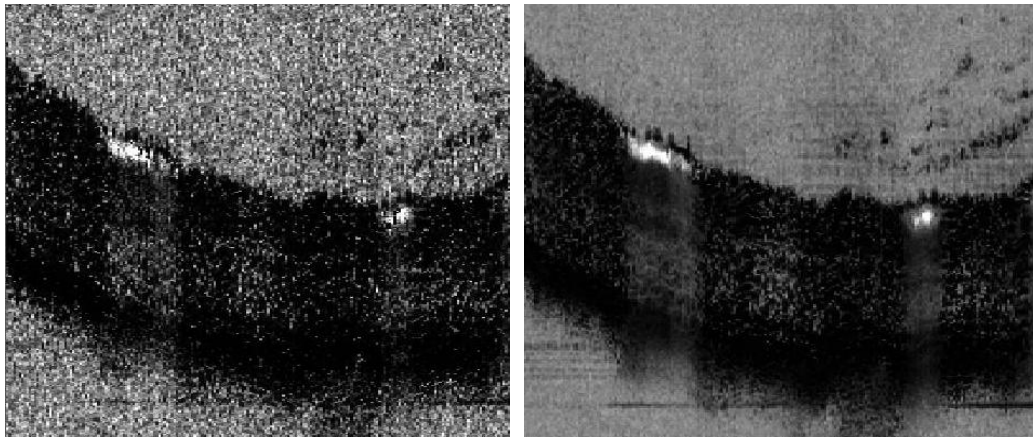


Figure 5.10: MB-scan phase variance images for phase measurements from successive A-scans with a time separation is $40 \mu\text{s}$. The total number of phase changes used for the variance calculation at each transverse location is 10 (left) and 200 (right). The scale on these images is 0 to 6 radians².

One of the major anomalies of these images is the scale used to image the phase variance. The maximum of these images corresponds to 6 radians², twice as large as used for any previously demonstrated phase variance contrast images. Theoretically, a purely random phase would only produce a phase variance of approximately 3.3 radians², suggesting that the large variance contrast observed might be an artifact of the phase analysis procedure for this case. As discussed in Chapter 4.3, an axial motion of approximately π radians with a variance will result in a very large variance calculation while the mean value is miscalculated lower than expected. Further data is required to analyze the phenomena further.

From the phase variance calculations, it is clear that the sequential phase change situation is not properly representative of only the phase error of the image. To calculate the phase variance contrast images using the MB-scan, a numerical estimate identical to the BM-scan contrast method is applied for phase noise removal. Phase variance contrast is plotted for a range in phase change time separations from $40 \mu\text{s}$ to $320 \mu\text{s}$, with each case of time separation larger than $40 \mu\text{s}$ using the same statistics of 40 phase changes to calculate the phase variance. The scale used for all of the contrast images was 0 to 3 radians².

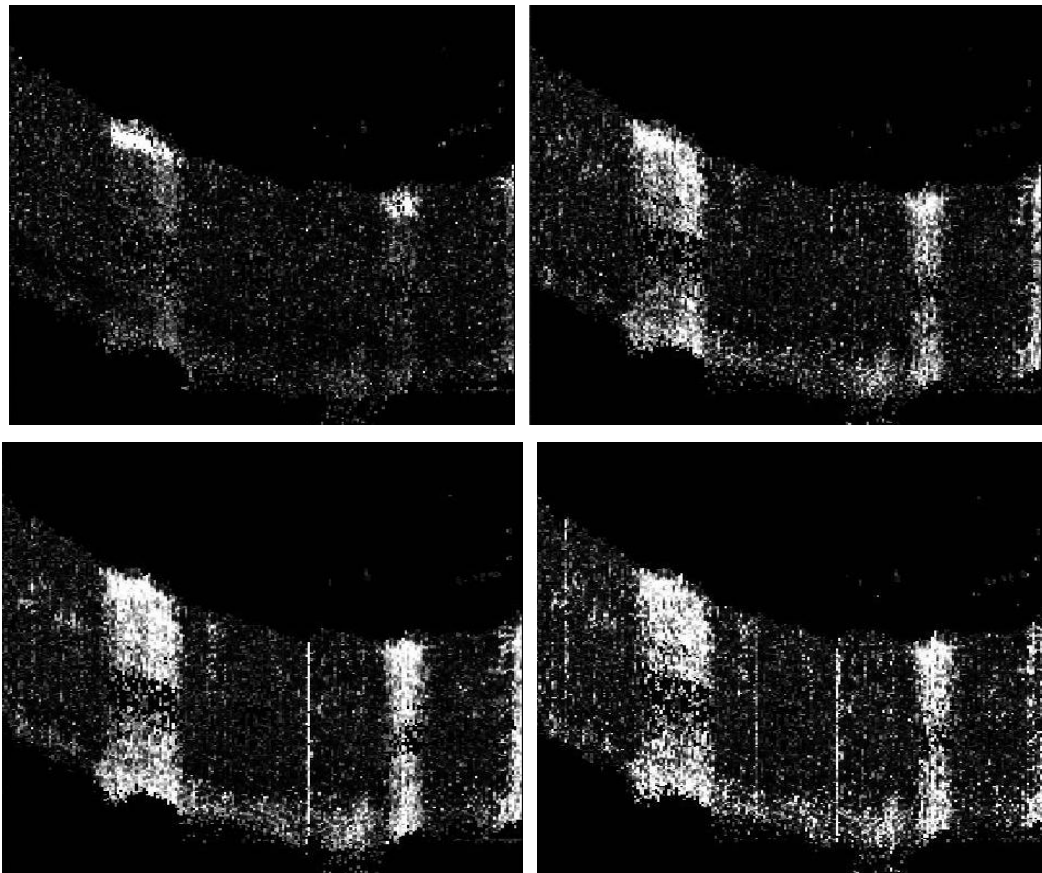


Figure 5.11: MB-scan phase variance contrast for the cases of $40 \mu\text{s}$ time separation with 10 phase changes (upper left) and for $160 \mu\text{s}$ (upper right), $240 \mu\text{s}$ (lower left) and $320 \mu\text{s}$ (lower right) time separation of phase changes using 40 phase changes to calculate variance.

From the demonstrated range of time separations of the phase contrast images, there are many trends that can be observed. With increased time separations comes an increase in the

calculated contrast shadowing below the large flowing vasculature. The shadowing across the entire depth can be observed even at the 160 μs time separation case, which was not observable in the zebrafish tail at time separations as long as 1 ms. The motion contrast observed in the choroidal region of the mouse retina was also observed to increase with time separation of the phase changes. The increased time separation also results in an increased amount of noise within the contrast image. Very narrow vertical lines of contrast appear in the image, which increase in frequency with larger time separations. These anomalous artifacts could be due to transverse motion occurring during the M-scan at a given transverse location and the inability of the bulk motion calculation to remove these effects.

5.4.2 Single Scan Contrast Method

With the demonstrated phase variance contrast at very short time separations, another type of phase contrast acquisition method can be used to efficiently obtain 3D phase contrast information. Phase variance contrast images can be created from a single B-scan sampled very densely along the transverse scan direction [5]. Rather than waiting on a stationary transverse location for each M-scan used within the MB-scan, the measurements of phase over time with this technique are separated spatially by the transverse scanning as well as separated in time. This contrast method will be referred to as the single scan phase contrast method. By planning the scan density such that the transverse scan is much smaller than the transverse resolution of the system, the expected transverse scanning errors described in Chapter 3.3.4 can be minimized.

With the single scan phase contrast method, the short time separation of 40 μs between phase measurements allows for the calculation of the Doppler axial flow as well as the phase contrast. For a B-scan containing 512 A-scans extended over approximately 2 mm for the mouse retina, contrast was determined using the phase from 5 transverse A-scans, all taken successively from each other. The plotted OCT intensity image was taken without any averaging. The Doppler flow was plotted using an image scale of ± 2 radians = ± 2.5 mm/s without any thresholds applied. The magnitude of the Doppler flow was plotted after

numerical removal of the estimated phase error and application of a threshold based on the intensity, with a scale of 0 to 2 radians. The phase variance was plotted without any numerical phase error removal or thresholds on the image. The first phase contrast image plots the phase variance after estimated phase error removal and thresholds applied. The second phase contrast image applies the same technique as well as using a median filter in both directions on the image. The scale used for the variance image is 0 to 3 radians² and for the phase contrast images is 0 to 2 radians². All of the contrast techniques use 5 total phase measurements to calculate the image at a given pixel.

To evaluate the capabilities of the single scan contrast method, the images with this method are compared to the images from the MB-scan data displayed in Figures 5.9, 5.10, and 5.11. The Doppler flow images show comparable flow amplitudes, suggesting that the retinal flow during both data acquisitions is consistent. While similar flow occurs within both situations, there is a discrepancy between the phase variance contrast images acquired for both cases. In the single scan phase contrast case, the phase variance of the flow regions was visible, but not as strong the MB-scan variance images. This discrepancy suggests that the large phase variance calculated in the MB-scan case was created by computational artifacts and phase wrapping of some of the flow data.

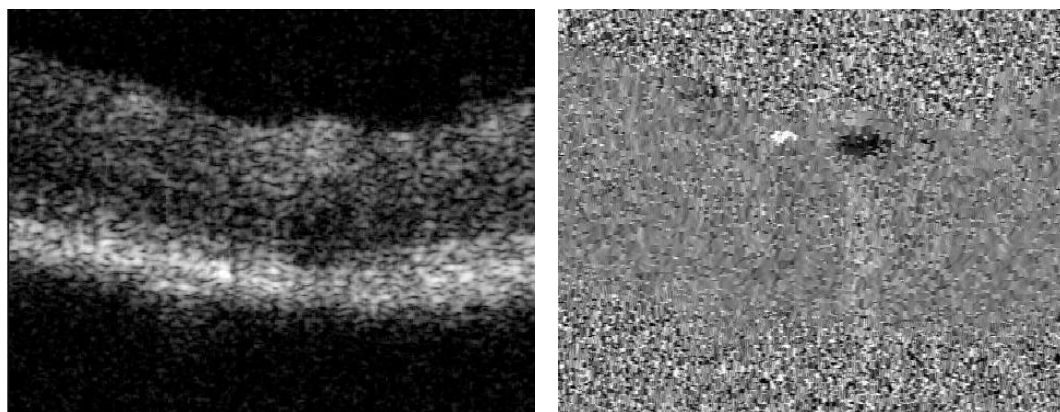


Figure 5.12 a): Single scan intensity image without averaging (left) compared to Doppler flow image over the same region. Doppler image uses 4 phase changes to calculate average flow, and is presented with a scale of ± 2.5 mm/s.

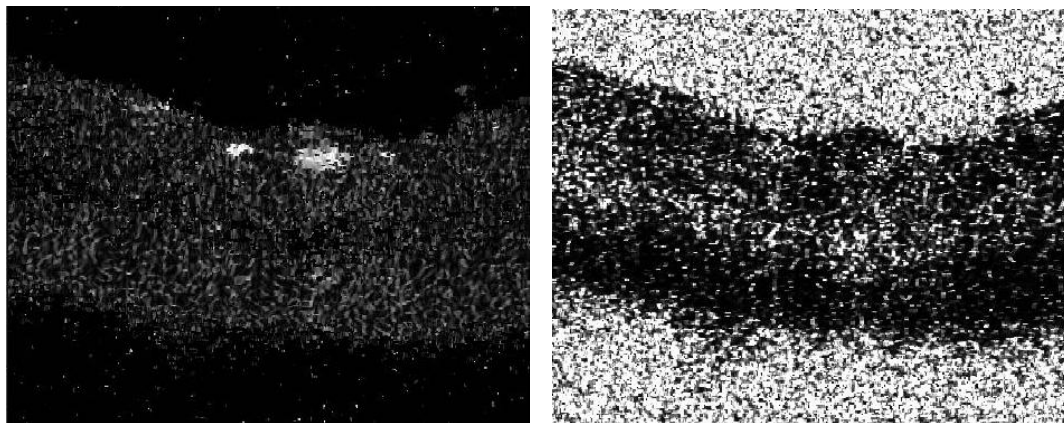


Figure 5.12 b): Magnitude of Doppler flow image with maximum scale of 2.5 mm/s (left), noise corrected using the phase variance noise measurement for the image (right) without any noise compensation or removal. Variance scale is 0 to 3 radians².

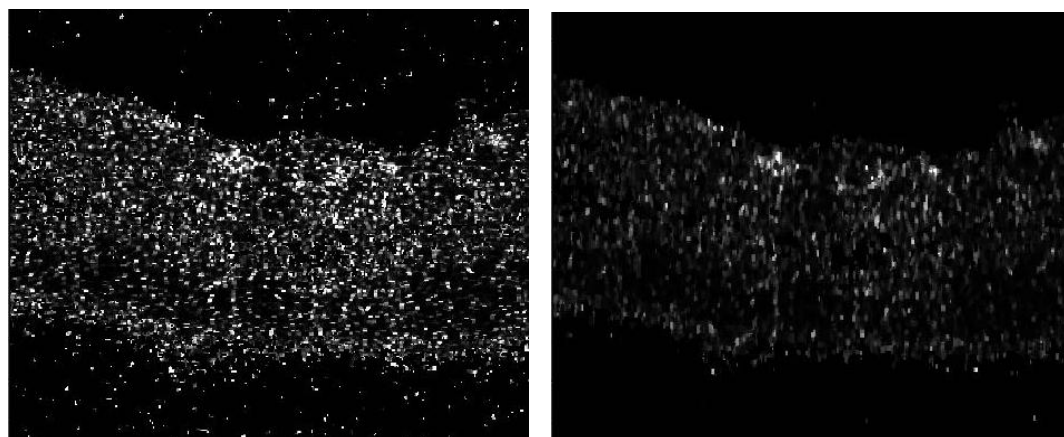


Figure 5.12 c): Phase variance contrast image presented before median filtering (left) and after it has been applied. Variance scale is 0 to 3 radians².

It is possible that the previously demonstrated single scan contrast was affected by the minimal density used in the B-scan. With 512 transverse pixels acquired over 2 mm each pixel separation is approximately 4 μm , resulting in phase contrast being calculated for data acquired over 20 μm transversely. Single scan phase contrast was acquired across 2 mm of retina for 4096 total A-scans, resulting in a transverse spacing between A-scans of approximately 0.5 μm . The phase contrast in this case was calculated over a transverse region of approximately 2.5 μm , much smaller than the expected transverse resolution of the imaging system. Only three images were calculated for this case: the averaged OCT

intensity image, the corrected magnitude of the Doppler flow calculation, and the phase variance contrast image for the region. The scale on the Doppler image was 0 to 1 radian and the phase variance contrast scale was 0 to 1 radians² in this case.

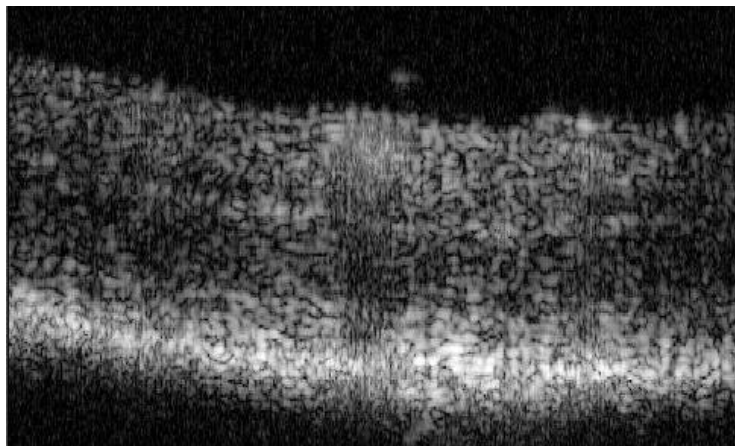


Figure 5.13 a): OCT intensity image from single scan acquisition of 4096 A-scans over approximately 2 mm, averaged over 5 neighbouring A-scans.

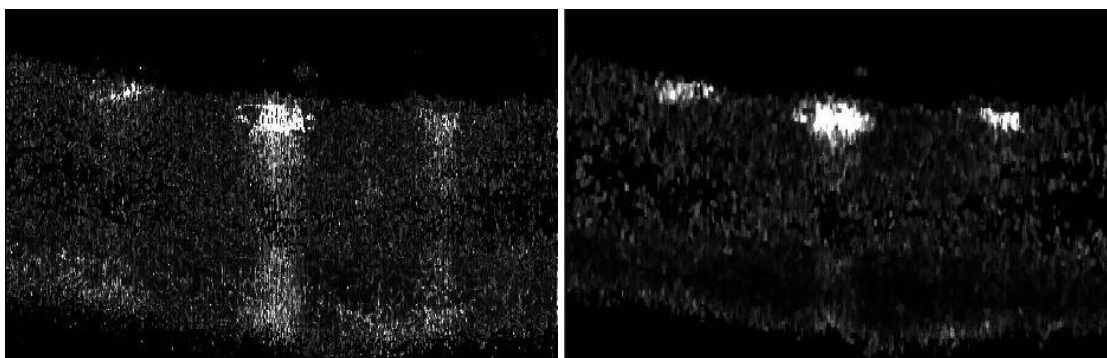


Figure 5.13 b): Single scan contrast images calculated from 4096 A-scans extending over approximately 2 mm. The magnitude of the Doppler image (left) and the phase variance contrast image (right) used numerical phase error removal and thresholds based on intensity. The image scales were 0 to 1 radian (left) and 0 to 1 radians² (right).

The averaged intensity image demonstrates some of the blurring below the flow regions within the image, but due to limited statistics the blurring is less substantial than the MB-scan image which uses 200 A-scans to perform the averaging. The motion contrast observed in this case appears different than the previous two demonstrated contrast

acquisitions. Two of the three flow regions which can be barely identified using the Doppler image can be clearly observed using the phase variance contrast method.

While the different forms of flow contrast observed for the retinal vessels can be investigated further, it is important to note that, for the short time separation contrast in the MB-scan and the single scan contrast method, there was no substantial motion contrast observed within the choroidal region of the retina. The goal of the contrast methods is the ability to visualize the earliest stages of choroidal neovascularization (CNV) in the human eye. If the choroidal vessels cannot be visualized, it is hard to argue that new vasculature growing from these methods will be able to be visualized.

5.4.3 BM-Scan

The BM-scan is used to image the mouse retina with the same parameters used for the majority of the zebrafish imaging: 200 transverse pixels, 5 B-scans per BM-scan and time between phase measurements $T = 10\text{ms}$. With a total of 1 GB of system memory and the chosen BM-scan parameters, a maximum of 51 BM-scans are acquired within one full buffered acquisition.

A BM-scan taken of the mouse retina over a section of the optic nerve head is presented with the averaged OCT intensity image. The phase variance was imaged using only a threshold based on the OCT intensity to remove the noise terms, demonstrating the requirement of not only the SNR-limited phase noise removal but the necessity of the median filtering on all of the contrast images. MB-scan phase variance contrast observed the appearance of non-negligible artifacts in the phase contrast image for time separations as short as $320\ \mu\text{s}$, much smaller than the 10 ms time separation of the BM-scan. The application of the median filtering into the phase contrast imaging analysis allows much clearer visualization of the flow regions within the image.

One very important note is that the BM-scan clearly observed motion contrast for the retinal vessels as well as motion located within the choroidal region of the retina. The only observation so far of the choroidal motion was using the MB-scan phase contrast images

for increasing time separation in Figure 5.11. Even in this case, the visualization was not as strong as with the BM-scan phase contrast image.

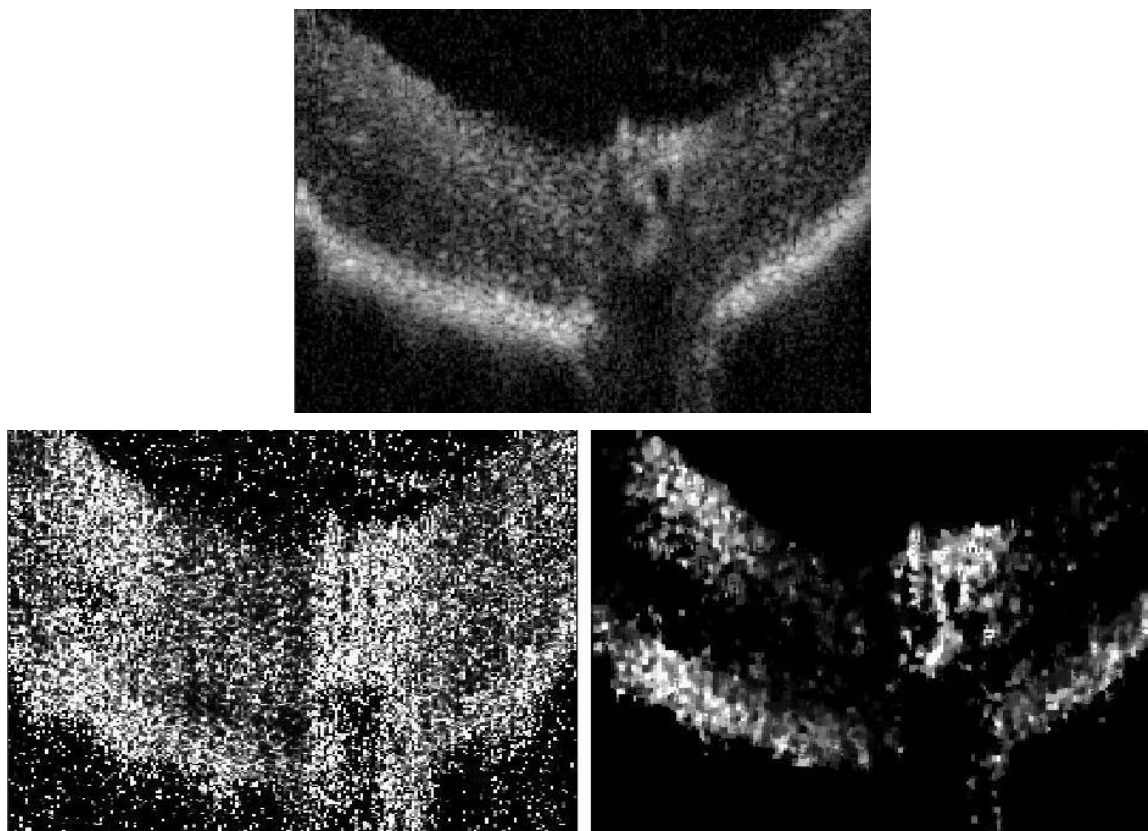


Figure 5.14: BM-scan images for mouse retina, including the averaged intensity image (top), the phase variance image (left) and the phase variance contrast image (right), which uses noise removal and median filtering. The variance images use the scale 0 to 3 radians².

5.4.4 Transverse Motion of Eye

For many stages of the retinal imaging, it was clear that the mouse was twitching during the imaging session. The impact to not only the alignment of the 3D data set, but also to the individual 2D phase contrast images needed to be determined. To demonstrate the alignment changes over time with the transverse motion, en face summation images were created by summing the linear form of the 3D OCT intensity data over the entire retina. OCT intensity data is presented in logarithmic form to improve the structural visualization of the image over the dynamic range of the reflections. By summing the linear form of the

intensity to create the en face image, the maximum reflection within the transverse location will dominate the resulting image. The en face image produced using this method is virtually identical to the image created by a scanning laser ophthalmoscope (SLO) discussed in Chapter 1.3.7.

The en face intensity images show the non-trivial transverse motion occurring during the 2.6s of image acquisition time. The motion observed within the image appears to be oscillatory in nature. With approximately nine oscillations in 2.6 s, this motion is at a frequency of ~ 3.5 Hz, very close to the expected heart rate of the mouse under anesthetic. If the oscillatory transverse motion creates motion artifacts within the phase contrast images, the en face contrast summation images will contain horizontal contrast lines which oscillate in intensity based on the effect of the transverse motion.

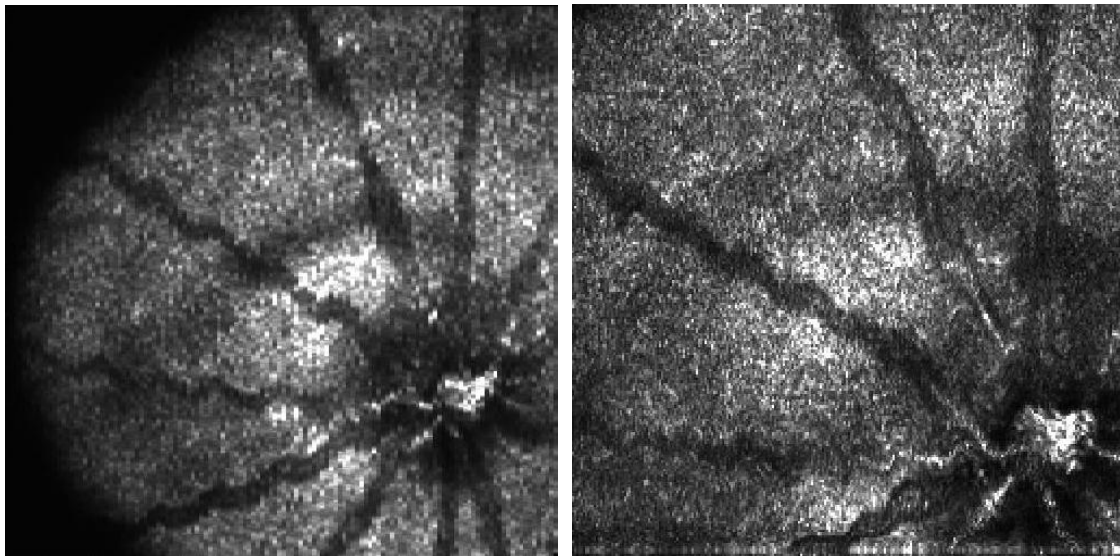


Figure 5.15: En face intensity summation images from two different acquisitions of 512 x 128 pixels (left) and 200 x 200 (right) over the mouse retina. Both images demonstrate the twitching in the mouse eye position over the 2.6 s acquisition time of images.

First, look at a 3D data set composed of single scan phase contrast images. With the short total time used for phase variance contrast (200 μ s), this method should not be affected much by the observed transverse motion. For a 1 GB memory buffer, 512 x 128 transverse locations can be acquired with this contrast method. Using the phase variance contrast data

to create the summation images, two different en face images were calculated. The first image summed the phase variance contrast over the entire depth of the retina, while the second image only summed the contrast terms which were greater than 2 radians^2 , trying to remove the effect of static terms which may have additional phase noise caused by the transverse motion scanning during the contrast calculation data. While the en face phase variance contrast images show the same expected oscillations in the vessel locations, there does not appear to be any major contrast variations caused by the transverse motion.

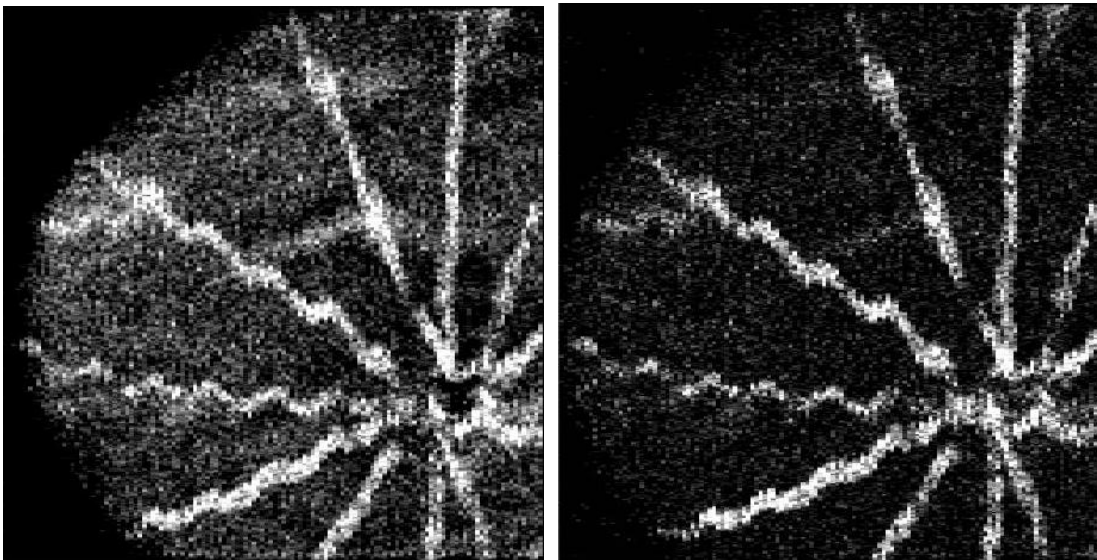


Figure 5.16: En face summation contrast images of phase variance contrast calculated using single scan contrast methods. The summations are performed over the full depth of the retina for the cases of all contrast data (left) and for only contrast data points $> 2 \text{ radians}^2$ (right). Image size is approximately $2 \text{ mm} \times 2 \text{ mm}$.

BM-scans are expected to be much more susceptible to artifacts caused by transverse motion because of the increased phase contrast time per pixel (50 ms) in this case. To observe the effect of the oscillatory motion on the summation contrast image, a buffered acquisition of BM-scans was taken over the same transverse scan location over time. The scan location was chosen to have several blood vessels for motion contrast as well as large regions of static retinal tissue, ideal to demonstrate the effect of this transverse motion on the motion contrast. There is a wide range of transverse motion measured within this data

set. The averaged OCT intensity image from a low noise BM-scan is compared to the phase variance contrast image for a high noise BM-case caused by transverse motion.

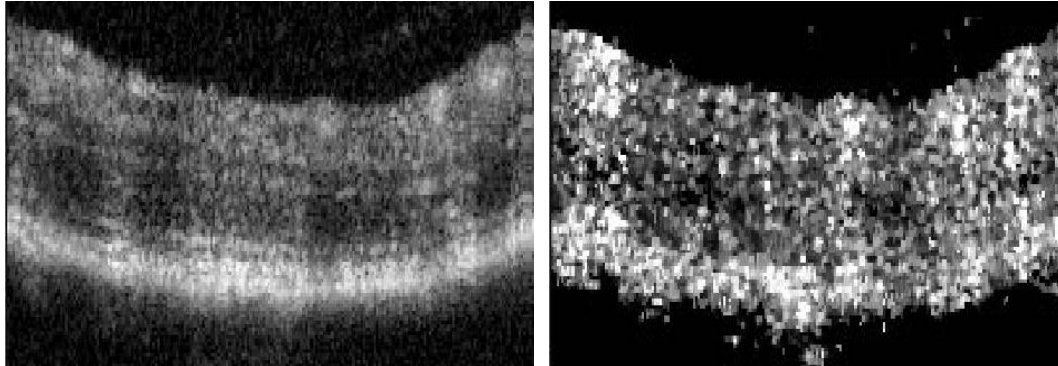


Figure 5.17: BM-scan data for retina undergoing transverse motion. The averaged intensity image (left) is calculated for a time point undergoing low transverse motion. The phase contrast image, after noise removal and median filtering, is taken from a time point experiencing large transverse motion.

The main approach to deal with this additional motion noise is to treat it as another noise source that needs to be removed. It is likely that this noise depends not only on the magnitude of the transverse motion, but on the properties of all the reflections in the sample, correlated and uncorrelated. In most cases, there is no ability to have a previous knowledge of the sample properties so a general method relies on the statistics of all the non-zero contrast pixels within the image. Any contrast pixel which is zero has had a threshold applied to it or has the entire phase error numerically removed. The remaining pixels are the data which was subject to the transverse motion, which is assumed to be experienced uniformly across the entire image. The mean μ and the standard deviation σ of the non-zero contrast pixels help to determine the contrast amount to be removed.

Using a numerical factor α , the contrast based on the statistics $\mu + \alpha\sigma$ is removed from the phase variance contrast image $C(x,z)$. Without additional processing, this method negatively affects the contrast regions which have achieved maximum phase variance contrast. With the limit imposed on phase changes of $\pm \pi$, the maximum phase variance for a random distribution is 3.3 radians^2 . Renormalizing the contrast data after removing the numerical factor gives us the adjusted contrast:

$$(C(x,z) - (\mu + \alpha\sigma)) \left(\frac{3.3}{3.3 - (\mu + \alpha\sigma)} \right) = C'(x,z) \quad (5.1)$$

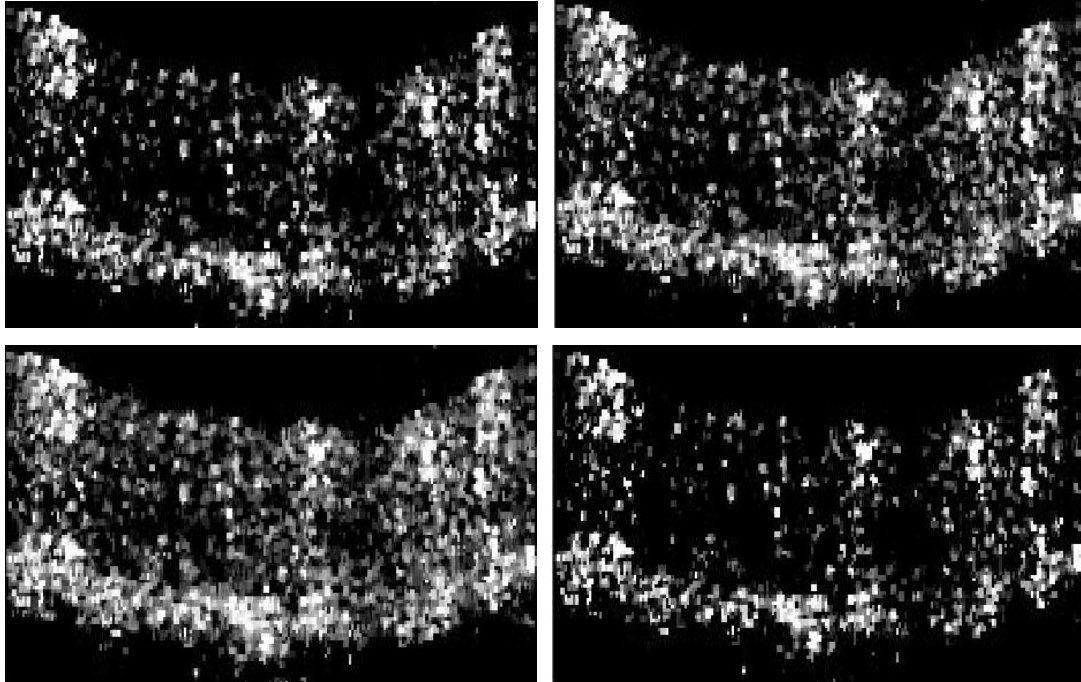


Figure 5.18: Additional noise removal method applied to the phase contrast image of Figure 5.17. The corrected contrast images are presented for the cases of $\alpha=0$ (upper left), $\alpha=-1$ (upper right), $\alpha=-2$ (lower left), and $\alpha=1$ (lower right).

The only factor left to determine is the numerical factor α , which determines how strong the contrast removal is. Altering α between -2 and 2, the decision of the optimal term to use is not well defined. With α too high too much contrast information is removed, but if α is too low then there is no apparent change. After comparing the contrast subtraction images, the case of $\alpha = 0$ was chosen for use in the contrast images.

The first comparison for this technique is between the non-corrected phase contrast image for a low transverse motion noise BM-scan and the corrected phase contrast image for a large transverse motion BM-scan. The low transverse motion noise BM-scan chosen was the same data used to create the OCT intensity image for Figure 5.17. The vessel

visualization is definitely improved compared to the non-corrected case, but there is room for improvement on this analysis method.

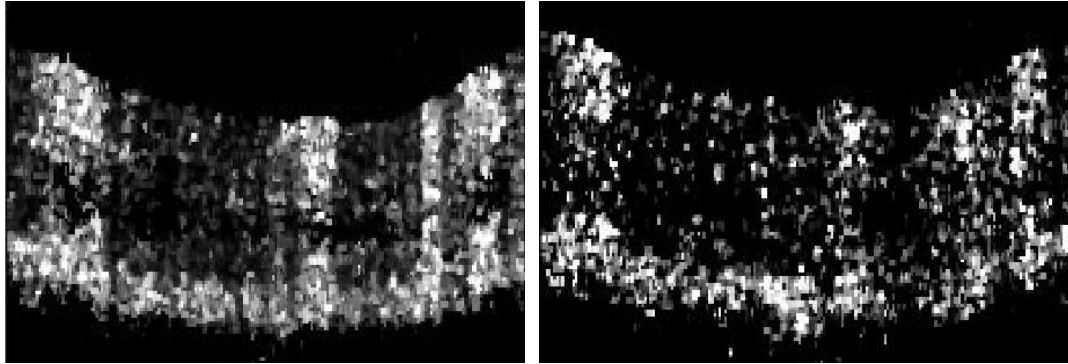


Figure 5.19: Comparison of phase contrast images between an uncorrected small transverse motion case (left) and a corrected large transverse motion case (right) with $\alpha = 0$ chosen.

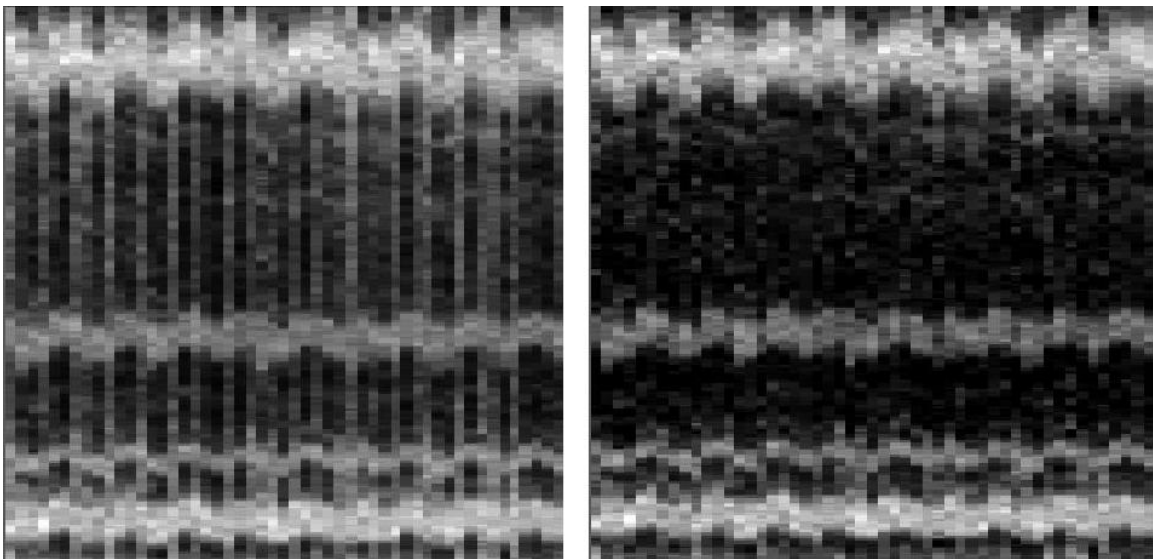


Figure 5.20: Contrast summation image over time summed over the full retinal depth, acquired over 2.6s. Images presented are before (left) and after (right) the additional motion compensation for the $\alpha = 0$ case.

Using the $\alpha = 0$ case on the en face phase contrast summation images, the improvement using this method is very obvious. The non-corrected data en face image contains vertical lines corresponding to the additional contrast motion added to the BM-scan phase variance by the transverse motion of the system, which appears to correspond to the oscillating

motion of the system. The corrected image does not appear to have any of these contrast artifacts while still experiencing the same spatial oscillations of motion due to the transverse motion.

There are limitations to using this approach to remove all of the effects of the additional transverse motion. This method makes the assumption of a primarily stationary sample. There are retinal cases in which the majority of the non-zero contrast in the image is composed of retinal flow and shadowing artifacts caused by the flow, causing this method to miscalculate the proper noise removal.

Using BM-scans acquired transversely over the retina, the transverse noise removal method is applied and the 200 x 51 transverse pixel contrast summation image was calculated. To put the contrast image into context, a 200 x 200 reflectance image created from a different buffered acquisition over the same transverse region is plotted. In this case, the noise removal technique does not remove all of the motion noise, but it is reduced for most of the BM-scans. To further improve the image quality of the contrast images, it is important to deal with the transverse motion with more than just software analysis.

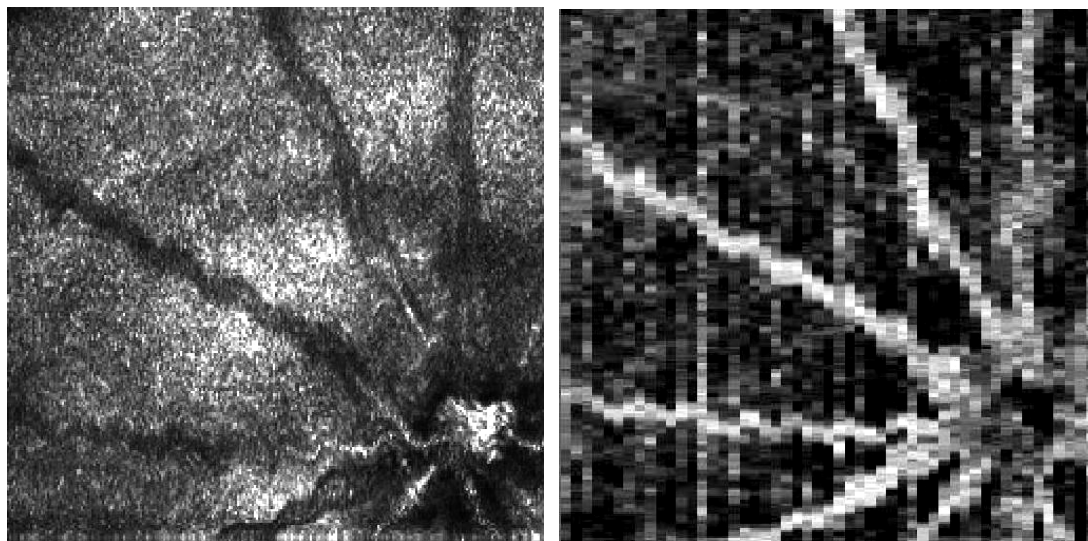


Figure 5.21: En face intensity and phase variance contrast images calculated using BM-scans and the additional noise removal method. The 200 x 200 pixel intensity image was acquired in a different buffered acquisition than the data used to calculate the 200 x 51 contrast image, but both acquisitions occurred over the same transverse scan region.

The source of the twitching of the mice was discovered to be dependant on several factors, the most important being the dosage of the anesthetic used. If the dosage was too low, the mouse would not be fully paralyzed and motion would occur over time. If the dosage was too high, there would be twitching associated with the heart beat, or due to laboured breathing. The motion due to laboured breathing also occurs when the restraints on the mouse are too tight and the airway is constricted. The ideal drug dosage of the ketamine/xylazine solution described earlier was 0.5 mL–0.6 mL for the animals used in this experiment. The animals were stable during the imaging session and also took longer to wake up afterwards. The anesthetic dosage required for each individual mouse can vary between animals, depending on several factors including the size of the animal. To properly determine the ideal dosage for future imaging sessions, a dosage response test should be performed on each animal.

5.5 En face Motion Contrast Images

With proper anesthetic dosages, the mice remained much more stationary during the data acquisition of the system. For this situation, all of the phase contrast techniques capable of 3D contrast data are reacquired to try and determine the detection limits when transverse motion is not a major concern. The first 3D phase contrast technique to re-analyze is the single scan contrast method, using 128 B-scans containing 512 A-scans each. The en face images created from the intensity, phase variance, and Doppler magnitude data use the same method as described previously. The phase variance contrast and the Doppler magnitude summation images do not have any thresholds applied before summation in this case. The Doppler shift image sums the average phase change over the entire depth of the retina. In order to avoid conflicts with the bulk motion removal algorithm, only data which has a magnitude greater than 1 radian was used within this image.

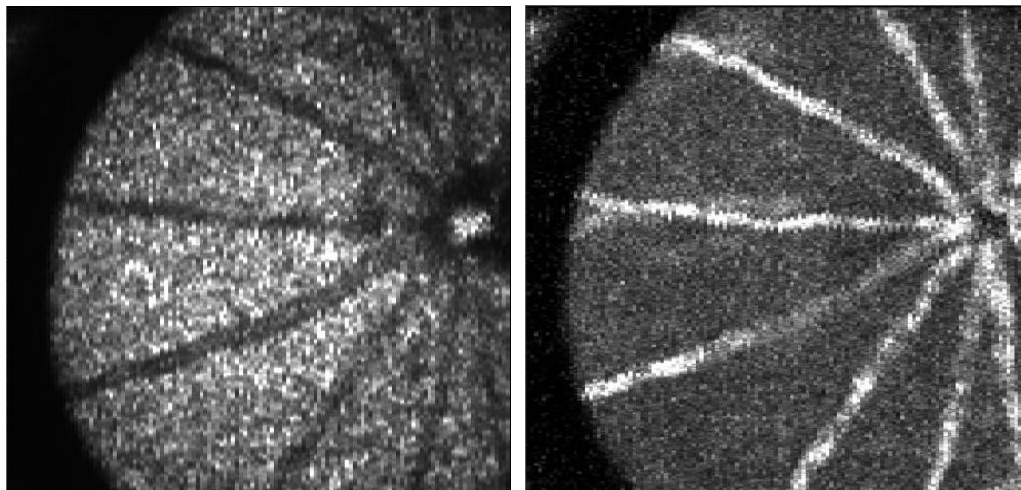


Figure 5.22 a): En face images created using 128 B-scans, each containing 512 A-scans. The intensity image (left) and the phase variance contrast image (right) sum the respective images over the entire depth of the retina.

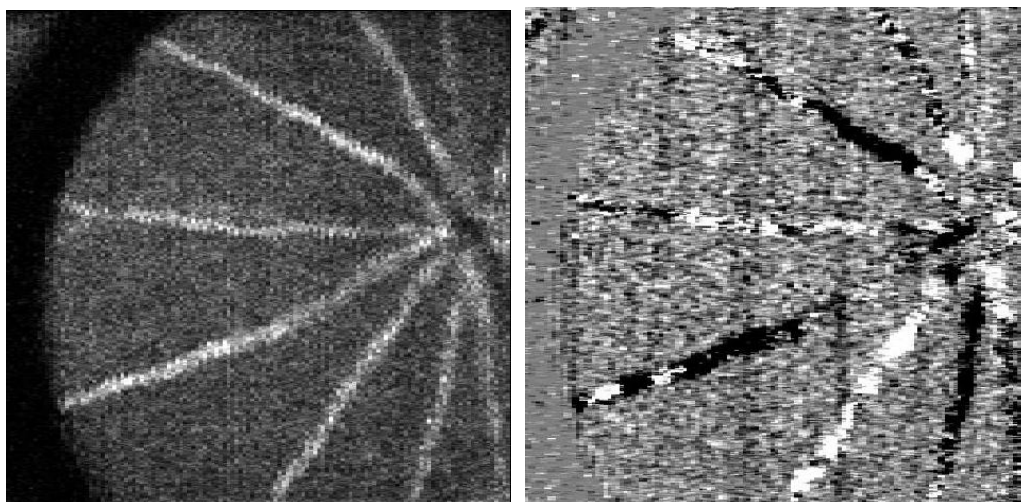


Figure 5.22 b): En face images created using 128 B-scans, each containing 512 A-scans. The Doppler magnitude image (left) sums all of the noise corrected data over the entire depth of the retina. The Doppler shift image (lower right) only sums axial flow components with a magnitude larger than 1 radian over the depth of the retina.

The conclusion for the single scan phase contrast method appears to be the same as before; the contrast analysis methods demonstrated can easily visualize the major retinal vessels with fast flow. Smaller, slower vessels and choroidal vessels do not appear to have much visualization in this method.

For the BM-scan contrast data, the intensity and phase contrast summation images were used from the same data set containing 200 x 51 transverse pixels over the retina. Although there was no obvious transverse motion occurring during the data acquisition, the phase contrast image appears to have a few locations of additional noise at random time points. The additional noise removal method was used to reduce the effect of this noise within the contrast image. Both summation images were calculated through the depth summation over the entire retina.

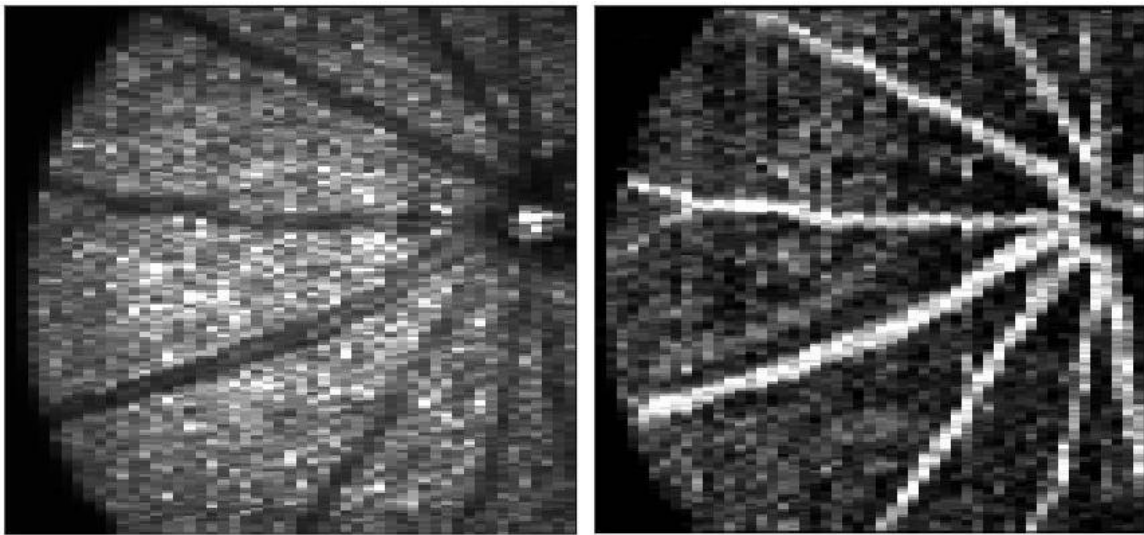


Figure 5.23: BM-scan en face intensity and phase contrast images summed over the entire retina.

To improve visualization of the smaller retinal vessels, the simplest method is to not include the choroidal vessels in the depth summation image. The problem lies in the fact that the retina is a curved surface and any chosen depth region within the retina will encounter different layers at different transverse locations. To properly isolate retinal layers of interest, the retinal image needs to be flattened.

In an ideal case, the boundaries of the retina could be automatically identified and the retina could be flattened without any assistance. Another alignment method uses cross-correlation techniques to line up successive A-scans to each other. Each aligned B-scan can be aligned to each other to flatten the entire 3D data set. Some problems arise when encountering

transverse locations with blood vessels, where the RPE and choroidal reflections can be reduced but reflection off the top of the retina is much higher than normal. Cross-correlation work can misalign the RPE of one A-scan to the top of the retina on the next A-scan. Highly absorptive regions lacking retinal layers such as the optic nerve head also provide some problems on the automatic alignment techniques. With no high-accuracy requirement of the flattening, a manual alignment of the retina was performed, accurate enough to be able to separate the contrast from the top of the retina from the choroidal motion contrast.

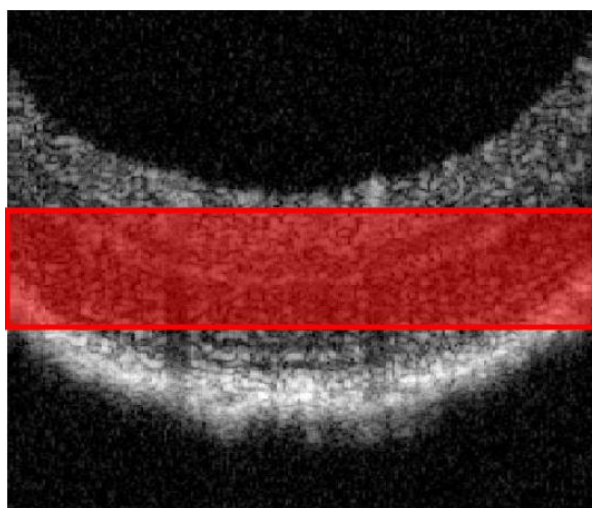


Figure 5.24: Schematic of a summation region chosen for an en face depth summation image over a curved retinal image.

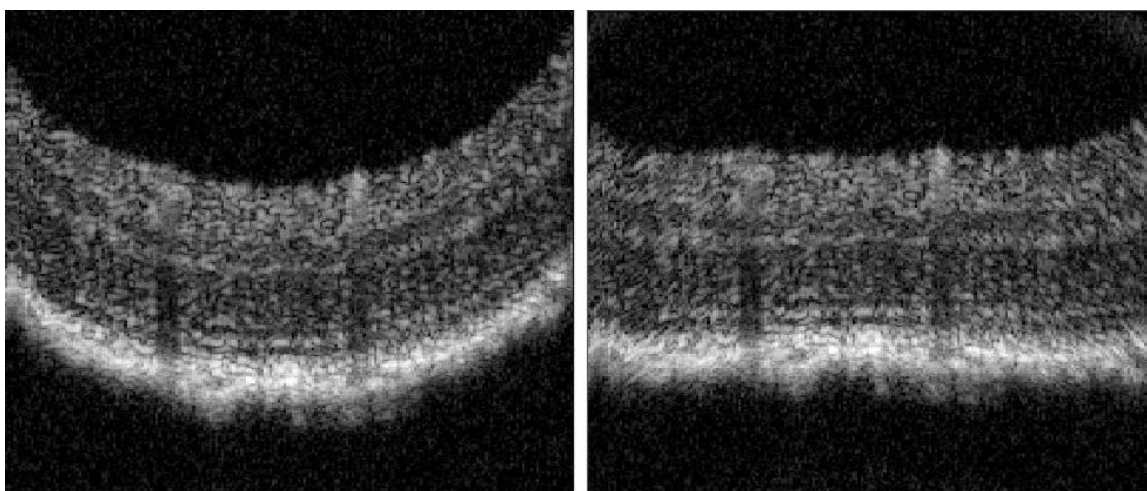


Figure 5.25: Averaged B-scan intensity image before and after realignment to flatten retina.

To observe where the motion contrast exists within the mouse retina, an overlay contrast image is produced for a flattened retinal image. While the side-by-side comparison of the averaged OCT intensity image and the phase variance contrast image provides valuable insight, combining these two images can allow for more visualization. For this demonstration, every phase variance contrast pixel with a value greater than 1 radians² will completely remove the OCT signal in the overlay image. The phase contrast image has a scale of 0 to 3 radians².

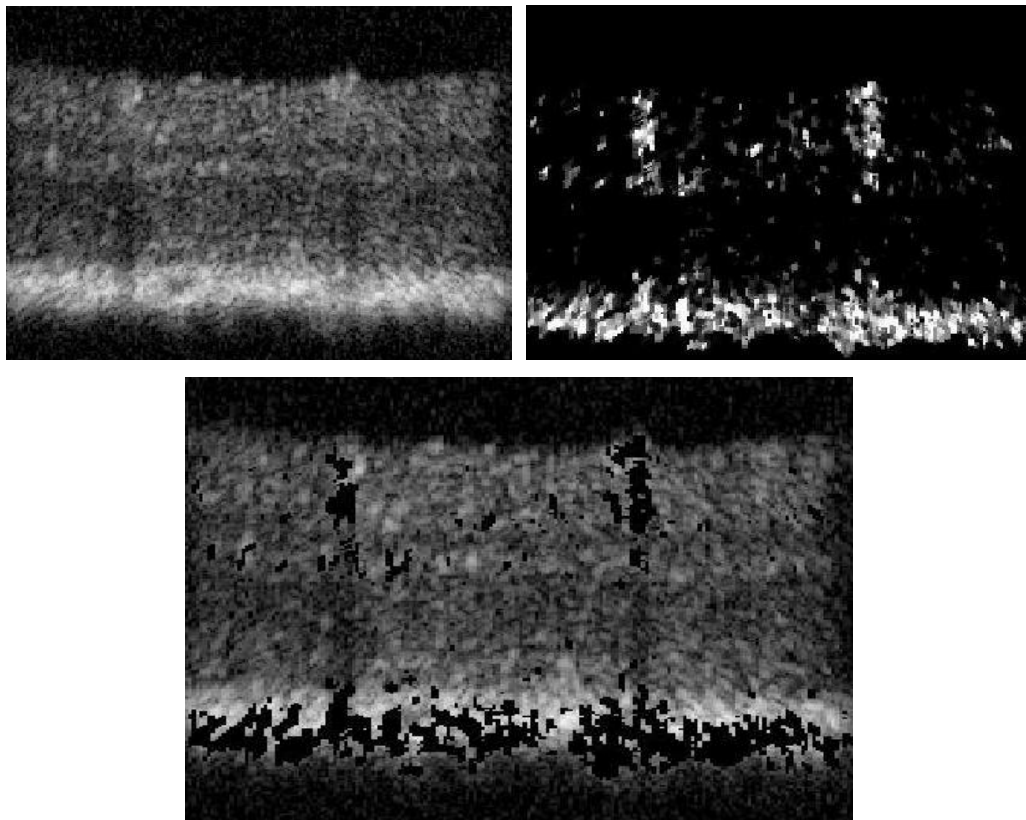


Figure 5.26: Averaged intensity image (upper left) and the phase contrast image (upper right) from a BM-scan after retinal flattening. An overlay of the phase contrast and the intensity images (bottom) was created by removing all signal from the intensity image where the phase variance contrast was greater than 1 radians².

The larger retinal vessels with the shadowing of contrast are observed in the retina as well as some smaller regions of contrast which might be associated with smaller retinal vessels. More information is required to determine whether they are true motion or just artifacts.

While it is not possible to separate out the choroid and RPE regions on the intensity image for the mouse retina in this system, the relatively static regions of the RPE can be observed above the motion of the choroidal vessels in the overlay image.

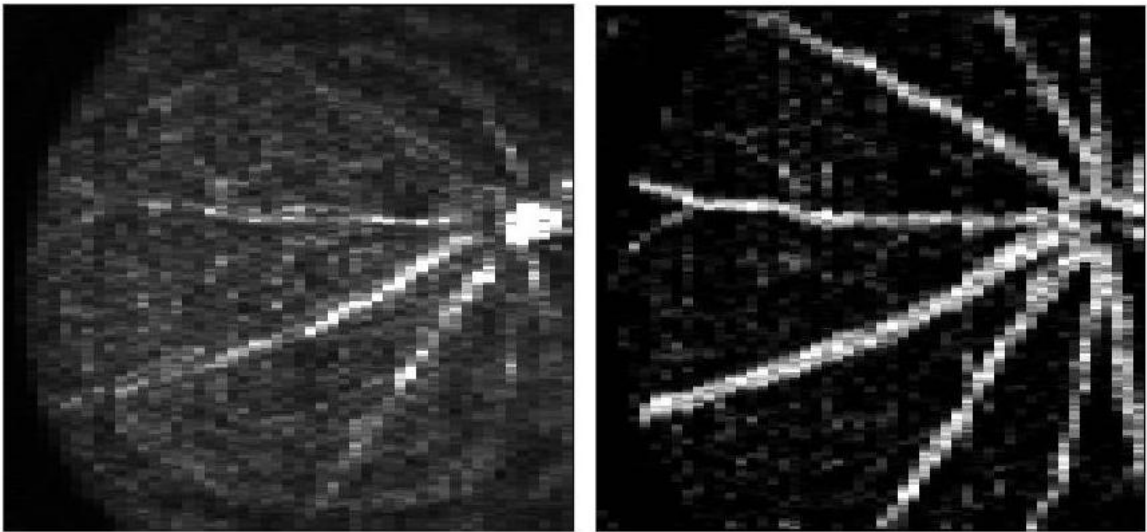


Figure 5.27: En face summation images of the intensity (left) and the phase variance contrast (right), with summation chosen to be over only the top half of the retina.

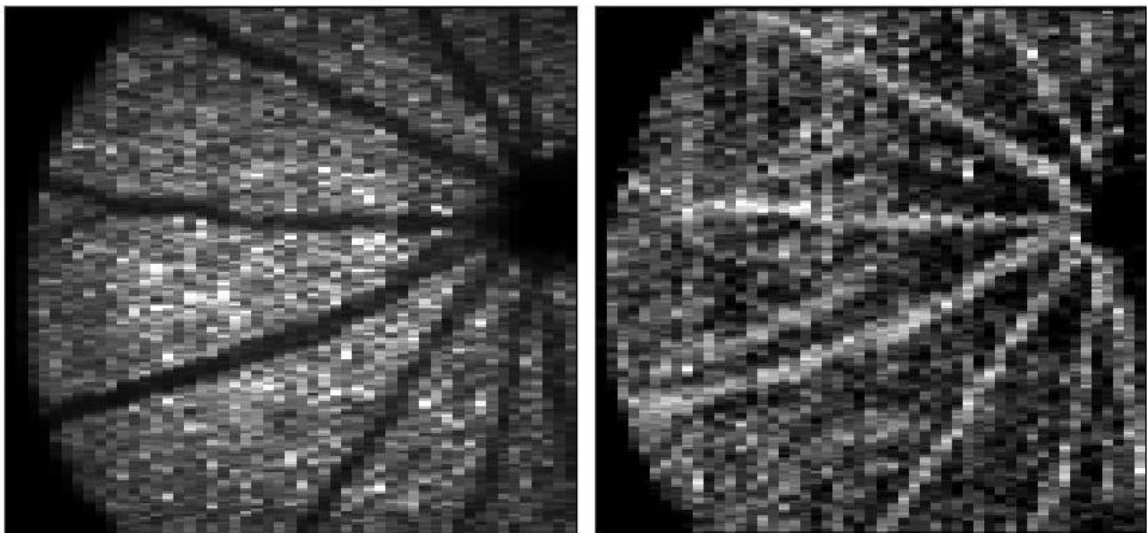


Figure 5.28: En face depth summation images of the intensity (left) and the phase variance contrast (right), summed over the bottom half (choroidal region) of the retina.

En face summation images were created using the flattened retinal data to create intensity and phase contrast images for the top half of the retina as well as images for the choroidal regions of the retina. With the RPE reflection removed, the primary reflection observed for the top half of the retinal intensity image comes from the top of the blood vessels near the optic nerve head. The choroidal region intensity image observes the expected RPE reflection overlapped with the blood absorption of the major retinal blood vessels in the eye.

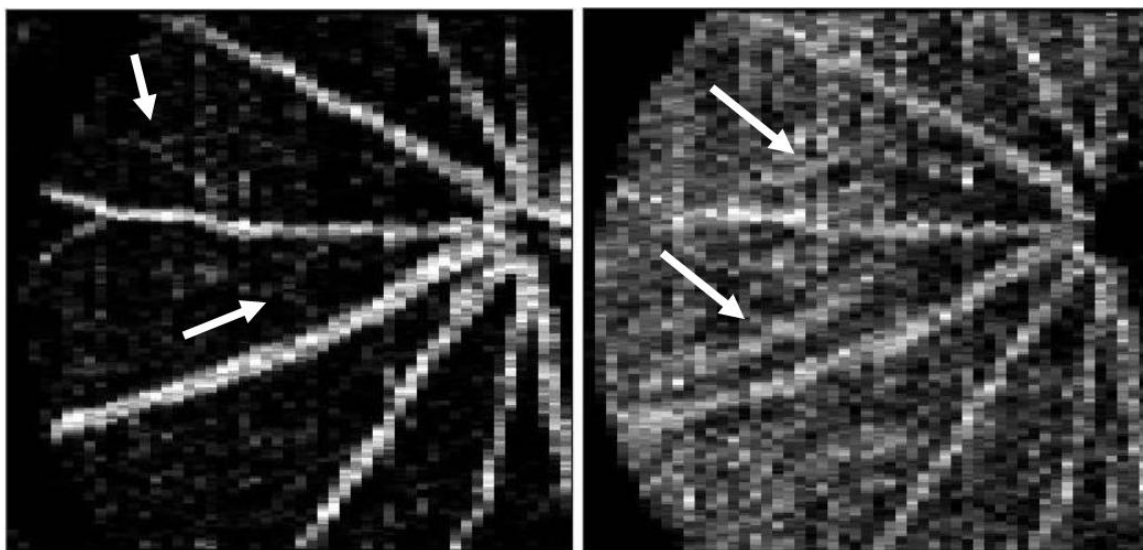


Figure 5.29: Comparison of en face phase variance contrast images with different summation regions of the same data. The contrast images correspond to the surface retinal vessels (left) and the choroidal vessels (right) as well as the shadowing contrast of the major retinal vessels. Arrows correspond to locations of identified blood vessels not present in the comparison image.

The separation of the en face phase variance contrast images for the different depths allows visualization of vessels that may not have been identified with the full depth summation. The summation image over the top of the retina observes small vasculature connected to the major retinal vessels which were not visible in the full summation image. The choroidal region contrast image contains a portion of the shadowed motion contrast due to the major retinal vessels above those locations, but there are several vessels that can be identified in addition which are located only within the choroidal region. These are major choroidal vessels located within the mouse eye. With the identification of choroidal vessels and tiny

vasculature, there appears to be potential for the BM-scan to be used to detect CNV in retinal imaging situations. There is still room for improvement for this data acquisition method to be able to improve the visualization of the tiniest vessels in the eye.

Fluorescein angiography is the gold standard of visualizing vasculature in the retina. The expected vasculature in the mouse retina using this technique is much more substantial than visualized with the retinal phase contrast summation image of Figure 5.29 [6,7]. If we assume that the smallest retinal vessels observed act like the segmental vessels of the zebrafish, blood passes through them only a fraction of the total time. Fluorescein angiography utilizes a CCD camera to take the picture of the fluorescence over the integration time, resulting in a measure of the average blood over the integration time for the fundus of the eye. Thinner blood vessels containing blood only a fraction of the time will appear much less bright in the angiography image than the major blood vessels which saturate the image, which is the case for the demonstrated image. With an understanding of the smallest vessels, the OCT phase contrast images can be improved to obtain the same visualization.

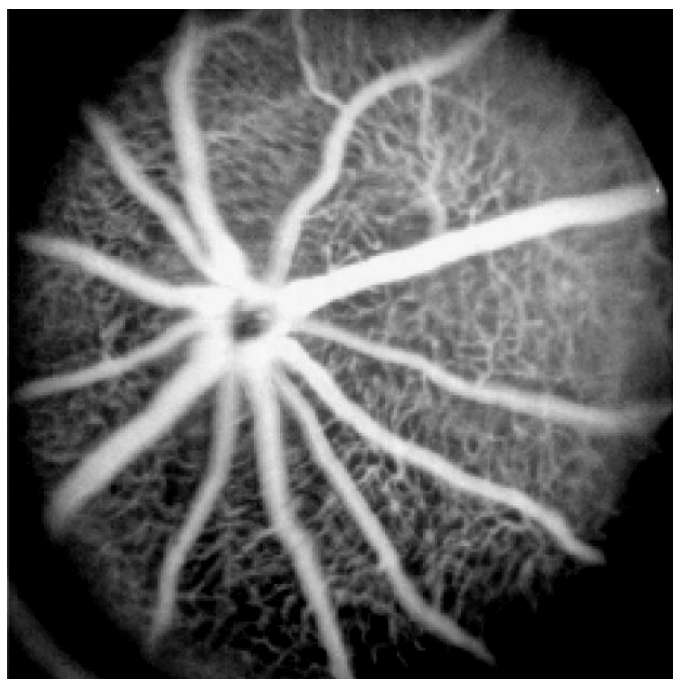


Figure 5.30: Fluorescein angiography image of mouse retina. Image reproduced from [7].

5.6 Improving BM-scan Capabilities

With the assumption that the smallest vessels in the eye act like the segmental vessels in the zebrafish, there is a limit to the vascular visualization that can occur in a single contrast image. If the blood is not located within the vessel when the image is taken, there is no contrast to be obtained. Statistically, for any given phase contrast image acquired for the retina, there will be regions of vasculature which do not contain any blood or motion contrast at all. This is not a problem with the increase of statistics; with multiple images taken over the same location, the chances of imaging a region when blood is present increases. To reduce the alignment requirements for multiple contrast images taken over several buffered acquisitions, the BM-scan is optimized by maximizing the statistics for the memory buffer of the system through repeating the contrast measurements within one buffered acquisition.

With an improvement to the acquisition computer memory to 2 GB, the maximum buffered acquisition is approximately 512 x 256 total A-scans. The optimized BM-scan parameters use a 100 transverse pixel B-scan with an x-scan duty cycle of approximately 80%, 5 B-scans for each BM-scan, 50 transverse pixels in the y-scan direction and repeated 4 times. The y-scan duty cycle in this case is approximately 98%. The resulting acquisition is a BM-scan phase contrast transverse scan region of 100 x 50 pixels, repeated 4 times. The time between phase measurements for the BM-scan in this case is 5 ms and the time between each of the 3D BM-scan data sets is 1.3 s.

With smaller transverse pixel numbers for the BM-scan and faster fly-back speeds required of the scanners, a smaller image scan range is required. For the 100 transverse pixel BM-scan, the scan range in each direction was chosen to be less than 1 mm. The exact size of the image depends on the optical alignment of the system at the time of the data acquisition. In order to compare the results of the repeated 100 transverse pixel BM-scan to previous techniques, the previously defined 200 transverse pixel BM-scan was used to image over the same transverse scan region extending over less than 1 mm for each scan direction.

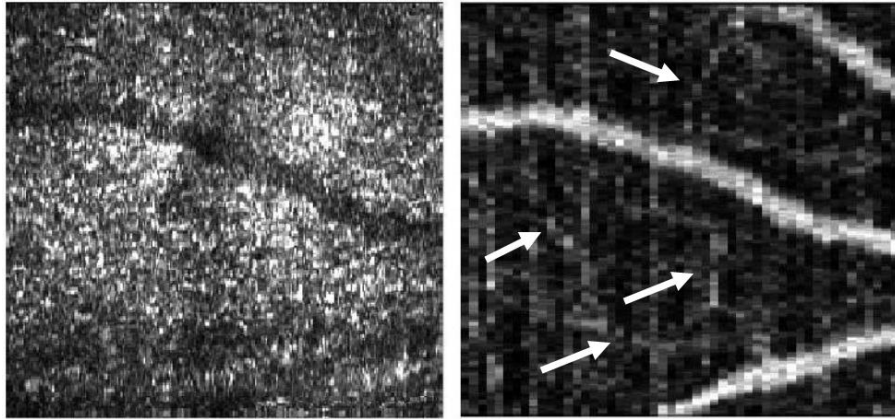


Figure 5.31: BM-scan en face summation images of intensity (left) and phase variance contrast (right). The intensity image was summed over the entire retina, while the contrast image was summed over the top half of the retina for the 200 transverse pixel BM-scan data across retina. Arrows identify some of the smaller visible blood vessels.

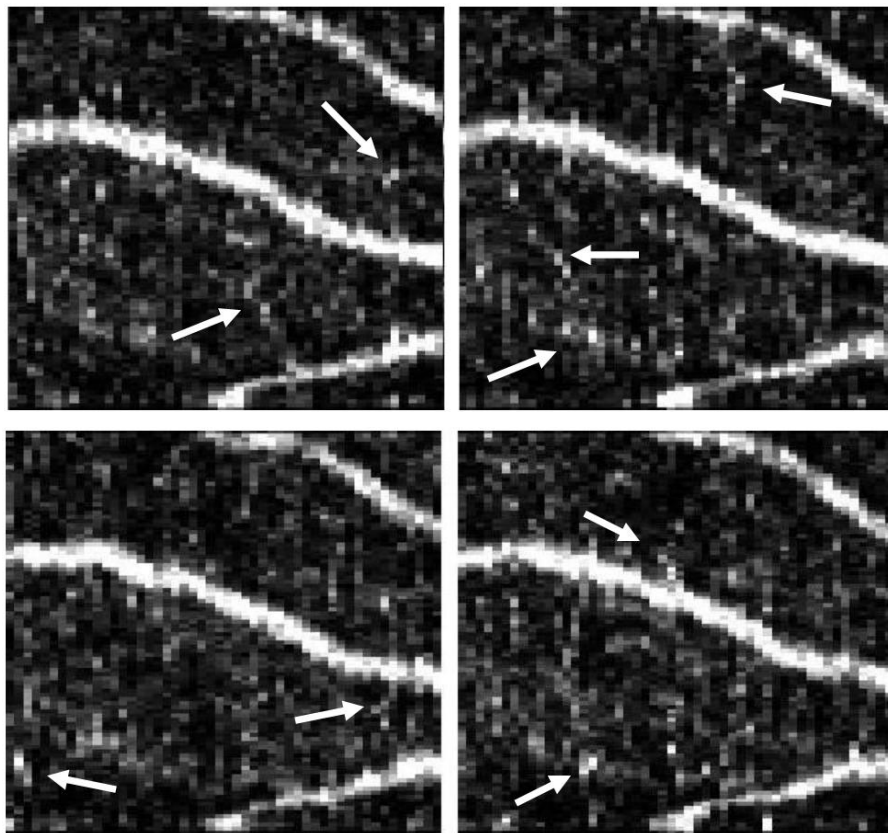


Figure 5.32: En face phase contrast summation images created from the top of the retinal data acquired from the repeating 100 transverse pixel BM-scan method. Arrows identify vascular events not visualized within all four contrast images. Transverse scan region of image is identical to Figure 5.31.

The BM-scan data acquired in both the 200 transverse pixel case and the repeating 100 transverse pixel case can visualize the smaller retinal vessels of interest. Within the five different contrast images, there were different regions of the vasculature that were able to be identified as expected for randomized flow within the vessels. To combine the visualization capabilities of the individual contrast images, the four 100 transverse pixel BM-scan contrast images were averaged without any transverse realignment. To improve the contrast of the image, the data was gamma corrected using $\gamma = 0.85$. For an intensity image $I(x,y)$ with a maximum defined as I_0 , the gamma corrected image is of the form:

$$I'(x,y) = I_0 \left(\frac{I(x,y)}{I_0} \right)^\gamma. \quad (5.2)$$

The averaging technique of the four individual contrast images was repeated for the phase contrast summation over the entire retina.

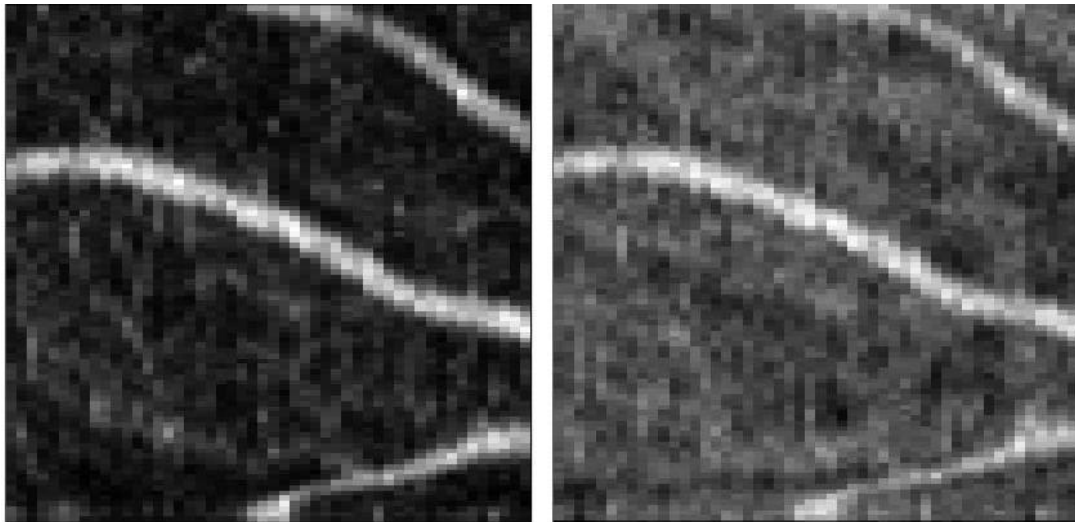


Figure 5.33: Mean en face contrast images from the repeating BM-scan method. The images created were for the top half of the retina (left) as well as the full retinal summation (right). Each image was gamma corrected to improve visualization of the weaker contrast regions.

In many cases, there may be transverse sample motion occurring during the data acquisition of the BM-scans. For this situation, vertical contrast lines may appear in the

phase variance contrast image that can obfuscate the vascular visualization. If two different buffered acquisitions were acquired successively but with the primary scan direction in perpendicular directions, the contrast lines due to transverse motion will occur in two different directions. These two images could be aligned and analyzed to allow improved vascular visualization.

Two sequential buffered acquisitions were taken using the repeating 100 transverse pixel BM-scan method, each with a primary transverse scan direction perpendicular to each other. In order to properly compare the images, the phase contrast summation images for the top of the retina were extrapolated into 100 x 100 pixel images. To improve visualization of the lower signal from the small vessels, the scale of the image was set to 75% of the same data in Figure 5.33.

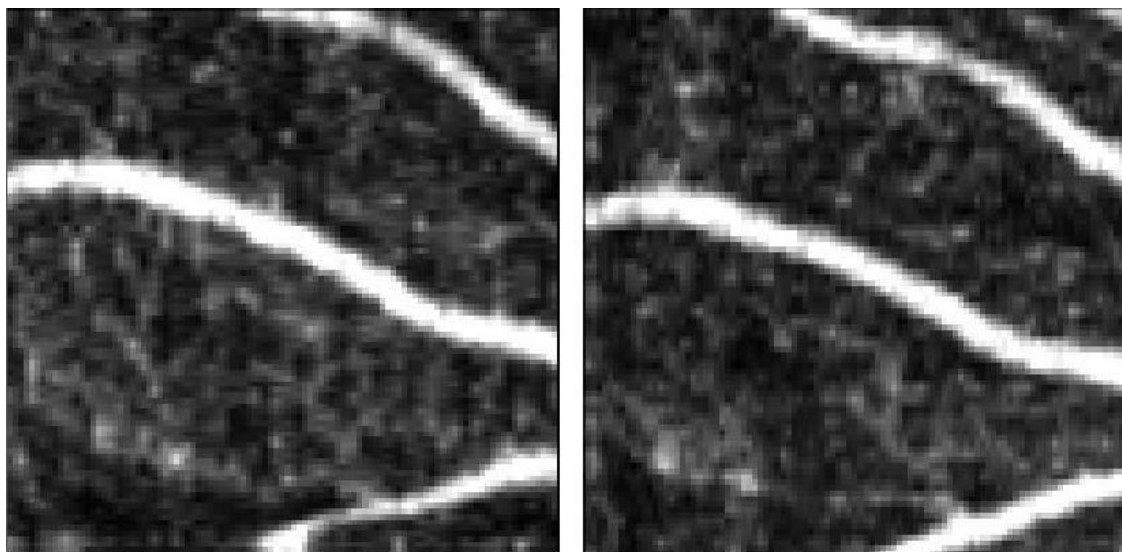


Figure 5.34: Mean contrast summation images from two different acquisitions of the repeating BM-scan method, summed over the top half of the retina. Images were acquired with perpendicular primary transverse scan directions. Images were extrapolated to the size of 100 x 100 pixel for comparison.

Aligning these two images to each other removes the motion between successive buffered acquisitions and takes the mean results in the image of Figure 5.35.

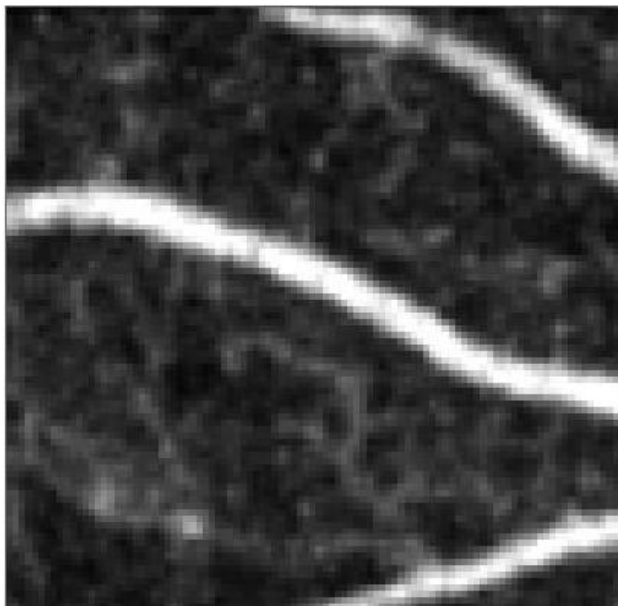


Figure 5.35: Mean of the two different mean en face contrast images of Figure 5.34 after transverse alignment.

The image in Figure 5.35 is basically the mean contrast from 8 different phase contrast summation calculations, trying to reduce the possible noise in the system while improving the vascular visualization. To adequately compare how well this technique visualizes vasculature, it needs to be placed side-by-side to the expected vasculature of the fluorescein angiography image of Figure 5.30, scaled to approximately the same size. Both images are taken from completely different mice and locations within the retina, so an exact comparison of specific vessels is not possible.

It needs to be noted that a direct comparison between the two images is not completely appropriate. Fluorescein angiography images are a gauge of the average blood occupying the transverse location at a given time, which is dependent on the thickness of the blood vessels. The mean phase contrast summation image also is dependent on the thickness of the blood vessel which is summed over, but the larger vessels also contain shadowing contrast which increases their contrast in comparison. Also, the contrast within the vessels in this case depends partially on the flow velocity properties, which can further reduce the relative contrast between the larger fast blood vessels and the smaller vasculature. The comparison that should be made between the averaged phase contrast summation image

and the fluorescein angiogram is the ability of both to observe the smallest vessels expected within the retina.

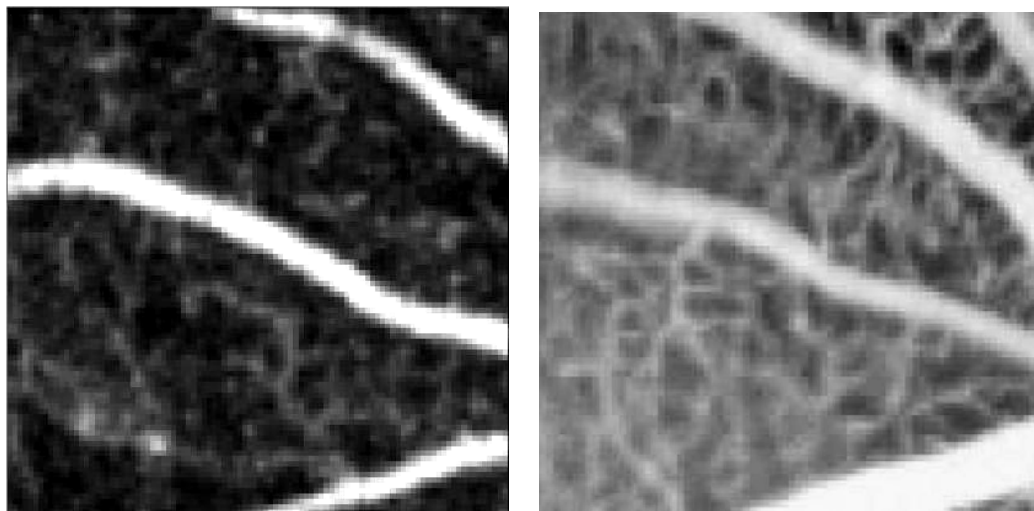


Figure 5.36: Comparison of the averaged phase contrast image to the expected form of fluorescein angiography. The phase contrast image, taken over the top half of the mouse retina presented in Figure 5.35 is compared to the angiography image of Figure 5.30, zoomed in to approximate a similar region of the mouse eye.

The contrast image presented in Figure 5.35 is just one possible form of analysis of what can be referred to as the 4D phase contrast data; 3D phase variance contrast information acquired repeatedly over time. Each stage in the image calculation uses a mean calculation: each en face contrast summation image is essentially a representation of the mean contrast over the chosen depth slice in the image, the mean contrast was calculated from all four en face images created from one buffered acquisition, and the two independent mean contrast images were aligned and averaged to create the final contrast image.

There are many other types of analysis that can be performed on the phase contrast data. If the final contrast image was created by using the maximum value of all of the individual contrast images, the signal from all the vasculature regions could be improved. Unfortunately, the maximum method would amplify the noise of any one image within the analyzed set. With any analysis technique, there is a tradeoff which comes from trying to separate the signal and noise when they are very similar. By trying to amplify the weak

contrast signal from regions, the noise of the image can be similarly amplified. By trying to exclude the noise terms from the contrast image, actual motion contrast signal can be lost due to the similarity.

For the small vascular regions, the contrast is very similar to noise. When flow occurs within the vessel during the imaging session, contrast is observed; otherwise, any possible contrast is obfuscated by the noise analysis of the image processing. Since the time in which flow occurs is random, the contrast observed for a flow location is also random in time, making it hard to distinguish from simply noise. Assuming that the contrast associated with flow from a vessel appears as a spatially localized pocket of high contrast, another form of analysis was used to isolate these regions from the weaker but spatially larger regions of noise which would create comparable summation image intensities. For a chosen depth region typically used for a contrast summation, a smaller window of approximately 20 μm was chosen to slide across the entire depth region, performing summations over the depth locations identified by the sliding window. The maximum summation within the depth region was used as the en face contrast image pixel.

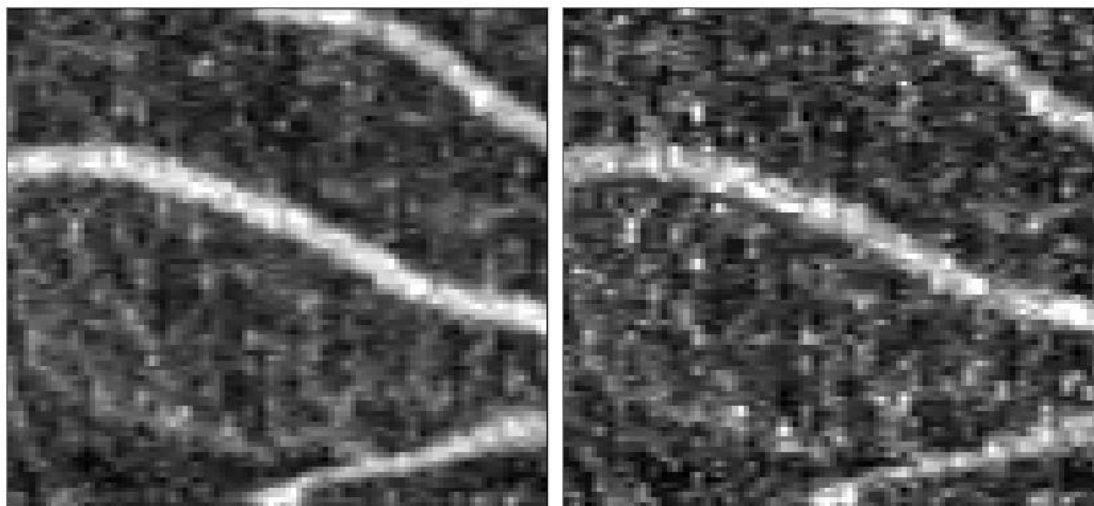


Figure 5.37: En face contrast summation images for the sliding window technique of 20 μm were calculated for the repeating BM-scan phase contrast data. The mean (left) and the maximum (right) of the four individual contrast images was calculated for the data set. Both images were gamma corrected and extrapolated to 100 x 100 pixels.

The sliding window technique was used on the repeating BM-scan phase contrast data to identify the largest localized contrast within the depth region and create en face images with these results. To allow multiple analysis techniques to be used, the mean and the maximum image of the four en face images within the buffered acquisition were calculated and presented in Figure 5.37. Both analysis techniques have definite visualization benefits, identifying potential vascularization regions not clearly visible in the other image. The data used for analysis and the depth region chosen was identical to the left image of Figure 5.34, allowing for a direct comparison of the analysis techniques for the same data.

With the demonstration of vascular visualization and all of the information available with the 4D phase contrast data set, there is a lot of potential of contrast improvements. With the available 3D contrast information, these techniques can develop into a form of 3D fluorescein angiography, which can be useful for a whole range of ophthalmic diagnostics beyond just AMD. For this to happen, one of the most important required factors is the ability to identify vascular contrast regions from a single 2D phase contrast image. The main problem in many images is the inability to identify contrast regions as sample motion contrast or simply contrast noise that needs to be removed. Further work and analysis will allow more properties of the vascular contrast regions to be identified for easier extraction, which results in improved visualization of the vascularization.

5.7 Discussions of Human Imaging

The phase contrast demonstrations of mouse retinal vascular imaging demonstrate the potential of these techniques for future ophthalmic diagnostics. While further study in mouse retinas may help the understanding of the contrast images and the noise experienced in the images, there are no experimental reasons to not move these contrast techniques into human retinal imaging. Safety standards have been in place for a long time with this technology and it will be very useful to determine how well these contrast methods can image the intended ocular disease symptoms (like leaking neovascularization).

The human retina, as opposed to the mouse retina, has many fairly well identified layers around the RPE and choroidal region. Even the rat has a more distinguished layering for the RPE and choroid compared to the mouse [4], even with a very high axial resolution. With the lack of separation observed between the RPE reflection and the choroidal reflections, the overlay of contrast and intensity images of Figure 5.26 is the only suggestion of two distinct regions. Human retinas will allow the confirmation that the regional difference in contrast observed is actually between the choroidal flow and the relatively static RPE.

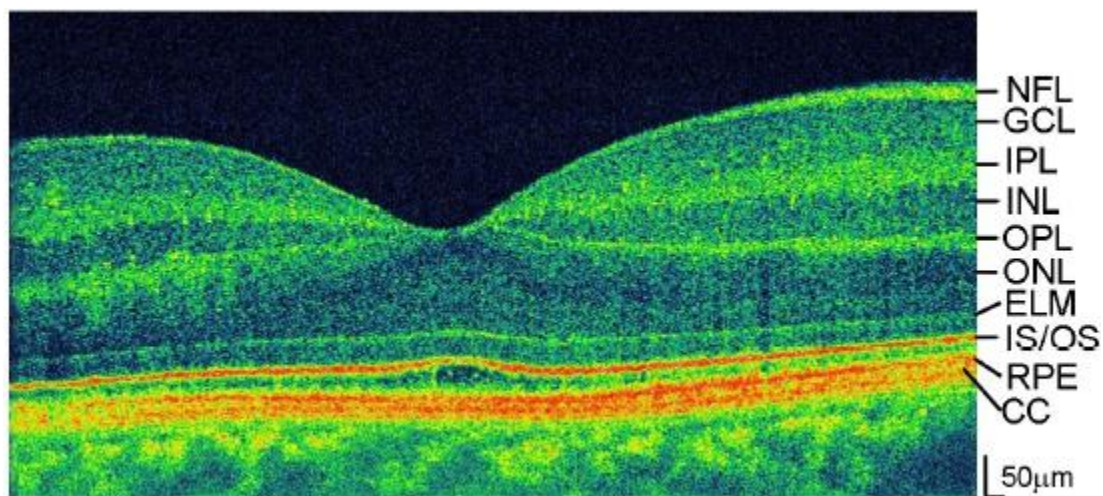


Figure 5.38: High density human retinal B-scan images created from 3000 A-scans across approximately 2.5 mm over the fovea. The image was reproduced from [8]. Axial resolution in tissue is approximately 2 µm for the imaging system.

Human retinal imaging also incorporates the ideal scenario for testing phase noise analysis and removal techniques which only comes from eyes containing high visual resolution: the blood vessel-free region of the fovea. By imaging healthy eyes, the region of the fovea provides the perfect negative control; any contrast observed in this region above the choroid is due to uncompensated phase error, transverse motion occurring of the sample, or some other effect which has not currently been considered. These images can be acquired simultaneously with the neighbouring regions which contain a well defined vascular structure, as demonstrated with fluorescein angiography.

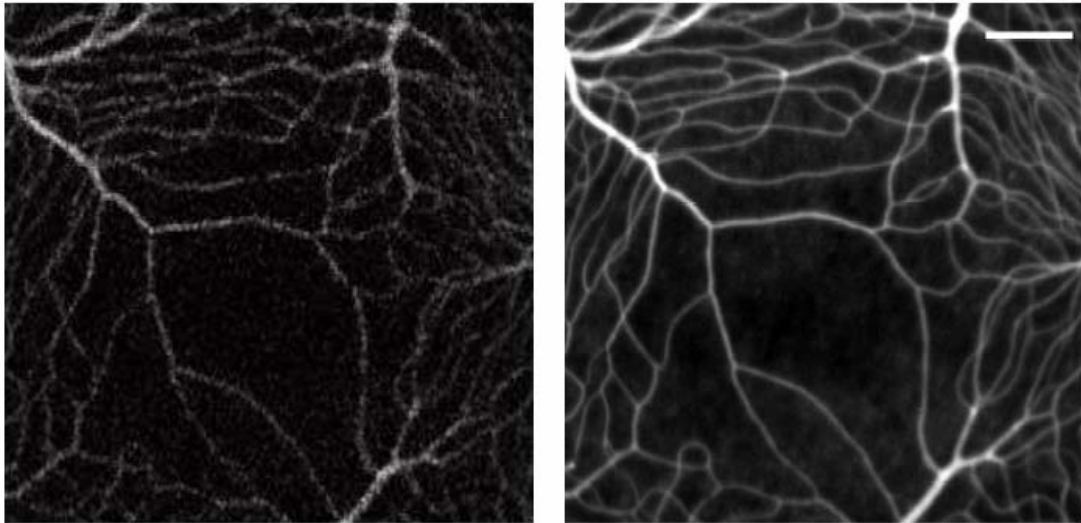


Figure 5.39: Fluorescein angiography images of monkey retina acquired with a high resolution high speed camera. A single frame of the camera (left) is compared to an image averaged from more than 1000 aligned images. Image reproduced from [9]. Scale bar on averaged image is 150 μm .

Fluorescein angiography of the monkey retina demonstrates a vascular structure very comparable to human retinas. The presented images are a single frame of the high speed camera in the system and the image after transverse motion alignment and averaging of more than 1000 separate frames from the camera. The foveal avascular zone in the center of the image is surrounded by a complete capillary bed. The small fluorescein signal observed around foveal region in Figure 5.39 is likely a fraction of the choroidal vascularization, not easily observed with fluorescein imaging due to the absorption of the light by the RPE.

The single frame of the angiography image is a great example of what might occur for the ideal case of a single en face contrast summation image in the retina. The major blood vessels surrounding the fovea have contrast in the vasculature, but the blood is not in all regions for any given time point. The faint fluorescein signal observed in the averaged image, which might be choroidal flow, is not observed at all within a single angiography image from the high speed camera. With additional noise, the single camera image would also have a hard time observing some regions of the vasculature with the finer structure,

making a situation very similar to the introduction of phase noise to the en face contrast image. With improvements to the analysis techniques, the phase contrast methods demonstrated for SDOCT have the potential to not only mimic the imaging capabilities of fluorescein angiography but add additional information not available with the previous technique.

5.8 References

1. E. Garcia de la Cera et al., "Optical aberrations in the mouse eye," *Vision Research* 46, 2546 (2006).
2. M. Paques et al., "High resolution fundus imaging by confocal scanning laser ophthalmology in the mouse," *Vision Research* 46, 1336 (2006).
3. "Cell tracking using SLO angiography – Bio-Medical Physics & Bio-Engineering, University of Aberdeen," <http://www.biomed.abdn.ac.uk/Abstracts/A00665/>.
4. V. Srinivasan et al., "Noninvasive Volumetric Imaging and Morphometry of the Rodent Retina with High Speed, Ultrahigh-Resolution Optical Coherence Tomography," *Invest. Ophthalmol. Vis. Sci.* 47, 5522 (2006).
5. S. Makita et al., "Optical Coherence Angiography," *Opt. Express* 14, 7821 (2006). <http://www.opticsexpress.org/abstract.cfm?id=97672>.
6. R. D'Amato et al., "Microscopic Visualization of the Retina by Angiography with High-Molecular-Weight Fluorescein-Labeled Dextran in the Mouse," *Microvascular Research* 46, 135 (1993).
7. N.L. Hawes et al., "Mouse fundus photography and angiography: A catalogue of normal and mutant phenotypes," *Molecular Vision* 5, 22 (1999).
8. M. Wojtkowski et al., "Ultrahigh-resolution, high-speed, Fourier domain optical coherence tomography and methods for dispersion compensation," *Opt. Express* 12, 2404 (2004). <http://www.opticsexpress.org/abstract.cfm?id=80147>.
9. D.C. Gray et al., "In vivo fluorescence imaging of primate retinal ganglion cells and retinal pigment epithelial cells," *Opt. Express* 14, 7144 (2006). <http://www.opticsexpress.org/abstract.cfm?id=96196>.

SUMMARY AND CONCLUSIONS

The work in this thesis is based around applying similar phase variance analysis techniques to different imaging situations in order to produce the optimal motion contrast images in the most efficient method. There are many observations that can be summarized for the phase variance contrast experimental data:

1) Waiting longer can help motion contrast measurements

In Chapter 3.3, the phase measurements resulting from several different types of motion were theoretically calculated. For each case, an increase in time between phase measurements resulted in an increase in the measured phase change (up to the limits of phase wrapping and complete randomness in the phase measurements). This fact has been experimentally demonstrated in Figure 3.14 for the case of Brownian motion. The main accuracy limitation of phase measurements is the SNR-limited phase noise, which is a property independent in time. Instead of trying to reduce this lower bound on phase measurements, waiting longer between phase measurements allows for the slow motions to move beyond the accuracy limitations of the system (e.g., if the phase accuracy for a given reflection is 0.5 radians, the time separation between measurements must be large enough that the reflection is able to move more than 0.5 radians for motion to be seen).

Increasing the time separation between phase measurements improves the visualization of slow motions but adds complications to regions of fast flow. With faster motions comes an increased likelihood of phase wrapping, with the possibility that fast transverse motion will move the reflection completely out of the imaging beam waist. In Doppler flow imaging, the maximum axial flow that can be quantitatively measured is reduced when the time separation between phase measurements is increased (due to phase wrapping).

Phase variance calculations do not suffer the same limitations for regions of fast flow in the cases of increased time separation between phase measurements. Phase wrapping and transverse motion out of the imaging beam cause the variance measurement to saturate at a maximum level consistent with a purely random signal. Waiting longer between phase measurements has the added benefit of increasing the ability to observe random occurrences due to the increased time in which the phase measurements are acquired.

2) Waiting longer can increase motion noise in measurements

From the experimental data, the main sources of phase noise observed were SNR-limited phase error and noise created from transverse motion occurring during the contrast image acquisition time. While numerical calculations can remove most of the SNR phase error, the demonstrated removal techniques of the transverse motion error are in the very early developmental stages. It is much easier to simply create a situation in which no transverse motion error occurs within the phase contrast image. The longer the time separation between phase measurements in the contrast image, the more likely that transverse will occur within that image.

It becomes a tradeoff between increasing the observed motion contrast and trying to avoid potential transverse motion of the sample. The optimal imaging parameters depend on the sample properties: the expected motion of the reflections of interest as well as the amplitude and frequency of bulk transverse motion. If the motion signal within the sample is fast enough that the variance measurements become saturated for a given time separation (identical to a completely random phase measurement), increasing time separations further will only increase susceptibility to motion noise in the system without adding any additional motion contrast to the image. Flexibility of the time separation between phase measurements used for the contrast image allows for adjustment to optimize the imaging for a given sample.

3) Minimum BM-scan time is hardware limited

The BM-scan acquires multiple successive B-scans over the same transverse location in order to calculate the phase change that occurs during the time it takes for the acquisition to return to the same original location. The minimum time between phase measurements is defined as the minimum time between B-scans, which is limited by the A-scan acquisition time of the spectrometer and the speed of the transverse scanners. A uni-directional scan pattern for the BM-scan consists of the transverse scan of the B-scan acquisition as well as the fly-back to quickly return to the starting transverse position of the scan. This scan pattern is a very efficient method of ensuring a constant time separation between phase measurements, with the fly-back portion of the scan as the only wasted time within the acquisition. The fly-back time of the transverse scan is limited by the maximum achievable speed of the transverse scanner, which is a hardware limitation of galvanometer scanners like those used in the experimental systems.

The B-scan acquisition time is limited by the number of transverse locations chosen and the A-scan acquisition speed. In some of the presented mouse retinal imaging data, the BM-scan was altered by reducing the number of transverse locations by a factor of two. The majority of the observed flow within the mouse retina was fast enough such that the phase variance measurements were saturated with time separations of 10 ms. In this case a reduction of the time separation to 5 ms did not substantially reduce the observed motion contrast, suggesting that the same motion contrast may be observed in the mouse retina for even shorter time separations of the BM-scan. Technological improvements are allowing faster data transfer rates of SDOCT cameras as well as the development of SSOCT light sources with A-scan rates that are faster than experimentally demonstrated SDOCT. These A-scan speed improvements would allow for shorter BM-scan time separations, potentially maintaining the same motion contrast while reducing the phase noise created by bulk transverse motion from the sample. Sometime in the near future, BM-scan contrast methods can be implemented on systems with different limitations on the minimum time of BM-scans to explore this possible improvement.

Even if the fly-back of transverse scanning was not a problem and the A-scan rate could be as fast as possible, the optimal time separation between phase measurements might be very similar to the currently chosen parameters. In zebrafish imaging, phase variance contrast was visible but not saturated for time separations of 1 ms in the MB-scan. To improve this visualization, an increase in the time separation would be suggested. The minimum time of the BM-scan presented was 5 ms for the 100 transverse pixel repeating BM-scan case. The only case where minimizing the BM-scan time further would be beneficial is when all of the expected motion in the system is relatively much faster than the zebrafish. Without any parameters known of the expected motion of the choroidal neovascularization, it would be premature to predict a benefit to any substantial reduction to the minimum BM-scan time. Hardware improvements resulting in increased A-scan acquisition rate and improved transverse scanning could result in larger B-scans in each BM-scan for the exact same time separation of phase changes. This would improve the scan region and the data throughput for the same phase contrast images if multiple buffered acquisitions were required.

4) MB-scan can be useful – just not as a screening tool

In all of the demonstrated 3D contrast images, no MB-scan data was shown at all. This is largely due to the inefficiency of data acquisition with this method, requiring multiple buffered acquisitions to acquire any 3D contrast data. Also, the contrast images were frequently unable to produce strong phase variance contrast from the flow within vessels of zebrafish, which was approximately 0.5 mm/s. The inefficiency of this acquisition technique and the requirement of fast flows for the phase variance contrast severely limit the usefulness of the MB-scan as a vascular screening tool. Once vascular events have been identified within a sample using the BM-scan techniques, the MB-scan can act as a quantitative diagnostic of the vasculature. The MB-scan has the ability to measure axial flow and incorporate increased statistics to the flow and variance calculations. With vascular directionality extrapolated from the 3D BM-scan data, flow velocity can be extracted from the axial component measured with the MB-scan data. As a companion technique to the BM-scan vascular screening capabilities, the MB-scan can find its place within diagnostics.

One of the main issues with the MB-scan is that transverse motion cannot be easily dealt with in this case. While it becomes less likely that motion will occur for a given M-scan due to the shortened time separation compared to the BM-scan, when transverse motion does occur, the developed techniques for the BM-scan can not be applied. BM-scan transverse motion analysis relies on the fact that the entire BM-scan experiences approximately the same transverse motion during the phase contrast acquisition. This correlation provides the basis for the additional noise removal, which is information not available in the MB-scan data. Further work would be required to develop removal techniques of any transverse motion occurring during an MB-scan.

The situation in which the MB-scan variance contrast method might have potential as a screening tool is in cases with extremely stable sample position and no restrictions on total data acquisition time. With all of the available statistics acquired in this method, more analysis techniques become available including the analysis of the evolution of phase contrast for different time separations. For the agarose/Intralipid images, increasing time separation between phase measurements in the phase variance contrast image changed the total image contrast. The functional form of these changes can provide another type of information that can be the basis of additional image contrast.

Retinal imaging does not have the transverse motion stability required to produce a 3D phase contrast data set from MB-scans of sequential memory buffers. While choroidal flow motion contrast was visible with some of the larger time separations of the MB-scan, the susceptibility of the method to transverse motion noise reduces the feasibility of use in retinal imaging situations.

5) Human retinal contrast imaging looks very promising

Experimental systems producing aberration-corrected high-transverse resolution confocal images of the human retina have demonstrated images without any obvious transverse motion at an image rate of approximately 20 Hz, equaling 50 ms image acquisition time. This means that the average human can be considered essentially transverse motion-free for

any given 50ms time period. Each BM-scan contrast method presented for the mouse retinal imaging acquired each 2D phase variance contrast images data in 25 ms or 50 ms for 100 and 200 transverse pixels, respectively. This suggests that the current contrast parameters implemented directly into human retinal imaging should produce contrast images without much transverse motion noise.

The three main sources of transverse motion of human retinal imaging are tremor, drift, and microsaccades. Tremors are usually small-amplitude, high-frequency motions of the eye that will most likely limit the ultimate performance of the imaging for a given patient. With enough information, improved noise removal might be able to deal with this completely. Drift is a slow motion of the fixation and transverse position of the eye. Fixation targets for the patient to focus on, as well as head rests reduce a lot of these factors over the course of the imaging session. Microsaccades are sharp jerks of the transverse position of the eye that can occur randomly in time for human eyes. This motion is a major issue in retinal imaging and requires additional work to identify and re-align the images when microsaccades occur. For contrast imaging with OCT, each microsaccade will likely cause contrast noise within several BM-scans that will require them to be thrown out of the data set due to the excess phase noise. While increased statistics and phase analysis can reduce the effect of these motions, implementing realignment techniques previously developed for confocal retinal imaging can further improve the imaging capabilities of the system.

Conclusions

Phase changes calculated from OCT measurements are capable of determining very small motions on the scale of nanometers. Phase change variance calculations have demonstrated motion contrast for several types of motion including mobility and flow, independent of the flow orientation. Within the memory buffer limitations of the acquisition system used in the experiments, 3D phase contrast has been demonstrated in 5.2 seconds of acquisition time. Within the microscopy imaging of the zebrafish and within the mouse retinal images, the calculated phase contrast data represents 3D vascular visualization. Future directions on

phase contrast techniques can refine the analysis procedure, focusing on improving the noise removal techniques associated with transverse motion. These techniques have excellent potential for transitioning into human retinal imaging, which may have new forms of motion noise within the sample that require removal.

The major source of motion expected within retinal imaging is microsaccades, fixation adjustments of the eye. With the reduction of acquisition time of the 3D phase contrast data set, the noise created due to the microsaccades of the patient is reduced as well. Increased statistics and re-alignment can be used with other improved analysis tools to improve the motion contrast visualization of the vasculature within the human retina. The resulting contrast data has the potential of matching the visualization capabilities produced by fluorescein angiography images, but with the added benefit of 3D visualization.

3D vascular visualization capabilities using motion contrast techniques with OCT imaging of retina are ideal as a screening tool. With some development, these techniques can be implemented for early identification of wet age-related macular degeneration. Doppler flow imaging capabilities of the OCT system were previously determined not to be ideal as a screening tool but combined with the visualization capabilities of the phase variance contrast techniques, it can be a useful diagnostic. With the location and directionality of vasculature determined using vascular visualization, Doppler flow imaging techniques can quantify vascular flow within the images, which is an important metric for a variety of retinal diseases beyond AMD. 3D screening and diagnostic capabilities of the OCT imaging system offers many possibilities for improvements to retinal disease diagnosis and treatments. In time, the techniques developed in this thesis may become standard for clinical diagnosis of retinal vascular diseases.